UNIVERSIDAD DEL PAÍS VASCO / EUSKAL HERRIKO UNIBERTSITATEA
Programa de Doctorado de Física

eman ta zabal zazu

Universidad del País Vasco   Euskal Herriko Unibertsitatea

Towards a Comprehensive and Extended Use of Nitrogen-Vacancy Centers in Diamond for Quantum Technologies

DOCTORAL THESIS

Submitted for the degree of Doctor in Physics by:

Iván Panadero Muñoz

Director:

Erik Torrontegui Muñoz

July, 2025

Universidad del País Vasco Euskal Herriko Unibertsitatea

UNIVERSIDAD DEL PAÍS VASCO / EUSKAL HERRIKO UNIBERTSITATEA
Programa de Doctorado de Física

Doctoral Degree in Physics

Towards a Comprehensive and Extended Use of Nitrogen-Vacancy Centers in Diamond for Quantum Technologies

DOCTORAL THESIS

Submitted for the degree of Doctor by:

Iván Panadero Muñoz

Under the supervision of:
Dr. Erik Torrontegui Muñoz

March, 2025

Title: Towards a Comprehensive and Extended Use of Nitrogen-Vacancy Centers in Diamond for Quantum Technologies
Author: Iván Panadero Muñoz
Doctoral Programme: Physics

Thesis Supervision:

Dr. Erik Torrontegui Muñoz, position Universidad Carlos III de Madrid

External Reviewers: Boris Naydenov and Nir Bar-Gill

Thesis Defense Committee:

Thesis Defense Date:

A Judit

Acknowledgement

This thesis is a dim shadow of an almost four-year journey that has shaped me both professionally and personally. It involved leaving Madrid, my home, to move to Tenerife to seek new research challenges. This work was born out of the collaboration between a private research company, Arquimea Research Center, and two universities: Universidad Carlos III de Madrid and Universidad del País Vasco. This stimulating environment provided me with the opportunity to meet dozens of researchers and professionals from whom I have gained invaluable skills and knowledge. They placed their trust in me and, thanks to their support, I have been able to reach this point in my journey.

First, I would like to express my gratitude to my supervisor, Erik Torrontegui, for his invaluable guidance and patience throughout this process. He showed me how to navigate between the complexities of research and the practicalities of the real world and taught me the importance of attention to detail.He has always been keen to help and generously shared his knowledge, ensuring that I could overcome obstacles and continue progressing. His support has been fundamental not only in shaping the direction of my research, but also in helping me grow as a scientist.

Hilario Espinós and I started the PhD together and throughout these years he has been an invaluable support during times of uncertainty and frustration. He has constantly inspired me to improve and pursue my goals with dedication and patience. Looking back, it is incredible how much we have grown and changed together and how our journey has turned him into an indispensable friend. His good mood and character has been a source of strength and motivation. I am truly grateful for all the experiences and good moments we have shared and enjoyed. Our journey goes far beyond this thesis, and I look forward to all the future challenges and successes in which we will continue to support each other.

I also thank the postdocs who were part of this project and with whom I had the privilege of working closely: Ander Tobalina and Ricardo Puebla. It fills me with pride to have witnessed their growth into important research positions. They were a constant source of support in solving the most challenging technical problems and their advice has consistently proven invaluable.

I am grateful to Jorge Casanova, who introduced us to NV centers and shared his expertise. I also thank Pablo Acedo, whose guidance advanced our experimental progress and whose passion for science inspired enthusiasm and curiosity in those around him. I am also grateful to Yue Ban for his invaluable help in reviewing some of this work. Also, thanks to Gloria Platero, who mentored me early in my research journey.

This work would not have been possible without the support of external collaborators. I am deeply grateful to Boris Naydenov for welcoming me into his lab in Berlin, fostering my curiosity, and being a warm and supportive mentor. Thanks also to Lucas Tsunaki, Ksenia Volkova, Sergei Trofimov, and Eva Starykh, whose insights and kindness made my stay unforgettable while teaching me the art of single NV detection.

During the final months of my PhD Daniel Wirtitsch and Michael Trupke welcomed me to their lab in Vienna. They were excellent hosts, providing valuable feedback and fostering an enriching collaboration. Their work inspired me to explore new research directions and broaden my perspective on the field.

I would like to thank Maabur Sow and Fedor Jelezko from Ulm University for traveling to Tenerife to assist with technical challenges and lending us the implanted diamond that contributed to some of the key results of this work. I am grateful for their time, generosity and for sharing their expertise with such patience and support.

I am deeply grateful to Cristina de Dios, my Arquimea supervisor. Her professionalism and kindness were a constant source of admiration, not only for me but for everyone who worked with her. She was an exceptional mentor who taught me the value of teamwork, taking pride in one's work, and how to face and learn from failure. She knew how to motivate her team and played a pivotal role in driving the progress of this thesis forward. Her achievements have shown me the transformative power of science and its profound impact on society, inspiring me to dream big and to strive for meaningful contributions.

I am grateful to all the wonderful people I had the privilege of working with during my nearly four years at Arquimea. Roberto Barreiro, who guided me when I first arrived in Tenerife and taught me to embrace the challenges and joys of lab work. Francisco Belda, whose boundless energy and enthusiasm were truly motivating. Eva Caravaca, whose discipline, commitment, and dedication were a constant source of inspiration. Alejandro Lorenzo, who taught me the value of perfectionism and attention to detail in the lab. Borja Jerez, a mentor who helped me navigate difficult decisions, stressed the importance of professional growth and clear goals. Julio Posada, with his deep curiosity and determination to answer every question. Victor Vilvazo, who showed me the importance of well-organized projects and effective risk management. We give special thanks to Jose Carlos Guerra, who became a confidant and partner in the lab. His friendship will be a lasting highlight of this journey.

I would also like to thank Saúl Vikran, who was always willing to answer my inquiries regarding the confocal microscope. To Alfonso Fernández, whose passion for learning was truly inspiring. And especially to Marta Arceiz, who worked closely with me, always as a respectful and enjoyable companion, encouraging me to become a better scientist.

All of them were close collaborators who played a key role in the development of this thesis. However, the list of people in Tenerife who became friends, inspired me, helped me when I needed, or taught me invaluable professional and personal lessons is immense. Although it is impossible to include personal thanks for each of them here, I want to list them and acknowledge them collectively because they became a vital source of support and camaraderie when I was far from home. In the years to come, when I look back on this thesis, their names and the memories they evoke will undoubtedly bring a smile to my face. Marta Portela, Sergio Capitán, Rubén Criado, Miguel López, Yézer Gonzalez, Orlando Avila-García, Daniel Eusebio, Guillermo Laso, Doramas Baez, Carlota Martín, Fernando Rivas, Raquel de la Rosa, Tony, Rocío, Borja, Eduardo

Martín, Mario Calleja, Nacho Planelles, Alejandro Hernández, Manuel Breogan, Sara Vidal, Andrea Montón, Lucia Morillo, Laura Trigueros, Eduardo Mata, Alejandro Torres, Daniel Padrón, Humberto Gonçalves, Jaime Bravo, María Alba Martín, María Azpiroz, Paula Sempere, Jorge Arbelo, Jorge Rapp, Alan Frenquel, and Elena Lopez. Special thanks to Carlos Abengoza and his strong hugs and to Catalina Cobos, who was a constant source of joy and affection and now one of my favorite persons.

I could not have completed this journey without the unwavering support and encouragement of my family. My dad, Teo, and my mom, Sonia, have always cared for me with love, supported my scientific career, and served as role models, teaching me to value what truly matters in life. To my grandparents, Marcelino and Teo, and my grandma, Engracia, who instilled in me the importance of knowledge and hard work, and whose love and tenderness have always been a source of strength. Thank you grandma for all the ham and tea you send me to Tenerife. And to my sister, Elena, whose determination, immense empathy, and genuine willingness to listen when it matters most continue to inspire me and help me. Thanks for every time they picked me at the airport and solved my problems with the car and the house. I am so grateful for every recipe you shared over the phone and the countless ways you have been there for me.

The same gratitude extends to my friends in Madrid, who have believed in me every step of the way. My heartfelt thanks go to Pablo, Blanca, Gloria, Eva, Jorge, Isa, Jose, Pascu, and Marcos. I hope they feel as proud of me as I do of them. This thesis is the culmination of all the moments we have shared together. It represents another step of a much longer journey I share with them, one that began in high school, continued through university, and goes beyond...

Finally, I want to thank Judit, to whom I dedicate this thesis. We met just weeks before embarking on this journey and she has been with me every day since the very beginning. She has stood by me through every achievement, failure, and decision, as if each moment were her own. I have always found answers in her natural wisdom, and her joy has been a constant source of light and inspiration. Thank you for every visit, for everything you have done for me, and for teaching me to live with intensity and joy. Our journey together has run in parallel with my own path through this thesis, and it has been a privilege to share this experience with you.

Resumen

Casi un siglo después del desarrollo de la mecánica cuántica, tanto sus fundamentos teóricos como los avances tecnológicos han progresado rápidamente. La mecánica cuántica, con propiedades como la superposición y el entrelazamiento, ofrece el potencial para tecnologías inalcanzables mediante medios clásicos. La primera revolución cuántica, hace casi un siglo, dio lugar al desarrollo de tecnologías fundamentales. Estas tecnologías se hicieron posibles gracias a nuestra comprensión de la mecánica cuántica, pero no aprovechan completamente su potencial, el cual requiere un control preciso sobre unidades cuánticas aisladas.

En los últimos treinta años, los métodos para aislar sistemas cuánticos han avanzado, lo que nos ha permitido controlar y confinar sistemas cuánticos individuales. Esto ha iniciado la segunda revolución cuántica, que promete avances en computación cuántica, comunicación y sensado. Sin embargo, escalar los sistemas cuánticos sigue siendo un desafío, particularmente el equilibrio entre aislar los qubits y crear interacciones fuertes y coherentes entre ellos.

Mientras la tecnología para la computación cuántica madura, aún podemos avanzar en aplicaciones del mundo real de la mecánica cuántica que exploten sus propiedades. El sensado cuántico aprovecha justamente la propiedad que la computación cuántica busca evitar: la interacción con el entorno. Los sensores cuánticos capitalizan la debilidad central de los sistemas cuánticos: su alta sensibilidad a las perturbaciones externas. En el sensado cuántico, el objetivo es explotar la extrema sensibilidad de los sistemas cuánticos a señales externas para medirlas con alta precisión. Esto requiere que el sistema cuántico esté deliberadamente acoplado al entorno externo para detectar cambios sutiles. Como resultado, mientras los sistemas de computación cuántica buscan el aislamiento para proteger la coherencia, los sistemas de sensado cuántico están diseñados para ser altamente sensibles a interacciones específicas, lo que hace que el equilibrio entre aislamiento y acoplamiento sea una consideración central en el desarrollo de tecnologías cuánticas.

Los sensores cuánticos vienen en diversas formas, cada una adecuada para aplicaciones específicas. Entre ellos, los sistemas de espín en estado sólido, particularmente los defectos de espín en materiales como diamante y silicio, han ganado gran atención debido a su estabilidad y potencial de miniaturización. Los defectos de espín, como los centros de nitrógeno-vacancia (NV) en diamante, han atraído atención considerable debido a su capacidad para operar a temperatura ambiente y su estabilidad en cristales muy pequeños y nanostructuras. El centro NV es un defecto puntual que consiste en un átomo de nitrógeno adyacente a una vacancia en la red de carbono. Su fluorescencia dependiente del espín permite la detección óptica de campos magnéticos, proporcionando una herramienta altamente sensible para sondear diversas cantidades físicas, como campos magnéticos, lo que convierte a los centros NV en una plataforma líder para tecnologías de sensado cuántico.

La fluorescencia del centro NV ha permitido estudios exhaustivos de sus propiedades

físicas, incluyendo el comportamiento de excitación, la dependencia con la longitud de onda, los procesos de ionización, la dinámica de espín y los efectos térmicos, entre otros. Su fluorescencia generalmente se modela utilizando ecuaciones de tasas para las poblaciones de niveles, pero esta tesis introduce un nuevo marco teórico para modelar las estadísticas de emisión de fotones (PES) del centro NV.

Aunque los modelos tradicionales basados en ecuaciones de tasas han sido útiles para describir las propiedades ópticas de los centros NV, estos enfoques no permiten capturar de manera precisa la emisión de fotones, que depende no solo de las poblaciones de los estados electrónicos del sistema, sino también de las transiciones dinámicas entre los estados cuánticos.

Para abordar estas limitaciones, esta tesis propone un modelo basado en el formalismo de saltos cuánticos, que permite una descripción más completa de la emisión de fotones, esencial para entender el comportamiento de los centros NV en situaciones experimentales. Estos modelos se habían aplicado anteriormente a otros sistemas cuánticos, pero no al estudio de la fluorescencia del centro NV. A través de este modelo, se puede estudiar cómo la emisión de fotones está influenciada por el estado de espín del centro NV, lo que permite una lectura óptica dependiente del espín altamente sensible, una característica crucial en aplicaciones como el procesamiento de información cuántica y la detección de campos magnéticos.

Además de proporcionar una visión más detallada de la emisión de fotones, el modelo propuesto permite obtener funciones de autocorrelación temporal, que son fundamentales para caracterizar la coherencia temporal y la interferencia cuántica en los centros NV. Esta nueva aproximación no solo mejora la comprensión de las propiedades de fluorescencia de los centros NV, sino que también abre la puerta a la optimización de protocolos experimentales para el sensado de campos magnéticos y otras aplicaciones cuánticas, permitiendo una conexión directa entre el estado cuántico del sistema y la secuencia de fotones detectados.

La contribución a la caracterización va más allá de los centros NV, ya que el método PES puede adaptarse a otros centros de color y sistemas cuánticos. La capacidad del modelo para incorporar fenómenos complejos, como la ionización, la dependencia con la longitud de onda y la absorción de dos fotones, ofrece una herramienta potente para mejorar las mediciones actuales de centros NV, proponer nuevas técnicas de lectura y aumentar la sensibilidad y precisión de los dispositivos de sensado cuántico.

La validez del modelo PES fue confirmada mediante una comparación exhaustiva con datos experimentales obtenidos de sistemas de centros NV en el laboratorio. Los resultados experimentales demostraron que el modelo puede replicar con alta precisión fenómenos clave, como la distribución temporal de los fotones emitidos y las funciones de autocorrelación de segundo orden. Esto valida no solo la exactitud del modelo en la representación de la dinámica de emisión de fotones, sino también su capacidad para predecir el comportamiento de los centros NV bajo diversas condiciones experimentales. Además, el modelo facilita el estudio de fenómenos de detección imperfecta, como las ineficiencias en los detectores ópticos, lo que permite evaluar el impacto de estos errores en la caracterización de los centros NV y optimizar el diseño de sistemas experimentales. La mejora en la caracterización de los centros NV es esencial para aplicaciones de sensado cuántico en campos como la metrología, la detección de biomoléculas y la navegación cuántica.

El modelo PES desarrollado en esta tesis marca un avance significativo en el entendimiento de la fluorescencia de los centros NV. Este modelo no solo mejora nuestra capacidad para modelar las interacciones cuánticas en estos sistemas, sino que también abre nuevas oportunidades para diseñar protocolos de sensado cuántico más eficientes y precisos. La posibilidad de simular dinámicas complejas, como la llegada de fotones y la ionización, proporciona una herramienta esencial para optimizar el rendimiento de las aplicaciones cuánticas basadas en centros NV, desde la metrología cuántica hasta la computación cuántica.

Una comprensión profunda de la fotofísica de los centros NV es crucial para avanzar en la tecnología basada en centros NV. Mientras que la investigación fundamental continúa explorando las propiedades electrónicas y de espín de los centros NV, este conocimiento se está aprovechando cada vez más para investigar fenómenos cuánticos, como el entrelazamiento y la superposición, y para sondear sistemas a escala nanométrica con una precisión sin precedentes. Estos estudios han allanado el camino para aplicaciones prácticas de los centros NV, incluyendo avances en bio-sensores y técnicas de RMN a escala nanométrica. Sin embargo, realizar completamente el potencial de los centros NV en escenarios del mundo real presenta varios desafíos técnicos.

Esta tesis presenta un microscopio confocal compacto como una solución innovadora a la limitación de tamaño y costo que enfrentan los sistemas cuánticos basados en centros NV. Los sistemas experimentales utilizados para detectar y controlar centros NV suelen ser grandes, costosos y complejos, lo que hace que su adopción sea limitada a laboratorios de investigación altamente especializados. Este microscopio confocal compacto fue diseñado con el objetivo de reducir el tamaño del sistema sin comprometer su rendimiento y precisión. El microscopio compacto desarrollado en esta tesis integra las funciones esenciales para manipular centros NV—desde la inicialización óptica y la lectura de espín hasta el control coherente de estados cuánticos—y su diseño accesible abre la puerta a que instituciones con recursos limitados puedan incursionar en investigaciones cuánticas de vanguardia.

El microscopio fue diseñado para ser portátil y modular, lo que facilita su uso en una variedad de entornos experimentales, más allá de los laboratorios especializados. Esto es particularmente importante para llevar las tecnologías cuánticas a aplicaciones prácticas fuera del laboratorio, como en la industria, la biomedicina o la investigación de campo. Además, el sistema es lo suficientemente flexible como para ser adaptado a diferentes tipos de experimentos y configuraciones, lo que lo convierte en una herramienta versátil para los investigadores.

La eficacia del microscopio confocal compacto fue validada mediante una serie de experimentos que incluyeron la detección de centros NV individuales y el control de espín con alta fidelidad. Los resultados mostraron que el microscopio es capaz de realizar mediciones cuánticas avanzadas con una precisión comparable a la de los sistemas más grandes y complejos. Este logro demuestra que el microscopio compacto puede realizar las mismas tareas fundamentales necesarias para trabajar con centros NV, pero con un tamaño y coste significativamente reducidos.

Uno de los aspectos más notables de la validación experimental fue la capacidad del microscopio para realizar mediciones cuánticas de control coherent en centros NV individuales. Estos experimentos confirmaron que el microscopio confocal compacto es capaz de obtener mediciones de alta precisión y sensibilidad, lo que refuerza su potencial para aplicaciones en sensado cuántico y otras áreas que requieren la detección precisa de señales cuánticas.

El microscopio confocal compacto desarrollado en esta tesis tiene un impacto directo en la accesibilidad de las tecnologías cuánticas basadas en centros NV. Al reducir el tamaño y costo de los sistemas experimentales, este microscopio permite que las tecnologías cuánticas sean más accesibles para instituciones con recursos limitados. Además, su versatilidad y portabilidad lo hacen ideal para su uso en una amplia gama de aplicaciones, desde la investigación fundamental hasta las aplicaciones industriales y biomédicas. Este avance experimental no solo mejora la eficiencia de las mediciones cuánticas, sino que también democratiza el acceso a las tecnologías cuánticas, permitiendo su adopción a una escala más amplia.

Desarrollar sistemas robustos para la interrogación de centros NV es esencial, pero lograr un control coherente del espín del centro NV es igualmente crucial para realizar mediciones de alta precisión y sensibilidad. Esto requiere mantener estados cuánticos coherentes durante períodos prolongados. Tanto la computación cuántica como el sensado cuántico dependen de esta coherencia para procesar información y medir cantidades físicas. Las técnicas desarrolladas inicialmente para minimizar la decoherencia y optimizar la fidelidad de las puertas cuánticas en ordenadores cuánticos, como el desacoplamiento dinámico y los protocolos de corrección de errores, pueden adaptarse para mejorar el rendimiento de los sensores cuánticos. Además, los algoritmos cuánticos que aprovechan el entrelazamiento y la superposición deben aplicarse en el sensado cuántico para mejorar la detección de señales débiles y lograr mediciones de alta precisión.

El aprendizaje automático cuántico (QML, por sus siglas en inglés) es un conjunto de algoritmos cuánticos que presenta una frontera emocionante en el aprovechamiento de las propiedades de los sistemas cuánticos. Los algoritmos QML pueden ofrecer aumentos significativos en la velocidad para procesar grandes conjuntos de datos y resolver problemas complejos de optimización que serían intratables para los sistemas clásicos. Esta tesis investiga arquitecturas de redes neuronales cuánticas (QNNs), con el fin de mejorar las capacidades de modelado y predicción de funciones complejas.

Las QNN son capaces de realizar tareas de regresión complejas y optimización de manera más eficiente que los métodos clásicos, gracias a la capacidad de los qubits de explorar múltiples soluciones simultáneamente mediante la superposición cuántica. En esta tesis se explora cómo crear QNNs más eficientes, y cómo el entrelazamiento cuántico y las mediciones entrelazadas pueden mejorar aún más la capacidad de estas redes.

El análisis de las capacidades de las redes neuronales cuánticas (QNNs) se realizó mediante herramientas analíticas avanzadas, como la descomposición de Fourier, que permitió evaluar la expresividad de las redes. Los resultados mostraron que las QNNs pueden actuar como aproximadores universales de funciones, alcanzando altos niveles de precisión y capacidad de generalización. Un aspecto clave que mejoró el rendimiento de estas redes fue la utilización de mediciones entrelazadas globales, que aumentan la cantidad de información que puede ser extraída de los qubits y mejoran la capacidad de la red para modelar funciones complejas y no lineales. El estudio también reveló cómo la profundidad de la red y el número de qubits juegan un papel fundamental en el rendimiento de las QNNs. Cuantos más qubits se integren en la red y mayor sea su profundidad, más complejas y precisas son las soluciones que las QNNs pueden generar.

También se plantea la integración de QNN en centros NVs. Las aplicaciones potenciales de las QNNs basadas en centros NV son vastas y tienen un gran impacto en múltiples áreas científicas y tecnológicas. En el ámbito del sensado cuántico, las QNNs pueden mejorar la precisión en la detección de campos magnéticos, lo que permite avanzar en áreas como la metrología cuántica, la microscopía magnética y la detección biomédica. Gracias a su capacidad para procesar señales no lineales con gran sensibilidad, los centros NV y las QNNs pueden ser utilizados para detectar señales débiles en presencia de ruido, lo que mejora la resolución de las mediciones en condiciones experimentales complejas.

Además, las técnicas de control tradicionales empleadas en el sensado cuántico pueden ser mejoradas con el aprendizaje automático cuántico (QML) para mitigar el ruido y la decoherencia, mejorando aún más la fiabilidad y precisión de los sistemas cuánticos. En esta tesis se implementan técnicas de estimación bayesiana de parámetros y otras técnicas de regresión en la detección de campos magnéticos variables en el tiempo utilizando centros NV, lo que permite una extracción más precisa y eficiente de los parámetros de la señal en entornos ruidosos.

El trabajo presentado en esta tesis sienta las bases para futuras investigaciones y desarrollos en las tecnologías cuánticas basadas en centros NV. A medida que la eficiencia en la detección de fotones mejora, se abrirán nuevas posibilidades para las aplicaciones de sensado cuántico en áreas como la biomedicina, la investigación material, la navegación cuántica y la computación cuántica. La escalabilidad de los sistemas NV es otro desafío importante que se deberá abordar en el futuro. El desarrollo de redes cuánticas basadas en centros NV, que sean coherentes y eficientes, abrirá nuevas fronteras en la comunicación cuántica y la computación cuántica a gran escala.

Esta tesis ha realizado contribuciones significativas al avance de las tecnologías cuánticas basadas en centros NV, mediante el desarrollo de un modelo teórico avanzado para las estadísticas de emisión de fotones, la construcción de un microscopio confocal compacto y la exploración de arquitecturas de aprendizaje automático cuántico. La integración de centros NV en redes neuronales cuánticas ofrece un camino hacia aplicaciones prácticas más poderosas, mientras que el microscopio compacto facilita el acceso a estas tecnologías, permitiendo que más instituciones puedan beneficiarse de sus ventajas. Los resultados de esta tesis sientan las bases para el futuro de las tecnologías cuánticas, con un impacto significativo en áreas como el sensado cuántico y el aprendizaje automático cuántico.

Abstract

Nitrogen-Vacancy (NV) centers in diamond hold transformative potential in quantum technologies, leveraging their unique spin-optical properties, long coherence times, and room-temperature operation. However, challenges such as inefficient photon detection and bulky experimental setups hinder their broader deployment. This thesis addresses these issues through advancements in theoretical modeling, experimental design, and computational integration of NV centers.

A key contribution is a novel framework for modeling Photon Emission Statistics (PES) in NV centers. Building on the quantum jump formalism, this model improves upon traditional rate-equation approaches by explicitly linking photon emission streams to NV quantum states. This detailed understanding enables the optimization of quantum sensing protocols, particularly for magnetic field measurements, by enhancing sensitivity and efficiency. The PES framework also supports simulations of photophysical properties, facilitating analysis of photon arrival times and autocorrelation functions.

To transition NV-based systems from laboratories to real-world applications, the thesis introduces a compact confocal microscope for optical initialization and coherent control of NV states. This miniaturized system addresses size, complexity, and cost barriers, broadening accessibility and enabling deployment in diverse environments.

The integration of NV centers into Quantum Machine Learning (QML) is another focus, exploring their role in quantum neural network (QNN) architectures. NV centers are shown to enable high-fidelity qubit operations and entangling gates, enhancing QNNs' ability to perform complex regression tasks. The analysis reveals how network depth, qubit count, and entanglement influence QNN performance, underscoring the potential of NV centers in quantum-enhanced computation.

These advancements are supported by theoretical, experimental, and computational validations. The PES framework improves NV center characterization, the portable microscope achieves efficient NV control, and the QNN research demonstrates NV center utility in advanced computational frameworks.

Looking forward, this work lays the foundation for several promising directions. Future research could focus on improving photon detection efficiency to further enhance sensing performance. Additionally, scaling NV center-based systems for use in quantum networks remains a critical challenge that warrants continued investigation. The integration of NV centers into scalable quantum machine learning models also offers significant potential for advancing both fields. By addressing these challenges, the findings of this thesis will help to unlock the full potential of NV centers in quantum technologies, bridging the gap between fundamental research and practical applications.

List of Publications

This thesis is based on the following publications:

I. Panadero, H. Espinós, L. Tsunaki, K. Volkova, A. Tobalina, J. Casanova, P. Acedo, B. Naydenov, R. Puebla, and E. Torrontegui. Photon-emission statistics for single nitrogen-vacancy centers. *Phys. Rev. Appl.*, 22:014035 (2024)

I. Panadero, J.C. Guerra, E. Caravaca, F.J. Hidalgo, P. Acedo, C. de Dios, E. Torrontegui. Harnessing individual nitrogen-vacancy centers with a compact and portable confocal microscope. *EPL* **149** 20001 (2025)

I. Panadero, Y. Ban, H. Espinós, R. Puebla, J. Casanova, E. Torrontegui. Regressions on quantum neural networks at maximal expressivity. *Sci Rep* **14**, 31669 (2024)

Other publications not included in this thesis:

H. Espinós, C. Munuera-Javaloy, I. Panadero, P. Acedo, R. Puebla, J. Casanova, E. Torrontegui. Enhancing polarization transfer from nitrogen-vacancy centers to external nuclear spins via dangling bond mediators. *Commun Phys 7, 42 (2024).*

H. Espinós, I. Panadero, J.J. García-Ripoll and E. Torrontegui. Quantum control of tunable-coupling transmons using dynamical invariants of motion. *Quantum Sci. Technol. 8 025017 (2023)*

List of other relevant contributions:

- Summer School: Machine Learning in Quantum Physics and Chemistry.
  24 August - 3 September 2021, Warsaw, Poland.
  Presented a contributing talk titled: *Quantum Camera.*
- Conference LEAPS meets Quantum Technologies.
  15 May - 20 May 2022, Elba, Italy.
  Presented a poster titled: *Fluorescence model for Nitrogen Vacancy Centers.*
- Conference SPIE Quantum West.
  28 January - 2 February 2023, San Francisco, EEUU.
  Presented a contributing talk titled: *Counting photons emitted by a single quantum defect in diamond.*
- Hasselt Diamond Workshop 2023 - SBDD XXVII
  15 March - 17 March 2023, Hasselt, Belgium.
  Presented a poster titled: *Counting photons emitted by a single quantum defect in diamond.*
- QUANTUMatter2023 Conference
  23 May - 25 May 2023, Madrid, Spain.

Presented a poster titled: *Photon counting statistics in nitrogen vacancy centres*

- Quantum Technologies for Young Researchers Workshop
  4 July - 7 July 2023, Madrid, Spain.
  Presented an oral contribution titled: *Photon Statistics in Nitrogen Vacancy Centers.*

- Okinawa School in Physics: Coherent Quantum Dynamics
  26 September - 5 October 2023, Okinawa, Japan.
  Presented a poster titled: *Characterization of the photon emission statistics in nitrogen-vacancy centers.*

- Quantum Science Generation Workshop 2024
  06 May - 10 May 2024, Trento, Italy.
  Presented a contributing talk titled: *Enhancing readout in nitrogen vavancy center in diamond: leveraging photon statistics for analyzing ionization dynamics*

List of abbreviations

AWG	Arbitrary waveform generator
CVD	Chemical Vapor Deposition
ML	Machine learning
MO	Microscope objective
MRI	Magnetic Resonance Imaging
MW	Microwave
NMR	Nuclear Magnetic Resonance
NV	Nitrogen-vacancy
ODMR	Optically detected magnetic resonance
PES	Photon emission statistics
PL	Photoluminescence
QML	Quantum machine learning
QNN	Quantum Neural Network
SQUID	Superconducting Quantum Interference Device
SPAD	Single-photon avalanche diode
STM	Scanning Tunneling Microscopy
ZPL	Zero-Phonon Line

Contents

Chapter 1

Introduction

1.1 Quantum Technologies

Almost a century after the development of quantum mechanics, both its theoretical foundations and its technological advancements have rapidly progressed. Quantum mechanics, with properties such as the Heisenberg uncertainty principle, superposition, and entanglement, offers the potential for technologies unattainable by classical means [1]. The first quantum revolution, nearly a century ago, has led to the development of fundamental technologies such as nuclear magnetic resonance (NMR) spectroscopy and imaging (MRI) [2], lasers [3], atomic clocks [4], semiconductors and transistors [5]. These advancements have facilitated numerous applications in other areas of fundamental physics research, including the precise measurement of fundamental constants [6], laser frequency combs [7], scanning tunneling microscopy (STM) [8], and superconducting quantum interference devices (SQUIDs) [9]. These technologies have become possible due to our understanding of quantum mechanics, but they do not fully harness their potential, which requires precise control over isolated quantum units.

In the past thirty years, methods for isolating quantum systems have advanced, allowing us to control and confine single electrons [10], atoms [11], ions [12], and spin qubits [13]. This has initiated the second quantum revolution [14], promising breakthroughs in quantum computing, communication, and sensing. However, scaling quantum systems remains challenging, particularly when trying to balance the isolation of qubits with the control of strong and coherent interactions among them. [15]. Promising candidates such as trapped atoms face limitations, such as the complexity of scaling and confinement challenges [16], which is generating interest in solid-state systems such as quantum dots [17], superconducting qubits [18], and atomic defects in crystals [19].

While the technology for quantum computing matures, we can still advance real-world applications of quantum mechanics that exploit its properties. Quantum sensing leverages the very property that quantum computing aims to avoid: interaction with the environment. Quantum sensors capitalize on the central weakness of quantum systems, their strong sensitivity to external disturbances [20]. In quantum sensing, the goal is to exploit the extreme sensitivity of quantum systems to external signals to measure them with high precision. This requires the quantum system to be deliberately coupled to the external environment to detect subtle changes. As a result, while quantum computing systems strive for isolation to protect coherence [21], quantum sensing systems are designed to be highly sensitive to specific interactions [22], making the trade-offs between isolation and coupling a central consideration in the development of quantum technologies [23].

Quantum sensors come in various forms, each suited to specific applications. Notable examples include spin-based sensors [24], cold-atom interferometers [25], and SQUIDs [26]. Among these, solid-state spin systems, particularly spin defects in materials such as diamond and silicon, have gained significant attention due to their stability and miniaturization potential [27]. Spin defects, such as nitrogen-vacancy (NV) centers in diamonds [28], possess unique quantum properties that allow precise measurements of magnetic fields [29], electric fields [30], temperature [31], and even strain [32] at the nanoscale. NV centers, in particular, have gained substantial attention due to their ability to operate at room temperature and their stability in very small crystals and nanostructures [33]. The NV center is a point defect in diamond consisting of a nitrogen atom adjacent to a vacancy in the carbon lattice. Its spin-dependent fluorescence enables optical detection of magnetic fields [34], providing a highly sensitive tool for probing various physical quantities, making NV centers a leading platform for quantum sensing technologies [35].

The fluorescence of the NV center has allowed extensive studies of its physical properties, including excitation behavior [36], wavelength dependence [37], energy gaps [38], ionization processes [39], spin dynamics [40], and temperature effects [41], among others. Its fluorescence is typically modeled using rate equations for level populations, but Chapter 2 introduces a new theoretical framework for modeling the photon emission statistics (PES) of the NV center [42], enhancing our understanding of the relationship between its internal states, the qubit state, and the detectable photons emitted. This model aims to optimize detection protocols, maximizing sensitivity for quantum sensing applications.

A deep understanding of NV center photophysics is crucial for advancing NV center-based technology. Although fundamental research continues to explore the electronic and spin properties of NV centers, this knowledge is increasingly being leveraged to investigate quantum phenomena, such as entanglement and superposition [43, 44, 45], and to probe nanoscale systems with unprecedented precision [46, 47]. These studies have paved the way for practical applications of NV centers, including advances in biosensing [48, 49] and nanoscale NMR techniques [50, 51]. However, fully leveraging the potential of NV centers in real-world scenarios presents several technical challenges. Key challenges include the size, complexity, and cost of the sophisticated optical systems currently used for the manipulation and measurement of NV centers [52, 53]. Addressing these challenges is critical to moving beyond laboratory setups and towards scalable, deployable technologies. In Chapter 3, we present a new compact and portable confocal setup specifically engineered for efficient detection and control of single NV centers. Our system not only facilitates the optical initialization and readout of individual NV center photoluminescence signals, but also enables precise coherent spin control. This compact design represents a significant step toward making NV center-based technologies more accessible and practical for both research and industrial applications.

Developing robust systems for NV center interrogation is essential, but achieving coherent control of the NV center spin is equally crucial for high-precision and sensitivity measurements [54]. This requires maintaining coherent quantum states over extended periods. Both quantum computing and quantum sensing depend on this coherence to process information and measure physical quantities. Techniques initially developed to minimize decoherence and optimize quantum gate fidelity in quantum computers—such as dynamical decoupling and error correction protocols—can be adapted to enhance the performance of quantum sensors [55, 56]. Additionally, quantum algorithms that leverage entanglement and superposition need to be applied in quantum sensing to improve weak signal detection and achieve high-precision measurements [19].

Quantum machine learning (QML) is a set of quantum algorithms that present an exciting frontier in leveraging the properties of quantum systems [57, 58]. QML algorithms can offer significant speedups in processing large datasets and solving complex optimization problems that would be intractable for classical systems. In particular, NV centers can serve as qubits within hybrid quantum-classical frameworks [59], where their quantum states are used to encode and manipulate high-dimensional data in ways that accelerate machine learning tasks. This opens up new possibilities for developing quantum-enhanced models capable of recognizing patterns [60], optimizing systems [61], and making predictions with unprecedented accuracy [62]. In Chapter 4, we explore the potential of Quantum Neural Networks (QNNs) for regression tasks.

This thesis is organized into five chapters. Chapter 1 introduces the physics of the NV center and provides an overview of the current state of research. Chapter 2 introduces a phenomenological model that characterizes the fluorescence properties of NV centers, validating it through experimental benchmarks and optimizing readout techniques for quantum sensing. In Chapter 3 we present the design and development of a compact confocal system for the detection and control of single NV centers, detailing its implementation and addressing performance enhancement strategies. Finally, Chapter 4 investigates a quantum neural network (QNN) architecture for regression tasks, examining how entanglement and encoding strategies influence the expressivity of the network and approximation capabilities. The thesis concludes in Chapter 5 with discussions of future research opportunities for NV centers and applications of QNNs in quantum technologies.

1.2 The nitrogen-vacancy center

Nitrogen-vacancy (NV) centers in diamond have emerged as highly promising candidates for quantum technologies. Embedded within a robust solid-state device, NV centers exhibit atom-like characteristics, including long-lived spin quantum states and well-defined optical transitions [33]. In particular, the electron spins of the NV centers can be

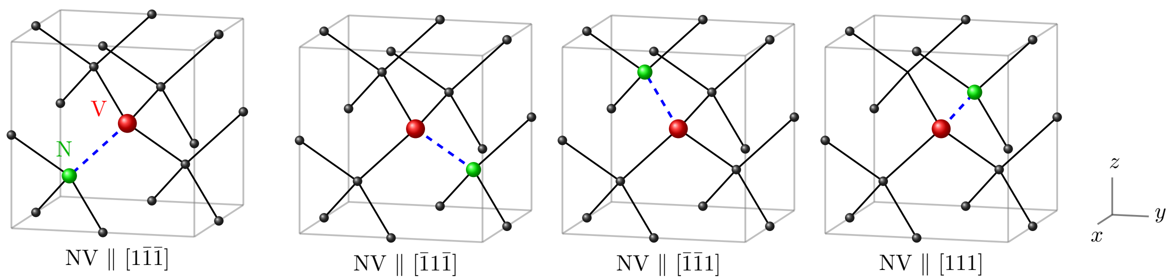

Fig. 1.1: Four possible orientations of nitrogen-vacancy (NV) color centers in diamond. Carbon atoms are depicted in black, nitrogen (N) atoms in green, and vacancies (V) in red.

easily initialized, controlled, and read at room temperature under ambient conditions [54]. This feature simplifies experimental setups and enhances the practicality of employing NV centers in quantum technology development.

Diamond is a wide bandgap material (5.47 eV) composed purely of carbon atoms [33], traditionally valued for its macroscopic properties such as hardness and thermal conductivity. Although pure diamonds are made up entirely of carbon, both synthetic and natural diamonds can contain a variety of impurities. These defects may arise from lattice irregularities or impurities introduced during or after diamond growth, typically on the nanometer scale. Defects significantly influence the properties of diamonds, particularly its color and electrical conductivity, and are commonly known as color centers. Each of these centers introduces an absorption band that can impart a strong coloration to diamond crystals, especially when present in high concentrations [63].

Because of the exceptionally rigid lattice of diamond, it can only accommodate a restricted range of impurities, such as boron and nitrogen. The existence of defects in solid-state materials, including diamond, establishes a foundation for implementing quantum technologies in wide-bandgap materials. Certain defects introduce isolated electronic spins into the lattice, which can be controlled optically. These isolated spins create a mechanically robust system that, when coupled with advanced fabrication techniques, becomes highly scalable and holds promise for applications in nanoscale sensing and quantum information. The NV center is a notable example of a defect center in diamond that has garnered extensive research attention due to its long coherence times, even at room temperature [33].

The NV center consists of a substitutional nitrogen atom at one of the carbon sites in the diamond lattice and a vacancy in an adjacent site. The symmetry axis of the NV center can be oriented along one of four possible crystallographic directions, as illustrated in Fig. 1.1. NV centers are typically formed from single substitutional nitrogen centers (often referred to as P1 centers in diamond literature) through a process involving irradiation followed by annealing at temperatures above 700°C [64, 65]. Various high-energy particles such as electrons, protons, neutrons, ions, and gamma photons can be used for irradiation, creating lattice vacancies. These vacancies remain immobile at room temperature and require annealing to become mobile. Single substitutional nitrogen atoms induce strain in the diamond lattice, effectively capturing these vacancies during annealing and forming NV centers. The NV center can also be created through chemical vapor deposition (CVD) of diamond [66], where a small fraction of single substitutional nitrogen impurities (typically <0.5%) traps vacancies generated by plasma synthesis, with NV centers aligning preferentially along the growth direction. Delta doping of nitrogen during CVD growth can further create two-dimensional ensembles of NV centers near the diamond surface, thereby enhancing sensing or simulation capabilities.

The NV center primarily exists in one of two charge states [39]: the neutral NV^0 and the negatively charged NV^-. These states exhibit distinct spectral properties, with NV^- having a characteristic zero-phonon line (ZPL) at 637 nm, while NV^0 shows a ZPL at 575 nm [33]. Both forms of the NV center have well-defined vibronic bands extending from their respective ZPLs, which are associated with NV-phonon coupling. Throughout this work, we primarily refer to the NV^- state simply as the NV center, as it is the state whose spin can be polarized and read out. However, in Section 2.5, we delve deeper into the ionization dynamics of the NV center and its influence on the readout of the NV^- state.

1.2.1 Electronic structure and optical properties

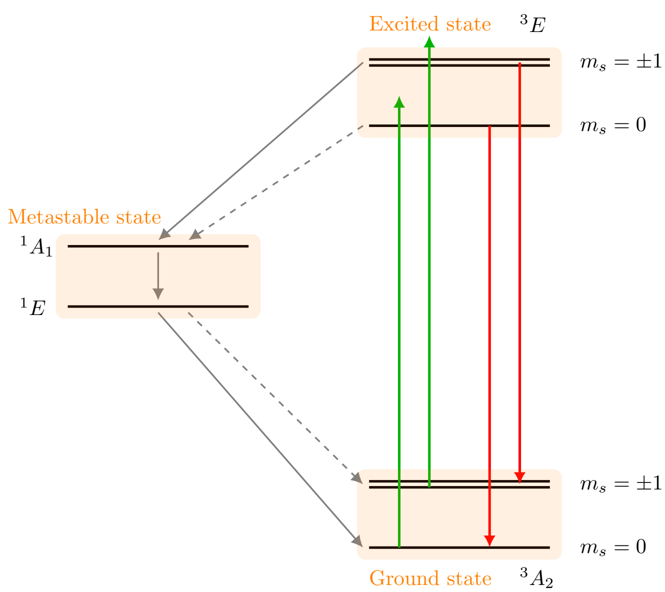

Fig. 1.2: Energy level diagram of the NV center. The optical transitions are spin conserving. Green arrows indicate optically induced transitions, while red arrows indicate decays that lead to the emission of a red photon. Dashed arrows indicate weak transitions.

The electronic structure and optical properties of the NV center make it an exceptionally interesting system for research, enabling optical readout and initialization of its ground state [67]. The photophysics are governed by three electronic levels, depicted in Fig. 1.2: a triplet ground state $^3A_2$, a triplet excited state ^3E, and a metastable singlet state comprising two levels $^1A_1$ and ^1E. The optical transition between the ground state and excited state occurs at a resonant wavelength of 637 nm (Zero-Phonon Line). Efficient excitation of the NV center is achieved with light within its vibronic absorption band (480-637 nm). Non-resonant light couples the ground states to the phononic band of the excited-state manifold, from where the system rapidly decays - in a timescale of femtoseconds - into the corresponding spin-conserving excited state [42]. This decay process through vibrational sidebands disrupts optical coherence between the ground states and the excited states, resulting in a broad emission spectrum (630-800 nm).

Despite extensive research on the NV center structure over the past thirty years, ongoing investigations continue to explore its fundamental properties, including its excitation behavior under different wavelengths [68], the energy gaps between levels [69], its ionization process [39], and its temperature dependence [70]. These properties are primarily studied through measurements of NV fluorescence, as well as electrical readout and spectroscopy. Although various models exist to explain different phenomena related to the NV center, each with different proposed transitions and decay rates, the fluorescence is consistently modeled by solving rate equations for level populations.

In Chapter 2, we introduce a novel theoretical framework based on the quantum jump formalism, which improves the modeling of NV fluorescence by directly accounting for the complete photon emission statistics [71]. Unlike conventional models, which focus primarily on steady-state solutions and population dynamics, our approach explicitly simulates the time-dependent emission process, providing a more accurate and detailed characterization of the NV center evolution. This method allows us to clarify the relationship between the spin dynamics of internal quantum states and the stream of photons arriving at the detector.

This model not only provides deeper insight into the emission processes of the NV center but also enables the simulation of autocorrelation measurements [72], which are essential for understanding quantum coherence and entanglement in NV-based quantum sensors. Furthermore, the framework supports the development of more efficient detection protocols that optimize energy and time resources while enhancing system sensitivity in applications such as magnetic-field measurements. The ability to simulate photon emission at this level of detail opens up new avenues for designing more precise and reliable NV-based quantum sensors, making it a significant advancement over existing methods.

1.2.2 Spin properties

The two triplet states, the ground state $^3A_2$ and excited state ^3E, are further split by spin-spin interaction into three spin sublevels: $m_s = \pm 1$ and $m_s = 0$, denoted by the manifolds $\{|0\rangle, |1\rangle, |-1\rangle\}$ for the ground state and $\{|e0\rangle, |e1\rangle, |-e1\rangle\}$ for the excited state [73]. Due to the axial symmetry of the NV center, the two $m_s = \pm 1$ states are degenerate in the absence of a magnetic field, while the $m_s = 0$ state has a lower energy. The energy difference between the spin sublevels $m_s = 0$ and $m_s = \pm 1$, known as the zero-phonon line (ZPL), is D =2.87 GHz for the ground state and $D_e = 1.42$ GHz for the excited state. The degeneracy between $m_s = \pm 1$ states can be lifted by applying an external magnetic field B along the NV quantization axis, causing these levels to split. This energy splitting, known as the Zeeman splitting, is given by $2\gamma_e B$, where γ_e is the electron gyromagnetic ratio. This magnetic field dependence forms the basis of all magnetic sensing applications for the NV center.

Two important features of the NV center as a quantum system are its ability to be initialized into the ground state spin level $|0\rangle$ when optically excited and its spin-dependent fluorescence, allowing the spin state of the NV center to be optically addressed. Optical readout is possible because the decay process from the excited states is spin-dependent [67]. Both the $|0\rangle$ and $|\pm 1\rangle$ states can relax either directly to the ground state through radiative decay or to the metastable state. The probability of decaying to the metastable state rather than through the bright radiative transition is higher for the $|\pm e1\rangle$ states than for the $|e0\rangle$ state . Consequently, the NV center appears darker when optically excited from $|\pm 1\rangle$ state. The optical contrast between the states $|0\rangle$ and $|\pm 1\rangle$ is approximately 30%, with some studies reporting even higher optical contrasts [39]. On the other hand, initialization is achievable because the electronic spin is not conserved during the transition from the excited state to the metastable state. However, the metastable state relaxes to the $|0\rangle$ state of the ground state with higher probability than to the $|\pm 1\rangle$ states. This means that after excitation, the $|0\rangle$ state will become more populated than the $|\pm 1\rangle$ states, effectively polarizing the NV center [74].

Another remarkable property is that the spin state of the NV center can be coherently controlled by applying microwave (MW) radiation resonant with the ground state transition $|0\rangle \leftrightarrow |+1\rangle$ or $|0\rangle \leftrightarrow |-1\rangle$ [54]. This induces coherent population oscillations between the spin sublevels, resulting in an observable drop in the NV center fluorescence. This transition can have a very long spin coherence time, approaching the second-time regime [33]. Many magnetometry applications rely on this principle, leveraging the fact that transition energies are influenced not only by external magnetic fields but also by factors such as temperature, pressure, and electric fields [73]. This coherent control facilitates the implementation of various control pulsed sequences, such as the Ramsey sequence for precise magnetic field measurements, the Hahn-Echo sequence to assess the coherence time of the NV center, and dynamical decoupling sequences aimed at extending coherence by shielding the system from environmental influences. These capabilities underscore the versatility of the NV center and its potential in a wide range of applications.

1.3 NV center applications

NV centers demonstrate versatility across a wide range of quantum applications. They extend the range and efficiency of quantum information transfer by functioning as quantum repeaters in quantum communication [75]. In quantum computing, NV centers serve as quantum memories [76], enabling the storage and retrieval of quantum data. Moreover, NV centers have been proposed as fundamental units for quantum information processing in quantum simulation [77], contributing to the exploration and understanding of quantum systems. The adaptability of NV centers in these diverse roles underscores their pivotal role in advancing quantum technologies.

NV centers are particularly valuable for sensing magnetic fields because of their spin-based capabilities. However, these capabilities extend naturally to a wide range of other physical quantities, including temperature [70], electric fields [78], pressure [79], and angular precession [80]. The foundation for these sensing applications lies in the long-lived quantum coherence of NV centers, which can persist for up to several milliseconds, enabling the creation of robust, calibration-free sensors. Coherent control of qubits, utilizing techniques such as dynamical decoupling, is crucial to achieving optimal performance in these applications. NV centers are distinguished for their high sensitivity and impressive spatial, spectral, and temporal resolution [81].

Diamond, as the host material for NV centers, offers significant advantages for the development of this technology. Its intrinsic properties, such as strength, transparency, and excellent thermal conductivity, enhance the functionality of the NV centers. In addition, the ability to fabricate photonic structures directly from diamond crystals, such as microlenses [82], microcavities [83], and nanopillars [72], simplifies the creation of efficient optical interfaces for the interrogation of the NV center. Furthermore, the compatibility of diamond with biological systems makes it highly suitable for quantum biosensing applications, particularly when employing nanodiamonds. This unique combination of properties positions NV centers as versatile and powerful tools for a broad spectrum of sensing applications, ranging from fundamental physics research [84, 85] to biomedical diagnostics [86, 87].

The NV center, despite its promising applications, faces several challenges [52, 88], such as the lack of spatial control in its implantation [89] and low photon collection efficiency [90]. Another critical hurdle is the need for the development of portable and accessible experimental instruments to broaden the impact and applicability of this quantum platform [91]. Recent advances have led to the miniaturization and integration of NV center technology based on ensembles into compact platforms and systems [92, 93, 94, 95, 96, 97]. These developments not only reduce setup footprint but also significantly lower costs, making the technology more accessible across industries and to the broader public. This breakthrough in size, compactness, and affordability holds the potential to revolutionize applications ranging from quantum computing and sensing [98] to biomedical imaging [48].

However, these advancements have not yet been fully realized for the detection of single NV centers, which require highly sensitive and efficient detection capabilities. Detecting single NV centers is crucial for harnessing their quantum capabilities to the fullest extent. In the realm of quantum sensing and diamond-based technologies, the detection of single NV centers has been extensively studied [99, 33]. Various methodologies, such as confocal microscopy and wide-field imaging, have been employed in previous studies to experiment with NV centers [100, 101]. Although these approaches have contributed significantly to understanding and exploiting quantum phenomena at the nanoscale [102], challenges persist in the existing experimental setups, mainly arising from issues related to size, complexity, and cost. Recent advances have introduced novel processing techniques [103] and optical components [104] that enhance the sensitivity and efficiency of detecting a single NV center. Despite these strides, the current literature highlights the ongoing need for compact solutions that strike a balance between performance and accessibility.

The need to detect individual NV centers with a compact and portable setup arises from the increasing demand for practical and cost-effective quantum sensing devices. In Chapter 3, we investigate the development of a compact confocal setup to detect and control single NV centers, taking advantage of recent technological advancements to ensure practicality, cost-effectiveness and seamless integration with other experimental components. By miniaturizing the traditionally bulky and complex confocal microscope set-up, we achieve flexibility in conducting experiments across diverse environments beyond conventional laboratory settings. This portability eliminates the need for specialized infrastructure, enabling measurements on the go and facilitating rapid data collection and analysis. Furthermore, the compact microscope increases accessibility, allowing institutions with limited resources to explore the phenomena and applications of the NV center.

Beyond magnetometry and sensing, the spin of the NV center can be controlled for numerous applications. The spin of the NV center can be coupled to adjacent spins, such as ^{13}C atoms from the diamond lattice or external spins on the surface, to transfer polarization to them or utilize them as quantum registers [105, 106]. To create quantum networks, NV centers can be optically coupled to each other [88]. In addition, they have been coupled to various quantum and photonic systems, including superconducting qubits [107] and microcavities [83]. A control pulse sequence can achieve durable universal quantum gates with excellent fidelity for single-qubit systems [108]. The scalability of the NV centers is promising, as entanglement between two NV electron spins has been demonstrated [109], and further enhanced by achieving high-fidelity gates with the aid of surrounding nuclear spins [110]. Progress continues towards an integrated system with fault-tolerant multi-qubit gates. However, generating a large number of individually accessible and coherently coupled NV centers remains a challenging task. Understanding practical algorithms that can be implemented in a single NV center or a small network of NV centers is therefore an active area of research.

Remarkably, as diamond-based technology finds increasing applications, the field is naturally shifting its focus from proof-of-principle experiments to practical engineering implementations for technological advancement [111]. This evolution is driving two parallel and complementary avenues of research. The first is hardware-driven, leveraging advancements in material science to fabricate improved diamond materials with tailored properties. This includes achieving controlled densities of color centers and enabling access to individual emitters with high photon extraction efficiencies, which is the focus of Chapter 3, as well as desirable spectral and coherence properties.

The second avenue is software-driven, centered on designing innovative experimental protocols for data acquisition and analysis. This approach aims to maximize the speed and resolution of specific measurements, thereby enhancing the efficacy of quantum technologies based on NV centers. The field of Quantum Machine Learning (QML) naturally fits into this focus. In this context, two distinct strategies have emerged. The first strategy uses traditional machine learning (ML) to control NV centers, optimizing measurement processes through advanced data analysis, offering novel computing approaches that can achieve measurement speeds and / or accuracies approximately 1-2 orders of magnitude higher than traditional statistical methods [59]. For example, in [112], a ML algorithm processes noisy readouts of single NV centers at room temperature, requiring only an average of one photon per algorithm step to sense magnetic field strength with precision comparable to cryogenic experiments [113]. In contrast, the second strategy takes advantage of the quantum nature of the NV centers to improve ML tasks. For instance, NV centers have been employed as hardware for training Quantum Neural Networks (QNNs) to perform tasks such as pattern recognition [114].

1.4 Quantum Machine Learning

NV centers have emerged as particularly promising candidates for quantum sensing because of their unique quantum properties. Quantum sensing, in general, is a powerful approach that involves measuring the interaction of a quantum probe - such as an NV center - with its surrounding environment to estimate a quantity of interest with exceptional sensitivity and precision [113]. This interaction encodes the parameter of interest (such as a magnetic field or temperature) into the quantum state of the probe, enabling measurement techniques that take advantage of the principles of quantum mechanics.

In the context of quantum sensing, statistical estimation theory becomes essential [115, 116]. Introduces quantities such as Fisher information, which quantifies how much information a measurement carries about an unknown parameter, which, in turn, directly influences the precision of the estimation [117, 118]. Thus, statistical estimation theory not only offers insight into the achievable precision of sensing tasks but also guides the design and optimization of quantum sensing protocols.

In this work, we explore advanced techniques for parameter estimation in quantum sensing, focusing on methods that enhance the precision and adaptability of quantum measurements. Parameter estimation is essential in quantum sensing applications, as it allows us to extract meaningful information about unknown quantities from measurement data with maximum accuracy.

Bayesian estimation is a central strategy in parameter estimation, employing a probabilistic framework that improves parameter estimates by incorporating prior knowledge and continuously updating them as new measurement data are acquired [119, 120]. This method is particularly well-suited to dynamic or uncertain environments, as its iterative nature allows quantum sensors to adapt swiftly to environmental changes. By continuously updating estimates, Bayesian methods ensure that quantum sensors maintain high precision and reliable performance, even under fluctuating conditions. In the context of photon emission statistics, Section 2.4.7 will benchmark the Bayesian Parameter Estimation algorithm to assess its effectiveness in sensing time-dependent magnetic fields using an NV center. We implement Bayesian Parameter Estimation and other regression techniques in the detection of time-varying magnetic fields using NV centers, enabling more precise and efficient extraction of signal parameters in noisy environments.

Quantum Machine Learning (QML) is another emerging technique for parameter estimation [57, 121]. Unlike traditional methods, QML algorithms can analyze complex datasets and identify intricate patterns in quantum measurements, enhancing both the sensitivity and robustness of quantum sensors. Through the integration of QML, researchers are developing quantum sensing protocols capable of achieving unprecedented levels of precision [122], making these methods useful for applications in high-resolution imaging [103], magnetometry [123], and navigation [124, 125].

In recent years, QML has gained significant traction due to advances in computational power and data availability, which has proved to be highly effective in tasks such as pattern recognition or classification problems. QML encompasses two main approaches: (i) using traditional machine learning to enhance the measurement of a quantum process, and (ii) leveraging inherently quantum systems to perform machine learning tasks more efficiently. In this thesis, we specifically use the term QML to refer exclusively to approach (ii).

In the context of approach (i), traditional machine learning significantly contributes to the advancement of diamond-based quantum technologies [126]. For example, classification algorithms have been employed to rapidly distinguish between a photon emitter originating from a single NV center and one from an ensemble of NV centers [127]. Furthermore, ML techniques have improved the readout of the spin state of NV centers [128] and improved optical resolution [103]. Furthermore, machine learning strategies have been developed to overcome the inherent resolution limits of NV centers [112, 129], achieving an average one-photon readout from a single NV center at room temperature with sensitivity comparable to cryogenic conditions.

In this thesis, we focus on the second approach (ii), where quantum resources are harnessed to enhance machine learning models, as detailed in Chapter 4. The idea of leveraging quantum systems to improve machine learning algorithms has gained popularity. Quantum versions of artificial neural networks have been developed [130, 131], and there are proposals to execute subroutines of classical machine learning algorithms on quantum computers to achieve speed up [132, 133]. Adiabatic quantum machine learning is also emerging as a promising approach to specific optimization problems [134]. Stochastic models such as Bayesian decision theory or hidden Markov models can be seamlessly translated into the framework of open quantum systems. Despite increasing interest in this field, a comprehensive theory of quantum machine learning - exploring how quantum information can fundamentally improve artificial intelligence - is still in its early stages of development [135, 136].

To identify suitable tasks for QML models, it is crucial to understand their strengths and weaknesses [137, 138, 139]. A key starting point is studying the expressivity of QML models, which refers to their ability to approximate continuous functions. Chapter 4 investigates the expressivity of a Quantum Neural Network (QNN) capable of regression tasks even with a single qubit. Certain quantum circuit architectures have been shown to act as universal function approximators [140], capable of approximating any classification function with precision.

In Chapter 4, we analyze the expressivity of a universal deep quantum network structured with nested qubit rotations and adjustable data encoding. This ability of the QNN to approximate continuous functions in regression tasks is quantified using partial Fourier decomposition of the output, systematically benchmarked through a teacher-student scheme. The maximal expressivity increases with network depth and qubit number, but is fundamentally constrained by the data encoding mechanism. Importantly, we demonstrate that the choice of the measurement scheme significantly affects the ability of the network to reach this maximal bound. Global-entangling measurements on the network can saturate the maximal expressivity bound, enhancing its approximation capabilities compared to local qubit readouts in non-entangling networks. This enhancement is attributed to a broader set of surviving Fourier harmonics in the output signal decomposition. We discuss how to implement these QNNs using NV centers as qubits. While we focus on the theoretical aspects of the QNN, we take into account the specific characteristics and capabilities of NV centers, including their ability to perform single-qubit rotations and entangling gates.

Chapter 2

Photon Statistics

2.1 Introduction

The nitrogen-vacancy (NV) center in diamond has emerged as a prominent platform in the field of quantum technologies [73, 141] due to its formidable optical transitions that enable initialization and spin state discrimination, in addition to exceptional stability, extended coherence time of up to several milliseconds, even at room temperature, and effective control with microwave (MW) and optical methods [142, 74]. Its level structure and coherence time are sensitive to different physical fields, making it a versatile sensor with nanoscale spatial resolution and high sensitivity. NV centers have demonstrated great potential in applications of magnetic field [29, 49], temperature [143], electric field [78], and strain [144] sensing, as well as in nuclear magnetic resonance [145]. Additionally, they can be used as quantum emitters [146, 147]: when optically excited,they can absorb a photon and transition to an excited state, and then relax back to the ground state by the emission of a single photon. Fluorescence properties depend on the spin state of the NV, allowing a spin-dependent readout [42, 67]. Understanding spin-dependent photon emission is crucial for characterizing the dynamics of the NV center and optimizing its performance in quantum information processing, sensing, and communication tasks [147, 148, 149].

The fluorescence properties of the NV center have been modeled using rate equations for specific energy levels [74, 42, 150]. This method provides the fluorescence properties on the basis of the populations of the NV electronic states. Different energy models and sets of transition rates have been explored for the NV center in various contexts, including ionization dynamics [39], hyperfine couplings [151, 152], level anticrossing [153] and optically detected magnetic resonance (ODMR) experiments [74]. However, these methods typically either rely on a steady-state approximation of the NV dynamics or simply focus on state populations via rate equations. In either case, these approaches do not directly allow for a precise characterization of the key experimental quantity, namely the emitted stream of photons [154, 155].

Given the limitations of current approaches, we use a formalism based on quantum jumps [156] to investigate the NV center fluorescence. This technique was previously used to model the emission of different quantum systems such as single molecules [157], qubit readout of transient charge states [158], quantum dots [159], electron transport [160], and NV ionization [161]. As we experimentally demonstrate, the quantum jump formalism can be adapted to account for the full photon-emission statistics (PES) of the NV center within a modelization of the seven electronic states involved in the fast intrinsic dynamics [162]. The PES are defined as the probabilities $P(n,t)$ of having emitted a certain number n of photons in the interval $[0,t]$, and serve as a phenomenological framework for establishing the connection between the quantum state of an NV center and the stream of detected photons. The proposed model fully characterizes the emission properties of a single NV, providing physical insight into the NV fluorescence, giving access to different relevant measurable quantities, and allowing the design of efficient magnetic-field sensing protocols. Alternative approaches that use a numerical stochastic method using Monte Carlo simulations to depict the evolution of the quantum system [163, 164] require simulation of the evolution of the system across multiple trajectories, which for most cases is more computationally demanding, especially for larger systems or longer integration times.

This chapter is structured as follows. First, we introduce the analytical PES of a two-level system in Sect. 2.3.1. We then describe the PES for an NV center model in Sect. 2.3. In Sect. 2.3.1, we discuss the relevant energy levels of the NV center model, followed by the dynamics solved through a quantum jump formalism in Sect. 2.3.2. Sect. 2.4.1 details the experimental setup for benchmarking and applications. Sect. 2.4.2 explores how statistical analysis enables optimized state readout, while Sect. 2.4.3 examines emitter properties via computation of the autocorrelation function from photon statistics. Additional simulations, such as the saturation curve of the NV center in Sect. 2.4.4, and sensitivity optimization in continuous wave ODMRs with MW and laser excitation in Sect. 2.4.5, are also discussed. Imperfect detection is analyzed in Sect. 2.4.6, where we also introduce new simulation techniques. In Sect. 2.4.7 we investigate the detection of time-dependent magnetic fields using the PES formalism. Finally, Sect. 2.5 expands the NV center model to include ionization processes, exploring new implications and predictions provided by the PES. The chapter concludes with a summary of the main findings in Sect. 2.6.

2.2 Two level model

A fundamental question we might ask is: which is the probability $P_n(t)$ that a two-level system emits n photons at a given time t when the atom is irradiated by a monochromatic electromagnetic field? This question is intriguing not only because it addresses a fundamental aspect of the atom-field interaction, but also because the distribution $P_n(t)$ can be measured through photon detection. The statistical distribution of emitted photons is determined by the dynamics of the atom and its interaction with the laser field, and it is influenced by environmental effects.

The treatment of the problem begins with the time-dependent Hamiltonian of a

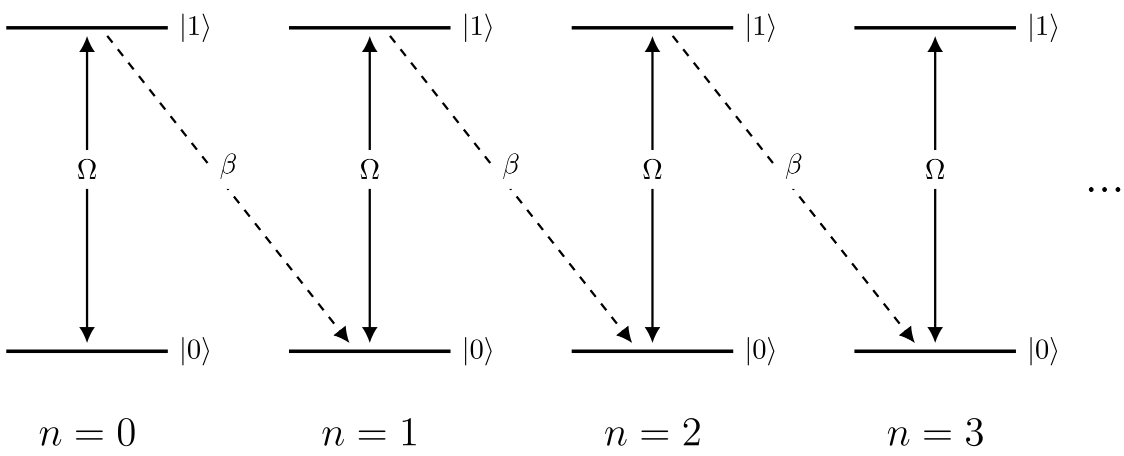

Fig. 2.1: The states accessed by a two-level atom when driven by a coherent field. Arrows labeled Ω denote induced transitions and those labeled β spontaneous transitions. After an spontaneous transition we increase the photon emission label n by one.

two-level system driven by a rotating transverse field of constant amplitude

$$\hat{H} = \frac{\omega_0}{2}\hat{\sigma}_z + \frac{\Omega}{2}\left(\cos\left(\omega_L t + \phi\right)\hat{\sigma}_x + \sin\left(\omega_L t + \phi\right)\hat{\sigma}_y\right), \tag{2.1}$$

where σ_x and σ_y are the Pauli matrices in the space of the excited $|a\rangle$ and ground $|b\rangle$ states. We have taken $\hbar = 1$. The energy split between these two levels is ω_0, Ω is the Rabi frequency, and ω_L is the frequency of the applied driving field and ϕ its phase.

To eliminate the time dependency of $\hat{H}$ we can move to a co-rotating frame by applying a rotation transformation about the z-axis by angle $\omega_L t$. This frame transformation is achieved using the unitary operator:

$$U_I = \exp\left\{-i\frac{\omega_L t}{2}\hat{\sigma}_z\right\}. \tag{2.2}$$

We can relate $|\phi_S\rangle$ states in the Schrödinger picture with the $|\phi_I\rangle$ states in the transformed frame picture as:

$$|\phi_I(t)\rangle = \hat{U}_I^\dagger(t)\,|\phi_S(t)\rangle\,. \tag{2.3}$$

Using the fact that $\hat{U}_I^\dagger\hat{U}_I = \mathbb{I}$, the Schrödinger equation in the rotation frame is

$$\begin{aligned}\partial_t\,|\phi_I(t)\rangle &= \partial_t[\hat{U}_I^\dagger\,|\phi_S(t)\rangle] = \hat{U}_I^\dagger[\partial_t\,|\phi_S(t)\rangle] + [\partial_t\hat{U}_I^\dagger]\,|\phi_S(t)\rangle = \\ &= [-i\hat{U}_I^\dagger\hat{H} + \partial_t\hat{U}_I^\dagger]\,|\phi_S(t)\rangle = [-i\hat{U}_I^\dagger\hat{H}\hat{U}_I + (\partial_t\hat{U}_I^\dagger)\hat{U}_I]\,|\phi_I\rangle = \\ &= -i\hat{H}_I\,|\phi_I(t)\rangle\,,\end{aligned} \tag{2.4}$$

where the new Hamiltonian in the transformed frame is given by

$$\hat{H}_I = \hat{U}_I^\dagger\hat{H}\hat{U}_I + i(\partial_t\hat{U}_I^\dagger)\hat{U}_I, \tag{2.5}$$

and from where we can compute

$$\hat{H}_I = \frac{\Delta}{2}\hat{\sigma}_z + \frac{\Omega}{2}\left(\cos(\phi)\hat{\sigma}_x + \sin(\phi)\hat{\sigma}_y\right), \tag{2.6}$$

with $\Delta = \omega_0 - \omega_L$ the detuning between the atom precesion frequency and the frequency of the applied field. Without loss of generality, we will consider $\phi = 0$ in the following derivations.

At this point, in our closed two-level system, we introduce the decay process from the $|1\rangle$ state to the $|0\rangle$ state due to spontaneous emission (and no other source of dephasing or decay). This scenario cannot be accurately described using the Schrödinger equation for a wave function alone. Instead, we must employ the density matrix ϱ and describe the evolution of the system using the Liouville equation:

$$\dot{\varrho} = -i[\hat{H}, \varrho] + L[\varrho], \tag{2.7}$$

where $L[\varrho]$ is the Lioville super-operator describing the dissipative evolution

$$L[\varrho] = 2\beta\hat{\sigma}_+\varrho\hat{\sigma}_- - \beta(\hat{\sigma}_-\hat{\sigma}_+\varrho + \varrho\hat{\sigma}_-\hat{\sigma}_+), \tag{2.8}$$

where β is the decay rate and $\sigma_\pm = \frac{1}{2}(\hat{\sigma}_x \pm \hat{\sigma}_y)$. To solve the previous equation, it is helpful to write the density matrix components for the two-level system as follows:

$$\varrho = \begin{pmatrix} \varrho_0 & \varrho_{01} \\ \varrho_{10} & \varrho_1 \end{pmatrix} = \frac{1}{2}(\mathbb{I} + \vec{u}\cdot\vec{\sigma}) = \frac{1}{2}\begin{pmatrix} 1-w & u+iv \\ u-iv & 1+w \end{pmatrix}, \tag{2.9}$$

where $u, v, w \in \mathbb{R}$ and (u, v, w) is know as the Bloch vector. From (2.7) we can obtain the equations for each component,

$$\begin{aligned} \dot{u} &= \Delta v - \beta u, \\ \dot{v} &= -\Delta u - \beta v + \Omega w, \\ \dot{w} &= -\Omega v - 2\beta(1 + w). \end{aligned} \tag{2.10}$$

These are the usual optical Bloch equations describing the internal motion of the two-level atom, expressed here in the rotating reference frame where the Bloch vector varies slowly over time. The master equation, defined in (2.7), provides insight into the time evolution of the density matrix of the system. However, it does not directly convey information about the number of photons emitted during this evolution.

Since the system undergoes a discrete number of emissions during its evolution, the matrix $\varrho(t)$ is generalized to include information about the number of spontaneous photon emission events that have occurred prior to time t [156]. The starting point for the derivation of the quantum jump formalism is the definition of a reduced density operator in the subspace that contains exactly n emitted photons [165]. This generalization allows us to resolve the full density matrix into individual components $\rho(n, t)$, representing a quantum trajectory with n photons being spontaneously emitted during the time interval $[0,t]$,

$$\varrho = \sum_n \rho(n) = \begin{pmatrix} \rho_0(n) & \rho_{01}(n) \\ \rho_{10}(n) & \rho_1(n) \end{pmatrix}. \tag{2.11}$$

Let us consider our two-level atom in the ground state under constant electromagnetic radiation. The states can be labeled by the probabilities $\rho_0(n)$ and $\rho_1(n)$ that the states are occupied, where n determines the number of photons emitted by the system. A pair of states connected by an induced transition (driven by Ω) have the same n, while the spontaneous transition (driven by β) causes n to increase by one unit, see Fig. 2.1. For example, an atom initially at rest in the ground state is promoted from $\rho_0(0)$ to $\rho_1(0)$ by absorption. From there it can return to $\rho_0(0)$ by stimulated emission or it can drop to state $\rho_0(1)$ by spontaneous emission; from which it can again absorb a photon and be promoted to state $\rho_1(1)$, and so on.

The connection with photon emission statistics (PES) is made by observing that for the atom to arrive in state $\rho_0(n)$ or state $\rho_1(n)$ it must spontaneously emit exactly n photons, and hence the probability that n photons are emitted is

$$P_n = \rho_0(n) + \rho_1(n) = \mathrm{Tr}\{\rho(n,t)\}. \tag{2.12}$$

To derive the equations of motions for $\rho(n,t)$ we can decompose (2.7) as

$$\dot{\varrho} = \mathcal{L}\varrho = (\mathcal{L}_0 + \mathcal{J})\varrho, \tag{2.13}$$

in such a way that we have singled out the jump superoperator $\mathcal{J} = 2\beta\,|1\rangle\langle 0|$ associated to the stochastic radiative spontaneous decay. We can define the equations of motion for $\rho(n,t)$

$$\dot{\rho}(n) = \mathcal{L}_0\rho(n) + \mathcal{J}\rho(n-1), \tag{2.14}$$

describing each photon emission as increasing the cumulative photon count by one, $\rho(n-1,t) \to \rho(n,t)$. This equations couple n and $n-1$ terms and therefore are hard to solve. We can express this equations in component terms as:

$$\begin{aligned}
\dot{\rho}_0(n) &= i\frac{\Omega}{2}(\rho_{01}(n) - \rho_{10}(n)) + 2\beta\rho_1(n-1), \\
\dot{\rho}_1(n) &= -i\frac{\Omega}{2}(\rho_{01}(n) - \rho_{10}(n)) - 2\beta\rho_1(n), \\
\dot{\rho}_{01}(n) &= -i\Delta\rho_{01}(n) - i\frac{\Omega}{2}(\rho_1(n) - \rho_0(n)) - \beta\rho_{01}(n), \\
\dot{\rho}_{10}(n) &= i\Delta\rho_{10}(n) + i\frac{\Omega}{2}(\rho_1(n) - \rho_0(n)) - \beta\rho_{10}(n).
\end{aligned} \tag{2.15}$$

Introducing the change of variables

$$\begin{aligned}
P_n &= \rho_0(n) + \rho_1(n), \\
W_n &= \rho_0(n) - \rho_1(n), \\
U_n &= \rho_{01}(n) + \rho_{10}(n),
\end{aligned}$$

$$V_n = -i(\rho_{01}(n) - \rho_{10}(n)). \tag{2.16}$$

equation (2.15) takes the form:

$$\begin{aligned}
\dot{P}_n &= \beta(P_{n-1} - P_n) + \beta(W_{n-1} - W_n), \\
\dot{U}_n &= \Delta V_n - \beta U_n, \\
\dot{V}_n &= -\Delta U_n - \beta V_n + \Omega W_n, \\
\dot{W}_n &= -\Omega V_n - \beta(W_{n-1} + W_n) - \beta(P_{n-1} + P_n).
\end{aligned} \tag{2.17}$$

We allow the index n to range overall integers, with $P_n = U_n = V_n = W_n = 0$ for $n < 0$. We can check that $\sum_n P_n = 1$, and therefore $\sum_n \dot{P}_n = 0$. By taking the sum over n in each equation in (2.17) and defining $u = \sum_n U_n$, $v = \sum_n V_n$ and $w = \sum_n W_n$ we arrive at the Bloch equations (2.10) previously discussed. In view of (2.10), we can interpret (U_n, V_n, W_n) as a partial Bloch vector associated with the pair of states of index n. Let (u_0, v_0, w_0) be the atomic Bloch vector at $t = 0$, describing the initial state of the system. The initial conditions for equation (2.17) are then $P_0(0) = 1$, $U_0(0) = u_0$, $V_0(0) = v_0$, and $W_0 = w_0$ and $P_n(0) = U_n(0) = V_n(0) = W_n(0) = 0$ for $n > 0$. Lets define the generating functions

$$\begin{aligned}
G(z,t) &= \sum_{n=0}^{\infty} z^n P_n(t), \qquad & I(z,t) &= \sum_{n=0}^{\infty} z^n U_n(t), \\
J(z,t) &= \sum_{n=0}^{\infty} z^n V_n(t), \qquad & K(z,t) &= \sum_{n=0}^{\infty} z^n W_n(t),
\end{aligned} \tag{2.18}$$

where we introduce the variable z. The photon number distribution, $P_n(t)$ is derived from the generating function $G(z,t)$ as follows

$$P_n(t) = \frac{1}{n!} \frac{\partial^n G(z,t)}{\partial z^n}\bigg|_{z=0}. \tag{2.19}$$

It will be useful to compute the expectation value and higher-order moments of the emitted photon number over time. These averages can be obtained by taking derivatives of G with respect to z and then evaluating them at $z = 1$. For instance, the expectation value and second moment of the photon number are expressed as follows

$$\begin{aligned}
\langle n \rangle &= \frac{\partial G(z,t)}{\partial z}\bigg|_{z=1}, \\
\left\langle n^2 \right\rangle &= \frac{\partial^2 G(z,t)}{\partial^2 z}\bigg|_{z=1} + \langle n \rangle .
\end{aligned} \tag{2.20}$$

The equations of motion for G, I, J and K are derived by multiplying each of the equations (2.17) by z^n and adding to n. After a shift of the summation index in the sums containing P_{n-1} and W_{n-1}, we get:

$$\begin{aligned}
\dot{G} &= \beta(z-1)(G+K), \\
\dot{I} &= \Delta J - \beta I, \\
\dot{J} &= -\Delta I - \beta J + \Omega K, \\
\dot{K} &= -\Omega J - \beta(z+1)(K+G).
\end{aligned} \tag{2.21}$$

With the initial conditions $G(z,0) = 1$, $I(z,0) = u_0$, $J(z,0) = v_0$, $K(z,0) = w_0$. These steps enable the conversion of a differential equation with an infinite number of coupled terms into a finite differential equation, but introducing an additional variable denoted z.

Now let $\tilde{G}(z,s)$, $\tilde{I}(z,s)$, $\tilde{J}(z,s)$, $\tilde{K}(z,s)$ be the Laplace transform of $G(z,t)$, $I(z,t)$, $J(z,t)$ and $K(z,t)$. Then in the transformed space, remembering that $\tilde{\dot{F}}(t) = s\tilde{F}(s) - F(0)$, equations (2.21) take the form:

$$\begin{pmatrix}
s+(1-z)\beta & 0 & 0 & \beta(1-z) \\
0 & s+\beta-\Delta & -\Delta & 0 \\
0 & \Delta & s+\beta & -\Omega \\
\beta(z+1) & 0 & \Omega & s+\beta(1+z)
\end{pmatrix}
\begin{pmatrix} \tilde{G} \\ \tilde{I} \\ \tilde{J} \\ \tilde{K} \end{pmatrix}
=
\begin{pmatrix} 1 \\ u_0 \\ v_0 \\ w_0 \end{pmatrix}, \tag{2.22}$$

which allows to solve for $\tilde{G}$:

$$\tilde{G} = \frac{a(s) + b(s)\beta z}{f(s) - \beta\Omega^2(s+\beta)z}, \tag{2.23}$$

with

$$\begin{aligned}
a(s) &= (s+\beta)^3 - \beta w_0(s+\beta)^2 + (\Omega^2\Delta^2 + \beta\Omega v_0)(s+\beta) - \beta\Delta(\Omega u_0 + \Delta w_0), \\
b(s) &= (1+w_0)(s+\beta)^2 - \Omega v_0(s+\beta) + \Omega\Delta u_0 + \Delta^2(1+w_0), \\
f(s) &= (s+\beta)^4 + (\Omega^2 + \Delta^2 - \beta^2)(s+\beta)^2 - \beta^2\Delta^2.
\end{aligned} \tag{2.24}$$

Using the expression for (2.23) in the Laplace transform of (2.19), we get

$$\tilde{P}_n(s) = \frac{\beta^n\Omega^{2n}(s+\beta)^n a(s)}{f(s)^{n+1}} + (1-\delta_{n0})\frac{\beta^n\Omega^{2n-2}(s+\beta)^{n-1}b(s)}{f(s)^n}. \tag{2.25}$$

The problem has been shifted to evaluating the inverse Laplace transform of expression (2.25). We can deduce that $\tilde{P}_n(s)$ has, at most, four isolated singularities at the zeros of $f(s)$, and therefore, $P_n(t)$ is the sum of the residues of $\tilde{P}_n(s)e^{st}$ at these singularities. The zeros of $f(s)$ are:

$$\begin{aligned}
s_1 &= -\beta + \alpha, \qquad & s_2 &= -\beta - \alpha, \\
s_3 &= -\beta + i\gamma, \qquad & s_4 &= -\beta - i\gamma,
\end{aligned} \tag{2.26}$$

where

$$\begin{aligned}\alpha &= \frac{1}{\sqrt{2}}\sqrt{\beta^2-\Omega^2-\Delta^2+\sqrt{(\beta^2-\Omega^2-\Delta^2)^2+4\beta^2\Delta}},\\ \gamma &= \frac{1}{\sqrt{2}}\sqrt{\Omega^2+\Delta^2-\beta^2+\sqrt{(\beta^2-\Omega^2-\Delta^2)^2+4\beta^2\Delta}}.\end{aligned} \tag{2.27}$$

Since $f(s) = \prod_i (s-s_i)$ appears as powers of $n+1$ and n in the denominators of (2.25), the singularities of these terms are poles of order $n+1$ and n, respectively; and we can use the derivative formula to evaluate the residues of $\tilde{P}_n(s)e^{st}$. The sum of the residues is

$$\begin{aligned}P_n(t) = \beta^n \sum_{i=1}^{4} \frac{\Omega^{2n}}{n!}\frac{d^n}{ds^n}\left(\frac{(s-s_i)^{n+1}(s+\beta)^n a(s)e^{st}}{f(s)^{n+1}}\right)_{s=s_i} &+ \\ + \frac{\Omega^{2n-2}}{(n-1)!}\frac{d^{n-1}}{ds^{n-1}}\left(\frac{(s-s_i)^n(s+\beta)^{n+1}b(s)e^{st}}{f(s)^{n+1}}\right)_{s=s_i}&.\end{aligned} \tag{2.28}$$

By using the Leibniz formula for the derivative of a product we can we can extract the explicit time dependence of the photon number distribution:

$$\boxed{P_n(t) = \sum_{i=1}^{4} e^{s_i t}\sum_{k=0}^{n} C^n_{ik} t^k} \tag{2.29}$$

where

$$\begin{aligned}C^n_{ik} = \frac{\beta^n\Omega^{2n}}{k!}\Bigg[\frac{d^{n-k}}{ds^{n-k}}\left(\frac{(s-s_i)^{n+1}(s+\beta)^n a(s)}{(n-k)!f(s)^{n+1}}\right)_{s=s_i} &+ \\ \frac{d^{n-k-1}}{ds^{n-k-1}}\left(\frac{(s-s_i)^n(s+\beta)^{n-1}b(s)}{(n-k-1)!\Omega^2 f(s)^{n+1}}\right)_{s=s_i}\Bigg]&.\end{aligned} \tag{2.30}$$

In Fig. 2.2 we plot $P_n(t)$ for an atom initially in the ground state. We observe that the probability of emitting no photons $P_0(t)$ monotonically decays over time. In Fig. 2.2a, where the driving is stronger than the dumping, we can observe population oscillations in the photon emissions. However, when the dumping is higher than the driving, as in Fig. 2.2b, for $n > 0$, the probability increases to a maximum and then vanishes.

Although this analytic method excels in deriving photon emission statistics for the two-level atoms, its applicability is constrained to small systems and does not accommodate the introduction of time-dependent controls such as $\Delta(t)$ or $\Omega(t)$. To overcome these limitations, we propose a generalization of this method capable of solving for the photon emission statistics of any system subjected to arbitrary driving conditions and transitions of interest. Whereas the method originally targeted resonant transitions, our extended approach accommodates non-resonant transitions as well. This numerical formalism involves iterating equations such as (2.17) up to a given cutoff N, ensuring

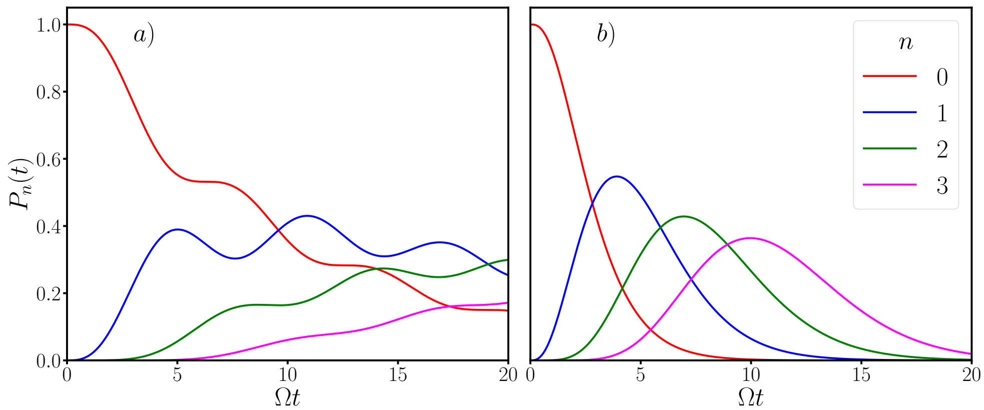

Fig. 2.2: Photon emission probabilities for an atom initially in the ground state for $\Delta = 0$ when, (a) $\beta = 0.2\Omega$, (b) $\beta = \Omega$. When the damping is weaker than the driving, the emission probabilities clearly reveal the signature of Rabi oscillations—namely, the coherent population oscillations between the bright and dark states.

that N substantially exceeds the average number of emitted photons $\langle n \rangle$. Using this framework, we aim to explore the optical properties of the NV center.

2.3 NV photon counting statistics

2.3.1 Energy levels

The NV center in diamond consists of a substitutional nitrogen atom adjacent to a vacant lattice site, as schematically shown in Fig. 2.3a. As we are interested in the readout of a negatively charged NV center, we consider the fast intrinsic dynamics [162] responsible for the radiative and non-radiative transitions between the electronic states. The NV states are distributed in two different spin $S = 1$ manifolds, the $^3A_2$ electronic ground state with the $\{|0\rangle, |1\rangle, |-1\rangle\}$ states used to encode a qubit and the ^3E excited-state manifold containing the $\{|e0\rangle, |e1\rangle, |-e1\rangle\}$ states. Non-resonant laser light is used to couple the ground states to the phononic band of the excited-state manifold. These vibrational states quickly decay into the corresponding spin-conserving excited state [42], destroying the optical coherence between the ground-state and excited-state manifolds. The excited states relax either directly through a spin-conserving transition that emits red fluorescence at a wavelength of approximately 637 to 800 nm, or through a non-spin-conserving channel through a metastable spin-singlet state $|s\rangle$ responsible for initialization and readout of the NV center. The energy levels together with the allowed transitions between them are depicted in Fig. 2.3b.

Ground state

The coherent dynamics of the electronic ground state under MW resonant control and a static magnetic field B_z aligned with the NV axis is described by the Hamiltonian

$$\hat{H} = D\,\hat{S}_z^2 - \gamma_e\,B_z\,\hat{S}_z\; + \sqrt{2}\Omega\hat{S}_x\cos(\omega t), \tag{2.31}$$

where we have ignored hyperfine interactions. The NV operators $\hat{S}_x$, $\hat{S}_y$ and $\hat{S}_z$ correspond to spin-1 matrices. The first term is the intrinsic zero-field splitting with $D = (2\pi)2.87$ GHz. The second term is the Zeeman splitting of the $|m_s\rangle = |\pm 1\rangle$ states due to the static magnetic field B_z, proportional to the electron gyromagnetic ratio $\gamma_e = (2\pi)28.024\ \frac{\text{MHz}}{\text{mT}}$. The last term represents the MW control with a Rabi frequency Ω proportional to the square root of the microwave power $\Omega \propto \sqrt{P_{MW}}$.

Expanding now the cosine into exponential terms and decomposing the spin operators $\hat{S}_x$ and $\hat{S}_z$ into the spin basis we can write:

$$\hat{H} = \omega_+ \,|1\rangle\langle 1| + \omega_- \,|-1\rangle\langle -1| + \Omega\left[|1\rangle\langle 0| + |0\rangle\langle 1| + |-1\rangle\langle 0| + |0\rangle\langle -1|\right]\cos(\omega t) \tag{2.32}$$

where $\omega_\pm = D \pm |\gamma_e| B_z$.

We can set the applied frequency in terms of a detuning with one of the transitions $\omega = \omega_+ + \Delta$. The Hamiltonian in the interaction picture is obtained through the transformation

$$\hat{U}_I(t) = \exp\Big\{-i(\hat{H}_0 + \Delta\hat{S}_z)t\Big\}, \tag{2.33}$$

with $H_0 = D\hat{S}_z^2 - \gamma_e B_z \hat{S}_z$. Then, following (2.5), the new Hamiltonian in the transformed frame is given by

$$\begin{aligned}\hat{H}_I &= \hat{U}_I^\dagger \hat{H} \hat{U}_I + i(\partial_t \hat{U}_I^\dagger)\hat{U}_I = \\ &= \hat{U}_I^\dagger(\hat{H}_0 + \hat{V}(t))\hat{U}_I - \Delta\hat{S}_z - \hat{H}_0 = \hat{U}_I^\dagger V(t)\hat{U}_I + \Delta\hat{S}_z\end{aligned} \tag{2.34}$$

As $\hat{H}_0 + \Delta\hat{S}_z$ is diagonal in the spin basis with eigenvalues $\lambda = \{\omega, 0, -\omega + 2D\}$, we ca calculate $\hat{U}_I$ as:

$$\hat{U}_I = e^{-i\omega t}\,|1\rangle\langle 1| + |0\rangle\langle 0| + e^{+i(\omega - 2D)t}\,|-1\rangle\langle -1| \tag{2.35}$$

Evaluating (2.34), the Hamiltonian in the interaction picture is then given by

$$\begin{aligned}\hat{H}_I &= \Delta\hat{S}_z + \frac{\Omega}{\sqrt{2}}\cos(\omega t)\,\Big(e^{i\omega t}\,|1\rangle\langle 0| + e^{-i(\omega-2D)t}\,|-1\rangle\langle 0| + \text{h.c.}\Big) = \\ &= \Delta\hat{S}_z + \frac{\Omega}{2\sqrt{2}}\Big(|1\rangle\langle 0| + |1\rangle\langle 0|\,e^{2i\omega} + e^{i2Dt}\,|-1\rangle\langle 0| + e^{2i(\omega-D)t}\,|-1\rangle\langle 0| + \text{h.c.}\Big)\end{aligned} \tag{2.36}$$

Hence, over any appreciable evolution time, the fast oscillations $\exp\{2i\omega t\}$, $\exp\{2iDt\}$ and $\exp\{2i(\omega - D)t\}$ will quickly average to zero. The rotating wave approximation is thus the claim that these terms may be neglected, so that the Hamiltonian can be written in the interaction picture, using $\hat{S}_z = |1\rangle\langle 1| - |-1\rangle\langle -1|$, simply as

$$\hat{H}_I \simeq \Delta(|1\rangle\langle 1| - |-1\rangle\langle -1|) + \frac{\Omega}{2}(|1\rangle\langle 0| + |0\rangle\langle 1|) \tag{2.37}$$

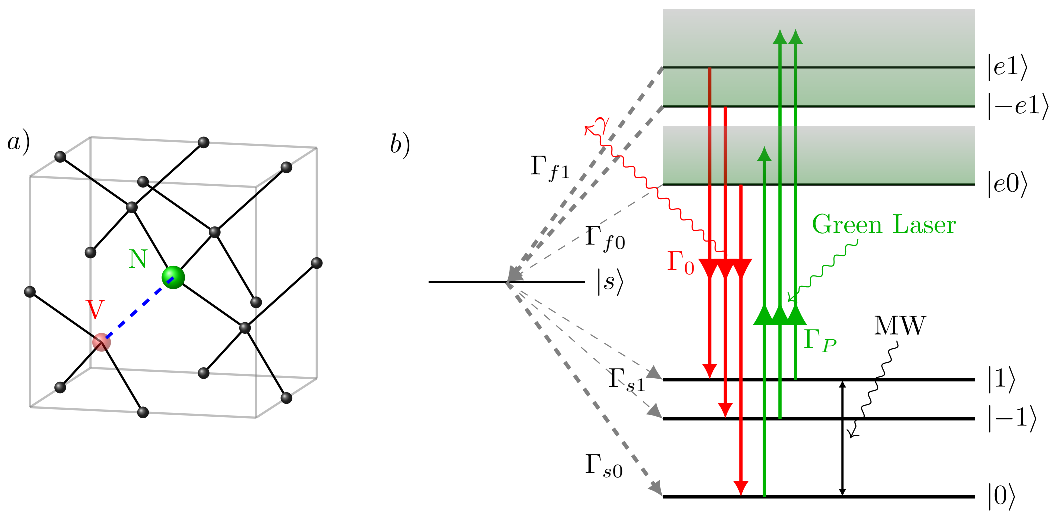

Fig. 2.3: (a) Diagram illustrating the nitrogen-vacancy center within the diamond lattice, showcasing the vacant position (transparent red), the substitutional nitrogen atom (green), and the adjacent carbon atoms surrounding the vacancy (black). (b) Representation of the levels of an NV center showing the system dynamics. The electronic ground states $|0\rangle$ and $|1\rangle$ encode the qubit and are coupled with a MW field of Rabi frequency Ω and detuning Δ. Laser light excites the states $|0\rangle$ and $|1\rangle$ with equal rate Γ_P to the excited states $|e0\rangle$ and $|e1\rangle$. The excited states decay to the ground state with rate Γ_0 emitting a photon. The state $|e1\rangle$ also decays to the singlet state $|s\rangle$ with rate $\Gamma_{f1} \gg \Gamma_{f0}$. The state $|s\rangle$ can decay to either ground state $|0\rangle$ or ground state $|1\rangle$ with rates Γ_{s0} and Γ_{s1}, respectively.

Since the driving does not produce transitions to the $|-1\rangle$ state of the NV center, we completely ignore this state of the Hamiltonian from now on and introduce the operators $\hat{\sigma}_x = |1\rangle\langle 0| + |0\rangle\langle 1|$, $\hat{\sigma}_z = |1\rangle\langle 1| - |0\rangle\langle 0|$ and $\hat{\mathbb{I}} = |1\rangle\langle 1| + |0\rangle\langle 0|$. The resulting Hamiltonian is

$$\hat{H}_I \simeq \frac{\Delta}{2}(\hat{\sigma}_z + \hat{\mathbb{I}}) + \frac{\Omega}{2}\hat{\sigma}_x \simeq \frac{\Delta}{2}\hat{\sigma}_z + \frac{\Omega}{2}\hat{\sigma}_x, \tag{2.38}$$

where we have discarded the term $\frac{1}{2}\Delta\hat{\mathbb{I}}$ because it corresponds to an energy shift that can be ignored in the dynamics.

Non-unitary dynamics

On the other hand, the nonunitary dynamics of the system, described by the density matrix $\varrho(t)$, follows the Lindblad master equation:

$$\dot{\varrho} = -i[\hat{H}_I, \varrho] + L\varrho = \mathcal{L}\varrho, \tag{2.39}$$

were $\hat{H}_I$ is the Hamiltonian of the whole system. Only the states $|0\rangle$ and $|1\rangle$ evolve coherently under $\hat{H}_I$; all remaining levels are governed by incoherent jumps described by $L[\varrho]$, with

$$L\varrho = \sum_k \Gamma_k(\hat{A}_k\varrho\hat{A}_k^\dagger - \frac{1}{2}\{\hat{A}_k^\dagger\hat{A}_k, \varrho\}), \tag{2.40}$$

where $\hat{A}_k$ is a jump operator that accounts for the dissipative part of the dynamics with rate Γ_k [151]. This Lindbland equation accounts for the interaction of the system with an external bath that causes decoherence and where the NV center excitations (e.g., photons) can be emitted.

Using this master equation, one can go beyond a basic-rate-equation model and comprehensively consider the impact of transverse fields and coherent spin-polarization exchange. Laser light excites the electronic ground states to the excited states with rate $\Gamma_0^{eo} = \Gamma_1^{e1} = \Gamma_{-1}^{-e1} = \Gamma_P$ through a spin-conserving transition, where their associated jump operators $\hat{A}_k$ are of the form $|e0\rangle\langle 0|$, $|e1\rangle\langle 1|$ and $|-e1\rangle\langle -1|$, respectively. The excitation rate Γ_P is modeled assuming a linear dependency on the laser power P_L, $\Gamma_P = c_L P_L$ [74]. The parameter $c_L \simeq 0.1$ MHz/μW, is estimated for our current setup by fitting the PES model to the experimental data through the saturation curve; see Sect. 2.4.4. Electronic excited states can spontaneously decay with rates $\Gamma_{e0}^0 = \Gamma_{e1}^1 = \Gamma_{-e1}^{-1} = \Gamma_0$ to the ground states.

The operators $\hat{A}_k$ not only represent incoherent jumps between different states but can also account for other nonunitary processes such as those producing longitudinal and transverse relaxation of the ground state, with rates $\gamma_1 = 1/T_1$ and $\gamma_2 = 1/T_2$. Without external excitation, the populations of the ground states $|0\rangle$ and $|\pm 1\rangle$ are assumed to decay toward equal populations at rate γ_1 through the operators $\hat{A}_+ = \hat{S}^+$ and $\hat{A}_- = \hat{S}^-$ with rate $\Gamma_\pm = \gamma_1/2 = 1/2T_1$. The transverse relaxation enters via a jump operator $\hat{A}_z = \hat{S}_z$, whose associated rate is given by $\Gamma_z = \gamma_2 = 1/T_2$.

Optical readout is possible because the $|e1\rangle$ and $|-e1\rangle$ states can also decay to the metastable singlet state $|s\rangle$ with rates $\Gamma_{e1}^s = \Gamma_{-e1}^s = \Gamma_{f1}$ much faster than the decay from the $|e0\rangle$ to the metastable state $\Gamma_{e0}^s = \Gamma_{f0}$. Thus, the $|0\rangle$ state is brighter than the $|\pm 1\rangle$ states when excited with the green source, as more population relaxes back to the ground state through radiative transitions in that case. Furthermore, optical polarization occurs because the state $|s\rangle$ decays with different rates $\Gamma_s^0 = \Gamma_{s0}$ and $\Gamma_s^1 = \Gamma_s^{-1} = \Gamma_{s1}$ to the ground states $|0\rangle$ and $|\pm 1\rangle$. Typical values of the decay rates are $\Gamma_0 \simeq 63$ MHz, $\Gamma_{f0} \simeq 12$ MHz, $\Gamma_{f1} \simeq 80$ MHz, $\Gamma_{s1} \simeq 2.4$ MHz and $\Gamma_{s0} \simeq 3.3$ MHz [151]. Similar values can be found in [74, 42, 39, 166].

2.3.2 Quantum jumps

In this section, we use the quantum jump formalism to compute the PES of the NV center [167]. The master equation, as defined in Eq. (2.39), offers insight into the time evolution of the density matrix. However, it does not directly yield information regarding the number of emitted photons during this evolution. As we previously did for the two level atom in Sec.2.2, we can decompose Eq. (2.39) as

$$\dot{\varrho} = \mathcal{L}\varrho = (\mathcal{L}_0 + \mathcal{J})\varrho, \tag{2.41}$$

in such a way that we have singled out the jump superoperator $\mathcal{J}$ associated with the stochastic radiative spontaneous decays from the excited states $\{|e0\rangle, |e1\rangle, |-e1\rangle\}$ into the ground states $\{|0\rangle, |1\rangle, |-1\rangle\}$ with rate Γ_0. Explicitly,

$$\mathcal{J}\varrho = \Gamma_0 \sum_{i\in\{0,1,-1\}} (|i\rangle\langle ei| \varrho |ei\rangle\langle i| - \frac{1}{2}\{|ei\rangle\langle i|, \varrho\}). \tag{2.42}$$

On the other hand, $\mathcal{L}_0$ governs the nonradiative dynamics of the NV center.

Since the NV center undergoes a discrete number of emissions during its evolution, the matrix $\varrho(t)$ is generalized to include information about the number of spontaneous photon emission events (or jumps) that have occurred before time t [156]. This generalization allows us to resolve the full density matrix into individual components $\rho(n,t)$, representing an event with n photons being spontaneously emitted during the time interval $[0,t]$,

$$\varrho(t) = \sum_n \rho(n,t). \tag{2.43}$$

Here $\rho(n,t)$ are not density matrices. We can define the equations of motion for $\rho(n,t)$

$$\dot{\rho}(n,t) = \mathcal{L}_0\rho(n,t) + \mathcal{J}\rho(n-1,t), \tag{2.44}$$

describing each photon emission as increasing the cumulative photon count by 1, $\rho(n-1,t) \to \rho(n,t)$. These equations couple n and $n-1$ terms and therefore are hard to solve.

The Lindblad equation (2.44) can be explicitly expanded into the projectors $\rho_{ij}(n,t) \equiv \rho^n_{ij}$, leading to a set of generalized Bloch equations. Defining the populations $\rho_{ii}(n,t) = \rho^n_i$, these equations read

$$\begin{aligned}
\dot{\rho}^n_0 &= -i\frac{\Omega}{2}(\rho^n_{01} - \rho^n_{10}) - \frac{\gamma_1}{2}(\rho^n_0 - \rho^n_1) - \frac{\gamma_1}{2}(\rho^n_0 - \rho^n_{-1}) - \Gamma_P\rho^n_0 + \Gamma_0\rho^{n-1}_{e0} + \Gamma_{s0}\rho^n_s,\\
\dot{\rho}^n_1 &= i\frac{\Omega}{2}(\rho^n_{01} - \rho^n_{10}) + \frac{\gamma_1}{2}(\rho^n_0 - \rho^n_1) - \Gamma_P\rho^n_1 + \Gamma_0\rho^{n-1}_{e1} + \Gamma_{s1}\rho^n_s,\\
\dot{\rho}^n_{-1} &= \frac{\gamma_1}{2}(\rho^n_0 - \rho^n_{-1}) - \Gamma_P\rho^n_1 + \Gamma_0\rho^{n-1}_{-e1} + \Gamma_{s1}\rho^n_s,\\
\dot{\rho}^n_{01} &= -(\frac{\gamma_1}{2} + \frac{\gamma_2}{2} + \Gamma_P - i\Delta)\rho^n_{01} + i\frac{\Omega}{2}(\rho^n_1 - \rho^n_0),\\
\dot{\rho}^n_{10} &= -(\frac{\gamma_1}{2} + \frac{\gamma_2}{2} + \Gamma_P + i\Delta)\rho^n_{10} - i\frac{\Omega}{2}(\rho^n_1 - \rho^n_0),\\
\dot{\rho}^n_{e0} &= \Gamma_P\rho^n_0 - \Gamma_0\rho^n_{e0} - \Gamma_{f0}\rho^n_{e0},\\
\dot{\rho}^n_{e1} &= \Gamma_P\rho^n_1 - \Gamma_0\rho^n_{e1} - \Gamma_{f1}\rho^n_{e1},\\
\dot{\rho}^n_{-e1} &= \Gamma_P\rho^n_{-1} - \Gamma_0\rho^n_{-e1} - \Gamma_{f1}\rho^n_{-e1},\\
\dot{\rho}^n_s &= \Gamma_{f1}\rho^n_{e1} + \Gamma_{f1}\rho^n_{-e1} + \Gamma_{f0}\rho^n_{e0} - (\Gamma_{s0} + \Gamma_{s1})\rho^n_s.
\end{aligned} \tag{2.45}$$

From the first three equations, note that the emission of n photons is affected by the $(n-1)$-photon process, where the state decays from the electronic ^3E manifold to the corresponding electronic ground state $^3A_2$.

We numerically solve the set of coupled differential equations (2.45) that dictate the

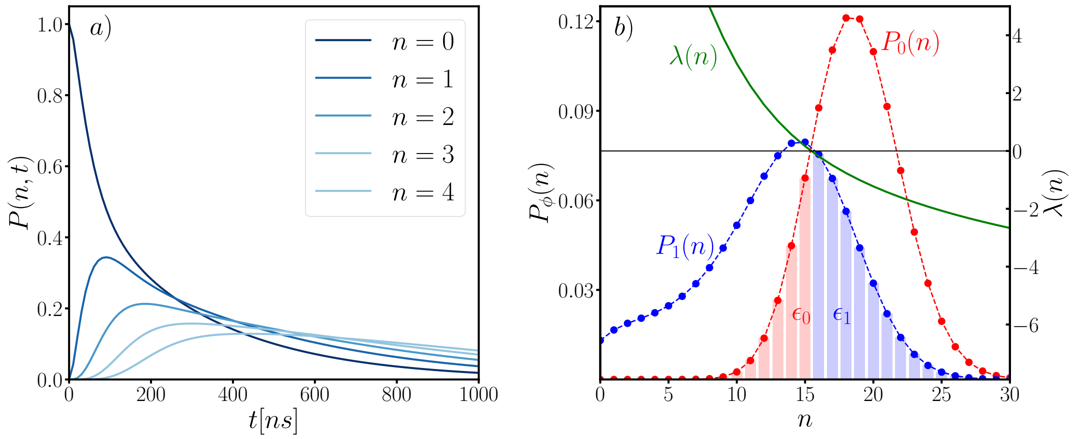

Fig. 2.4: (a) Emission probability of different numbers of photons n as a function of time for excitation of the NV center initially in a thermal state with a laser source of $\Gamma_P = 10$ MHZ. (b) After 700 ns of laser irradiation, we plot the probability distributions of measuring n photons for the initial state $|0\rangle$ in red $[P_0(n)]$ and $|1\rangle$ in blue $[P_1(n)]$. The error $\epsilon = (\epsilon_0 + \epsilon_1)/2$ is represented by the area of the overlap between both functions. We plot in green the log-likelihood ratio λ given by Eq. (2.57), which can be understood as the value of how confidently we can assign a photon number n to each state.

dynamics described by Eq. (2.44) under time-dependent laser intensity, MW power, and detuning by iteration up to a specific cutoff of emitted photons. Recall that for smaller and simpler systems, the problem can be solved analytically by introducing generating functions [156, 157, 158, 159]: this is no longer the case for general time-dependent laser and/or MW controls.

The PES of the system are obtained by tracing the atomic states $\rho(n,t)$ [159]:

$$P(n,t) = \mathrm{Tr}\{\rho(n,t)\}. \tag{2.46}$$

This formalism captures the probability distributions of an NV center regardless of its initial configuration, going beyond the steady-state configuration. The probabilities $P(n,t)$ are represented in Fig. 2.4a as a function of time for different values of n and in Fig. 2.4b as a function of n at a fixed time for two different initializations of the NV center. From these distributions we compute the expectation value of the number of emitted photons as a function of time, as well as higher moments of the distribution,

$$\langle n^m(t)\rangle = \sum_n P(n,t) n^m, \tag{2.47}$$

and also derive the counts per second, i.e. the photon intensity $\langle I\rangle$, that the NV center emits through the time derivative of the average number of photons,

$$\langle I(t)\rangle = \langle \dot{n}(t)\rangle\,. \tag{2.48}$$

Using these tools, we perform numerical simulations to compute the PES and use them to analyze different physical scenarios of interest in the following sections. Overall, the model provides a comprehensive framework for understanding the photon emission dynamics of NV centers and can be used to make predictions under a range of experimental conditions.

2.3.3 Arrival time

The function $P(n,t)$, evaluated at a specific time t, represents the probability of detecting exactly n photons within the time interval $[0,t]$. By analyzing the time evolution of $P(n,t)$, we can extract insights into the probability distribution that governs the detection time of the n-th photon. To facilitate this analysis, we introduce the probability densities $w(n,t)$ [168], which are defined as follows:

$$w(n,t)\mathrm{d}t = \text{probability that the } n\text{-th photon is detected in } [t, t+\mathrm{d}t]. \tag{2.49}$$

This probability density reflects the likelihood of detecting $n-1$ photons within the interval $[0,t]$ and then observing one additional photon within $[t, t+\mathrm{d}t]$. Given that only one photon or none can be detected within an infinitesimal time interval, we derive the following relations:

$$\begin{aligned} \dot{P}(0,t) &= -w(1,t), \\ \dot{P}(n,t) &= w(n,t) - w(n-1,t), \end{aligned} \tag{2.50}$$

and we can solve for $w(n,t)$ as:

$$w(n,t) = -\sum_{k=0}^{n-1} \dot{P}(k,t) \tag{2.51}$$

From (2.49), we derive the following interpretation:

$$\int_0^t w(n,\tau)\mathrm{d}\tau = \text{probability that the } n\text{-th photon is detected in } [0,t]. \tag{2.52}$$

and from (2.51) we find the following:

$$\int_0^t w(n,\tau)\mathrm{d}\tau = 1 - \sum_{k=0}^{n-1} P(k,t) = \sum_{k=n}^{\infty} P(k,t). \tag{2.53}$$

This expresses that the probability of detecting the n-th photon in $[0,t]$ is equal to the probability of detecting n or more photons in $[0,t]$.

In this context, an interesting quantity will appear to be the average elapsed time before the n-th photon is detected. We define the waiting time as

$$T_n = \int_0^{\infty} t w(n,t)\,\mathrm{d}t \tag{2.54}$$

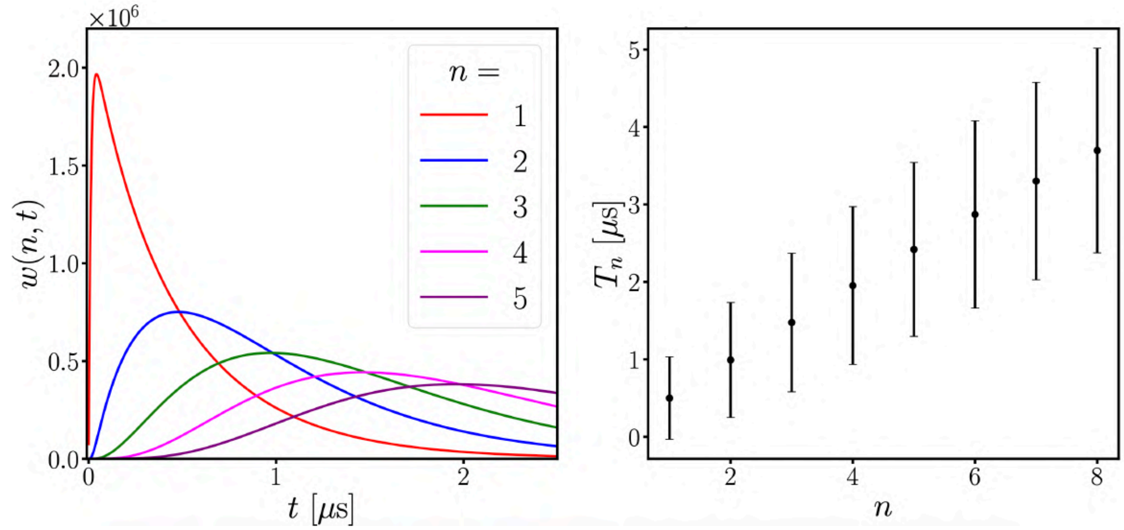

Fig. 2.5: For an NV center initialized in the $|1\rangle$ excited state with a rate $\Gamma_P = 2.5$ MHz: (a) probability densities $w(n,t)$, (b) waiting times T_n for the emitted photons, where the first photon is emitted on average at $T_1 = 500$ ns.

and again with equation (2.51) we can express directly in terms of $P(n,t)$

$$T_n = \sum_{k=0}^{n-1} \int_0^{\infty} P(k,t)dt, \tag{2.55}$$

and

$$\Delta T_n^2 = \int_0^{\infty} (t - T_n)^2 w(n,t)\, \mathrm{d}t = -\sum_{k=0}^{n-1} \int_0^{\infty} (t - T_n)^2 \dot{P}(k,t)dt. \tag{2.56}$$

In Fig. 2.5a, we depict the waiting time distribution for an NV center, providing a valuable insight into the behavior of this quantum system. The average emission times are depicted Fig. 2.5b, for the first photon is estimated at $T_1 = 500$ ns.

Studying the photon waiting time distribution can further enhance our knowledge of their behavior as photon emitters and help optimize their applications in quantum technologies. The photon waiting time distribution refers to the statistical distribution of time intervals between consecutive photon emissions from a quantum system [168]. It provides valuable information about the temporal characteristics of the photon emission process [169, 170]. Understanding this distribution is crucial for designing efficient quantum communication and sensing systems.

Understanding the waiting time sets the stage for a deeper exploration of the Purcell effect in NV centers [171], a phenomenon that has garnered considerable attention in the field of quantum optics. By manipulating the local density of optical states - by coupling them to optical resonators such as Fabry–Pérot microcavities, photonic crystal cavities, or plasmonic nanostructures - the Purcell effect offers a potential avenue to enhance the emission rates of NV centers, opening up exciting possibilities for applications in quantum information processing, quantum information, and quantum sensing [90, 172].

2.4 Applications

2.4.1 Experimental methods

The experimental measurements to validate the model presented in Sect. 2.3 were performed on an NV center of a diamond layer grown by chemical vapor deposition on a high pressure, high temperature substrate. Optical characterization of the NV centers was performed with a custom confocal microscope with continuous-wave excitation ODMR experiments. The confocal setup used to interrogate single NV centers is similar to the one used in the work reported in [72]. For NV optical excitation, we use a diode laser with a wavelength of 515 nm. NV center fluorescence was collected with an oil objective $\times 100$ with a numerical aperture of 1.4. The emitted photons were detected by a single-photon avalanche diode (SPAD) and counted with a FAST ComTec MCS8 multiple event time digitizer. The QUDI software suite [173] was used to control the experiments and collect data. The static magnetic field was generated with a permanent magnet. The microwave source used for the ODMR experiments was a TTi TGR600 signal generator with a Mini-Circuits ZHL-16W-43-S+ amplifier. Tektronix AWG7122C arbitrary-waveform generator was used to create the pulses for the Rabi experiment. Both MW signals were delivered to the sample through a cable antenna. All experiments were performed with the same selected NV center, except for the Rabi oscillations, where we used another NV center from another diamond implanted with ^{15}N with an implantation energy of $20-30$-keV.

2.4.2 State readout

NV center-based sensing applications rely on standard control sequences that involve spin initialization, manipulation, and readout. The effectiveness of the spin-readout process is crucial to the overall performance of the sensor, which can be evaluated within the PES model [174]. PES provides a useful framework for proposing new measurement strategies, increasing sensitivity based on Bayesian estimation [175], performing efficient single shot readout measurements [176], or speeding them up through a real-time adaptive decision rule [161], which can substantially decrease the average measurement time without significantly affecting readout fidelity. In the context of NV centers, a readout process usually consists of discriminating between the $|0\rangle$ and $|1\rangle$ states of the NV center that encode the qubit. These states can be distinguished through the number of emitted photons that have different statistical properties depending on the internal levels involved in the transition [67, 177].

The single repetition error rate ϵ is a commonly used merit figure for readout performance in a single repetition [174], defined as the average probability in a binary assignment of the incorrect state to the observed outcome. For an ideal measurement, with $\epsilon = 0$, the distributions associated with each state do not overlap [113], so we can discriminate between the $|0\rangle$ and $|1\rangle$ states in a single readout. However, a readout is subject to uncertainties in discrimination, leading to non-ideal measurements and overlap between the probability distributions $P_0(n,t)$ and $P_1(n,t)$ that hinder the $\{|0\rangle, |1\rangle\}$ state discrimination, see Fig. 2.4b. The assignment rule that minimizes ϵ is obtained by one calculating the log-likelihood ratio

$$\lambda(n,t) = \ln \frac{P_0(n,t)}{P_1(n,t)}. \tag{2.57}$$

When $\lambda(n,t)$ is larger (smaller) than 0, the state $|1\rangle$ ($|0\rangle$) is assigned; see Fig. 2.4b. The logarithmic likelihood ratio can be interpreted as the level of confidence of the observer in the state assignment given the number of photons collected n. The average single-repetition error rate is given by $\bar{\epsilon} = \frac{1}{2}(\epsilon_0 + \epsilon_1)$, where

$$\epsilon_0(t) = \sum_{n \leq n_c} P_0(n,t), \qquad \epsilon_1(t) = \sum_{n > n_c} P_1(n,t), \tag{2.58}$$

are the error rates conditioned on preparation of $|0\rangle$ and $|1\rangle$ with n_c defined such as $\lambda(n_c, t) = 0$. The error rates ϵ_0 and ϵ_1 are represented by color bars in Fig. 2.4b.

Although a single readout cannot determine with certainty whether the NV center is in the $|0\rangle$ state or the $|1\rangle$ state due to measurement uncertainty, repeated readouts 'average out' the noise, mitigating readout errors. Performing N repetitions of the readout process provides a set of photon count outcomes $D = \{n_1, n_2, ...n_N\}$. All outcomes are independently sampled from the same distribution, so the joint distribution of the readout outcomes conditioned on the intial state $a = 0/1$ is

$$p_a(D) = \prod_{k=1}^{N} P_a(n_k) \tag{2.59}$$

The cumulative log-likelihood ratio for the entire string of outcomes D is thus:

$$l_N = \ln \frac{p_0(D)}{p_1(D)} = \sum_{k=1}^{N} \lambda(n_k) \tag{2.60}$$

As before, the eigenvalue $a = 0$ ($a = 1$) is assigned when $l_N > 0$ ($l_N < 0$). Equation (2.60) shows that in the general case, each outcome must be weighed by $\lambda(n_k)$ in order to perform optimal assignment. Therefore, discarding information contained in each repetition is necessarily suboptimal. The average cumulative error rate is now $e_N = (e_N^0 + e_N^1)/2$, where

$$e_N^0 = p_0(l_N < 0) \qquad e_N^1 = p_1(l_N > 0) \tag{2.61}$$

are the cumulative error rates conditioned on preparation of $a = 0$ and $a = 1$, respectively. The cumulative log-likelihood ratio l_N is the sum of the independent and identically distributed variables $\lambda(n_k)$. According to the central-limit theorem, the distributions $p_0(l_N)$ and $p_1(l_N)$ asymptotically converge to Gaussian distributions. Thus, one might hope to evaluate the cumulative error rates in equation (2.61) using the cumulative distribution function of a Gaussian distribution. As was first noted by Cramer, however, this approach produces wildly inaccurate results [178]. Indeed, according to the Berry-Esseen theorem [179, 180], the cumulative distribution function of $p_0(l_N)$ and $p_1(l_N)$ converge only polynomially to a Gaussian as N increases. Meanwhile, the error rates e_N^0 and e_N^1 decrease exponentially with N. Therefore, the relative accuracy in e_N^0 and e_N^1 explodes as $N \to \infty$ and the central-limit theorem fails. This problem is solved with the theory of large deviations. Because the noise is sampled independently in each repetition, the cumulative error rate e_N is expected to decrease exponentially as N increase:

$$\ln e_N(t) \to -C(t)N \text{ as } N \to \infty. \tag{2.62}$$

for some constant C. The constant C is the Chernoff information, which is an appropriate figure of merit for repetitive qubit readout[174]

$$C(t) = -\min_{0\leq s\leq 1} \ln\,[\sum_n P_0(n,t)^s P_1(n,t)^{1-s}]. \tag{2.63}$$

The Chernoff information [181] is a symmetric distance measure between the distributions $P_0(n,t)$ and $P_1(n,t)$ that can be interpreted as a rate of information gain per repetition. Like the single-repetition readout error rate ϵ, the Chernoff information depends only on the statistics of readout outcomes in a single-repetition. Unlike ϵ, however, it depends on the relative value of $P_0(n)$ and $P_1(n)$. Consequently, the Chernoff information encodes information contained in the level of confidence $\lambda(n)$ in each readout outcome. As a result, readout outcome distributions $P_0(n,t)$ and $P_1(n,t)$ with the same single repetition error rates ϵ do not necessarily have the same Chernoff information.

The calculated Chernoff information is a useful tool for analyzing the statistical properties of the fluorescence. It can be used to estimate the minimum number of photons that need to be measured to discriminate between two different quantum states of a light source with a certain level of confidence [174, 182], thereby providing the sensitivity limits of a quantum system. Thus, the Chernoff information provides useful insight into the optimal experimental parameters for maximizing state discrimination.

In Fig. 2.6a, the Chernoff information is plotted for different laser intensities as a function of time, for a constant laser irradiation. For a specific laser intensity, the Fig. 2.6a shows a maximum, indicating the optimal duration of the laser pulse for reading out the ground state of the NV center. In Fig. 2.6b, the maximum value of the peak and the time t_{max} at which it occurs are plotted for different values of Γ_P. As the laser intensity is increased, the peak becomes higher and occurs faster, resulting in better and faster state discrimination. However, it also increases the background noise introduced in the measurement. This is discussed in Sec.2.4.4. Both the Chernoff peak and t_{max} saturate for high laser intensities, meaning that increasing the laser power beyond this point will not result in better measurement outcomes.

To illustrate the relevance of the Chernoff information, we used the PES to simulate the readout of Rabi oscillations. A MW pulse takes the NV to a superposition state, which after a readout laser pulse emits fluorescence with a $P(n,t)$ distribution for a given

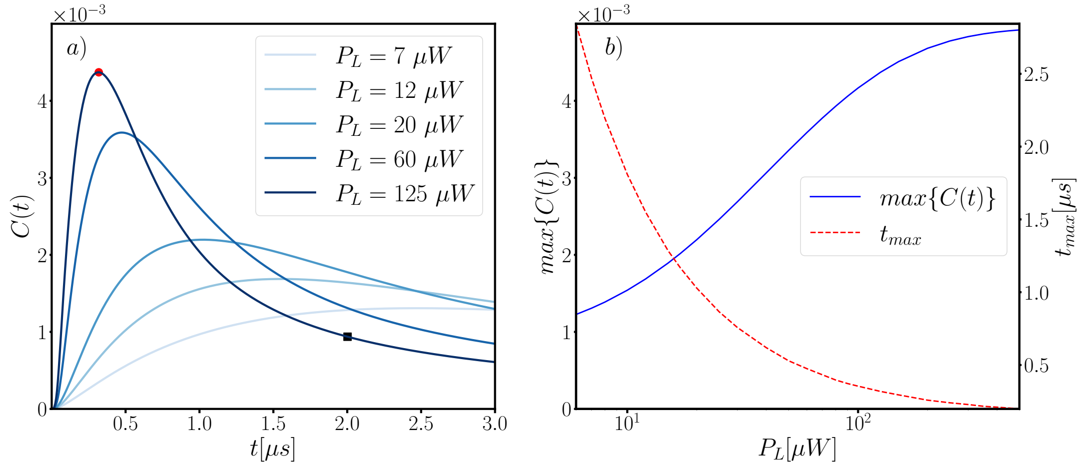

Fig. 2.6: (a) Calculated Chernoff information for different laser powers as a function of time. The red circle and the black square correspond to the pulse power and the length at which we simulate two different Rabi oscillations in Fig. 2.7b. (b) Maximum value achieved by the Chernoff information $max\{C(t)\}$, and the time at which this value is achieved t_{max}, as a function of the laser intensity. This allows to investigate how fast and well we are able to discriminate the NV center state and the required power. The maximum value and time saturate as the power increases.

irradiation time t. A photon measurement n can be simulated by sampling a point from this distribution. Thus, N measurements consist of sampling a set of readouts outcomes $\{n_1, n_2, ..., n_N\}$. On the one hand, as the number of repetitions increases [see the symbols in Fig. 2.7a the distribution of the sampled photons converges to the average of the distributions (dashed red line), since the error of repeated measurements averages out the uncertainties. On the other hand, the working conditions for a larger Chernoff parameter (see Fig. 2.6a favor the discrimination of the $|0\rangle$ and $|1\rangle$ states, increasing the amplitude of the Rabi oscillations; see Fig. 2.7b. The increased amplitude of the Rabi oscillations resulting from larger Chernoff value leads to improved discrimination of the state of the NV center, higher readout fidelity, and ultimately, better experimental outcomes. As seen, the photon statistic model allows us to predict and improve measurement sequences by optimizing relevant experimental parameters.

2.4.3 Autocorrelation measurements

Temporal photon correlations and the photon statistics carry information on the dynamics of the radiating NV center. Autocorrelation measurements are a valuable technique for studying the temporal dynamics of fluorescence signals and the statistical behavior of photons in a light source [183, 184]. By measuring the correlation between the intensity of the signal at different delay times, one can extract information about the decay rates of the states of an NV center [185], categorize an emitter as a single-photon source [186], investigate NV centers embedded in different physical structures [72, 187, 188, 189],

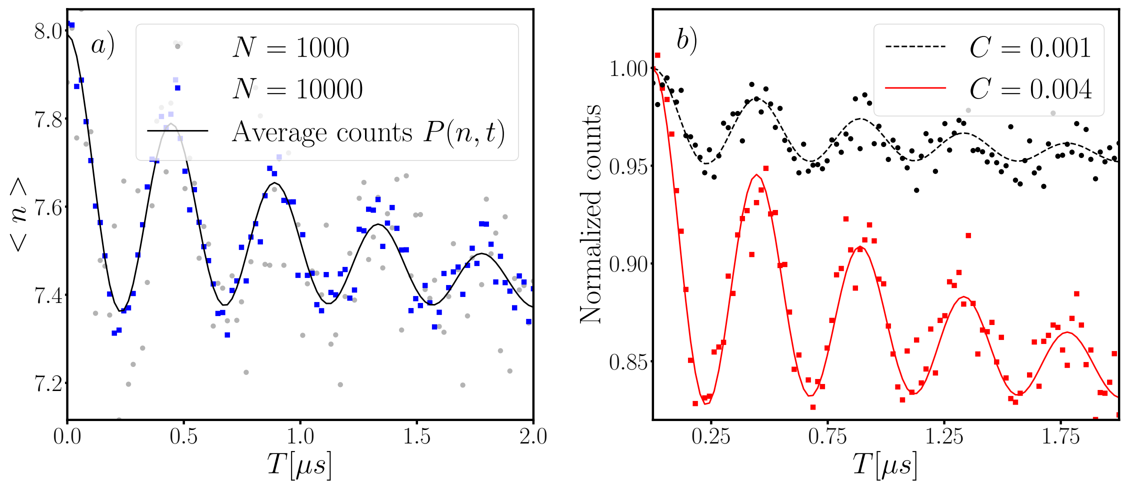

Fig. 2.7: (a) Measured Rabi oscillations for initialization and readout pulses of 2 μs and a MW field with $\Omega = 2.70$ MHz, $\Delta = 0$ MHz and $\Gamma_P = 20$ MHz. The dashed line represents the mean photon number $\langle n \rangle$ computed by Eq. (2.47) from the theoretical $P(n,t)$, symbols correspond to sampling N photon counts, while the black-solid line is the measured Rabi oscillations using the procedure and setup described in Sec. 2.4.1. (b) Simulated Rabi oscillations for different Chernoff informations with $\Omega = \Delta = 10$ MHz and readout excitation rate $\Gamma_P = 12.5$ MHz for two different time pulses. In red $t = 300$ ns corresponding to the Chernoff maximum $C = 4 \cdot 10^{-3}$ and in black $t = 2$ μs for $C = 1 \cdot 10^{-3}$. We plot the normalized counts deduced from the same emission probability $P(n,t)$ considering $N = 3000$ measurements (points) and its average (lines).

and characterize the interactions with other quantum systems [146, 190, 191, 192]. The second-order temporal coherence $g^{(2)}(\tau)$ measures the photon autocorrelation, which, in terms of the intensity $I(t)$, reads

$$g^{(2)}(\tau) = \frac{\langle I(t)I(t+\tau)\rangle}{\langle I(t)\rangle^2}. \tag{2.64}$$

Alternatively, it can also be computed with the use of the delay function $D_1(t)$ describing the distribution of delay times before the next emission occurs. This function is calculated from the survival probability $P(0,t)$ as [193]

$$D_1(t) = -\dot{P}(0,t). \tag{2.65}$$

The conditional probability of an NV center emitting any photon between time τ and time $\tau + d\tau$, after having emitted a photon at time $\tau_0 = 0$, is $D(\tau)d\tau$. The photon emitted at time τ can be the first to be emitted after that at time $\tau_0 = 0$ or the next

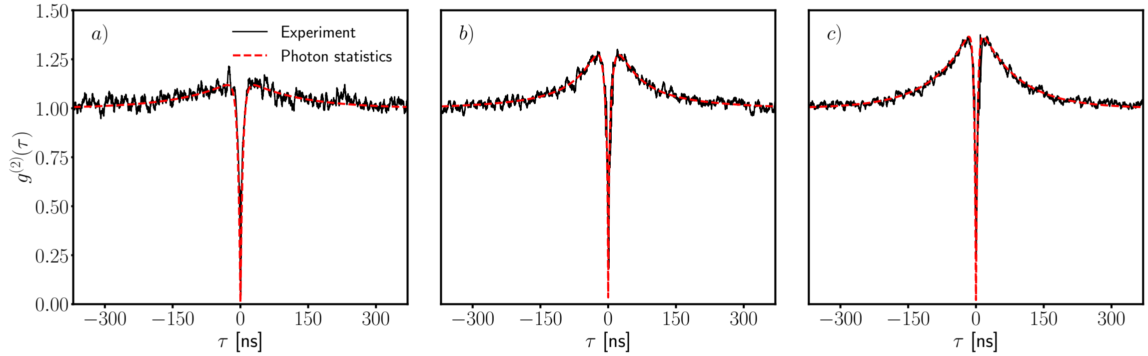

Fig. 2.8: Measured auto-correlation functions (black solid line) and the photon statistics model predictions (red dashed line) according to Eq. (2.67) for different excitation rates: (a) $\Gamma_P = 5$ MHz, (b) $\Gamma_P = 15$ MHz and (c) $\Gamma_P = 20$ MHz

after any other time τ' $(0 < \tau' < \tau)$, so

$$D(\tau) = D_1(\tau) + \int_0^\tau d\tau' D(\tau') D_1(\tau - \tau'). \tag{2.66}$$

This is a functional integral equation which can be solved numerically. The function $g^{(2)}(\tau)$ is the normalized correlation function for a photon detection at $\tau_0 = 0$ followed by the detection of any photon (not necessarily the next) at time τ. It follows that

$$g^{(2)}(\tau) = \frac{D(\tau)}{\lim_{\tau\to\infty} D(\tau)}. \tag{2.67}$$

In Fig. 2.8 we plot the background noise-corrected $g^2(\tau)$ [194] from a single NV center in a Hanbury Brown-Twiss (HBT) correlation experiment [192]. As the pumping rate increases (left to right), a higher $g^{(2)}(\tau) > 1$ region is observed. More photons are emitted at a fixed τ, leading to their larger bunching. The results predicted from the photon statistics model Eq.(2.67) perfectly fit the experimental data.

To perform the HBT correlation experiment the initial stream of emitted photons is directed towards a beam splitter, which is a partially reflecting mirror. The beam splitter divides the incoming light into two separate paths. Each of the two resulting beams is directed towards a separate SPAD detectors. The output signals from the detectors are then sent to correlation electronics. These electronics measure the time intervals between the detection events from photons at each detector. By definition

$$g^{(2)}(\tau) = \frac{\langle S_1(t) S_2(t+\tau)\rangle}{\langle S_1(t)\rangle \langle S_2(t+\tau)\rangle}, \tag{2.68}$$

here $S_i(t)$ is the signal intensity at the i-th detector. In the presence of noise $N_i(t)$, the total signal at the detector would be $I_i(t) = S_i(t) + N_i(t)$. The measured $\hat{g}^{(2)}(\tau)$, assuming that the noise is statistically independent of the signal, is

$$\hat{g}^{(2)}(\tau) = \frac{\langle I_1(t) I_2(t+\tau)\rangle}{\langle I_1(t)\rangle \langle I_2(t+\tau)\rangle} = \frac{\langle (S_1(t) + N_1(t))(S_2(t+\tau) + N_2(t+\tau)\rangle}{\langle S_1(t) + N_1(\tau)\rangle \langle S_2(t+\tau) + N_2(t+\tau)\rangle}. \tag{2.69}$$

Thus, the theoretical $g^{(2)}(\tau)$ can be connected to the measured noisy $\hat{g}^{(2)}(\tau)$ by simultaneously recording the average values $\langle I_i(\tau)\rangle$, $\langle N_i(\tau)\rangle$ during the correlation measurement process:

$$\begin{aligned} g^{(2)}(\tau) = \hat{g}^{(2)}(\tau) & \frac{\langle S_1\rangle \langle S_2\rangle + \langle N_1\rangle \langle S_1\rangle + \langle N_2\rangle \langle S_2\rangle + \langle N_1\rangle \langle N_2\rangle}{\langle S_1\rangle \langle S_2\rangle} - \\ & - \frac{\langle N_1\rangle \langle N_2\rangle + \langle N_1\rangle \langle S_1\rangle + \langle N_2\rangle \langle S_2\rangle}{\langle S_1\rangle \langle S_2\rangle}, \end{aligned} \tag{2.70}$$

with $\langle S_i\rangle = \langle I_i\rangle - \langle N_i\rangle$.

The Mandel Q parameter [157],

$$Q(t) = \frac{\langle n^2(t)\rangle - \langle n(t)\rangle^2}{\langle n(t)\rangle} - 1, \tag{2.71}$$

is another measurement for the correlation of emitted photons that relies on the variance of the photon number in the detected fluorescence. When $Q = 0$, the counting statistics $P(n,t)$ follow Poisson distributions with no correlation between the emitted photons. On the other hand, when $Q > 0$, the statistics are super-Poissonian, indicating photon bunching, where photons tend to be emitted together. Conversely, sub-Poissonian statistics ($Q < 0$) indicate photon antibunching, where photons tend to be emitted at well-separated times.

Using PES, we calculate $Q(t)$ at different power excitations, observing different bunching behaviors as a function of time for a thermal initialization of the NV center; see Fig. 2.9a. The photon emission begins with some degree of antibunching because the excited states are not yet populated. At time t_{min}, such that $Q(t_{min}) = \min\{Q(t)\}$, the emitted photons are maximally anticorrelated, showing a nonclassical antibunched character. Then, the statistics starts to bunch at time t_0, until it saturates at long times and the emitted distribution of photons becomes thermal. As presented in Fig. 2.9b and Fig. 2.9c, the model predicts a higher degree of antibunching for increasing power, albeit the time interval during which antibunching occurs is reduced.

The autocorrelation function and the Mandel parameter allow us to investigate the capabilities of NV centers as photon emitters since it has been found that NV centers exhibit both bunching and antibunching behavior depending for the specific excitation conditions [42, 195]. Bunching and antibunching phenomena have important consequences on the performance of devices that use quantum systems as a source of photons, such as those used in quantum communication. For example, bunching can lead to increased noise in the emitted light [196, 197], while antibunching can improve the use of NV centers for single photon generation [198, 199, 200].

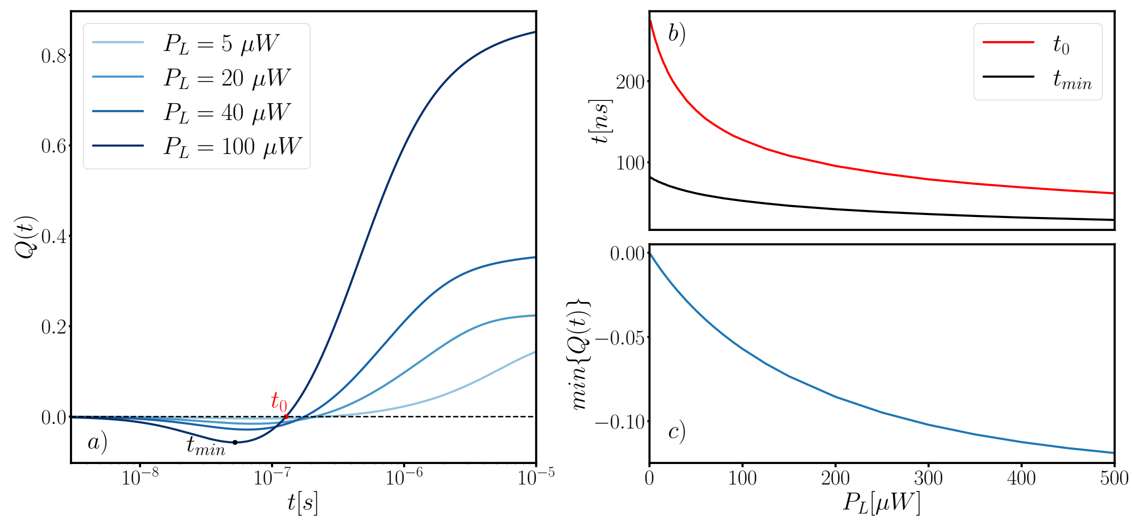

Fig. 2.9: (a) Mandel Q parameter (2.71) as a function of time for a thermal initialization of the NV center. The characteristic times t_{min} and t_0 correspond to a Mandel paramater value $Q(t_{min}) = \min\{Q(t)\}$ and $Q(t_0) = 0$ of the photon emission, respectively. (b) t_{min} and t_0 and (c) $Q(t_{min})$ as a function of the laser power.

2.4.4 Fluorescence saturation

As the laser power is increased, the NV center absorbs more photons and becomes excited more frequently. As the laser power continues to increase, the populations of the excited state and the ground state eventually become approximately equal, resulting in a saturation of the emission rate of the NV center. Using PES to compute the saturation curve for an NV center allows to optimize and compare the performance of an NV-based sensor [201, 202], and study its quantum efficiency [203] and its signal-to-noise ratio [204].

In Fig. 2.10 we plot the experimental saturation curve of the selected NV center (black dots) on top of the theoretical curve obtained using the PES model (dashed red line). Note that the PES model matches the NV counts computed by subtraction of the background counts from the total measured counts. We have also taken into account that not all the emitted photons are collected due to the geometry of the experiment and the efficiency of the detector by multiplying the saturation curve by a scaling factor c_E. This scaling factor provides insight into the collection efficiency of the setup and indicates improvement potential. It relates the measured NV center intensity I_M with the predicted by the PES by $I_M = c_E \langle I \rangle$. This factor effectively represents the overall collection efficiency of the setup. Is treated as a fitting parameter that scales the theoretical fluorescence predicted by the PES model to match the measured counts. This approach allows us to extract an effective collection efficiency from the experimental data, which also provides a way to benchmark and potentially improve the optical setup. Modeling of such saturation curves may be useful in scenarios where subtraction of the background counts from the total counts can be harder, for instance in experiments with NV ensembles.

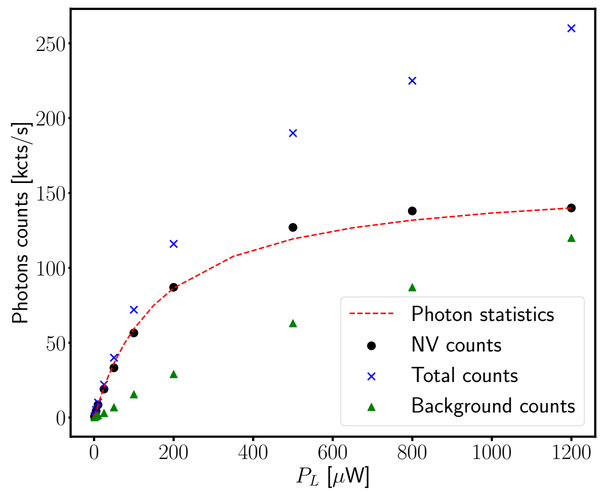

Fig. 2.10: Benchmark of the predicted saturation curve for an NV center as a function of the laser power computed by the photon statistic model (red line) against the detector photon counts (black points). The NV counts were computed by subtraction of the background counts (green triangles) from the total measured counts (blue crosses).

2.4.5 Continuous-wave optically detected magnetic resonance

Diamond NV centers have shown remarkable potential as a tool for detecting magnetic fields. This ability is based on the electronic spin level structure of the NV center and the Zeeman effect, which results in a lifting of the degeneracy between the states $|\pm1\rangle$ and when a magnetic field is applied, as discussed in Sect. 2.3. The energy splitting between these states is proportional to the applied magnetic field and can be measured via ODMR experiments.

In an ODMR experiment, a MW field is applied to the NV center, while a green laser initializes the NV center to the $|0\rangle$ state. When the MW field is resonant with the transition between the $|0\rangle$ state and one of the $|\pm1\rangle$ states, the fluorescence from the NV center drops, as some of the population is transferred from the bright state $|0\rangle$ to the darker states $|\pm1\rangle$ [74, 185]. This phenomenon enables the detection of magnetic fields by measuring the resonant transition frequency between the $|0\rangle$ and $|\pm1\rangle$ states.

The contrast c of cwODMR can be estimated from the PES, neglecting other external factors, by considering the average intensity $\langle I(t)\rangle$ in the steady state of the system, $t\to\infty$, when the NV center is driven by resonance $\Delta=0$, or off-resonance, $\Delta\to\infty$:

$$c = 1 - \frac{\langle I(t\to\infty, \Delta=0)\rangle}{\langle I(t\to\infty, \Delta\to\infty)\rangle} \tag{2.72}$$

We perform cwODMR experiments to benchmark the PES model. These experiments involve the continuous application of both the laser and the MW fields to the NV center. Although pulsed-ODMR experiments provide greater sensitivity, they require the generation and synchronization of fast MW and laser pulses, which can be demanding

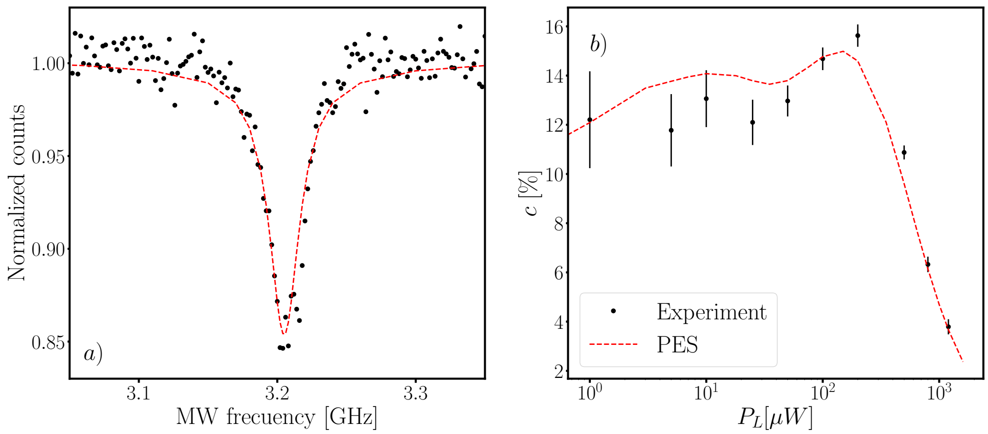

Fig. 2.11: (a) The black points correspond to an ODMR experiment with a MW power of $\Omega = 8$ MHz and an excitation rate of $\Gamma_P = 20$ MHz. We obtained a contrast $c = 15\%$. The red line is the result from the photon statistics simulation. (b) Contrast as a function of the laser power at a fixed MW power of $\Omega = 8$ MHz. The black points correspond to the values from Lorentzian fits to the experimental data and the red line the photon statistics model.

in terms of experimental setup. The advantages of cwODMR experiments include their simplicity, the ability to measure a wide range of magnetic fields, and the capability to detect weak magnetic fields. As a result, the cwODMR method is a valuable technique for a wide range of applications, such as sensing magnetic fields from biological systems [73], imaging magnetic materials [205], and detecting single-spin dynamics [206].

The accurate estimation of the cwODMR center resonance frequency and precise computation of the corresponding magnetic field require a high contrast c [74], a quantity that depends on the MW and laser powers, as well as other physical parameters. The photon statistics model predicts the behavior of c, allowing the optimization of MW and laser powers, which leads to the maximal sensitivity of the NV center. Note that the model was used successfully to simulate cwODMR, as demonstrated in Fig. 2.11a. In Fig. 2.11b, the contrast is plotted for different laser powers, with a fixed MW power of 8 MHz. The contrast increases at lower powers and reaches a maximum around 200 μW before decreasing. This maximum depends on the applied MW field and occurs because the NV center is optically excited at a faster rate than the spin transitions.

2.4.6 Imperfect detection

When conducting experimental investigations of the PES, it is crucial to consider that the detection process is not ideal. The PES takes into account the photons emitted by the NV center, but it is important to note that not all of them will reach the detector because of factors like optical losses or collection geometry, which results in limited collection efficiency. We can model this efficiency by assigning a probability to each

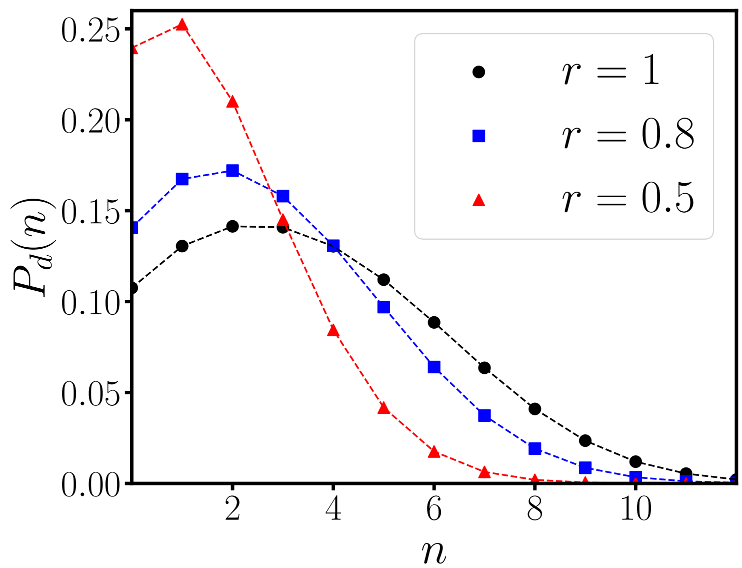

Fig. 2.12: Detection probabilities $P_d(n)$ for the ground state $|0\rangle$ as a function of the number of detected photons n for diferent detection rates r after 500 ns of excitation with $\Gamma_P = 20$ MHz.

emitted photon to reach the detector. The PES enables us to examine this efficiency by comparing the number of detection events with the expected emission, aiding in the enhancement and optimization of experimental setups.

Here we will explore the impact of non-ideal detection on the reading process. It is widely acknowledged that detection efficiency, which encompasses factors like detector quantum efficiency and fluorescence collection efficiency, plays a crucial role in determining how accurately photodetection statistics represent PES. Although other factors like afterpulsing and detector deadtime contribute to non-ideal detection, first we will concentrate solely on modeling detection efficiency as it is the most pertinent aspect.

We begin by considering that our optical system detects a fraction r of all emitted photons. To establish a connection between the probability of emitting n photons, denoted $P_e(n)$, and the probability of detecting them, denoted as $P_d(n)$, we must account for various scenarios. Detecting n photons could involve emitted exactly n photons and none being rejected, or more than n photons being emitted, say a number m, with n of them detected while the remaining $(m-n)$ are rejected. By accounting for all possible combinations in which m photons can be either rejected or detected, we can express the relationship between $P_e(n)$ and $P_d(n)$ as

$$P_d(n) = \sum_{m=n}^{\infty} P_e(m) P_B(n; m, r), \tag{2.73}$$

with $P_B(n;m,p)$ the binomial probability

$$P_{\mathrm{B}}(n;m,r) = \binom{m}{n} r^n (1-r)^{m-n}. \tag{2.74}$$

In Fig. 2.12 we see how lower detection rates r push the detection distribution towards smaller photon numbers.

Thus, we have that the moments of the emission and detection distributions are related as follows:

$$\left\langle n^k \right\rangle_d = \sum_{n=0}^{\infty} \left\langle n^k \right\rangle_{\mathrm{B}} P_e(n), \tag{2.75}$$

with $\left\langle n^k \right\rangle_{\mathrm{B}}$ the moments for the binomial probabilities:

$$\left\langle n^k \right\rangle_{\mathrm{B}} = \sum_{i=0}^{n} i^k P_{\mathrm{B}}(i;n,r), \tag{2.76}$$

which for $k=1$ and $k=2$ we have:

$$\begin{aligned} \langle n \rangle_{\mathrm{B}} &= nr \\ \left\langle n^2 \right\rangle_{\mathrm{B}} &= nr(1-r) + n^2 r^2. \end{aligned} \tag{2.77}$$

From the above, it is evident that $\langle n^k \rangle_d = r \langle n^k \rangle_e$, as expected. This implies that the intensity will be diminished by the same factor r,

$$\langle I \rangle_d = \langle \dot{n} \rangle_d = r \langle \dot{n} \rangle_e = r \langle I \rangle_e, \tag{2.78}$$

yet the autocorrelation function will remain unaltered because the term r will cancel out:

$$g_d^{(2)}(\tau) = \frac{\langle I_d(t) I_d(t+\tau) \rangle}{\langle I_d(t) \rangle^2} = \frac{r^2 \langle I_e(t) I_e(t+\tau) \rangle}{r^2 \langle I_e(t) \rangle^2} = g_e^{(2)}(\tau). \tag{2.79}$$

However, the Mandel parameter (Eq. (2.71)) will also decrease by a factor of r:

$$Q_d = \frac{\langle n^2 \rangle_d - \langle n \rangle_d^2}{\langle n \rangle_d} - 1 = \frac{\langle n \rangle_e r(1-r) + r^2 \langle n^2 \rangle_e - r^2 \langle n \rangle_e^2}{r \langle n \rangle_e} - \frac{r \langle n \rangle_e}{r \langle n \rangle_e} = \tag{2.80}$$

$$= r \frac{-\langle n \rangle_e + \langle n^2 \rangle_e - \langle n \rangle_e^2}{\langle n \rangle_e} = r \left(\frac{\langle n^2 \rangle_e - \langle n \rangle_e^2}{\langle n \rangle_e} - 1 \right) = r Q_e, \tag{2.81}$$

meaning that at low detection rates it will be hard to measure it.

The impact of these inefficiencies on $\lambda(n)$ and the Chernoff information is not straightforward to compute directly, but can be easily simulated. This underscores the significance of the Chernoff information, as another readout metric, contrast, which depends solely on the quotient between the intensities of the $|0\rangle$ and $|1\rangle$ states, will not be influenced by r, while the Chernoff information will provide insight into the role of this parameter in the readout.

However, this detection factor r is not the only source of noise in the detection process. The detectors are not perfect; not all arriving photons will be detected, and not all detections will be attributed to the emitted photons. The detector has a dead time, during which it is unable to register subsequent events because it is still processing a previous event. Afterpulsing describes a non-ideal behavior of the detector wherein an artificial count is generated shortly after a real photon pulse. Afterpulsing and dead-time will have a strong impact on the PES for extremely short photon-counting time intervals or very high count rates because the characteristic timescale of these processes is in the range of tens of nanoseconds. These phenomena can be addressed by analytically modifying the PES [207, 208] or through quantum trajectories, involving the simulation of several trajectories.

Quantum trajectories

A limitation of the formalism used to calculate the PES is that it does not allow the simulation of experimental realizations of independent photon emissions. These realizations can be useful for analyzing certain processes that might apply only to single photons, such as imperfections in the detection mechanism. However, we can directly simulate these emissions using the quantum trajectories approach. The main component of this method is evolving the wave function of the system in time with a pseudo-Hamiltonian; where at each time step, a discontinuous change may take place with some probability. The calculated system state as a function of time is known as a quantum trajectory, and the desired density matrix as a function of time may be calculated by averaging over many simulated trajectories. We can approximate the PES through multiple trajectories realizations, associating the jump from the excited states to the ground states with one photon emission.

We consider our system evolving under a Hamiltonian $\hat{H}$ which suffer decoherence and jumps with the operators $\hat{A}_k$ with rates Γ_k, following the dynamics given by Eq.(2.39). In order to solve the previous equation one can resort to a stochastic dynamics using quantum trajectories, also known as Monte Carlo wavefunction [209]. A quantum trajectory can be computed following a Schrödinger equation with a non-Hermitian Hamiltonian

$$\hat{H}_{\text{eff}} = \hat{H}_I - i\sum_k \frac{\Gamma_k}{2}\hat{A}_k^\dagger \hat{A}_k. \tag{2.82}$$

The unitary Hamiltonian $\hat{H}_I$ is defined in Eq.(2.38). Here, the strictly negative non-Hermitian portion of $\hat{H}_{\text{eff}}$ gives rise to a reduction in the norm of the wave function, that to first-order in a small time step $\mathrm{d}t$, its given by

$$\langle \psi(t+\mathrm{d}t)|\psi(t+\mathrm{d}t)\rangle = 1 - \mathrm{d}p, \tag{2.83}$$

where

$$\mathrm{d}p = \mathrm{d}t\sum_k \Gamma_k \langle \psi(t)| \hat{A}_k^\dagger \hat{A}_k |\psi(t)\rangle , \tag{2.84}$$

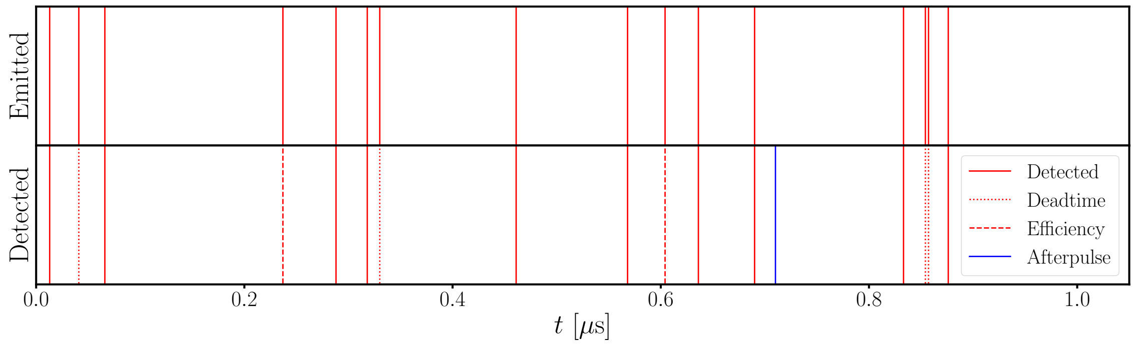

Fig. 2.13: Simulated discrete photon emission (red continuous) for a quantum trajectory realization. However, not all the emitted photons are detected, due to the dead-time of the detector (red dotted) and its efficiency (red dashed). Furthermore, some detections can be caused by non-emitted photons due to an after pulse (blue line). The power of the laser is $P_L = 1$ mW.

and $\mathrm{d}t$ is chosen such that $\mathrm{d}p \ll 1$. The probability of remaining in the state $|\psi(t+\mathrm{d}t)\rangle$ is given by $1-\mathrm{d}p$, and the corresponding quantum jump probability is thus given by Eq.(2.84). If the environmental measurements register a quantum jump, say via the emission of a photon into the environment, or a change in the spin of the NV center, the wave function undergoes a jump into a state defined by projecting $|\psi\rangle$ using the collapse operator $\hat{A}_k$ corresponding to the measurement

$$|\psi(t+\mathrm{d}t)\rangle = \frac{\hat{A}_k\,|\psi(t)\rangle}{||\hat{A}_k\,|\psi(t)\rangle\,||}, \tag{2.85}$$

otherwise, the state evolves freely under $\hat{H}_{\text{eff}}$,

$$|\psi(t+\mathrm{d}t)\rangle = \frac{\exp\left\{-i\hat{H}_{\text{eff}}\,\mathrm{d}t\right\}|\psi(t)\rangle}{||\exp\left\{-i\hat{H}_{\text{eff}}\,\mathrm{d}t\right\}|\psi(t)\rangle\,||}. \tag{2.86}$$

If more than a single collapse operator is present, the probability of collapse due to the i-th operator $\hat{A}_i$ is given by

$$p_i(t) = \frac{\langle\psi(t)|\hat{A}_i^\dagger\hat{A}_i|\psi(t)\rangle}{\mathrm{d}p}. \tag{2.87}$$

To evaluate the evolution to first-order in time we use the following algorithm to simulate a single realization of the quantum system. Starting from an initial state $|\psi(0)\rangle$

Ia. Choose a random number $r_a \in [0,1]$, representing the probability that a quantum jump occurs.

Ib. Choose a random number $r_b \in [0,1]$, used to select which collpase operator was

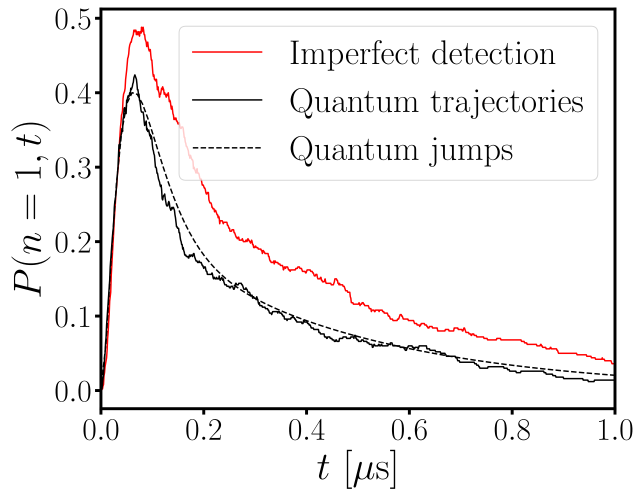

Fig. 2.14: Probability of having emitted one photon $P(1,t)$ computed with the quantum jump approach solving the generalized Bloch equation (dashed black) described in Sect. 2.3.2 and the quantum trajectories algorithm (solid black) for $N_r = 500$. The power of the laser is $P_L = 1$ mW. We compare the calculated $P(1,t)$ for an imperfect detection assuming a detector quantum efficiency of 80% a dead time of 30 ns and an after-pulse of 22 ns with probability of 0.8%.

responsible for the jump.

II. Integrate the Schrodinger, using $\hat{H}_{\text{eff}}$ until a time τ such that the norm of the wave function satisfies $\langle\psi(\tau)|\psi(\tau)\rangle = r_a$, at which point a jump occurs.

III. The resultant jump projects the system at time τ into one of the renormalized states given by Eq.(2.85). The corresponding collapse operator $\hat{A}_i$ is chosen so that i is the smallest interger satisfying:

$$\sum_{k=1}^{i} p_k(\tau) \geq r_b, \tag{2.88}$$

where the individual $p_k(\tau)$ are given by Eq.(2.87).

IV. Using the renormalized state from step **III** as the new initial condition at time τ, we repeat the above procedure until the final simulation time is reached.

In Fig. 2.13 we represent the emitted photons for one of these realizations. We then repeat the stochastic realization of a quantum trajectory a number N_r times. Denoting with the subscript r each trajectory realization $|\psi_r(t)\rangle$ we can compute the observable $\hat{M}$, so that

$$\bar{M}(t) = \frac{1}{N_r}\sum_{r=1}^{N_r} \langle\psi_r(t)|\hat{M}|\psi_r(t)\rangle \xrightarrow{N_r\to\infty} \text{Tr}\Big\{\varrho(t)\hat{M}\Big\}, \tag{2.89}$$

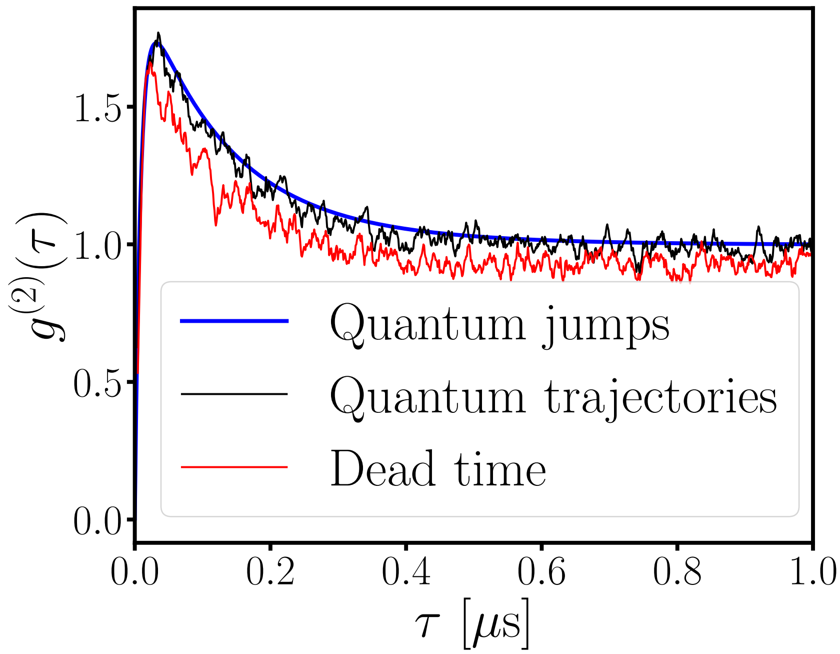

Fig. 2.15: Autocorrelation function computed using the PES computed using the quantum jump formalism (blue) and from the simulated detection clicks computed from the quantum trajectories for ideal detectors (black) and considering their dead time (red). To compute the autocorrelation functions we averaged over $N_r = 1000$ trajectories.

with $\varrho(t)$ obtained directly from Eq. (2.39). In Fig. 2.14, we compare the results for the emission probability of a single photon computed using both this method and the quantum jump approach by solving the generalized Bloch equation. Additionally, we demonstrate how an imperfect detection scenario alters the statistics of the detected photons compared to the emitted ones. This adjustment is achieved by modifying the realizations of the emitted photons to reflect the detection process, as illustrated in Fig. 2.13.

As we previously showed, the autocorrelation function is not affected by the detection efficiency of the detectors used in the Hanbury-Brown and Twiss (HBT) experiment. However, it can be influenced by the dead-time and after-pulsing of the detector. In Fig. 2.15 we compare the autocorrelation function computed by solving the generalized Bloch equation in the quantum jump framework. On the other hand, in the quantum trajectories framework, we simulate a stream of individual photons for each trajectory. This allows us to model the beam splitter in an autocorrelation measurement by randomly assigning each photon to one of two identical detectors. This allows us to simulate the autocorrelation function $g^{(2)}(\tau)$. When the detector dead-time is taken into account, the autocorrelation function shows a reduced level of bunching. Additionally, this method enables us to simulate cases where the photon splitting ratio in the HBT experiment deviates from the ideal 50:50 distribution, for example, to a 45:55 split.

2.4.7 Time dependent signals

In quantum sensing, the target information is typically encoded in the expectation value of some observable of the quantum probe. The state of the system is thus repetitively recorded and then the expectation value is obtained by averaging over the individual readouts. However, such a procedure requires that the interaction between the probe and the target be identical prior to all the measurements, assuming the repeatability of the process. Here, in contrast, we consider a scenario in which the target evolves irreversibly as the probe interacts with it, precluding averaging over the results of the measurements.

We investigated a system involving a single NV center coupled to an ensemble of nuclear spins through dipole-dipole interactions. This setup represents a magnetically active sample situated on the surface of a diamond crystal housing a shallow NV color center. An external magnetic field, denoted B_z, is applied along the z-axis, aligned with the magnetization axis of the NV center. In situations where the strength of the external magnetic field significantly exceeds the dipole coupling strength, we can employ a classical approach to model the magnetization of the nuclear ensemble, while still retaining the quantum characteristics of the NV center-based sensor [210]. The region probed by the NV center can be seen to have a statistically polarized volume [211, 212], resulting in an average magnetization of zero. Nevertheless, variations in magnetization arising from spin-spin interactions within the sample lead to a detectable net signal that can be captured by the NV probe.

This scenario can be described as the interaction between the NV center and a classical wave of the form:

$$B(t) = b(t)\cos(\nu t + \varphi), \tag{2.90}$$

where φ is a random phase [212, 101, 213]. The strength of the signal detected by the sensor, $b(t)$, is influenced by the number of nuclear spins within the sample. Consequently, it undergoes changes as the concentration of nuclei in the sample varies. Assuming that the frequency of the signal is known (which implies knowledge of the type of nucleus coupled to the NV center, such as $\nu = \gamma_N B_z$ with γ_N being the nuclear gyromagnetic factor), our objective is to determine the behavior of $b(t)$. To achieve this, we measure the NV state K times at different instants t_i during its evolution from $t_0 = 0$ to $t_K = t_f$. Between measurements, the NV center is subjected to a train of even MW pulses tuned for the $|0\rangle \leftrightarrow |1\rangle$ transition. We represent the detection protocol described in Fig. 2.16. The Hamiltonian of the NV under this magnetic field and an external resonant MW driving $\Omega(t)$ in the interaction picture can be written as [81]

$$\hat{H} = -\gamma_e B(t)\frac{\hat{\sigma}_z}{2} + \Omega(t)\frac{\hat{\sigma}_x}{2}. \tag{2.91}$$

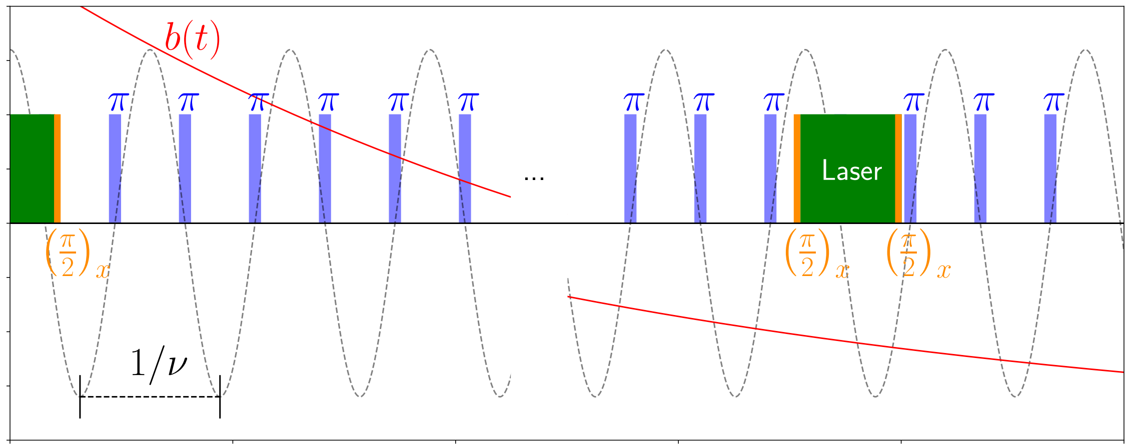

Fig. 2.16: Dynamical decoupling pulse protocol superimposed on the target field $b(t)$.

The MW radiation is delivered to the system in the form of pulse sequences, typically consisting of trains of π-pulses that alternately flip the NV electron spin, as indicated by the sequence $\hat{\sigma}_z \rightarrow -\hat{\sigma}_z \rightarrow \hat{\sigma}_z \rightarrow -\hat{\sigma}_z$.... In this context, we write the Hamiltonian in Eq. (2.91) in the rotating frame of $\Omega\frac{\sigma_x}{2}$, resulting in:

$$\hat{H} = -\gamma_e F(t) B(t) \frac{\hat{\sigma}_z}{2}. \tag{2.92}$$

Here, $F(t) = \pm 1$ represents a modulation function that characterizes the effect of each π-pulse on the dynamics of the NV center spin. For simplicity, as a first approximation, we assume instantaneous pulses. This modulation function is conceptualized as a square wave with frequency ν, effectively describing the action of each π-pulse on the dynamics as a flip-flop operation of the $\hat{\sigma}_z$ operator, that is, $F(t) = \pm 1$. The modulation function $F(t)$ can be expanded in Fourier terms as:

$$F(t) = \sum_k a_k \cos(k\nu t), \tag{2.93}$$

where a_k is given by:

$$a_k = \begin{cases} \frac{4}{k\pi}(-1)^{\frac{k-1}{2}} & \text{if } k \text{ is odd,} \\ 0 & \text{if } k \text{ is even.} \end{cases} \tag{2.94}$$

The alternation between free evolution and MW driven periods induces an oscillation in the sensor that resonates with the target signal, enabling the sensor to gather information about it. Specifically, the NV is subjected to N pulse blocks, each consisting of two π pulses, after which its state is measured and reinitialized. This scheme is repeated N times at different instants while the signal evolves, resulting in a vector composed of the results of the total N measurements.

The decomposition of $F(t)$ provided in Eq. (2.93) aids in investigating the evolution of the NV center between two measurements. If t_i denotes the time at which the measurement begins, then the NV evolves freely between $[\tilde{t}_i, t_i]$, with $\tilde{t}_i = t_{i-1} + t_L$, being t_L the length of the laser pulse. We write the evolution operator as follows,

$$\hat{U}_i = \exp\left(-i \int_{\tilde{t}_i}^{t_i} \hat{H}(t)\,\mathrm{d}t\right). \tag{2.95}$$

During an integration over a complete period $T = \frac{2\pi}{\nu}$, the Fourier components with $k \neq 1$ are effectively averaged to approximately zero. Therefore, when performing the integration over a time interval $[\tilde{t}_i, t_i]$ that encompasses several periods, it suffices to retain only the term $k = 1$:

$$\begin{aligned}
\int_{\tilde{t}_i}^{t_i} \hat{H}(t)\,\mathrm{d}t &\approx \frac{2|\gamma_e|\hat{\sigma}_z}{\pi} \int_{\tilde{t}_i}^{t_i} \cos(\nu t + \varphi)\cos(\nu t) b(t)\,\mathrm{d}t = \\
&= \frac{2|\gamma_e|\hat{\sigma}_z}{\pi} \int_{\tilde{t}_i}^{t_i} \left(\cos^2(\nu t)\cos(\varphi) - \sin(\nu t)\cos(\nu t)\sin(\varphi)\right) b(t)\,\mathrm{d}t = \\
&= \frac{|\gamma_e|\hat{\sigma}_z}{\pi} \int_{\tilde{t}_i}^{t_i} \left(\cos(\varphi) + \cos(2\nu t + \varphi)\right) e^{-t/\tau}\,\mathrm{d}t = \\
&= \frac{|\gamma_e|\hat{\sigma}_z}{\pi} \cos(\varphi) \int_{\tilde{t}_i}^{t_i} b(t)\,\mathrm{d}t + \epsilon\hat{\sigma}_z,
\end{aligned} \tag{2.96}$$

where

$$\epsilon = \frac{|\gamma_e|}{\pi} \int_{\tilde{t}_i}^{t_i} \cos(2\nu t + \varphi) b(t)\,\mathrm{d}t. \tag{2.97}$$

First, let's examine the scenario where the population of nuclei decreases exponentially, $b(t) = b_0 \exp\{-t/\tau\}$. We calculate ϵ when integrating over several periods T,

$$\begin{aligned}
\epsilon &= \frac{|\gamma_e| b_0}{\pi} \int_0^{NT} \cos(2\nu t + \varphi) e^{-t/\tau}\,\mathrm{d}t = \\
&= \frac{|\gamma_e| b_0}{\pi} \frac{\tau \cdot (\cos(\varphi) - 2\nu\tau\sin(\varphi)) \cdot \left(1 - \mathrm{e}^{\frac{-2\pi N}{\nu\tau}}\right)}{4\nu^2\tau^2 + 1} \approx \\
&\approx -\frac{N|\gamma_e| b_0}{\nu^2\tau} \sin(\varphi).
\end{aligned} \tag{2.98}$$

Hence, we can neglect this term when $\tau \gg \frac{|\gamma_e| b_0}{\nu^2}$. This provides a condition for the timescale of the signals considered for which we can neglect the term ϵ. Assuming $b_0 \approx 100$ nT, $B = 1$ T, $\gamma_N \approx (2\pi)10$ MHz/T, and $\gamma_e \approx (2\pi)2.8$ GHz/T, we require $\tau \gg 20$ ps, which is a more than reasonable condition. Thus, we can consider τ to be on the order of μs and ms. It is important to note that ϵ will also increase as the number of periods N increases. Although this condition was derived for an exponential decay, we can use it to extrapolate it for other behaviors, considering that $b(t)$ does not vary much faster than τ in the interval $[t_0, t_f]$. Therefore, we can take $\epsilon \to 0$ and consider

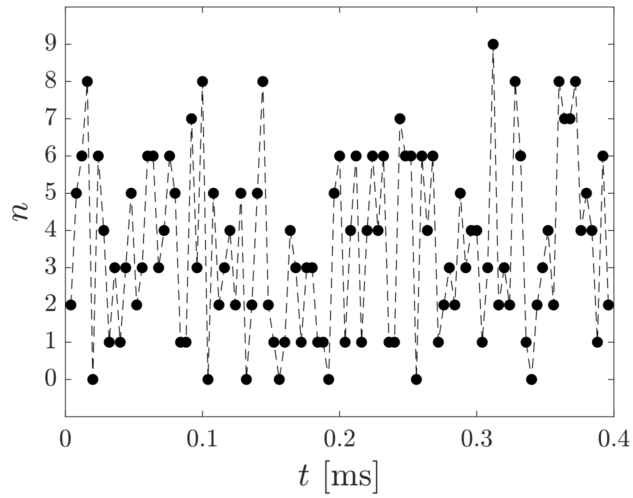

Fig. 2.17: Photon counts n at each measurement time for a evolution $b(t) = b_0 \exp\{-t/\tau\}$ with $b_0 = 0.4$ mT and $\tau = 0.1$ ms. The readout pulse length is 1 μs and the time between pulses 4 μs.

$$\hat{U}_i = \exp\left(\frac{|\gamma_e|\hat{\sigma}_z}{\pi}\cos(\varphi)\int_{-i\tilde{t}_i}^{t_i} b(t)\,\mathrm{d}t\right). \tag{2.99}$$

For an NV initially polarized in the x direction and evolved according to U the measured spin projection evolves as

$$\langle\sigma_x\rangle_i = \cos\left(\frac{2\gamma_e}{\pi}\cos(\varphi)\int_{\tilde{t}_i}^{t_i} b(t)\,\mathrm{d}t\right) \tag{2.100}$$

This expectation value is valid for a constant phase of the target signal φ. However, as the phase varies randomly among the nuclei ensemble, the harvested signal is

$$\overline{\langle\sigma_x\rangle}_i = \frac{1}{2\pi}\int_0^{2\pi}\langle\sigma_x\rangle\,\mathrm{d}\varphi = J_0\left(\frac{2\gamma_e}{\pi}\int_{\tilde{t}_i}^{t_i} b(t)\,\mathrm{d}t\right) \tag{2.101}$$

where $J_0(x)$ is the first Bessel function with argument x. Before the readout pulse the system is in the state given by

$$|\phi\rangle_i = \frac{1}{2}\left((1-\overline{\langle\sigma_x\rangle}_i)\,|0\rangle + (1+\overline{\langle\sigma_x\rangle}_i)\,|1\rangle\right). \tag{2.102}$$

Then, we simulate the number of photons emitted n_i for each measured state $|\phi\rangle_i$ through the PES. The result of the experiment is a string with the number of photons emitted at each measurement, here simulated using the PES,

$$D = [n_1, n_2, n_3, ..., n_K]. \tag{2.103}$$

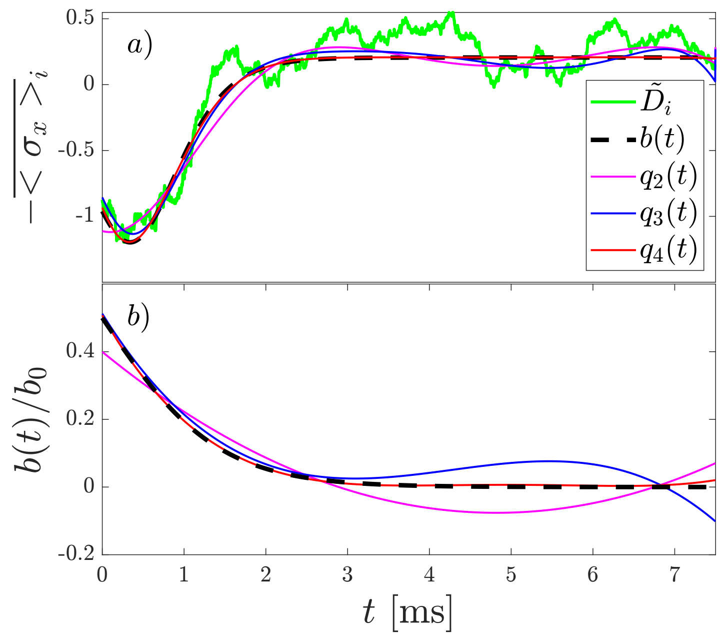

Fig. 2.18: (a) The $\tilde{D}$ (green) adjusted in the range of $\overline{\langle\sigma_x\rangle}_i$ for $b(t) = b_0\left(\frac{\exp\{-t/\tau\}}{1+\exp\{-t/\tau\}}\right)$ (dashed black), with $\tau = 0.7$ ms and $b_0 = 0.6$ mT. We plot the fits to $\tilde{D}$ from $\overline{\langle\sigma_x\rangle}_i$ computed for $q_2(t)$ (magenta), $q_3(t)$ (blue) and $q_4(t)$ (red). (b) We compare the target $b(t)$ with the fitted $q_2(t)$, $q_3(t)$ and $q_4(t)$

In Fig. 2.17 we plot the photon counts n_i at each measurement time. The goal now is to retrieve $b(t)$ from the list D.

If we do not have any prior information about $b(t)$ we can deduce the state of the system from the photon counts by taking the moving average of D, denoted by $\tilde{D}$. We compute this moving average by averaging L points from D:

$$\tilde{D}_i = \sum_{j=i}^{L} n_i. \tag{2.104}$$

In Fig. 2.18a we observe the moving average of the photon counts, processed to fit the range of $\overline{\langle\sigma_x\rangle}$, for $b(t) = b_0\left(1 - \frac{1}{1+\exp\{-t/\tau\}}\right)$. We note that $\tilde{D}$ follows a trend similar to that of $\overline{\langle\sigma_x\rangle}$, because the photon counts are directly related to the NV center state. Therefore, we can try to solve for $b(t)$ directly from Eq.(2.101). The problem with this approach is that the Bessel function does not have an inverse, which means that we cannot directly retrieve $b(t)$ from Eq.(2.101). Therefore, we determine $b(t)$ by adjusting it using a least squares (LSQ) fit against $\tilde{D}$. We can assume that $b(t)$ is given by $q_n(t)$, a polynomial of degree n, however, other models are possible. We then fit the expected $\overline{\langle\sigma_x\rangle}_i$ evolution under a signal evolving from $q_n(t)$ to $\tilde{D}$. The results of these fits are shown in Fig. 2.18a, and the predicted $b(t)$ is shown in Fig. 2.18b.

The analysis demonstrates that our LSQ fitting approach effectively captures the evolution of $b(t)$ despite the inherent stochastic noise in the photon count data. By modeling $b(t)$ as a polynomial $q_n(t)$, we are able to bypass the challenge posed by the non-invertible Bessel function in Eq.(2.101) and recover an estimate of the underlying signal. While all polynomial models provide a reasonable fit to the data, increasing the degree of the polynomial leads to a noticeably better approximation of $b(t)$ over the measured time period. This improvement is evident in the closer match between the predicted and observed trends, particularly for longer time intervals where subtle variations in the signal become more pronounced.

In summary, our method successfully leverages a polynomial model and LSQ fitting to infer the behavior of $b(t)$, offering a robust estimation even under noisy conditions. The ability to adjust the polynomial degree provides flexibility in balancing model complexity and fitting accuracy, thereby ensuring that the essential dynamics of the NV center state, as reflected in the photon counts, are accurately captured.

A related, but distinct, challenge arises when we incorporate prior knowledge about the function $b(t)$. For example, if we are aware that $b(t)$ adheres to an exponential behavior, and our objective is to determine the decay rate τ, then the question becomes how long we must conduct measurements to accurately estimate the value of τ. Bayesian analysis serves as a valuable tool in leveraging the information from the data set D to deduce the most likely value of the decay constant. Bayes rule can be written as:

$$P(\tau, D) = \frac{P(D|\tau)P(\tau)}{\int P(D|\tau)P(\tau)\,\mathrm{d}\tau}. \tag{2.105}$$

It establishes a connection between the likelihood $P(\tau)$ of a specific τ value that generates the observed data set D, and the probability of these parameters given the data. In essence, Bayesian analysis reverses the conditionality: while $P(D|\tau)$ represents the probability of the results given the parameters, it allows to calculate $P(\tau|D)$, enabling the estimation of the most probable values for the system parameters based on the observed data.

Alternatively, one can proceed with the analysis using any monotonically increasing function of the likelihood. A commonly adopted choice is the logarithm, leading to the log-likelihood function $L(D|\tau) = \ln P(D|\tau)$. This choice mitigates the risk of underflow, preventing the spurious occurrence of zeros that may arise when multiplying numerous small probabilities (in this context, the probabilities of the n_i shots). Furthermore, it is possible to add a constant value to $L(D|\tau)$ without affecting the location of the maximum with respect to the parameters. This manipulation is used here to facilitate the retrieval of $P(D|\tau)$ by exponentiating the log-likelihood. As the NV is reinitialized after each measurement, each shot can be considered independent, and the joint probability of all measurements is found by taking the product of all individual probabilities:

$$P(D|\tau) = \prod_{i=1}^{K} P(n_i|\tau) \tag{2.106}$$

Recall that the result of each shot is the number of detected photons rather than the

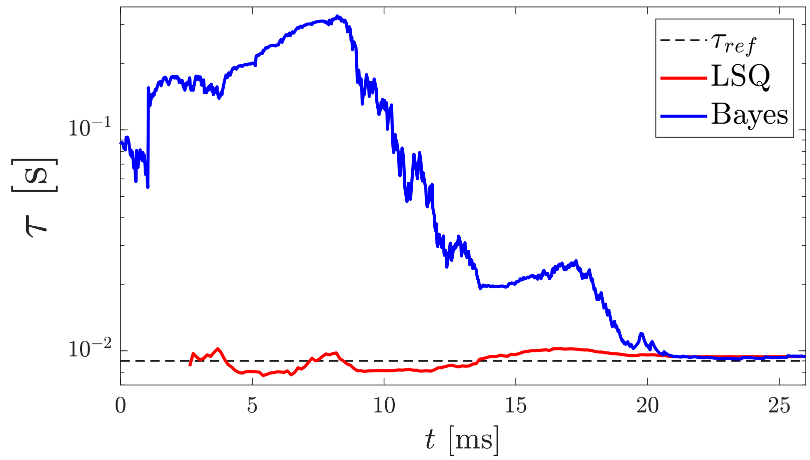

Fig. 2.19: Predicted values τ for $\tau_{ref} = 9$ ms for the model $b(t) = b_0 \exp\{(-t/\tau_{ref})\}$. The blue curve represents estimates derived from Bayesian inference, while the red curve shows results obtained via the least squares (LSQ) method. Measurements were acquired at intervals of 25 μs. While both methods converge to the correct value by 20 ms, the LSQ method consistently offers more accurate predictions. This trend was observed consistently throughout our analysis across various τ_{ref} values and $b(t)$ functions.

state of the NV. Its probability is thus given by the PES

$$P(n_i|\tau) = P(n, t_L||\phi\rangle_i), \tag{2.107}$$

which is the probability of emitting n photons during the readout of the state $|\phi\rangle_i$ with a readout pulse of length t_L. The goal of Bayesian inference is to iteratively update with each measurement a prior belief $P(\tau)$ about the unknown parameter τ. Initially, we assumed a uniform distribution for $P(\tau)$ within the range $[\tau_{\min}, \tau_{\max}]$. Finally, we compute $P(\tau, D)$ using the Bayes rule using the grid method. We discretize the parameter space and iteratively compute the posterior probability for each of the values.

However, for the problems under investigation, the Bayesian method did not yield superior results compared to a simpler least squares (LSQ) fit applied to $\tilde{D}$. In Fig. 2.19, we present a comparison between both approaches as the measurement time increases, considering the $\tau = 9$ ms and $K = 1000$ measurements. In the Bayesian approach, we set $\tau_{\min} = 1$ ms and $\tau_{\max} = 100$ ms. There are no data at the beginning of the Bayes curve because of the size of the moving average window. Although this could have been addressed using alternative techniques, doing so would have complicated the comparison between models.

Although both methods eventually provide accurate estimates of τ with similar uncertainty values, the LSQ method requires fewer measurements to achieve a reliable estimate. However, Bayesian inference can be advantageous in scenarios involving noisy data or when estimating multiple parameters. One limitation of the least squares (LSQ) method is that it assumes that the probability distribution of the estimated parameters follows a Gaussian distribution. In contrast, the Bayesian approach directly estimates the probability distribution without relying on this assumption. This allows for a more flexible modeling approach, especially when data is sparse or when the underlying distribution of parameters is not well understood. Moreover, Bayesian methods naturally handle situations where data are incomplete or where certain parameters may be correlated, offering robustness in complex modeling tasks. Additionally, Bayesian inference provides a coherent way to update beliefs as new data become available, making it suitable for dynamic environments where continuous learning and adaptation are crucial.

The PES has allowed us to simulate these measurement processes, whereas traditional method based on rate equations offers merely an averaged, steady-state view of the NV center fluorescence. In contrast, the PES captures the full temporal dynamics and stochastic nature of photon emissions, including transient quantum jumps and detector imperfections, and connecting the emission probabilities with the estimation theory. This comprehensive modeling capability not only provides deeper insight into the underlying quantum behavior but also facilitates the optimization of experimental protocols for enhanced sensitivity and accuracy in quantum sensing applications.

2.5 Ionization dynamics

The NV center exhibits multiple charge states [33], the negatively charged state, NV^-, being the most widely studied due to its optically addressable spin-1 ground state. However, interest in charge-state dynamics has grown in recent years, particularly with the discovery of spin-to-charge conversion, as highlighted by [214]. This conversion forms the basis for electrically detected magnetic resonance (EDMR) in NV centers, even down to the single-defect level [215, 216]. This advancement eliminates the need for traditional collection optics and single-photon detectors, making the NV center system more suitable for integration into compact diamond quantum sensors [217]. The sensitivity of these sensors is closely tied to the optical spin readout contrast and the strength of the signal. Typically, single-NV-center experiments achieve a readout contrast of around 30%.

Critical to enhancing readout contrast is the initialization of the NV center charge state. The presence of a population in the neutral state (NV^0) introduces unwanted background luminescence and reduces the overall brightness of the signal. To mitigate this, NV^0 fluorescence can be partially filtered out of the collected light using a 650 nm long-pass filter. However, a significant challenge arises from the unfavorable ionization dynamics, where excitation with wavelengths longer than the zero-phonon line of NV^0 only allows for unidirectional conversion from NV^- to NV^0. Unfortunately, no such mechanism has been shown for the transfer from NV^0 to NV^-. This limitation poses a challenge in maintaining the desired charge state for optimal readout contrast.

A recent experiment [39] demonstrated a method to enhance readout contrast and brightness by optimizing the initialization of the charge and spin state of the NV center.

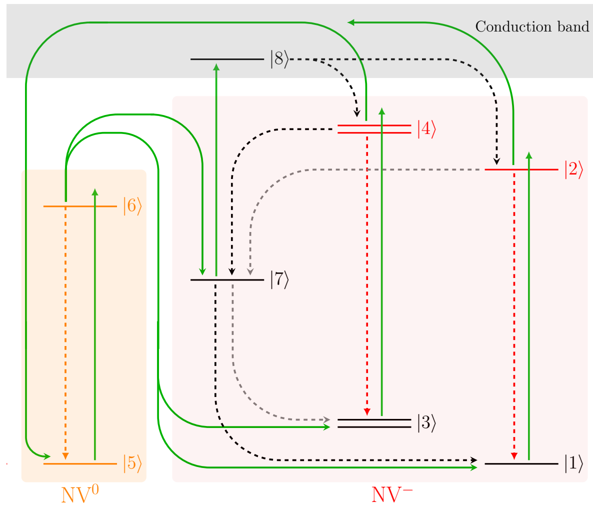

Fig. 2.20: The level diagram (levels 1–8) is employed for model simulations, incorporating a charge capture channel leading to the metastable state ($|7\rangle$). Laser-driven transitions are depicted with green arrows, while internal decay processes within the system are represented by dashed arrows.

This study identified a two-pulse laser sequence as particularly effective, providing superior initialization regardless of the measurement duration. The approach led to an 11% increase in the collected NV$^-$ photon rates and achieved a maximal optical contrast that exceeded 46%, marking a significant improvement in the read-out performance of the NV centers.

Our objective is to review the ionization model presented in [39] using the PES formalism to discover further refinements in the readout process. The treatment begins with an effective rate-equation model that encompasses both spin and charge dynamics to replicate experimental time traces and derived spin contrasts. The model involves decay rates Γ_{ji} and absorption cross sections σ_{ji}, where i and j correspond to the levels involved. The excitation rates Γ_{ji} are related to the cross section as $\Gamma_{ji} = \sigma_{ji} c_L P_L$, where P_L is the laser intensity and c_L a power scaling factor which will depend on the experiment and here is taken to be $c_L = 21$ MHz/mW, following the results of Ref. [39]. The level diagram for this ionization model is shown in Fig. 2.20 and the decay rates and cross sections values are provided in Table 2.1. Due to the newly introduced levels, we have changed the names of the levels of the NV$^-$ center compared to those used in previous sections.

We modeled the negative charge state of the NV center as a five-level system, which includes two ground states $|1\rangle$ and $|3\rangle$, two optically excited states $|2\rangle$ and $|4\rangle$, and one effective singlet state $|7\rangle$, all driven by off-resonant green laser excitation. In addition, levels $|5\rangle$ and $|6\rangle$ represent the neutral charge state NV^0.

In this model, optically excited NV$^-$ states can either return to the NV$^-$ ground state by emitting a red photon or decay to the singlet state $|7\rangle$ through a nonradiative and spin-dependent process. Green illumination does not provide enough energy to excite the system directly from the triplet ground states to the conduction band $|8\rangle$. Instead, charge state conversion occurs from the optically excited levels within the triplet manifold of NV^-. Conversion processes include either an Auger process [218] or direct ionization [219]. The Auger process leads to the decay into the ground state of the NV^0, whereas direct ionization results in an electron being elevated to the conduction band, effectively scattering the electron out of the NV^-.

Although metastable levels are not included in the neutral charge state, it is known that the NV^0 charge state possesses a metastable manifold observed by electron spin resonance [220]. Although a one-photon charge state conversion is energetically possible from this manifold [219], previous observations suggest that it plays an insignificant role in the charge state dynamics of the system [221].

The transition from NV^0 to NV^- is facilitated through a two-photon process involving level $|6\rangle$ [221]. The conversion from NV^0 to NV^- takes place directly from the optically excited NV^0 state (level 6) to levels 1 and 3, as well as through the metastable singlet state (level 7). This state exhibits a lifetime more than an order of magnitude longer than all optically excited states and has a small excitation cross-section, allowing the population to be shelved during illumination [185]. Understanding this conversion pathway highlights the complex interactions between spin, charge state, and shelving dynamics, providing new insights that were previously missing from simpler descriptions [216]. Controlling this conversion can lead to enhanced NV^- initialization and could lead to new readout protocols, as we want to investigate.

This optical transitions connects the dynamics of charge states with the shelving process occurring in the long-lived singlet state. When operating at high optical power, this mechanism enables efficient initialization through NV^- to NV^0 transfer and subsequent electron recapture. Therefore, the NV^- population increases at higher powers. However, increased shelving under high-power illumination, far beyond the saturation of the optical transition, would lead to continuously decreasing luminescence with higher laser powers. However, it has been shown that the NV center exhibits almost power-independent luminescence in this regime. To account for this behavior

Decay time [ns]		Normalized cross section	
$1/\Gamma_{2,1}$	13	$\sigma_{1,2}$	1
$1/\Gamma_{4,3}$	13	$\sigma_{3,4}$	1
$1/\Gamma_{6,5}$	20	$\sigma_{7,8}$	0.0059(3)
$1/\Gamma_{2,7}$	93.5(8)	$\sigma_{6,7}$	0.15(1)
$1/\Gamma_{4,7}$	14.98(6)	$\sigma_{6,3}$	0.3(2)
$1/\Gamma_{7,1}$	186.12(24)	$\sigma_{2,5}$	0.237(4)
$1/\Gamma_{7,3}$	2722(57)	$\sigma_{4,5}$	0.237(4)
$1/\Gamma_{8,4}$	54	$\sigma_{5,6}$	0.562(7)
$1/\Gamma_{8,2}$	146	$\sigma_{6,1}$	0.281(7)

Table 2.1: Model parameters used for the rate equations [39]

in the model, we consider the possibility of excitation out of the singlet state through single-photon absorption to a higher energy state (level 8) [222]. With the inclusion of this state, a slight decrease in luminescence is anticipated beyond the saturation point, while it is expected to remain relatively constant at higher laser powers, aligning with the previously observed anomalous saturation behavior [223]. Nevertheless, high-power illumination provides an effective method to significantly improve charge-state purity.

To investigate the read-out process using the proposed ionization model, we extend the previously presented PES model. Although our PES modeling initially focuses on the fluorescence of the NV^- charge state, it also extends to the NV^0 state. Incorporating the emissions from both charge states requires considering two separate $\mathcal{J}$ operators: one for the spontaneous emission associated with NV^0, denoted as $\mathcal{J}^0$, and the other for NV^-, denoted as $\mathcal{J}^-$. This approach allows us to accurately model the emission dynamics of both NV centers and their contributions to the overall readout process.

$$\begin{aligned} \mathcal{J}^0\varrho &= \Gamma_{65}\,|6\rangle\langle 5|\,, \\ \mathcal{J}^-\varrho &= \Gamma_{21}(|2\rangle\langle 1| + |4\rangle\langle 3|). \end{aligned} \tag{2.108}$$

To compute the PES, we can:

(a) Simultaneously solve both emissions, taking into account a total emission operator $\mathcal{J} = \mathcal{J}^0 + \mathcal{J}^-$, and obtain $P(n,t)$ by solving $\dot{\rho}(n,t) = \mathcal{L}_0\rho(n,t) + \mathcal{J}\rho(n-1,t)$. Here, the index n represents the cumulative photons emitted by both NV^- and NV^0, and we are unable to distinguish between them.

(b) To differentiate their counts, we can introduce two photon counting variable, k for the photons emitted by by the NV^-, and m for the photons emitted by the NV^0, and solve for:

$$\dot{\rho}(k,m,t) = \mathcal{L}_0\rho(k,m,t) + \mathcal{J}^-\rho(k-1,m,t) + \mathcal{J}^0\rho(k,m-1,t), \tag{2.109}$$

from where we can obtain $P(k,m,t) = \mathrm{Tr}\{\rho(k,m,t)\}$ the probability of having emitted k photons by the NV^- and m photons by the NV^0 at time t. From $P(k,m,t)$ we can arrive at their individual emission probabilities $P^-(k,t)$ and $P^0(m,t)$ directly as

$$P^-(k,t) = \sum_{i=0} P(k,i,t) \qquad\qquad P^0(m,t) = \sum_{i=0} P(i,m,t) \tag{2.110}$$

or the total emission probability, regardless of the photon origin:

$$P(n,t) = \sum_{j=0}^{n} P(n-j,j,t). \tag{2.111}$$

The problem with this method is that computationally it is very inefficient. If we set K and M as the numerical cut-offf when solving for (2.109) we need to solve a system of differentiable equations of size $K \times M \times L$, with L the number of levels involved here $L = 8$.

(c) In many cases, we will not be interested in the distribution $P(k, m, t)$, but only $P^0(m, t)$ or $P^-(k, t)$. We can directly solve for them by considering:

$$\begin{aligned}\dot{\rho}^-(k,t) &= \mathcal{L}_0\rho^-(k,t) + \mathcal{J}^-\rho^-(k-1,t) + \mathcal{J}^0\rho^-(k,t),\\ \dot{\rho}^0(m,t) &= \mathcal{L}_0\rho^0(m,t) + \mathcal{J}^-\rho^0(m,t) + \mathcal{J}^0\rho^0(m-1,t).\end{aligned} \tag{2.112}$$

And

$$P^-(k,t) = \mathrm{Tr}\Big\{\rho^-(k,t)\Big\} \qquad\qquad P^0(m,t) = \mathrm{Tr}\Big\{\rho^0(m,t)\Big\}. \tag{2.113}$$

Now we need to solve two differential equations of size $L \times K$ and $L \times M$, which for large M and L is more efficient.

(d) We can use a quantum trajectories approach, since in this case the complexity does not scale when considering new allowed transitions. We account for all the jumps that the system takes during its evolution. However, we will need to consider many trajectory realizations, and the resulting PES will be an approximation, converging to its analytical expression as we increase the number of realizations.

It is important to note that while we assume ideal filtering of the fluorescence emitted by NV^0, in practice, only approximately 60% of its emission spectrum is effectively filtered at room temperature due to spectral overlap. This incomplete photon filtering can degrade the readout process. We modeled this filtering effect by rejecting a fraction f of the total photons emitted by NV^0. Using the quantum trajectory approach, we can directly discard a fraction f of the photons emitted by NV^0 in each trajectory. To quantify this, we compute the total probability $P_f(n,t)$ of detecting n photons after filtering, using a method analogous to that described in Section 2.4.6. The probability $P_f(n,t)$ is given by:

$$P_f(n,t) = \sum_{j=0}^{n}\left[\sum_{m=j}^{\infty}\binom{m}{j}(1-f)^j f^{m-j} P^0(j)\right] P^-(n-j,t) \tag{2.114}$$

As a first approximation, we use approach (c) to compute only the PES of the negative charge state and assume perfect filtering of the NV^0 fluorescence. This assumption is valid because the PL signal from the NV^0 charge state is smaller than that of the NV^- charge state and can be introduced later as a correction.

The first phenomenon under investigation is the anomalous saturation behavior of the NV center [222, 223, 224]. Typically, the photoluminescence (PL) intensity of the NV center increases with laser power until it reaches saturation. However, an observed peak in the PL intensity as a function of excitation power may be unexpected. This behavior is illustrated in Fig. 2.21(a), where the blue curve represents the simulated saturation behavior including ionization mechanisms, and the red curve depicts the scenario with deliberately suppressed ionization mechanisms.

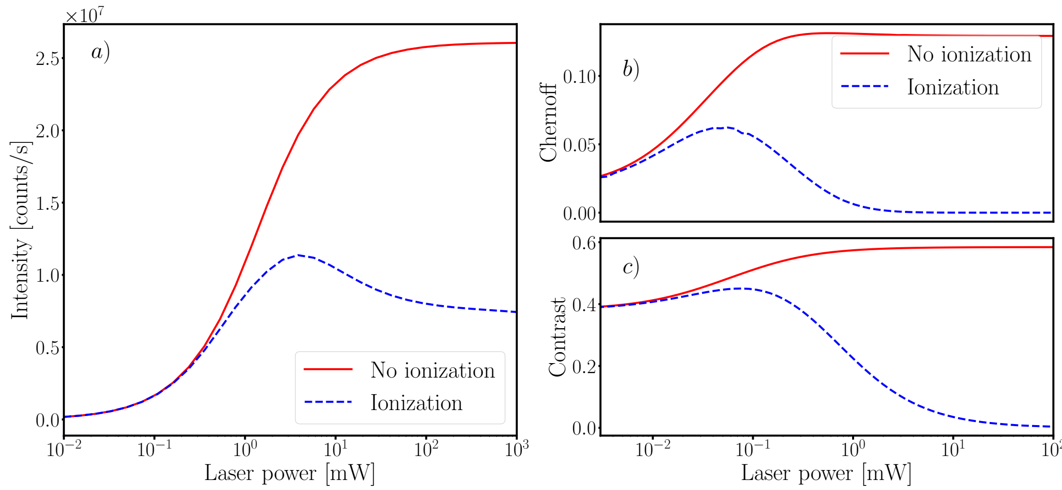

Fig. 2.21: (a) Saturation curve of fluorescence plotted against laser power intensity, showcasing results with and without ionization included in the model. While conventional expectation suggests luminescence should approach a maximum value asymptotically, considering ionization reveals a decrease, consistent with findings in prior experiments [224]. (b) Top: Maximum value achieved for the Chernoff information. (c) Bottom: Maximum value achieved for the contrast, plotted against different laser powers. Without considering ionization, increasing the laser power proves to be the optimal strategy until saturation, consistent with our findings in Fig. 2.6b. We observe again a convergence of both models at low powers. However, when ionization is considered, with increasing power, an optimal maximum is reached, after which both the contrast and Chernoff information plummet to zero. This loss in readability of the system's state is attributed to charge state transfer.

At low excitation powers, both models show similar behavior because insufficient energy prevents the occurrence of the two-photon ionization process. In the absence of ionization, fluorescence saturates at approximately 5-10 mW. However, when ionization is included, the saturation count is reduced by a factor of 2.5. Additionally, a noticeable peak in fluorescence appears around 8 mW with ionization, which is not observed in the model with ionization excluded. This peak arises due to the conversion of NV^- to NV^0 and the shelving of the metastable state, highlighting the complex ionization dynamics. These findings emphasize the need for further exploration into the dynamic behaviors associated with ionization, which could lead to enhanced NV center readout techniques.

Although earlier research primarily focused on exploring the initialization capabilities of the ionization model [39], our current investigation shifts its emphasis to the scrutiny of the read-out process. In Figure 2.21(b-c), we systematically examine the maximum values of the Chernoff information (top) and contrast (bottom) achieved for different laser powers. This analysis is carried out in both the presence and absence of ionization, enabling a comprehensive comparison between the two scenarios.

Once again, in the absence of ionization, we observe that both contrast and Chernoff values saturate as the excitation power increases, consistent with our previous findings

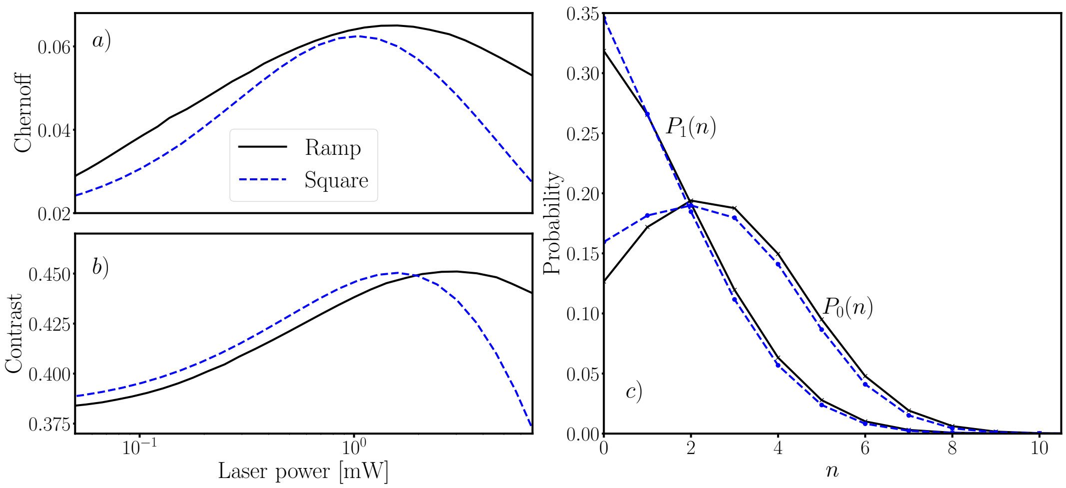

Fig. 2.22: The maximum values of the Chernoff information (a) and contrast (b) achieved as a function of the laser power excitation in the ramp pulse readout (solid black line) or the traditional square pulse (dashed blue line). The Chernoff is always better with the ramp pulse, however, the contrast is better for lower powers, while the maximum contrast achieved is higher with ramp pulse. (c) Photon emission statistics are compared between two readout strategies targeting the ground state. At a readout power of 2 mW, optimal contrast is attained with both the ramp pulse after 275 ns and the square pulse after 220 ns. Although the contrast remains identical for both readout distributions, the Chernoff information is 10% higher when employing the ramp pulse.

in Fig. 2.6b. However, with the introduction of ionization, a distinct pattern emerges, reaching a maximum beyond which both contrast and Chernoff begin to decay instead of saturating. Notably, the peaks of Chernoff and contrast occur at different laser powers, indicating different behaviors for each performance metric. The contrast value is consistent with the experimental results presented in [39]. The non-ionization model achieves 60% contrasts because it has not been adjusted to real experimental data; rather, we constructed it artificially based on the ionization model, which was adjusted to experiments by eliminating the transitions that connect both charge states. We present the simulations of the non-ionized model to illustrate the difference in trends between both models and to show that they converge at low powers. The fact that the ionization model has this interesting behavior opens the possibility to further investigate alternative readout scenarios.

As a further study, we investigate how the shape of the laser pulse influences the readout performance of NV centers. In most experimental sequences, the laser is modulated with a square pulse, which involves a rapid turn-on to full intensity, maintaining that level for the desired duration, and then a quick turn-off. To explore the impact of alternative pulse shapes on readout performance, we consider a ramp pulse as an alternative. In a ramp pulse, the laser intensity is linearly increased until it reaches a specified maximum, followed by a rapid switch-off.

For both ramp and square pulses, we compare the maximum Chernoff value Fig. 2.22a and the maximum contrast Fig. 2.22b achieved at various laser intensities. For the ramp pulse, the laser power is measured at the peak intensity of the pulse. Consistently using a ramp pulse results in an overall superior Chernoff value, with a peak of 0.0650, compared to 0.0625 for the square pulse.

At lower laser powers, the square pulse achieves a slightly better contrast, approximately 0.5% higher than the ramp pulse. However, after reaching its peak, the contrast for the square pulse decreases rapidly, whereas the contrast for the ramp pulse decays more gradually. Around 2 mW, both pulse shapes achieve the same contrast, but the ramp pulse yields a superior Chernoff value. In Figure 2.22(c), for each laser shape, we show the emission distributions at this power level for the NV center initialized in its two ground states, $|0\rangle$ and $|1\rangle$ (corresponding to $|1\rangle$ and $|3\rangle$ in Figure 2.20). Although both distributions produce the same intensity contrast, the distribution associated with the ramp pulse demonstrates a higher Chernoff value, indicating better state discrimination.

The maximum contrast achieved increases slightly from 45.0% to 45.1% when using a ramp pulse instead of a square pulse. Although this improvement may seem modest, it represents a meaningful improvement in performance. These maximum contrast values were obtained under specific conditions: the ramp pulse achieved its peak contrast with a power of 1.6 mW and a pulse length of 335 ns, while the square pulse reached its maximum with a power of 1.1 mW and a shorter excitation time of 305 ns. Although the square pulse is marginally shorter and requires less power, its energy consumption is 17% higher than that of the ramp pulse. This highlights the efficiency advantage of the ramp pulse, which, while requiring more power, consumes less overall energy because of its longer, more gradual excitation profile. This efficiency gain can be critical in applications where power consumption is a key consideration, particularly portable or battery-operated systems.

The ramp pulse is more energy efficient than the square pulse, offering higher Chernoff values and comparable contrast at lower powers, with even better performance at higher power levels. The next step in this research would be to experimentally validate these results. During this thesis, we collaborated with the IQOQI group in Vienna, which developed the two-pulse initialization sequence and the ionization model used. The main challenge lies in generating the ramp pulse quickly, as modulating a laser analogically can present some difficulties. Although we also explored other modulation shapes, the ramp pulse emerged as the most promising and experimentally feasible option.

In this analysis, we focus on Chernoff information and contrast as metrics to evaluate performance. These metrics are crucial in various applications, particularly in distinguishing between different quantum states and optimizing measurement schemes. However, when considering the sensitivity in magnetometry, the photon detection rate becomes a crucial parameter. Intuitively, the photon rate for a ramp pulse is expected to be approximately half that of a square pulse with the same maximum power. This reduction in the photon rate impacts the photon collection and, consequently, reduces the overall sensitivity. In the next analysis, including the photon rate and sensitivity in the evaluation of our metrics could offer new insights into the trade-offs between different pulse shapes and measurement strategies. For instance, while a ramp pulse may reduce power consumption and mitigate potential heating effects in some experimental setups, the decrease in photon rate could diminish the overall effectiveness. Another step we can take is to include in the modeling the contribution of the NV^0 fluorescence as background noise, as will also depend on the readout power.

The intricate interplay of spin polarization with charge state dynamics indicates that the mechanism implemented will depend on the excitation wavelength [221, 225, 68]. This matter underlines the necessity for further investigation, by both theoretical modeling and experimental characterization of the NV center response to different wavelength excitation. The PES can be an important tool in this modeling and in further research in this direction.

With these results, we aim to improve the readout of NV centers and enhance the overall sensitivity and efficiency of quantum sensing technologies, paving the way for more precise measurements in fields such as nanoscale magnetometry, quantum computing, and bioimaging. This advancement could significantly broaden the practical applications of NV centers, making them more accessible and effective in various scientific and industrial domains.

2.6 Outlook and conclusions

This chapter provides physical insight into the photon emission of an NV center, allowing its full characterization. The experimental benchmark validates the presented PES model for the fast intrinsic dynamics of the NV center. Within this framework, we were able to relate the qubit state of an NV center with the detected stream of photons, and investigate the properties of the NV center in a variety of scenarios, including state-readout optimization through the Chernoff information and exemplified with the Rabi oscillations, characterizing experimental autocorrelation measurements, and examine the properties of the emitted photons by the bunching and antibunching behaviors. Finally, the model allows us to determine the optimal regimes for laser and MW intensities in magnetic sensing experiments. Originally proposed to account for the PES of a two-level atom, the method introduced in Ref. [156] can be extended to include the relevant seven electronic levels of an NV center. This technique can be adapted to benchmark other color centers and quantum systems, as well as to include other phenomena such as ionization [39] or two-photon absorption [226]. Our work can also help refine current measurements on the NV center energy levels, leading to increased accuracy and precision in future experiments. Furthermore, PES are useful for proposing and evaluating new readout techniques [227] to increase the NV center sensitivity. Overall, our findings contribute to the understanding of NV centers and have potential implications for quantum sensing and related applications.

Chapter 3

Compact confocal microscope

3.1 Introduction

The NV center is an atom-like system with well-defined spin properties. The microscopic model and most optical properties of NV center ensembles were established in the 1970s on the basis of optical measurements. However, the first detection and characterization of a single NV center occurred in 1997 [228], and this has since become a highly competitive field.

The optical nature of NV center magnetometry and other experiments, which involve using laser light to spin-polarize the NV center and read out its spin state through emitted fluorescence, underscores the crucial role of optical components in instrument development. Changes in spin-dependent photoluminescence reveal the Zeeman splitting of the NV ground state. Consequently, the ability to detect changes in photoluminescence intensity at resonance directly impacts the sensitivity of magnetic field detection using NV centers. Thus, the lowest detectable magnetic field depends on the optical collection efficiency of the photoluminescence signal, making it essential for the most sensitive magnetometers to maximize photon collection. This can be achieved by increasing either the number of NV centers that contribute to the signal or by enhancing the optical collection efficiency of the instrument.

Increasing the number of NV centers is achieved by utilizing ensembles of NV centers. In this configuration, the magnetic field sensitivity increases as $\sqrt{N}$ compared to a single NV, and all possible NV orientations are present, enabling determination of both the strength and direction of the magnetic field. The higher number of emitted photons simplifies experimental setups but comes at the cost of lower spatial resolution and worse coherence time due to spin coupling between NV centers in a dense ensemble. To enhance the spatial resolution of the NV ensembles, delta doping of nitrogen during CVD growth can be employed to create two-dimensional ensembles of NV centers near the diamond surface for enhanced sensing. Furthermore, nanodiamonds (NDs) can be fabricated with a wide range of sizes and concentrations of NV centers, showing promise in many biological applications, although controlling their orientations is an important and challenging task. NV centers in both NDs and 2D ensembles provide good spatial resolution, but their coherence times suffer because of their proximity to the surface, where they are susceptible to interactions with dangling bonds and other surface effects. Although these configurations of NV centers offer higher collection efficiencies than single NV centers, many applications require working with single NV centers because of their superior coherence time and spatial resolution at the single-atom level. Therefore, maximizing the collection efficiency of optical instruments is crucial to fully realize the potential of NV centers.

Various imaging modalities have been demonstrated for collecting NV center photoluminescence (PL), each with different efficiencies and requirements. For ensembles and NDs, common approaches include wide-field [229] and confocal microscopes [205, 230], as well as custom instruments for specific applications. Although wide-field microscopes allow for simultaneous reading of the entire field of vision, they lack the necessary optical resolution for detecting single NV centers, which necessitates the use of confocal microscopes. Unlike traditional wide-field microscopy, confocal microscopy effectively excites and detects point-like emitters with a higher signal-to-noise ratio by confining the excitation and collection volumes. Although diffraction-limited, confocal microscopy restricts the excitation volume to approximately 250 nm, significantly larger than the size of a single NV center. Confocal microscopes are commonly used in scanning probe techniques, where the material is scanned to create a field map, and only the diffraction-limited spot is illuminated and measured. By rejecting photons emitted in planes above and below the confocal plane, confocal microscopy reduces background light and provides a signal-to-noise ratio better than that of wide-field equipment.

The ability to detect single NV centers is essential for fully harnessing their quantum capabilities. However, challenges remain with current experimental setups, mainly due to issues of size, complexity, and cost. Recent developments have introduced new processing techniques [103] that improve sensitivity and efficiency in detecting single NV centers. Despite these advances, there is still a strong need for compact solutions that effectively balance performance and accessibility.

The growing interest for portable and cost-effective quantum sensing devices underscores the need for detecting individual NV centers with compact and portable setups. To meet this demand, in this chapter we present a novel compact confocal setup of approximately 525 mm $\times$ 375 mm $\times$ 300 mm (L $\times$ W $\times$ H) size. The stated dimensions refer only to the optical components of the setup. Control devices and electronics are excluded from these measurements, as they are designed to be plug-and-play, allowing flexibility for adaptation to different applications and laboratory resources. Contrary to standard portable devices [92, 93, 94, 95, 96, 97, 231, 232] this benchtop system allows the detection and control of individual NV centers incorporating recent technological advancements such as a designed optics that allows a size reduction maintaining the stability and resolution, ensuring practicality, cost-effectiveness, and ease of integration with other experimental components.

By miniaturizing the traditionally bulky and complex confocal microscope setup, we gain the flexibility to conduct experiments in diverse environments outside the laboratory.

This portability eliminates the need for specialized infrastructure and facilitates on-the-go measurements, promoting rapid data collection and analysis. Additionally, the compact design enhances accessibility, enabling institutions with limited resources to explore single NV center phenomena and applications.

This chapter presents the setup where we explore this novel compact confocal microscope system and showcase its potential in harnessing individual NV centers through the characterization measurements performed. The subsequent sections will cover the theory and resolution limits of confocal microscopy, along with its applications in characterizing nanoscale samples and addressing NV centers. Our microscope system can optically read out the photoluminescence (PL) signal from individual NV centers and coherently control their spin states, while addressing the need for efficiency and portability in quantum experiments. Beyond the single NV detection, the system accommodates also both nanodiamonds and ensembles, making it a versatile tool for many applications. Coherent control is achieved by precisely synchronizing laser and microwave (MW) pulses, allowing for magnetic field sensing with nanoscale resolution and detailed characterization of NV center spin properties. This instrument aims to overcome existing barriers and facilitate broader adoption and exploration of quantum phenomena at the single NV center level.

3.2 Confocal microscopy

To comprehend confocal microscopy, one must consider the optical paths of both the excitation light and the resulting signal, which can be either backscattered light from a sample or photoluminescence (PL) from a target emitter. Given that PL confocal microscopy will be the primary mode of operation for use in an NV setup, this explanation will primarily focus on this technique. In both PL and reflectance modes, the excitation and detection optical channels remain identical, differing only in how the signal is spectrally filtered.

The optical path of the detection and excitation channels in confocal microscopy is illustrated in Fig. 3.1, demonstrating the elimination of out-of-plane light, leading to enhanced lateral resolution. A dichroic mirror directs light from the excitation source toward the microscope objective (MO). The dichroic mirror reflects shorter wavelengths and transmits longer ones. The MO then focuses the excitation light to a diffraction-limited spot at its focal plane. When this spot illuminates the target, the target emits photoluminescence (PL), which is collected by the MO.

The collected light is collimated by the MO, and directed towards the dichroic mirror. Since the emitted PL typically has a wavelength longer than that of the excitation source, it passes through the dichroic mirror while the backscattered excitation light is reflected away. A lens then focuses the transmitted PL to another diffraction-limited spot at the image plane, which is conjugate to the focal plane of the MO. Points in focus in the MO focal plane are also in focus at the image plane.

A pinhole placed in the image plane allows only the light that passes through it to

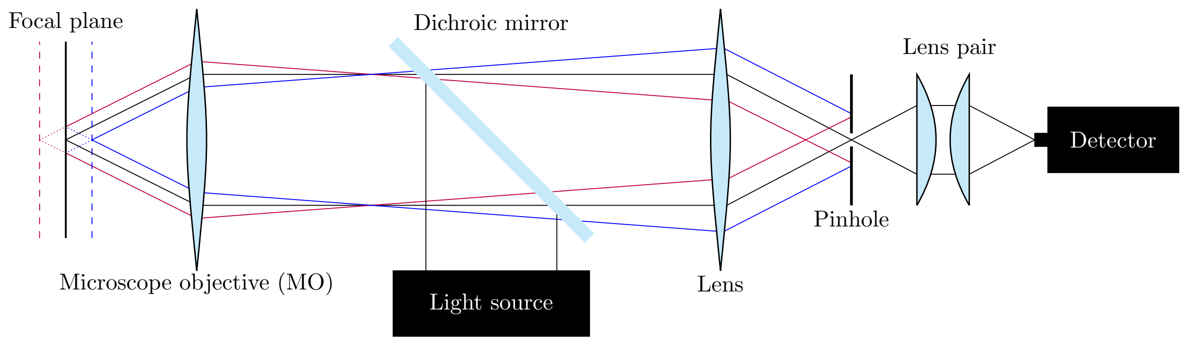

Fig. 3.1: Schematic illustration depicting the operational principles of a confocal microscope. A dichroic mirror reflects the collimated light into the microscope objective (MO), focusing it into a diffraction-limited spot. In the focus spot, the same MO gathers PL photons from the excited sample and collimates this light, allowing it to travel through the dichroic mirror. A lens focuses the light through the confocal pinhole. Planes above and below the MO focal plane produce light that is out of focus at the pinhole aperture, which causes it to be greatly attenuated at the detector and contribute very little to the intensity that is measured. Light coming from below the focal plane is shown by the red path, while light coming from a plane closer to the MO than the focal plane is shown by the blue path.

reach the detector. This configuration significantly attenuates light from planes above or below the focal plane of the MO, as this light is out of focus at the pinhole and thus rejected. The pinhole acts as a lateral spatial filter, suppressing light from points outside the confocal spot of the MO, and ensuring that only light from the focal plane contributes to the measured signal and the final image formation.

Confocal resolution

The previous discussion accounts only for an infinitely small light source converging to an infinitely small point at the focal plane of the microscope objective (MO). However, in reality, the image of the source has a finite width, described by a point spread function (PSF).

When considering the resolution of confocal microscopes, the PSF is often characterized using the paraxial approximation, especially with low numerical aperture (NA) objectives. In the paraxial approximation, the PSF originating from a MO with a circular aperture takes on a specific form in the MO focal plane, which is given by [233]:

$$\mathrm{PSF}(r) = \frac{J_1(\rho(r))}{\rho(r)^2}, \text{ with } \rho(r) = \frac{2\pi r}{\lambda}\mathrm{NA}, \tag{3.1}$$

where NA is the numerical aperture of the lens, λ is the wavelength of excitation light, r is the radial distance from the MO centre, and J_1 is the Bessel function of the first kind of order one. This intensity distribution within the plane is commonly referred to as an Airy pattern. The pattern is characterized by a central intensity maximum encircled by rings exhibiting decreasing intensity from the center outward. The central portion is termed an Airy disk, which has a radius of 1 Airy unit (AU), given by [233]

$$\mathrm{AU} = 1.22\frac{\lambda}{\mathrm{NA}}. \tag{3.2}$$

The resolution of confocal microscopes is fundamentally related to the spatial distribution of the intensity profile in the focal plane. The Rayleigh criterion provides a measure of resolution by stating that the minimum separation required to resolve two incoherently radiating point sources is 0.5 AU. This ensures that the maximum of an Airy pattern produced by one source is no closer than the first minimum of the adjacent Airy pattern. According to the Rayleigh criterion, the lateral resolution for a conventional wide-field microscope is determined by [233]

$$\Delta r_{\mathrm{Wide}} = 0.61\frac{\lambda}{\mathrm{NA}} \tag{3.3}$$

In a confocal microscope, this lateral resolution is further improved as a result of the pinhole, which filters out-of-focus light, enhancing the contrast and sharpness of the image. This narrows the PSF arising from the point-scanning nature of confocal microscopy, where the confocal PSF is determined by the product of the illumination and detection PSF. The improved resolution in a confocal system can be approximated by [233]:

$$\Delta r_{\mathrm{Confocal}} = 0.44\frac{\lambda}{\mathrm{NA}} \tag{3.4}$$

The introduction of the confocal pinhole results in the rejection of out-of-plane light, enabling the resolution of two objects along the optical axis, or z axis. Therefore, axial resolution can be defined as the measure of separation along the optical axis for which two point sources can be resolved. The resolution along the axial direction is determined by [233]:

$$\Delta z = 1.5\frac{\lambda n}{(\mathrm{NA})^2} \tag{3.5}$$

The distinctive confocal microscope capability to differentiate between sources along the optical axis is attributed to the pinhole ability to reject light from planes other than the MO focal plane. Hence, the size of the pinhole is a critical factor in any confocal microscope. If the pinhole is too large, the depth discrimination ability is compromised; if it is too small, the signal-to-noise ratio suffers significantly. Typically, lateral resolution is more sensitive to small variations in pinhole size compared to axial resolution. The choice of pinhole diameter depends on the specific application, and users often prioritize resolution over the amount of signal collected. In many commercially available confocal microscopes, the pinhole is not fixed but variable, using a pinhole wheel to change aperture sizes. Typically, pinhole diameters are chosen close to the size of the image of the Airy disk at the pinhole, which is determined by multiplying the

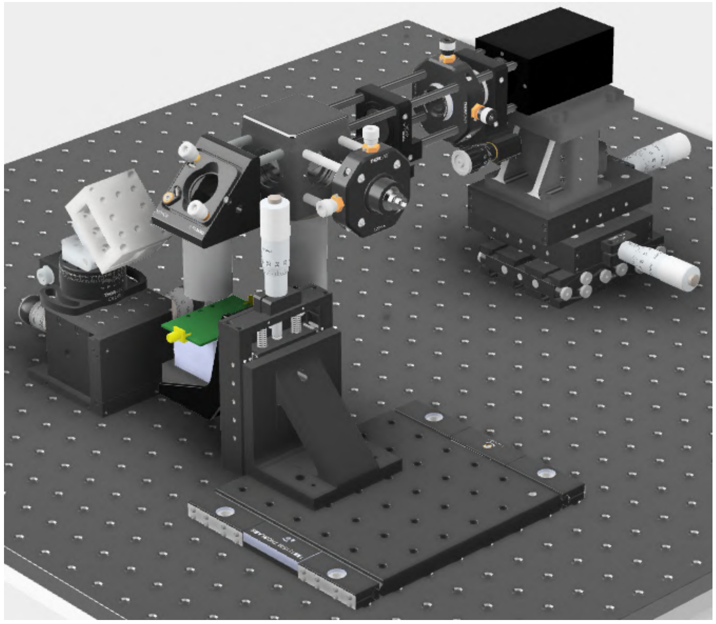

Fig. 3.2: 3D model design of the optomechanics of the compact confocal microscope.

Airy disk size in the MO focal plane by the total magnification at the pinhole.

The effectiveness of confocal microscopy stems from its ability to reject light originating from outside the MO focal plane and confine the excitation volume, thereby reducing the measurement volume to a diffraction-limited spot. Consequently, to collect information on a macroscopically sized sample, the measured point must be moved relative to the sample. There are two common methods for achieving this: sample scanning or beam scanning. Each method offers distinct advantages, but in our confocal microscope we use sample scanning. Sample scanning involves moving the sample beneath a stationary imaging point under the MO, typically employing piezoelectric scanning stages. The field of view (FOV) of a sample scanning confocal microscope is determined solely by the range of the sample scanning stage. A stage with a large range and nanometer precision is highly desirable.

In summary, confocal microscopy is recognized as a point-by-point imaging technique, generating 2D images through the sequential acquisition of PL signals from diffraction-limited measurement volumes. The imaging spot can be scanned either by translating the measurement spot in the MO focal plane using scanning mirrors or by scanning the sample beneath a stationary beam. The rejection of out-of-plane light and the confinement of the excitation volume make confocal microscopy an ideal optical technique for conducting experiments on atomically sized emitters, including optically addressing single NV centers mounted on a scanning probe for magnetometry applications.

3.3 Confocal design

The aim of this study is to develop, construct, and utilize a compact confocal system for optical readout of the photoluminescence (PL) signal from individual NV centers. This system aims to enable coherent control not only over individual NV centers but also over NDs containing NV centers and shallow ensembles of NV centers.

In shaping the optomechanics of the system, advanced 3D modeling software has been used. This deliberate approach allows for meticulous design and optimization, ensuring precision in the arrangement of optical and mechanical elements. The integration of 3D modeling facilitates a comprehensive understanding of the geometry of the system, helping to identify and mitigate potential challenges associated with compactness, alignment, and overall performance. In Fig. 3.2 we present the 3D model of the setup.

In Fig. 3.3, we depict a schematic overview of the components that make up the confocal system, while in Fig. 3.4 we provide a picture of the compact confocal system. Each component is labeled in both figures, and a list of components can be found in Table 3.1. The optical elements are mounted into a cage system, providing stability and alignment of the optical components. The precision in the optomechanical design ensures that the confocal setup maintains its alignment over time. To excite the NV centers, a green laser (1 - Toptica iBEAM SMART PT 515) that emits light at a wavelength of 515 nm is used. The power of this laser can be finely adjusted using a fiber variable optical attenuator (2 - Thorlabs V450A). The laser beam is then guided through a single-mode fiber and collimated (3 - Thorlabs F810APC-543). Subsequently, the beam passes through a 550 nm low-pass filter (4 - Thorlabs FESH0550), effectively eliminating second harmonics originating from either the laser or the fiber. Next, the beam is directed towards a dichroic mirror (5 - Thorlabs DMLP550R), which reflects the beam onto another mirror (6 -Thorlabs BB1-E02) that redirects the light towards the oil-immersion microscope objective (MO) aperture (7 - Olympus UPLXAPO 100X). Maintaining a beam size commensurate with the MO aperture is crucial to ensure that the focused spot size at the sample closely matches the diffraction-limited resolution. The MO used boasts a numerical aperture of 1.45, a magnification of 100, and a working distance of 135 μm. It is important to note that the MO serves as the cornerstone of a confocal microscope as it dictates both the efficiency of photon collection and the spatial resolution achieved. For this MO, the theoretical lateral resolution is 155 nm and the resolution along z is 850 nm.

The detection path begins in the MO focal plane, with light collected and collimated by the MO. The detection and laser path are split at the dichroic mirror, which transmits the longer wavelength PL light and reflects the laser light. To further isolate the PL signal from the detection signal and differentiate the PL of the NV^- from the PL of the NV^0, a 650 nm long-pass filter is placed in the optical path, enhancing the signal-to-noise ratio in the detected signal (9 - Thorlabs FELH0650). The collected PL is then focused with a 50 mm lens (10 - Thorlabs AL2550M-A) into a 20 μm pinhole (11 - Thorlabs P20HK), which enhances the axial and lateral resolution by allowing only focused light to contribute to the image, thus reducing background noise. The light exiting the pinhole is subsequently focused by a lens pair (12 - Thorlabs MAP051919-A) into the photon detector, a single-photon avalanche diode (SPAD) with single-photon sensitivity (13 -MPD PDM-050-CTB). Photon counts are analyzed using a Time-Correlated Single Photon Counting (TCSPC) card (16 - PicoQuant TimeHarp 260). For precise alignment, the pinhole is affixed to a xyz translation stage incorporated within the cage system,

#	Device	Model	Comments
1	Laser	Toptica / iBEAM SMART PT 515	λ = 515nm; Bandwidth = 10nm; Modulation bandwidth = 250 MHz; Maximum output power = 50 mW
2	VOA	Thorlabs / V450A	488 to 600 nm
3	Collimator	Thorlabs / F810APC-543	NA = 0.26; f = 34.74 mm
4	Shortpass Filter	Thorlabs / FESH0550	Cut-Off Wavelength: 550 nm
5	Dichroic Mirror	Thorlabs / DMLP550R	550 nm Cut-On
6	Mirror	Thorlabs / BB1-E02	400 - 750 nm
7	Objective	Olympus / UPLXAPO 100X	NA = 1.45; Working distance = 0.135 mm; Field of view = 0.265 mm; Depth of field = 0.2 μm
8	Piezo stage	Newport / NPXYZ100SG	XYZ Range = 100 μm; Close loop resolution = 0.4 nm; Open loop resolution = 4 nm
9	Longpass Filter	Thorlabs / FELH0650	Cut-Off Wavelength: 650 nm
10	Lens	Thorlabs / AL2550M-A	f = 50 mm
11	Pinhole	Thorlabs / P20HK	Pinhole diameter = 20 $\pm$ 2 μm
12	Lens pair	Thorlabs / MAP051919-A	f1 = 19.0 mm; f2 = 19.0 mm
13	Photon detector	MPD / PDM-050-CTB	Dead time: 75 ns
14	Acquisition card	NI / USB-6343 (BNC)	
15	Piezo controller	Newport / NPC3SG	
16	Photon counter	PicoQuant / TimeHarp 260	
17	AWG	Keysight / M8190A	12 GSa/s
18	MW source	Windfreak / SynthHD	
19	MW amplifier	MiniCircuits / ZHL - 16W-43-S+	

Table 3.1: Experimental equipment

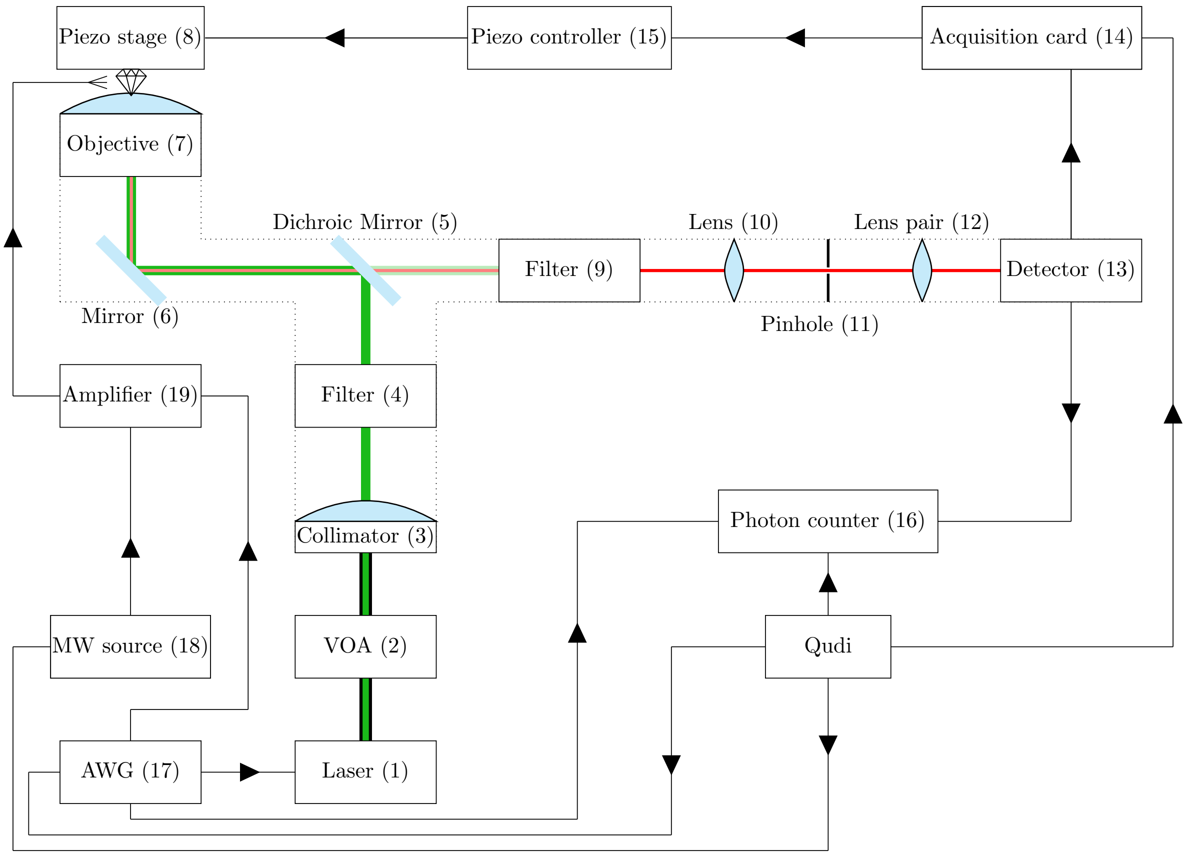

Fig. 3.3: Schematics of the main components of the compact confocal microscope and the devices used, listed on Table 3.1.

allowing meticulous adjustments, with the z axis aligned parallel to the beam, while the lenses are mounted on a z stage. Lastly, the SPAD is placed on an xyz stage securely attached to the table, ensuring stable positioning during experimentation.

The use of SPADs to register the photon events allows for high-sensitivity detection„ while also enabling the collection of temporal data of the PL signal. The output signal from the SPADS is delivered into a time tagger for time-correlated single-photon counting (TCSPC). Alternatively, for simple PL experiments, the signal is directed to a pulse counting data acquisition card (14 - NI USB-6343 (BNC)). For applications where the spectral composition of the optical signal is of interest, the SPAD can be substituted with a spectrometer.

To scan the sample beneath the MO, we secure it onto a nanopositioner featuring a piezo-based stage with a travel range of 100 μm, allowing for nanometer resolution motion along the xyz axes (8 - Newport NPXYZ100SG). The position of the stages is controlled using an analog signal from 0-10 V for each axis, with 0 V corresponding to the most retracted position on that axis (0 μm) and 10 V to full extension (100 μm) (15 - Newport NPC3SG). This piezo controller is then connected to the acquisition card to manage the confocal scans. The nanopositioner is then integrated into a coarse stage, facilitating the mounting and positioning of the sample.

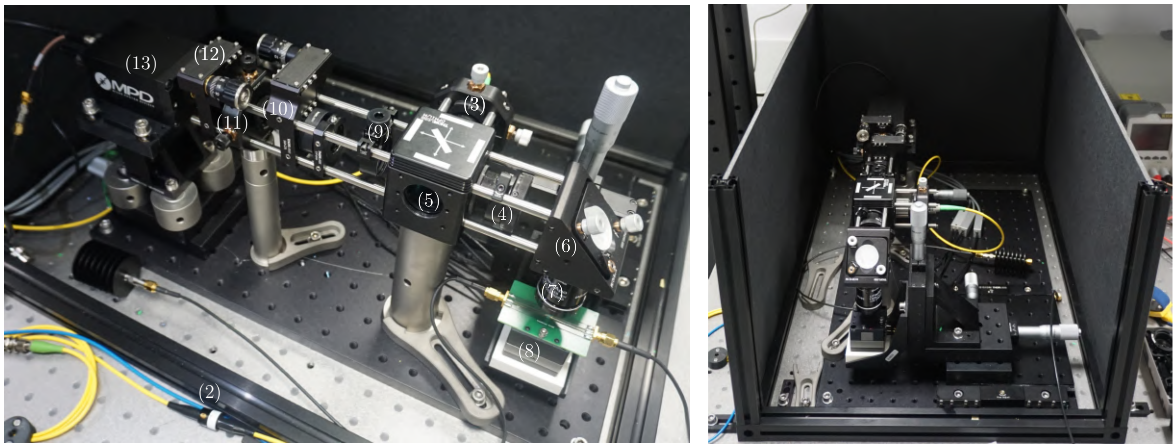

Fig. 3.4: Picture of the optical elements of the confocal setups, labeled as they appeared in Table 3.1.

MW signals, crucial for controlling the spin of the NV center, are transmitted via a cable antenna with a diameter of 20 μm securely affixed to the diamond surface. Pulsed sequences are generated using an Arbitrary Waveform Generator (AWG) (17 - Keysight / M8190A), while a simpler signal generator manages the continuous sequences (18 - Windfreak SynthHD). To increase the strength of the MW signals, a 45 dBm amplifier is utilized (19 - MiniCircuits ZHL - 16W-43-S+).

The confocal microscope is mounted on a breadboard with dimensions of 450 mm $\times$ 300 mm (W $\times$ H), allowing it to be transported without dismantling or optical misalignment. The breadboard can be fixed to an optical table for stability. When fully assembled, the instrument fits within a black optical enclosure measuring 525 $\times$ 375 $\times$ 300 mm^3 (L x W x H), with the exception of the control electronics, which are accommodated on a separate rack. This optical enclosure is designed to provide optical isolation from external light sources and to confine the working environment to prevent exposure to open beams.

Qudi

Qudi, a specialized software [173], orchestrates the scanning process, manages the acquisition and processing of fluorescence signals, and governs the control of both laser and MW pulses. Although originating from the University of Ulm and freely available, our contribution entails the development of new hardware modules tailored to our setup. Designed in Python 3, Qudi stands as an advanced, adaptable, and modular operating system suite, specifically designed for laboratory experiments. It delineates a structured framework by segregating its functions into distinct layers: hardware abstraction, experiment logic, and user interface.

At its core, Qudi has an extensive range of features, including a user-friendly graphical interface, real-time data visualization, seamless distributed execution, robust configuration management, and comprehensive data recording capabilities. The Qudi

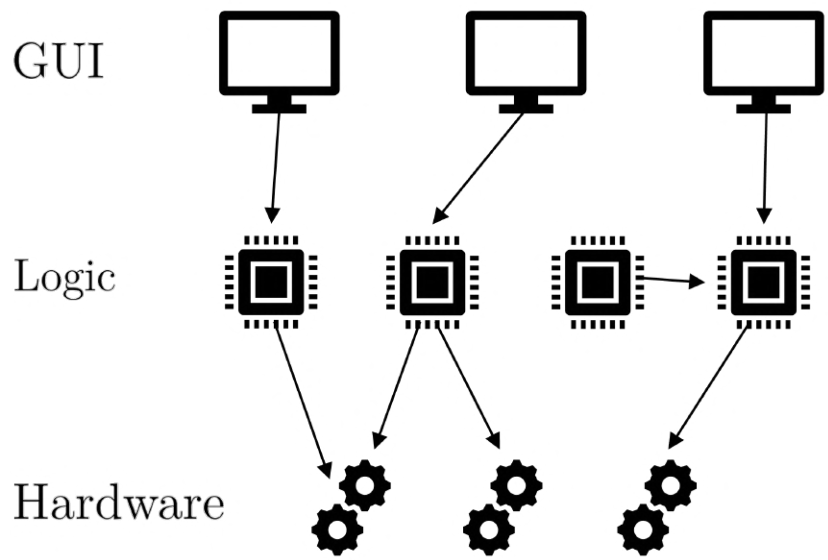

Fig. 3.5: Qudi structural design consists of a rigorously enforced three-layer architecture which governs the design of all experiment modules. Logic modules are crafted to encapsulate specific measurements, comprising necessary tasks and data analysis procedures. These logic modules establish connections with hardware modules through clearly defined interfaces, ensuring hardware agnosticism within the experiment framework, provided the hardware meets minimum requirements. GUI modules, on the other hand, interface with the logic layer, enabling user interaction with the experiment setup and facilitating the display of data and computed results.

suite comprises interconnected modules managed by a central component, as shown in Fig. 3.5. Initiated by a single executable Python file, the manager component facilitates core functions such as logging, error handling, configuration reading, and remote access. This foundational infrastructure expedites module development for new experiments by providing structured starting points.

Logic modules serve to control and synchronize experiments, facilitating the passage of input parameters from the user to hardware modules and processing measurement data as required. These modules manage the exchange of information between the hardware modules and perform the necessary computations and conversions. Equipped with their own thread and event loop, logic modules handle concurrent task execution and device synchronization, overseeing all steps from measurement initiation to completion, including data evaluation and storage.

To ensure maximum reusability, hardware modules must be interchangeable for measurement devices that offer similar functionality but operate and communicate differently. These hardware modules address these challenges by translating logic commands into hardware-specific language, achieved through defining an interface, a set of functions required for a hardware module of a specific type to function. This interface class is inherited by implementing hardware modules, necessitating the overriding of all inherited functions.

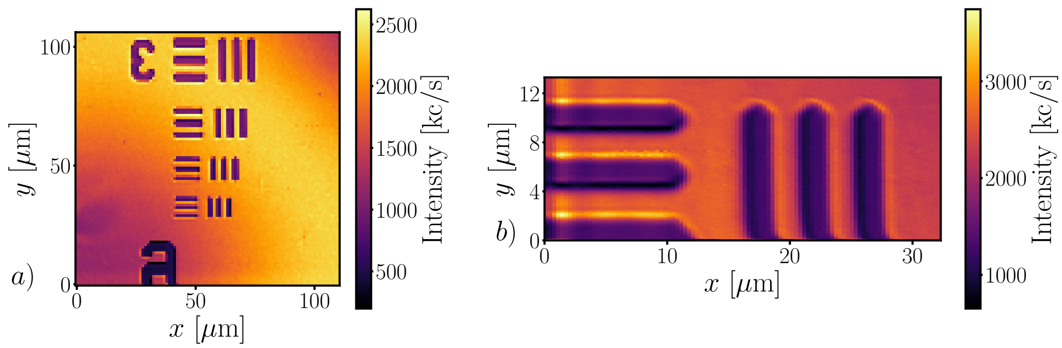

Fig. 3.6: (a) Wide confocal scan of the alignment target card. (b) Confocal scan of 2 μm lines of the alignment target card.

Qudi GUI modules facilitate user interaction through on-screen windows for experiment control and data visualization. While providing a convenient interaction method with logic modules, Qudi remains fully functional without GUI modules. GUI modules are restricted from direct interaction with each other or hardware and do not engage in data processing.

3.4 Single NV detection

The first task was to investigate the lateral resolution of the confocal microscope. An instrumental aid that facilitated the alignment and refinement of our setup was a reflective resolution target. These targets, commonly employed for gauging imaging system resolution, feature reference line patterns with precisely defined thicknesses and spacings. They are designed to be placed in the same plane as the object being imaged. They allow us to identify the largest set of indistinguishable lines, thereby determining the resolving power of our system. In Fig. 3.6a we can see a confocal scan of the different lines of the resolution target, while in Fig. 3.6b we resolve lines of a width of 2 μm.

To align and test the axial resolution, we considered a single crystal CVD diamond with a high NV concentration of 4.5 ppm. The fluorescence of this ensemble sample is visible to the naked eye and thus allows us to align the detection path of the confocal microscope. To verify that the measured fluorescence came from NV centers, we substituted the SPAD by a spectrometer, and measured the characteristic spectrum of the NV center, depicted in figure Fig. 3.7. We measure the zero-phonon line (ZPL) of both the NV^0 and the NV^- as the two narrow peaks in the spectrum. They correspond to the electronic transition occurring without any involvement of phonons, representing the energy difference between the excited and ground electronic states. To evaluate the axial resolution of the set-up, we conducted a confocal depth scan across the surface of this densely packed ensemble of NV centers. Although the high brightness of the sample presents a challenge in discerning individual NV centers because of collective fluorescence, these experiments aid in determining the sharpness of the surface. In Fig. 3.8a, the intense fluorescence at the top of the image represents the interior of the

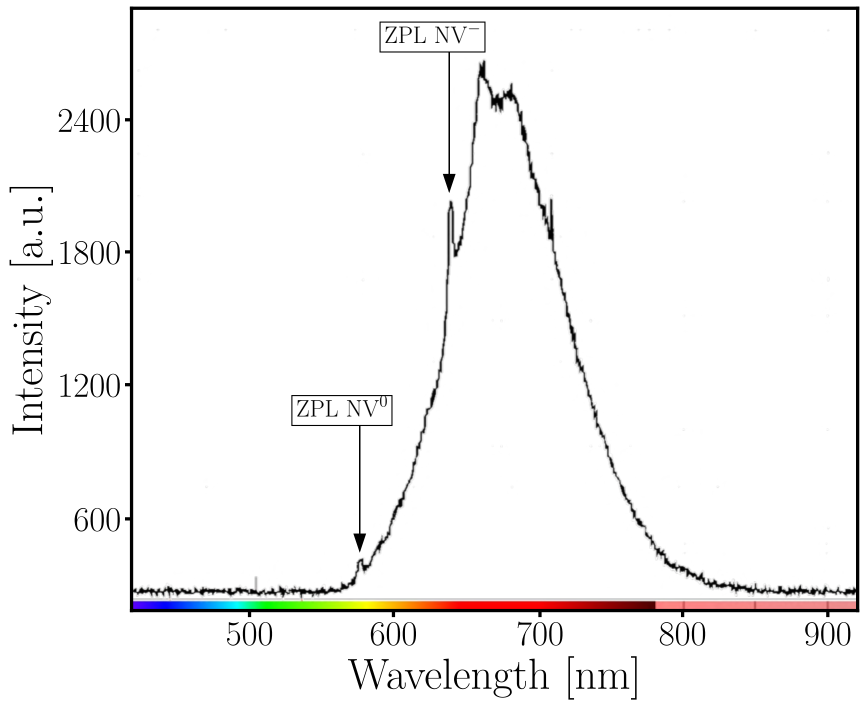

Fig. 3.7: Fluorescence spectrum of an ensemble of NV centers where we can distinguish the zero phonon line (ZPL) of the NV^0 at 575 nm and of the NV$^-$ at 637 nm. We use a Thorlabs CCT10 - Compact Spectrometer to measure the spectrum.

diamond. The interface between the diamond and the MO oil is distinguishable and a distinct black circular shadow appears at the bottom right, associated with the cable antenna known to have a width of 20 μm. The cable blocks part of the excitation beam, which produces a dim shadow in the confocal image.

To demonstrate the nanoscale resolution of our set-up, we imaged NDs with a diameter of 70 nm and an NV center concentration of 2.5 ppm. These NDs were provided at a mass concentration of 1 mg/mL in deionized water, which we diluted by a factor of 50. After allowing the solution to dry, we placed it under a thin cover glass with a thickness of 100 μm. As the size of the NDs falls below the diffraction limit of our setup (approximately 300 nm), they appear as small as single NV centers but significantly brighter, as illustrated in Figure Fig. 3.8b. Under green laser excitation, we observe the distinct spots associated with NDs containing NV centers. It is important to note that some bright spots may not correspond to ND; these brighter and larger spots may be generated by other particles. Over time, these non-ND spots experience a permanent loss of fluorescence due to prolonged exposure to excitation light, leading to chemical changes that render the molecules non-fluorescent.

To detect single NV centers, we examined a diamond substrate that we then implanted. In Fig. 3.9a, we present an image of the diamond sample affixed to a PCB

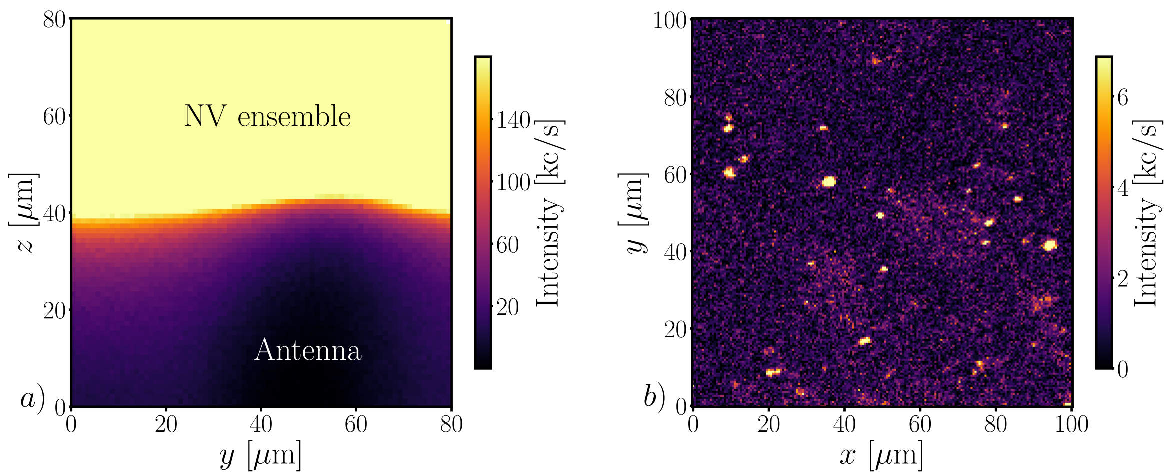

Fig. 3.8: (a) A yz confocal scan of a diamond sample containing an NV concentration of 4.5 ppm. The intense fluorescence at the top represents the diamond interior, with a distinguishable interface between the diamond and MO oil. A distinctive black circular shadow at the bottom right corresponds to the cable antenna, known for its 20 μm width. (b) Confocal scan of NDs.

board, with the wire securely welded to the top of the diamond. This setup is integral in ensuring the electrical connections required for subsequent manipulation and readout of the NV center. Typical methods for securing the diamond to the antenna include double-sided tape, glue, or optical grease. However, some adhesives can dissolve under immersion oil or degrade over time, compromising the stability and accuracy of the setup. Maintaining a clean surface on the diamond is crucial to minimizing the detection of elements other than NV centers. Contaminants on the diamond surface can significantly affect the optical properties and accuracy of the measurements. To ensure surface cleanliness, we employ a thorough cleaning process that includes acetone ultrasonic cleaning. This method effectively removes organic contaminants and residues that may have accumulated on the diamond surface during handling and preparation.

It is important for the diamond substrate to have a low defect concentration prior to implantation. Using a single crystal electronic (ELSC) grade as the substrate, we chose a high-purity chemical vapor deposition (CVD) diamond material engineered to minimize point defects. This material stands out as one of the commercially available options boasting the lowest Nitrogen (N) and Nitrogen-Vacancy (NV) center density. Interestingly, it has a nitrogen concentration of less than 5 parts per billion (ppb) and typically has an NV center concentration of less than 0.03 ppb.

The diamond substrate was subjected to a nitrogen ion implantation process with an energy of 5 KeV. The implantation energy determines the depth of the NV centers below the surface, in this case approximately 10 nm. The spot diameter was selected to be 200 μm. Different doses of $^{15}N^+$ were implanted in various regions of the diamond, as depicted in Fig. 3.9b. The implantation dose is responsible for determining the NV concentration of the spot. The preference for $^{15}N^+$ over ^{14}N arises from its simpler

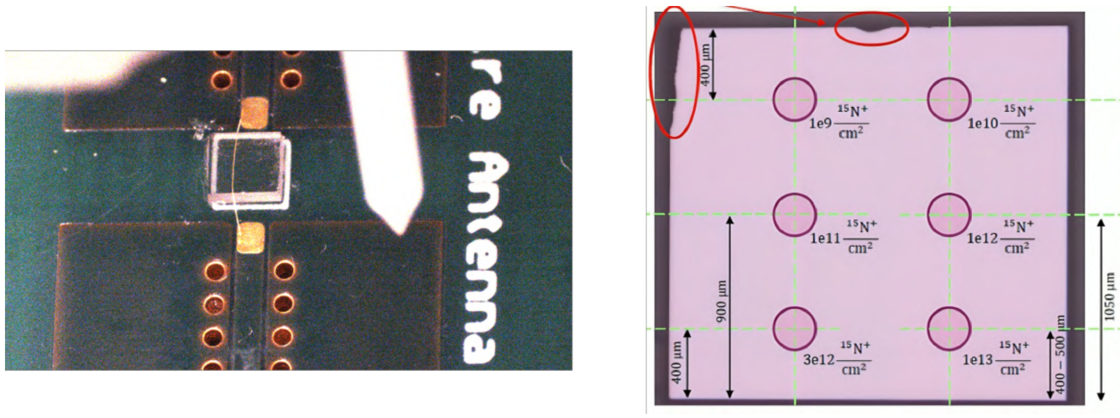

Fig. 3.9: (a) Diamond sample from ULM glued to the PCB antenna. Over it we can see the welded 20 μ cable. (b) Schematics of the implanted spots over the diamond surface with the different concentration energies.

hyperfine structure (due to spin-1/2), which leads to clearer spectral features and potentially longer coherence times in the NV center.

After the implantation process, the sample is subjected to annealing. This involves heating the diamond to a temperature ranging between 800° C and 1000° C, keeping it at this temperature for several hours, and then gradually cooling it down [234]. The precise arrangement and positioning of the NV centers within the diamond lattice can result in variations in their properties, potentially affecting their suitability for particular applications. Annealing serves to mitigate some of these issues by providing energy for atomic rearrangement, relieving lattice stresses, and potentially enabling NV centers to adopt more favorable configurations.

Varied implantation doses will result in different NV center densities. Low doses, such as 10^9 $^{15}\mathrm{N}^+/\mathrm{cm}^2$ and 10^10 $^{15}\mathrm{N}^+/\mathrm{cm}^2$, enable the detection of individual NV centers. The intense and uniform PL of these ensembles is ideal for initial calibration and alignment procedures. This ensures that the microscope is focused on the surface and precisely adjusted before moving on to detect single NV centers. Moreover, these ensembles are valuable for various applications beyond the initial setup due to their proximity to the surface, which allows for enhanced interaction with other samples positioned on the surface. In Fig. 3.9 we present two confocal scans of the spot with an implantation dose of 10^{12} $^{15}\mathrm{N}^+/\mathrm{cm}^2$. In Fig. 3.10a, we show an xy scan at the edge of the implanted spot, where the shadow of the antenna is visible. In Fig. 3.10b, we show a scan xz, where the upper half of the confocal image corresponds to the diamond and appears darker compared to the lower half representing the MO oil. This contrast is attributed to the elevated refractive index of the diamond. We can observe a narrow bright line at the interface because of the fluorescence of the NV centers, which are implanted 10 nm below the surface.

Once the surface is located, we can begin searching for sparse single NV centers at the edge of the implanted spot or in areas with a lower implantation dose. In Fig. 3.11,

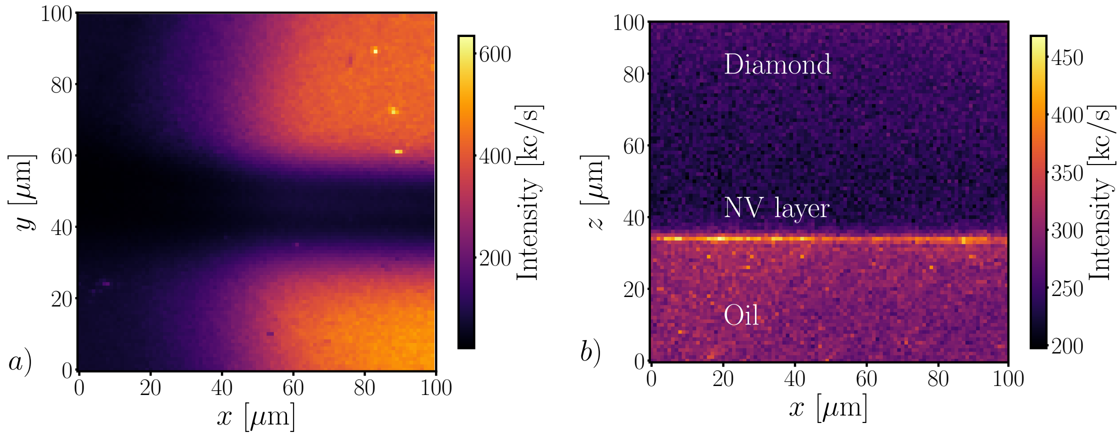

Fig. 3.10: Confocal scans on the implanted diamond in the spot with an 10^{12} implantation energy of $^{15}N^{+}/cm^{2}$. (a) A $100{\times}100\mu m^2$ xy confocal scan with a 10 nm pixel size of the edge of the implanted spot, where we can observe the 20μm shadow of the cable antenna. (b) A $100{\times}100\mu m^2$ xz scan where we can see the objective oil and and the bright dense layer of NV centers at the surface of the diamond.

the bright spots correspond to single NV centers in the region with an implantation dose of 10^{10} $^{15}N^{+}/cm^{2}$, with their diameter reflecting the optical resolution of the confocal microscope, approximately 300 nm. Fig. 3.11a shows a 20 μm × 20 μm area with a pixel size of 10 nm, while Fig. 3.11b provides a close-up view of a region of 5μm × 5μ m with a resolution of 2.5 nm. However, the optical contrast, reflected in the difference in counts between the NV center PL and the background, is not optimal and could be improved by reducing the laser power and refining the alignment and design of the set-up.

3.5 Coherent control

Once we have detected a single NV, our goal is to coherently control its spin state. The orbital ground state of the NV center is a spin-triplet. The static Hamiltonian of the NV center ground state, neglecting any interactions with nuclear spins or spin-strain interactions, and assuming that the NV-axis is oriented along the z-direction, parallel to an external applied magnetic field B_0, is given by:

$$\hat{H}_0 = D\hat{S}_z^2 + \gamma_e B_0 \hat{S}_z \tag{3.6}$$

where $D = 2.87$ GHz is the zero field splitting go the ground state, $\gamma_e = 28$ GHz/T is the electron gyromagnetic ratio and $\hat{S}_{x,y,z}$ are the spin-1 matrices. The second term accounts for the Zeeman splitting of the states $|{\pm}1\rangle$. In order to achieve magnetic spin resonance and coherent control, we need an external MW that induces transitions between the spin sublevels. For example, a resonant field enables us to controllably rotate the ground state spin states from $|0\rangle$ to $|1\rangle$ and back, process termed Rabi oscillations. This field is usually created using a MW signal generator and an antenna. We include the oscillating

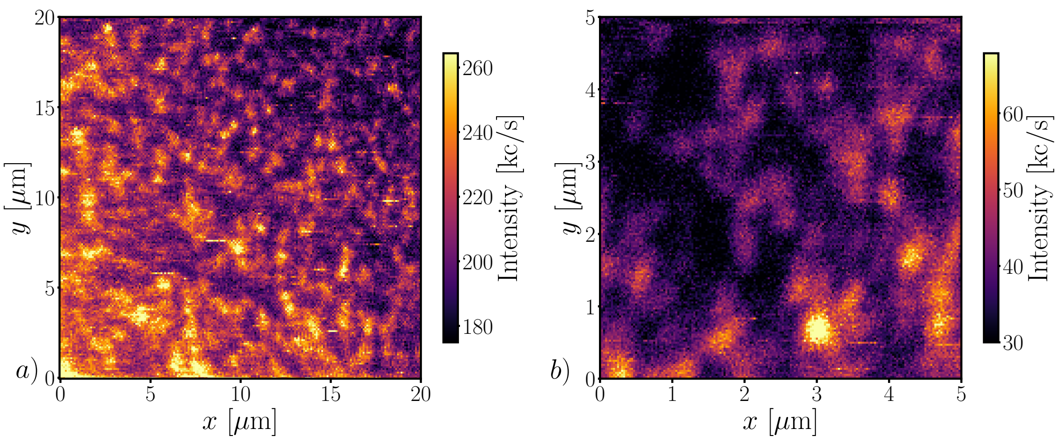

Fig. 3.11: (a) Confocal fluorescence scan of the sample of area 20μm×20μm with a 10 nm resolution. Bright spots correspond to single NV centers. The sample is a diamond implanted with $^{15}N^{+}$ ions at an energy of 5 eV and a dose of 10^9 ions per cm^2. (b) Smaller confocal scan over an area of 5 μm×5 μm with a resolution of 25 nm

magnetic field in the Hamiltonian as a time-dependent term given by

$$\hat{H}_1 = \Omega \cos(\omega t)\hat{S}_x. \tag{3.7}$$

Using a wire antenna, we generate an oscillating magnetic field to coherently manipulate the electronic spin of the nitrogen-vacancy (NV) center ground state. First, we measure the spin-transition spectrum of a single NV center. During this measurement, a laser continuously excites the NV center, and we record its fluorescence, which is linked to the spin state of the NV center. MW radiation is applied simultaneously to induce spin rotations in the ground state. When the MW frequency matches the transition frequency $|0\rangle \leftrightarrow |\pm1\rangle$, equal to the zero field splitting $D = 2.87$ GHz, population transfer occurs from the bright state $|0\rangle$ to the darker states $|\pm1\rangle$, resulting in a decrease in fluorescence. This procedure is referred to as optically detected magnetic resonance (ODMR). Fig. 3.12 illustrates the zero magnetic field ODMR spectrum, with the main peak centered at $D = 2.87$ GHz. We obtained a contrast Full Width at Half Maximum (FWHM) $\Delta\nu = 11$ MHz and a contrast of $c = 4\%$, defined as one minus the ratio between the signal intensity at resonance and non-resonant conditions. In Fig. 3.12b, additional ODMR spectra are presented, recorded for an arbitrary external magnetic field introduced by placing a permanent magnet in the proximity of the diamond crystal.

The energy splitting of the $|\pm1\rangle$ state depends on the orientation of the B_0 field with respect to the NV axis. We can compute the magnitude of the magnetic field in the projection of the NV axis by:

$$\nu_+ - \nu_- = 2\gamma_e B \tag{3.8}$$

where ν_+ and ν_- are the central frequencies of the two resonances, corresponding to the transitions $|0\rangle \leftrightarrow |+1\rangle$ and $|0\rangle \leftrightarrow |-1\rangle$ respectively. For the ODMR measurement shown

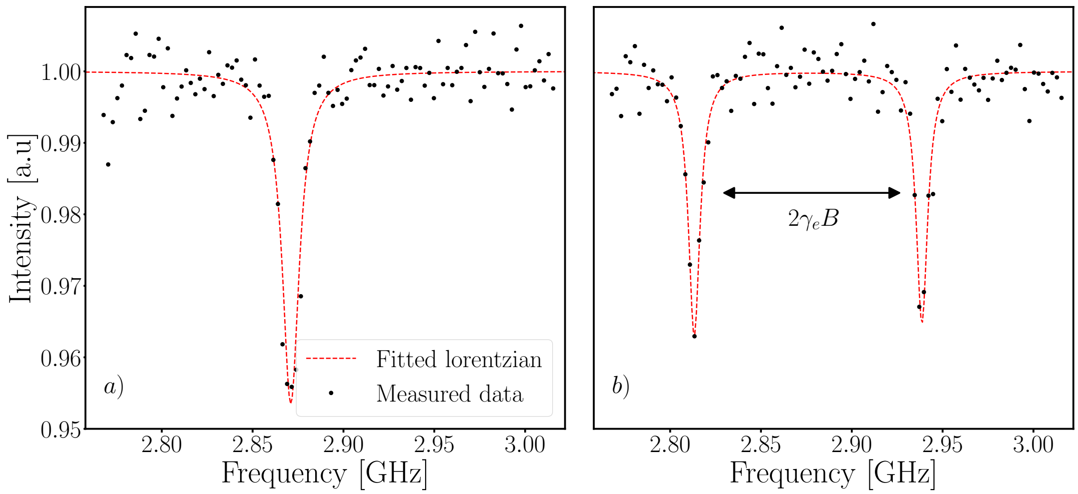

Fig. 3.12: (a) Normalized ODMR spectrum at zero magnetic field for a single NV center. (b) Normalized ODMR spectrum for an arbitrary magnetic field applied to the NV center. The central resonance is split into two resonances due to the Zeeman splitting of the $|\pm1\rangle$ states.

in Fig. 3.12b, the data was fitted to a double Lorentzian curve, yielding a frequency split of $\nu_+ - \nu_- = 125 \pm 1$ MHz. From this, the magnetic field projection was determined to be $B_z = 2232 \pm 6\ \mu$T.

From the ODMR spectrum we can investigate the projected sensitivity for a shot-noise limited measurement, which is of the order of [74]

$$S_{SN} \simeq \frac{2\pi}{\gamma_e} \frac{\Delta\nu}{c\sqrt{\mathcal{R}}}. \tag{3.9}$$

Here, $\mathcal{R}$ represents the rate of detected photons, which in this case was measured as $\mathcal{R} \simeq 4000$ counts per second and $\Delta\nu$ is the width of the resonance at half maximum with c the resonance contrast. We obtain $S_{SN} = 0.1\mathrm{mT}/\sqrt{\mathrm{Hz}}$, a relatively low sensitivity due to the low count rate when measuring a single NV center. However, the detection rate $\mathcal{R}$ can be improved by increasing the laser power and improving the collecting efficiency of the microscope. Additionally, both the contrast and line width can be improved by aligning the external magnetic field with the NV axis and carefully optimizing the MW and laser power.

In our initial experiment, we applied continuous-wave MW and laser fields to interrogate the NV center. However, using pulsed excitation offers distinct advantages: it provides higher optical contrast and allows for more precise control of the spin state. In a typical pulsed sequence, a laser pulse first polarizes the NV center into the $|0\rangle$ state. Then, a sequence of MW pulses is used, often comprising π and $\frac{\pi}{2}$ pulses resonant with a selected transition, to manipulate the spin state. For example, a π-pulse swaps the populations of $|0\rangle$ and $|\pm1\rangle$, while a $\pi/2$-pulse brings the $|0\rangle$ state into the superposition

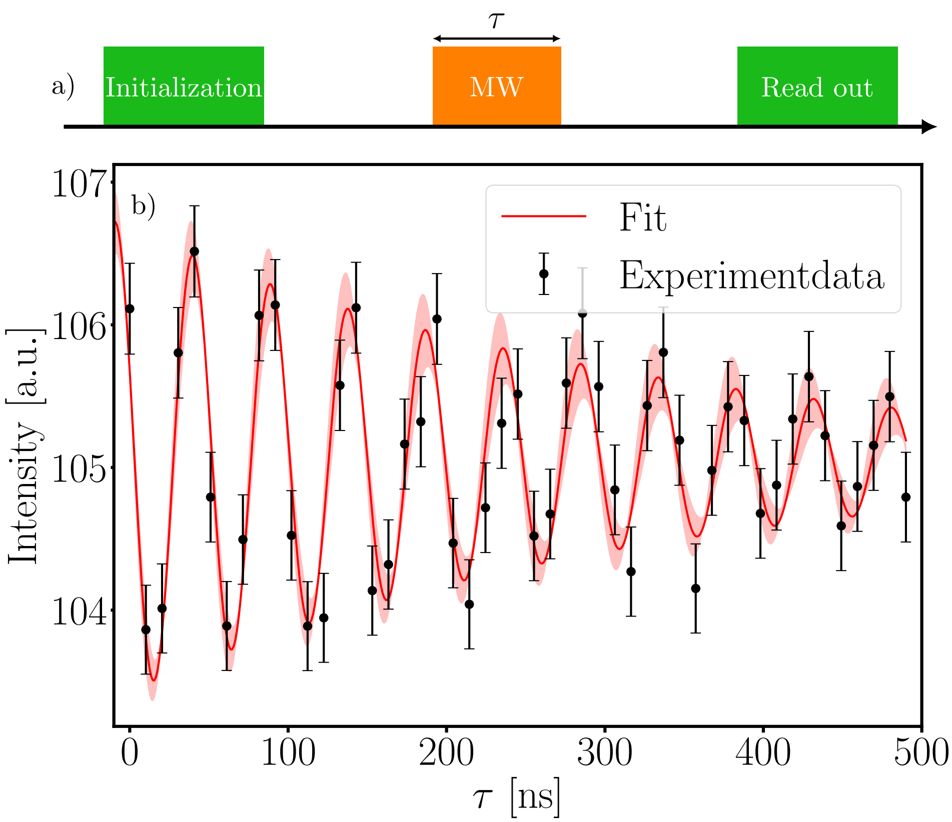

Fig. 3.13: (a) Pulse sequence to perform Rabi oscillations. The length of the laser pulse is 2 μs and the length of the MW pulse is varied. (b)) Rabi oscillations for a single NV center in the spot (see Fig. 3.9b) with an implantation dose of 10^9 $^{15}N^+/cm^2$ with MW frequency set to $\omega = 2.87$ GHz. We measured for 1 minute and obtained $\Omega = 20.4 \pm 0.1$ MHz and $T_2^{\mathrm{Rabi}} = 320 \pm 60$ ns

state $(|0\rangle + |\pm1\rangle)/\sqrt{2}$. Finally, a laser pulse is applied again to read out the spin state, with many protocols combining the initialization and readout steps for efficiency. The durations of these pulses are calibrated by measuring Rabi oscillations.

After a continuous-wave ODMR has been successfully performed on a single NV center, the next step is to probe the coherent dynamics of the NV center by measuring Rabi oscillations. These oscillations—characterized by the periodic exchange of population between the $|0\rangle$ and $|1\rangle$ states under an external resonant MW field—demonstrate the coherent control of the encoded qubit.

Successfully demonstrating Rabi oscillations indicates that we have achieved coherent control, a crucial step in validating the viability of any quantum system. To observe Rabi oscillations, we set the driving MW frequency to be in resonance with the ODMR transition frequency and vary the MW pulse length. An initial laser pulse of 3 μs is used to initialize the NV in the $|0\rangle$ state. Then a subsequent MW pulse of varying length τ rotates the spin. The next laser pulse serves as the readout pulse. The schematic of the pulse sequence implemented for this experiment is illustrated in Figure 3.13a.

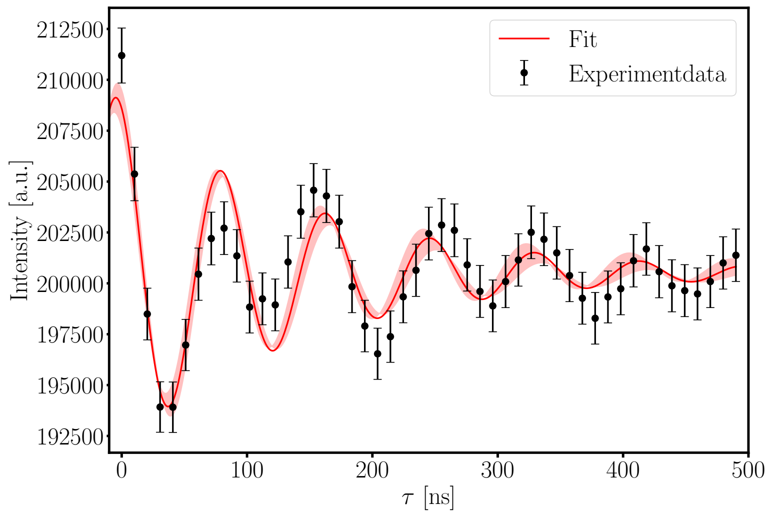

Fig. 3.14: Rabi oscillations in the shallow NV ensemble in the spot (see Fig. 3.9b) with an implantation dose of 10^{12} $^{15}N^+/cm^2$ with MW frequency set to $\omega = 2.87$ GHz. We measured for 1 minute and obtained $\Omega = 12.0 \pm 0.2$ MHz and $T_2^{\text{Rabi}} = 155 \pm 25$ ns

For a single NV center, from the spot with an implantation dose of 10^{10} $^{15}N^+/cm^2$, we observe oscillations in the spin-dependent PL signal as a function of the pulse length of the MW, as shown in Figure 3.13b, which indicates coherent rotations of the spin. The Rabi oscillations can be fitted to an exponentially decaying sinusoidal

$$S_{\text{Rabi}} = a\cos\left(2\pi\Omega\tau + \phi\right)\exp\left\{-\tau/T_2^{\text{Rabi}}\right\} + c \tag{3.10}$$

where a is the Rabi oscillation amplitude, c is an offset, Ω is the Rabi frequency, ϕ is a phase, and T_2^{Rabi} is the driven coherence time of the spin. The Rabi frequency Ω characterizes the coupling strength between the driving MW field and the NV center. The driven coherence time T_2^{Rabi} describes how long the $|0\rangle \leftrightarrow |\pm 1\rangle$ transition can be driven before the system dephases into a mixed-state. For the Rabi oscillations observed in the single NV center we determined $\Omega = 20.4 \pm 0.1$ MHz and $T_2^{\text{Rabi}} = 320 \pm 60$ ns. We can calibrate the exact $\pi/2$-pulse and π-pulse lengths as $\tau_{\pi/2} = 12.25 \pm 0.05$ ns and $\tau_\pi = 24.5 \pm 0.1$ [235]. We also measured Rabi oscillations in the shallow NV ensemble of the spot with an implantation dose of 10^{12} $^{15}N^+/cm^2$, shown in Fig. 3.14. For these Rabi oscillations observed using the same MW power as for the single NV center, we determined $\Omega = 12.0 \pm 0.2$ MHz and $T_2^{\text{Rabi}} = 155 \pm 25$ ns. The intrinsic dephasing time is influenced by magnetic noise from the surroundings, specifically, fluctuating spins that interact with the NV center spin. This noise can arise from various sources, including nuclear spins such as ^{13} C, ^{14} N, ^{15} N, ^{1} H, P1 centers or other unpaired electron spins. Similarly to NMR, this magnetic noise can be partially mitigated using decoupling sequences, resulting in an extended coherence time. We will demonstrate this approach later in a Hahn echo experiment.

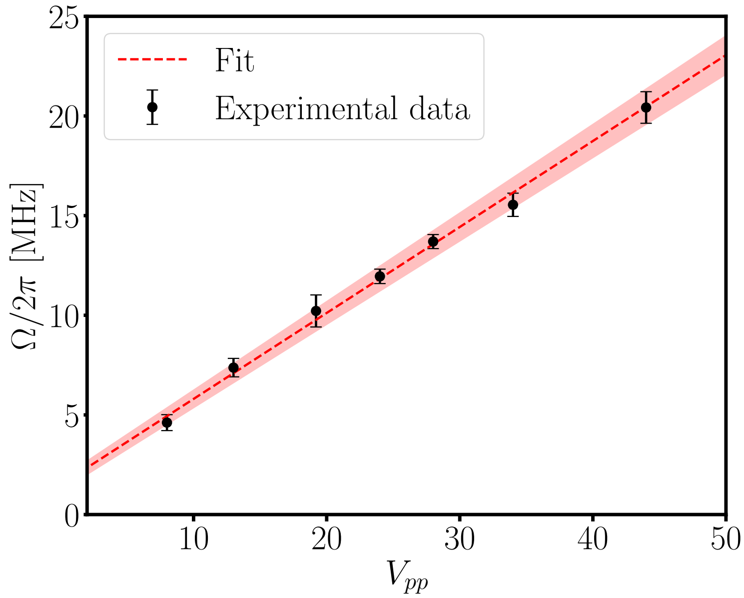

Fig. 3.15: Rabi frequency as a function of the applied voltage to the 20 μm cable.

Although typical coherence times for bulk NV centers can reach a couple of milliseconds, shallow NV centers exhibit dephasing times in the range of 10 to 100 μ s due to surface effects, such as unpaired electrons in surface dangling bonds. The smaller measured value in our case is attributed to considering a single NV in a spot with a high concentration of NV centers, which contributes to increased magnetic noise. For the shallow ensemble, we measured $\Omega = 12.0 \pm 0.2$ MHz and $T_2^{\mathrm{Rabi}} = 155 \pm 25$ ns, a smaller value due to the higher concentration of NV centers [236] and the inhomogeneous broadening of resonance frequencies across the measured NV centers. Although we do not individually resolve the NV centers in the shallow ensemble, as we still operate under confocal resolution, we anticipate that only a small number of NV centers will be excited. Each of them will have distinct couplings to the MW field and a different Rabi frequency, contributing to the combined Rabi oscillations illustrated in Fig. 3.14.

We also aim to characterize how Rabi frequency Ω depends on applied MW power, expecting to observe $\Omega \simeq \sqrt{P_{MW}}$ [74]. However, it is crucial to note that the Rabi frequency is influenced not only by the MW power but also by factors such as the distance from the spot to the MW source and the orientation of the NV center relative to the driving field. As we use a cable antenna, the radiated power will be $P_{MW} \simeq V^2/R$, where V is the applied voltage and R is the resistance of the wire. Hence, we anticipate a linear correlation between the applied voltage and the Rabi frequency, as demonstrated in Fig. 3.15. We observe faster oscillations as we increase the peak-to-peak voltage applied to the shallow ensemble of the spot with a 10^{12} $^{15}\mathrm{N}^+/\mathrm{cm}^2$. This linear tendency exhibits distinct slopes for different NV centers, depending on their proximity to the antenna and orientation relative to the radiation field.

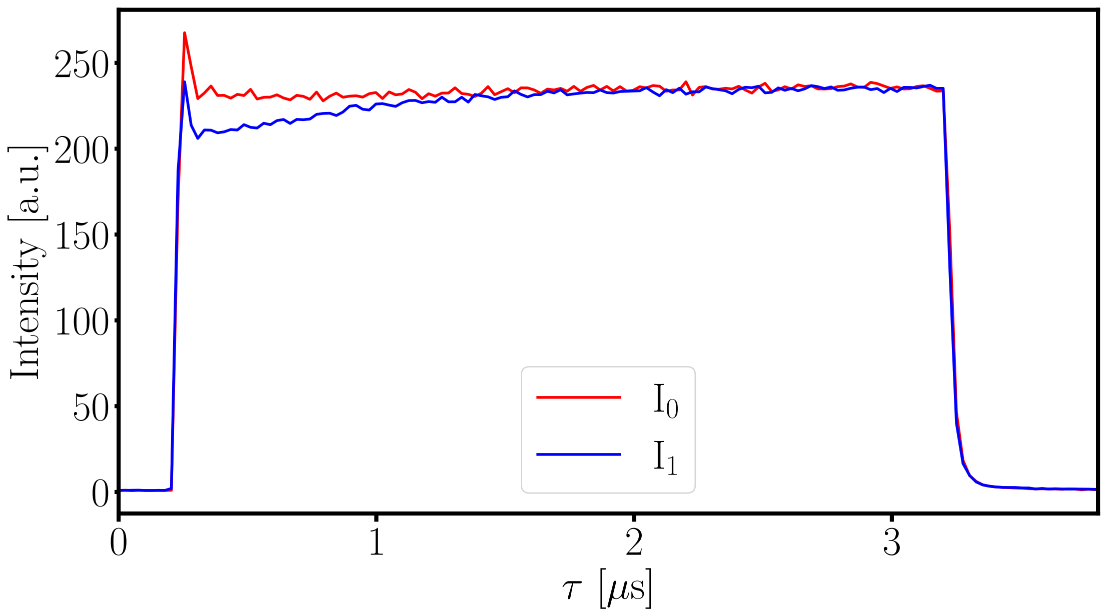

Fig. 3.16: Examples of time-dependent fluorescence, denoted as I_0 and I_1, corresponding to pure initial spin states $|0\rangle$ and $|1\rangle$ for a single NV center. The fluorescence is more intense when the system is initialized in the $|0\rangle$ state. After a time span of 750 ns, both initializations reach the same steady state, causing their intensities to become equal.

As discussed above, the PL intensity provides insight into the state of the NV center. To initialize the system into the $|0\rangle$ state, a 3 μs laser pulse is applied, and to initialize it into the $|\pm1\rangle$ states, a π-pulse follows this laser pulse. However, the described initialization procedures are not ideal and do not result in pure $|0\rangle$ or $|\pm1\rangle$ states. The PL data, collected from a single center, are accumulated over thousands of measurement repetitions. The SPAD sends short nanosecond pulses each time a photon is detected, and the TimeHarp assigns them a time tag according to an external trigger, which is then used to build the PL histogram presented in Figure 3.16, showing the time-dependent PL trace after a laser pulse for the NV initialized in the states $|0\rangle$ and $|1\rangle$, denoted as I_0 and I_1.

The contrast in the fluorescence of the pure spin states corresponds to the difference in intensity between the time traces. However, after 300 ns, the system depolarizes due to optical excitation, reaching a steady state, and we lose information about the initial state because both states initialization reach the same intensity. The time required to reach this steady state will depend on the optical excitation power. The optical dynamics of the NV center can be utilized to optically read out the spin state of the center and simultaneously spin-polarize the center to the $|0\rangle$ state.

After turning off the laser excitation, the population undergoes a rapid decay from the excited states to the ground state, leading to a swift reduction in fluorescence. This decay process plays a crucial role in characterizing the transition rates between different

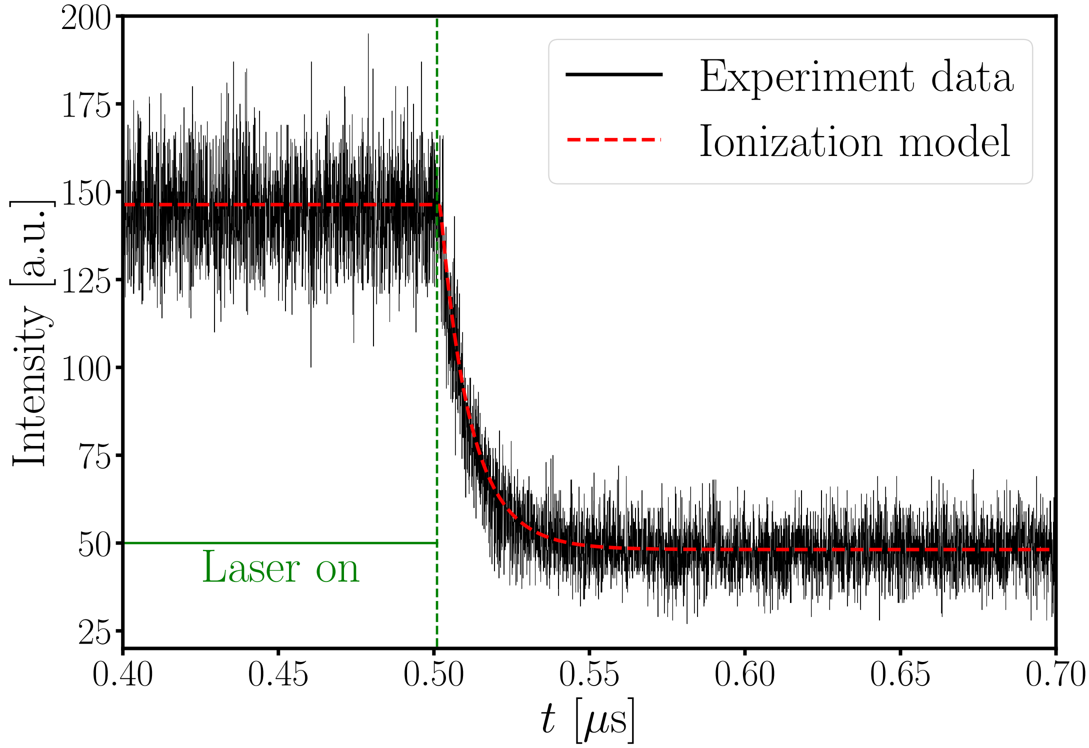

Fig. 3.17: Fluorescence lifetime measurement for a single NV center. Once the excitation is switched of the fluorescence rapidly decays with a lifetime of 12 ± 2 ns.

energy levels of the NV center. The contributions of NV^- and NV^0 in the decay process are influenced by the excitation power employed and the optical filtering conditions. In 3.17, we measure this decay time, revealing a decay behavior consistent with the predictions from the ionization model [39]. We measure a fluorescence lifetime time of 12 ± 2 ns, which is consistent with other experimental results [237], where the NV center fluorescence lifetime ranges from 10-30 ns.

The previous PL traces allow us to readout the NV center spin state in pulse experiments. We used the π-pulse length derived from the Rabi oscillations to formulate a pulsed ODMR sequence. In this pulsed ODMR approach, we initiate the NV center with a laser pulse, followed by the application of a MW pulse length equal to that of a π-pulse. Similarly to continuous-wave ODMR, we systematically vary the frequency of the MW pulse. When the MW frequency matches the transition energy, the applied π-pulse causes the initialized $|0\rangle$ state to convert to the $|1\rangle$ state, which appears darker, leading to a decrease in the optical signal. Conversely, if we are off-resonance, this conversion is less efficient, resulting in fewer population transfers to the $|1\rangle$ state. It should be noted that using a 2π-pulse would prevent observation of resonance, as it would return the initialized state to the $|0\rangle$ state. Pulsed ODMR efficiently utilizes optical and MW resources to precisely measure the resonance frequency of the NV

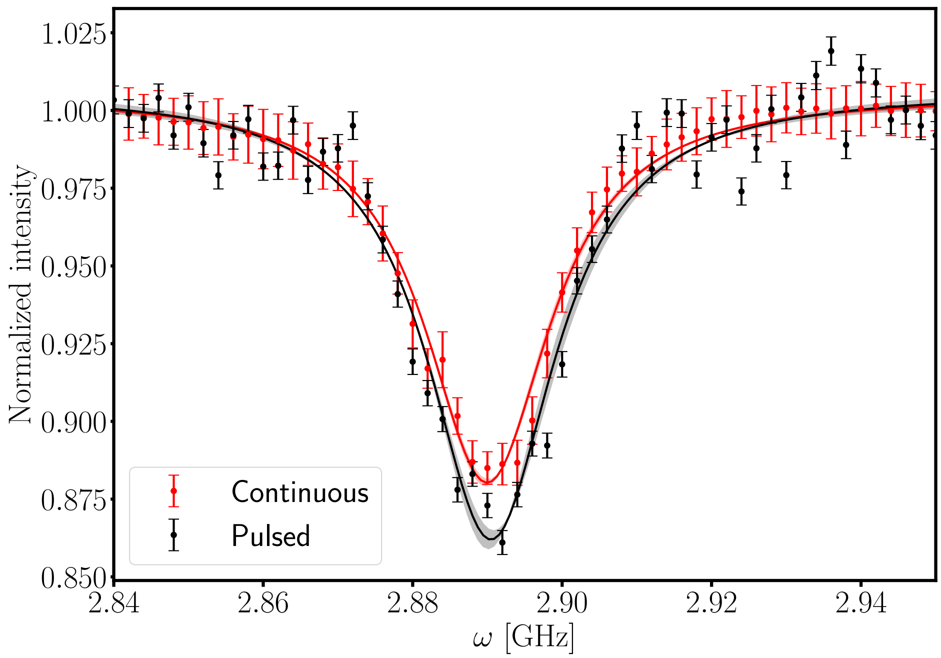

Fig. 3.18: A comparison between continuous wave ODMR and pulsed ODMR, utilizing identical laser and microwave power, reveals an enhanced contrast of $14.3 \pm 0.9\%$ for the pulsed protocol compared to the $12.4 \pm 0.3\%$ contrast observed in the continuous scheme. Notably, both sequences yield similar linewidth values.

centers. Unlike continuous-wave ODMR, where the ground state is continuously excited while simultaneously pumping it to transfer population from the bright state, pulsed ODMR separates the driving and readout processes. This allows for the application of precisely timed MW pulses, ensuring that the conversion of the bright state into the darker state occurs with optimal efficiency. This makes pulsed ODMR ultimately more sensitive and provides resonances with more contrast. A further benefit of pulsed ODMR is the ability to significantly narrow the microwave excitation bandwidth, which reduces the spectral linewidth and makes it possible to resolve hyperfine structures.

Continuous-wave ODMR involves the continuous irradiation of the sample with microwave radiation, potentially leading to undesired heating effects. In contrast, pulsed ODMR, with its intermittent application of microwave pulses, mitigates overall heating. This characteristic is particularly significant in experiments where precise temperature control is essential for accurate and reliable results. In Fig. 3.18, we present a comparison between continuous and pulsed ODMR protocols for a single NV center using identical laser excitation power and MW driving conditions. The pulsed ODMR exhibits a higher contrast of 14.3 ± 0.9 %, surpassing the contrast of 12.4 ± 0.3 % observed in the continuous wave counterpart. Despite this contrast difference, both protocols yield similar line width values. Specifically, for the pulsed protocol, we measure a line width

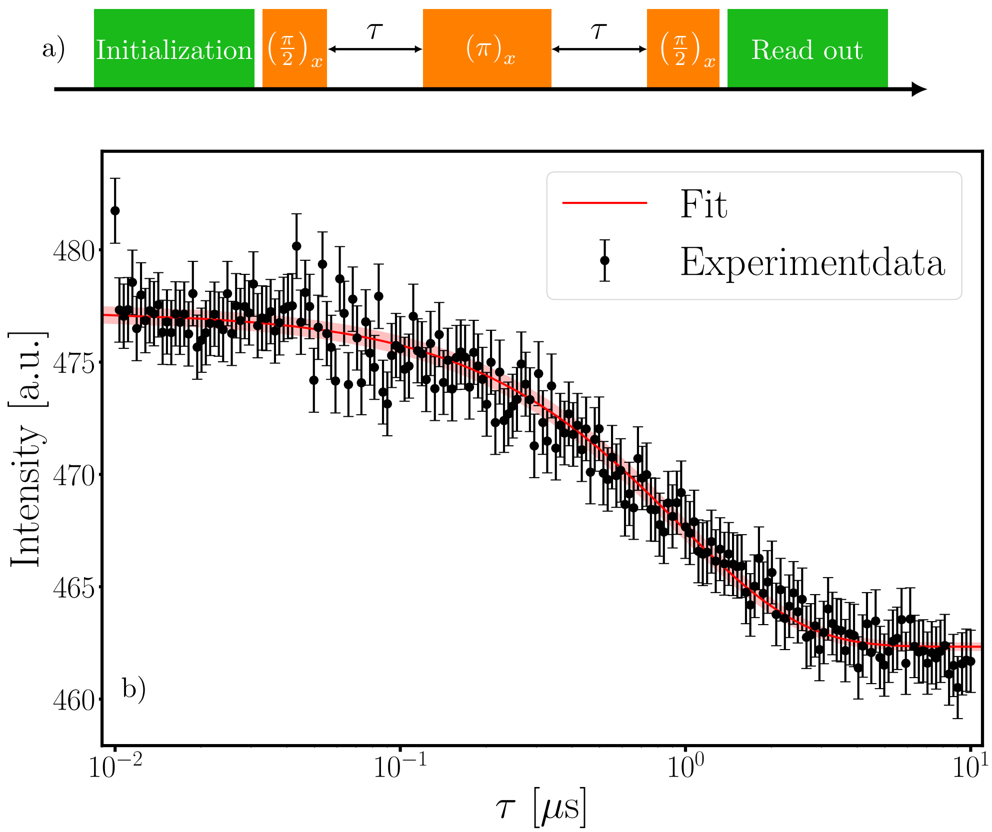

Fig. 3.19: (a) Pulse sequence to perform Rabi oscillations. The length of the laser pulse is 2 μs and the length between the pulses, the free precession time, is increased. (b) Hahn echo fluorescence decay for a single NV center, for which we measured $T_2^{\mathrm{Echo}} = 940 \pm 40$ ns

of $\Delta\nu = 21 \pm 1$ MHz, while the continuous experiment produces a comparable value of $\Delta\nu = 20.4 \pm 0.6$ MHz.

In the next characterization measurement, we will assess the coherence time T_2^{Echo} of the NV center using a Hahn Eco experiment. A Hahn echo is a dynamical decoupling sequence commonly used in the context of NMR and electron spin resonance (ESR) [54] to protect the spin dynamics and extend its bare coherence time T_2^{Rabi}. Unlike quantum systems operating at lower temperatures, room-temperature systems face significant thermal noise. Therefore, exploring the coherence times in room-temperature systems is particularly relevant. In Fig. 3.19(a), we present a schematic of the Hahn echo sequence. Initially, the spin of the NV center is prepared in the $|0\rangle$ state. Subsequently, a $\pi/2$-pulse is delivered to induce a 90-degree rotation of the spin. Following this, the spin evolves freely during a precession time τ. A subsequent π-pulse flips the spin, and after another precession period τ, a second $\pi/2$-pulse is applied before the spin state is read out. The second free precession period helps to cancel out any uncontrolled phase. Experimental data shown in Fig. 3.19(b) is obtained by varying τ until the phase relation is randomized and the spin signal saturates, indicating a completely mixed

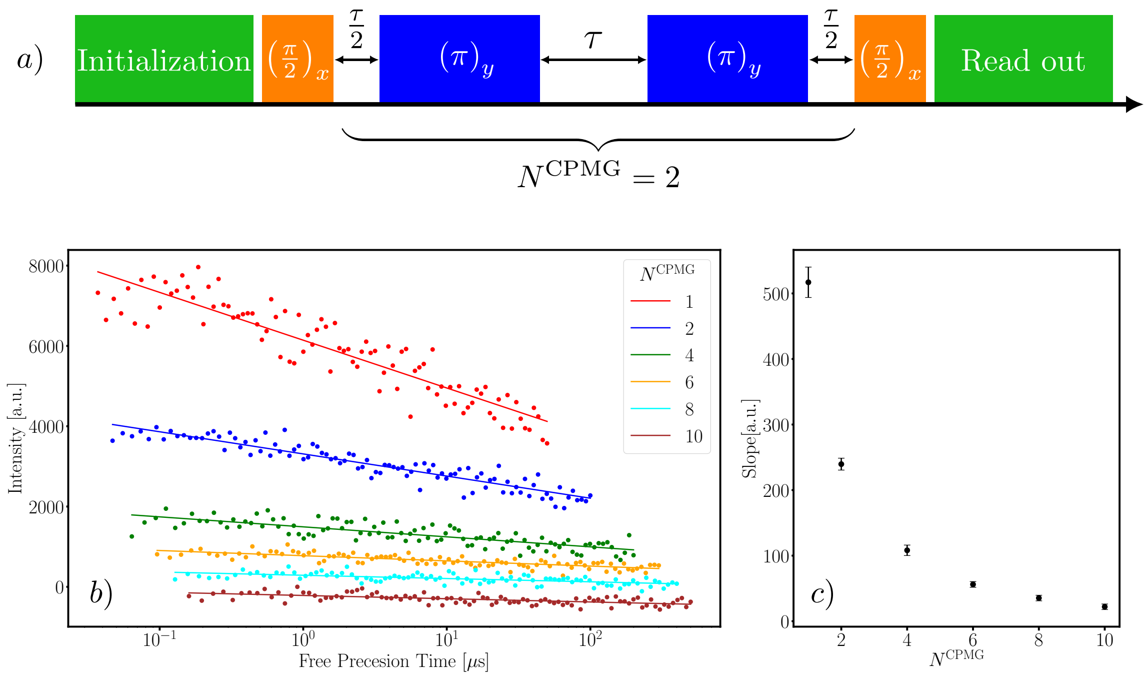

Fig. 3.20: (a) Pulse sequences for the CPMG spin-echo sequence, where N^{CPMG} is the number of refocusing pulses. (b) Examples of CPMG measurements for different N^{CPMG}. The arbitrary units of the y scale correspond to intensity, but to visualize the curves together we have modified their offset. (c) Extracted slope for all CPMG scans.

state. Fitting the data to an exponential decay yields to an extended coherence time of $T_2^{\text{Echo}} = 940 \pm 40$ ns. This enhancement compared to the measured intrinsic T_2^{Rabi} is attributed to the spin refocusing achieved by the Hahn echo sequence, which effectively reduces dephasing caused by low-frequency noise. It is important to note that potential contributions from nuclear spins, such as ^{13}C, and any associated electron spin echo envelope modulation effects are inherently reflected in the measured value of T_2^{Echo}.

Instead of a single refocusing pulse, multiple such refocusing pulses can be applied to further extend the spin coherence time. However, performing multiple pulses of refocusing on the $+x$ axis leads to an accumulation of pulse errors. Hence, refocusing pulses about the $+y$ axis - known as the Carr-Purcell-Meiboom-Gill (CPMG) spin-echo pulse sequence – are more advantageous [238, 239]. For the CPMG pulse sequence shown in Fig. 3.20a, N^{CPMG} is the total number of $(\pi)_y$-pulses and the total free precession time of the NV spin is given by τN^{CPMG}. The CPMG pulse sequence acts as a band-pass filter: increasing the number of refocusing pulses for a fixed τ sharpens the filter, while decreasing the time τ between refocusing pulses has the effect of shifting the center of the filter to higher frequency. The center frequency of the band-pass filter is given by π/τ [240].

In Fig. 3.20b, we plot the result of CPMG sequences with an increasing number of refocusing pulses N^{CPMG}. For the same total free precession time, a larger N^{CPMG}

implies a shorter τ, and hence a larger center frequency of the CPMG filter function [241]. For $N = 1$ the CPMG sequence behaves as a Hahn echo sequence, and as N increases the slope of the curve decreases, corresponding to an increase of the NV center coherence. The arbitrary units of the y scale correspond to intensity, but to visualize the curves together we have modified their offset. In Fig. 3.20c we plot the slope values extracted from the decays, suggesting that the noise spectral density of the NV center environment reduces toward higher frequencies. We would expect a decay tendency similar to the Hahn echo experiment from Fig. 3.19, however, we were only able to observe the tendency of the dynamical decoupling sequence employing the coherence time of the NV center.

A preliminary analysis suggests that incomplete capture of the full expected decay behavior, as we did in the Hahn echo experiment, is likely attributable to limitations in the temporal resolution of the AWG during the loading of the microwave pulse sequence. Our hypothesis is that the AWG was not able to load pulse sequences of sufficient duration to capture the full decay profile as the coherence time was extended. In other words, when the coherence time increased due to additional refocusing pulses, the limited memory of the AWG prevented a complete observation of the decay, leading to an under-representation of the extended coherence behavior. Future work will focus on employing an AWG with longer sequence capacity or optimizing the current system to ensure that the entire decay process is accurately recorded with enough resolution, thereby enabling a more precise quantification of the noise spectral density.

3.6 Outlook and conclusions

Although the setup reliably detects and controls single NV centers, several aspects have been identified that could enhance the setup performance. In its current design, we are unable to accurately measure the power of the laser delivered at the MO without manipulating the setup. Our initial idea was to place a photodiode detector behind the dichroic mirror to measure the residual transmitted laser light, but the signal is too weak for accurate measurement. We have identified three solutions. The first is to use a beam splitter instead of a dichroic mirror, which would divide the incident beam, directing half to the MO and the other half to the photodiode detector. Although this approach would degrade the wavelength filtering of the signal coming from the objective, this can be addressed by incorporating higher-quality filters. This solution allows simultaneous measurement of laser power and NV center PL, enabling one to correlate fluctuations in the laser intensity with fluctuations in the NV center PL.

The second option involves adding a mechanically removable photodiode detector in the laser path to measure laser power without altering other elements of the setup. However, this method cannot be used during sample excitation because the photodiode would obstruct the excitation path.

The third, though more expensive and complex, involves positioning the same single-photon avalanche diode (SPAD) used for detecting NV center fluorescence behind the dichroic mirror to measure residual laser photons. This approach enables balanced detection, which uses two detectors and differential measurement to cancel out noise from laser fluctuations, thus improving the sensitivity of optical measurements.

Another change that could improve the setup performance in the future is to attach the piezostage to the MO rather than to the sample. If the laser beam diameter is larger than the MO aperture by at least the size of the piezo-stage scanning range ($100\times100\mu m^2$), this modification would not affect the image formation. By moving the MO instead of the sample, we effectively isolate the optical components from the sample, creating a more integrated and versatile instrument.

In contrast, moving the sample with the piezostage imposes limitations on the applications. For instance, strong electric or magnetic fields intended for the NV center could interfere with the operation of the piezo, and heating the sample might damage the piezo, necessitating additional design considerations. Separating the piezostage from the sample and integrating it with the rest of the confocal system would increase the versatility of the system. In addition, improvements could be made to other aspects, such as the positioning and control of the magnet and the stability of the optical table.

A subtle change has been identified that could potentially enhance the stability of the setup. Currently, optical elements such as the SPAD, MO, dichroic mirror, pinhole, and lenses are mounted on top of optical posts. This arrangement makes them susceptible to vibrations and instabilities. To mitigate these issues, a more robust approach would be to mount these components closer to the optical table. This would necessitate changing the excitation geometry: currently, we excite the sample from above, but this new configuration would require excitation from below. However, while this excitation geometry offers improved stability, it may not be optimal for certain applications. However, exciting the sample from the top introduces its own set of challenges. For example, there is a risk that optical oil leaks down to the piezoelectric stage, potentially causing damage if not carefully managed. However, inverting the geometry would direct any oil leakage towards the MOobjective of the microscope, which is generally less susceptible to damage from such leaks.

For future work directions, a preliminary study has been carried out to assess the biocompatibility of our setup with *magnetospirillum bacteria*. *Magnetospirillum magneticum* AMB-1 possesses magnetic organelles that generate magnetic fields. Previous research used shallow ensembles of the NV center to create magnetic images of this bacteria with a wide-field microscope [229]. We are investigating another type of magnetic bacteria, *Magnetospirillum gryphiswaldense* MSR-1, using our confocal system. This strain is easier to cultivate in the laboratory and also produces magnetic organelles of similar size. Some studies propose that applying an alternating magnetic field to these organelles can induce hysteresis losses in the magnetic organelles [242]. Repetition of magnetization and demagnetization generates heat as a result of internal friction and energy losses in the hysteresis cycle. This heat can potentially kill nearby cells or bacteria, making the NV center valuable for measuring the local temperature and magnetization of the bacteria.

In summary, in this chapter, we have designed, developed, and benchmarked a compact confocal experimental setup that effectively isolates single NV centers and demonstrates coherent spin control. The experiments conducted with this setup enable the detection of NV center magnetic resonance and the implementation of pulse sequences. This confocal system serves as a precise and important tool for a wide range of applications in quantum technologies, including the characterization of spin defects in solids, nanoscale NMR, hyperpolarization, biosensing, quantum sensing, and quantum information processing. Although further work is needed to continue to miniaturize the system and enhance its accessibility, the integration of NV center detection into a portable and compact confocal microscope streamlines experimental workflows, accelerates research progress, and broadens the scope of NV center technology.

This confocal system and the accompanying experimental work represent one of the first demonstrations of single NV center detection and control in Spain, according to published records. It opens a new research line in quantum technologies and establishes a new experimental platform for the national quantum ecosystem, which currently lacks a substantial experimental quantum workforce compared to other European countries [243]. This system has already been utilized for training students in quantum principles, and future research projects and initiatives are being proposed.

Chapter 4

Quantum machine learning

4.1 Introduction

The convergence of machine learning (ML) and quantum computing leads to the birth of quantum machine learning [244, 57, 245], which takes advantage of both information processing paradigms to provide better algorithms. This is achieved either by using ML to improve the efficiency of quantum protocols [246, 247, 248, 249, 50] or by taking advantage of quantum resources to create new paradigms with better performance [130, 250, 251, 252, 253], such as quantum neural networks (QNN). Although there are several studies comparing the expressivity of classical and quantum artificial neural networks [131, 254], the goal of beating classical ML is under critical review [138]. Recent works, in the quest for better quantum models for ML purposes, characterize and compare expressivity among different network typologies [255, 256, 257, 258, 259]. This is made possible by the emergence of unitary-based QNNs [260, 261, 262, 140, 263, 264, 265], which offer experimental feasibility on multiple quantum platforms, such as trapped ions [266, 267] and superconducting circuits [140, 268, 269, 270].

On the one hand, a perceptron-type QNN, that can be implemented as a quasi-adiabatic passage in an Ising model [262, 264, 265], expresses any continuous function as a weighted linear combination of different adjustable sigmoids based on the universal approximation theorem [271]. Correlations resulting from the entanglement among various perceptrons provide these artificial networks with at least as much power as their classical counterparts. However, the entanglement is intrinsically generated along hidden layers, and understanding its role in improving the network approximation capability in classification and regression problems remains a challenge. On the other hand, QNNs based on parametric quantum circuits, by virtue of the Solovay–Kitaev theorem [272], are universal classifiers, and are implemented in repeat-until-success [260], random circuits [261, 273], or by data re-uploading [140]. A single qubit has already been used to approximate continuous functions, specifically in the context of regression problems [274]. Quantum resources may be introduced easily and easily controllable by adding entanglement gates to the topology of the network.

Although the expressivity of all these unitary-based QNN models is fundamentally bounded by the data encoding strategy [275], we show that the maximal performance in regression tasks is conditioned by the final QNN state readout. We refer to expressivity as the ability of a quantum neural network to approximate a continuous function, that as we will see later can be quantified through Eq. (4.5). To this end, we assess the expressivity of a universal deep QNN that follows a data re-uploading strategy, employing various measurements and architectures that vary in terms of network depth and number of qubits. This construction mitigates the discrepancies attributed to the use of different models, enabling a fair comparison of networks with the same topology but distinguished by the presence of quantum resources, such as entanglement. The expressivity of the QNN is quantified by employing a partial Fourier series representation, which allows us to bound the maximal expression power of the network. In particular, we find that the maximal performance is conditioned by the final QNN state readout. With the aid of the teacher-student scheme [257], we systematically benchmark network accuracy in regression problems, showing that global measurements of the multiqubit system or the use of a final entanglement layer leads to saturation of the maximal expressive bound, optimizing the performance of the network.

The chapter is structured as follows. We begin by introducing a universal quantum regressor based on re-uploading continuous input data in Sect. 4.2, which results in a trainable QNN. In Sect. 4.3, we explain how the QNN can be implemented on an experimental platform using NV center technology. Then, in Sect. 4.4 we analytically quantify the expressivity through a partial Fourier decomposition and systematically benchmark it in deep QNN differentiated by the presence of entanglement, Sect. 4.5. The chapter ends with the main conclusions and prospective research lines in Sect. 4.6.

4.2 Deep data re-uploading QNN

We propose an encoding scheme of arbitrary normalized real functions $f(\vec{x}) \in [0,1]$ through the degrees of freedom of a set of qubits. These qubits are assumed to constitute a circuit that performs a unitary transformation of the initial state $|\phi_0\rangle$ into the final output state

$$|\phi(\vec{x})\rangle = \hat{\mathcal{U}}(\vec{x})\,|\phi_0\rangle\,, \tag{4.1}$$

by the unitary transformation $\hat{\mathcal{U}}(\vec{x})$, where $\vec{x} = (x_1, x_2, \ldots, x_n) \in \mathbb{R}^n$ are independent input variables that set the topology of the circuit. The circuit is approximated by a data re-uploading QNN with an adjustable set of parameters $\vec{\theta} = \{\vec{\theta}_1, \vec{\theta}_2, \cdots \vec{\theta}_L\}$,

$$\hat{\mathcal{U}}(\vec{x}) \simeq \hat{U}(\vec{x}, \vec{\theta}) = \prod_{l=1}^{L} \hat{\mathcal{L}}_l(\vec{x}, \vec{\theta}_l), \tag{4.2}$$

where we adopt the convention $\prod_{n=1}^{N} A_n = A_N \cdot A_{N-1} \ldots \cdot A_1$, with the dot being the standard matrix multiplication. The l-th layer is represented by the unitary transformation $\hat{\mathcal{L}}_l(\vec{x}, \vec{\theta}_l)$, with input data $\vec{x}$ and undetermined parameters $\vec{\theta}_l$. Similar to perceptron-based neural networks [262], the complexity (or interconectivity) of the network increases with the number of layers L. We choose the unitary transformation for each layer to be constituted by a single qubit SU(2) rotation with the data encoded as the rotation angle,

$$\hat{\mathcal{L}}_l(\vec{x}, \vec{\theta}_l) = \hat{R}_x(2(\vec{\omega}_l \cdot \vec{x} + \beta_l))\hat{R}_y(2\alpha_l), \tag{4.3}$$

where $\hat{R}_\gamma(2\tau) = e^{i\tau\hat{\sigma}_\gamma}$ is the rotation around the $\gamma-$axis, with $\gamma \equiv \{x, y, z\}$ and $\hat{\sigma}_\gamma$ representing the standard Pauli matrices. For every layer, there are $n+2$ adjustable parameters $\vec{\theta}_l = \{\vec{\omega}_l, \beta_l, \alpha_l\} \in \{\mathbb{R}^n, \mathbb{R}, \mathbb{R}\}$, and the scalar product is defined as $\vec{\omega}_l \cdot \vec{x} = \omega_{l,1}x_1 + \cdots + \omega_{l,n}x_n$. Thus, the complexity of the circuit increases linearly with the dimension of the input data.

The output of the QNN, $F(\vec{x}, \vec{\theta})$, is used to approximate a target function $f(\vec{x})$, and it is obtained by calculating the expectation value of an observable $\hat{\mathcal{M}}$ in the output state $|\phi(x)\rangle$,

$$F(\vec{x}, \vec{\theta}) = |\langle\phi(\vec{x})| \hat{\mathcal{M}} |\phi(\vec{x})\rangle| \to f(\vec{x}). \tag{4.4}$$

Initially, we choose $\hat{\mathcal{M}} = \hat{\sigma}_z$, such that the mapping is done in the excitation amplitude of the qubit. However, more sophisticated mappings are possible, e.g., $\hat{\mathcal{M}} = \hat{O} = u_o\mathbb{I} + u_x\hat{\sigma}_x + u_y\hat{\sigma}_y + u_z\hat{\sigma}_z$, with $u_o, u_x, u_y, u_z \in \mathbb{R}$ also trainable parameters. The optimal network topology is constituted by the set of parameters $\vec{\theta}$ that minimizes a particular cost function $\mathcal{C}$, i.e., $\vec{\theta}_T = \mathrm{argmin}_{\vec{\theta}}\, \mathcal{C}(f; \vec{\theta})$. For the considered regression problems, we use the squared error loss function, which corresponds to

$$\mathcal{C}(f; \vec{\theta}) = \frac{1}{K}\sum_{k=1}^{K}\left[F(\vec{x}^k, \vec{\theta}) - f(\vec{x}^k)\right]^2, \tag{4.5}$$

where K is the total input samples of $\vec{x}$. The optimal parameters $\vec{\theta}_T$ for a particular target function are obtained minimizing Eq. (4.5) using gradient descent optimization, with $\vec{\theta}$ initialized randomly. To explore a larger region of the parameter landscape, the minimization is repeated R times.

Note that the topology given by Eq. (4.3) is able to connect any two states on the Bloch sphere. However, in order to capture non-trivial patterns in the original data $\vec{x}$ and to approximate an arbitrary real function $f(\vec{x})$, this data $\vec{x}$ needs to be reintroduced in the subsequent layers [140]. Meanwhile, the complexity and approximation power of the network can be increased by extending the model from one qubit to an arbitrary number of qubits, Q. We first consider that the qubits that form the QNN do not interact. Thus, the total transformation is the outer product of the unitary transformations of all qubits after each layer, such that

$$\hat{U}(\vec{x}, \vec{\theta}) = \prod_{l=1}^{L}\bigotimes_{q=1}^{Q}\hat{\mathcal{L}}_{l,q}(\vec{x}, \vec{\theta}_{l,q}), \tag{4.6}$$

where each qubit has a set of adjustable parameters $\vec{\theta}_{l,q} = \{\vec{\omega}_{l,q}, \beta_{l,q}, \alpha_{l,q}\}$ and the approximation of $f(\vec{x})$ is done via $\hat{\mathcal{M}} = \hat{\sigma}_z^{tot}$, with $\hat{\sigma}_z^{tot} = \sum_{q=1}^{Q}\hat{\sigma}_z^q$.

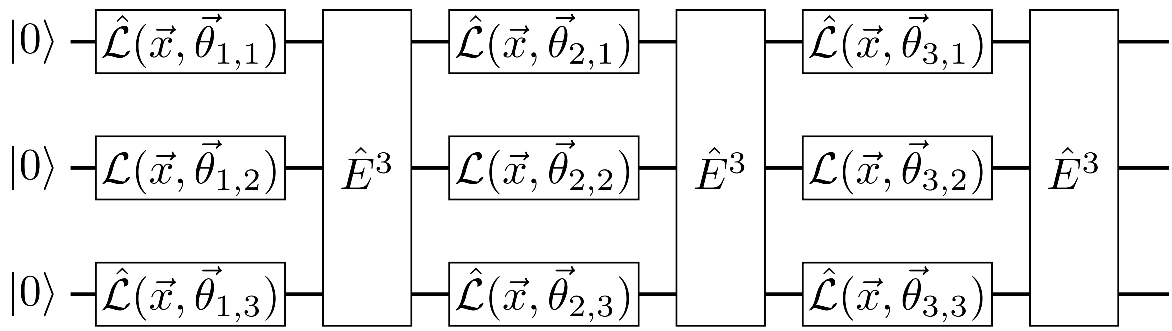

Fig. 4.1: Quantum circuit diagram of a data-reuploading quantum neural network (QNN) with three qubits and three layers. The circuit includes inter-layer entanglement and data reuploading mechanisms at each layer.

The QNN has a total number $N_p = LQ(n+2)$ of adjustable parameters $\vec{\theta}$. We now introduce entangling gates at each layer among the different qubits in the QNN model described by Eq. (4.6),

$$\hat{U}(\vec{x},\vec{\theta}) = \prod_{l=1}^{L} \hat{E}^l \cdot \left(\bigotimes_{q=1}^{Q} \hat{\mathcal{L}}_{l,q}(\vec{x},\vec{\theta}_{l,q}) \right). \tag{4.7}$$

Although there are different ways of introducing entanglement to enrich the network topology (by modifying either the entangling gates at each layer or the entanglement allocation), for simplicity, we consider here a fixed gate applied at each layer. In particular, to emphasize the role of entanglement, we define $\hat{E}^l$ as a gate that is maximally entangling, which produces a generalization of Bell states when applied to the computational basis [276],

$$\hat{E}^l = \prod_{i=1}^{Q-1} \left((\bigotimes_{i-1} \mathbb{I}) \otimes \hat{E}_2 \otimes (\bigotimes_{Q-i-1} \mathbb{I}) \right), \tag{4.8}$$

with

$$\hat{E}_2 = \frac{1}{\sqrt{2}}(\mathbb{I}\otimes\mathbb{I} + i\sigma_x \otimes \sigma_y). \tag{4.9}$$

Fig. 4.1 represents an scheme of this unitary evolution for a QNN with $Q = 3$ and $L = 2$. Note that the amount of entanglement is introduced as a fixed quantity, i.e., the gates in Eq. (4.8) do not introduce new adjustable parameters. To distinguish different architectures, we label the topology of the QNN as $\mathcal{A}_0(L,Q)$ ($\mathcal{A}_1(L,Q)$) with the subscripts 0 (1) indicating the absence (presence) of entangling gates. Two architectures, $\mathcal{A}_0(L,Q)$ and $\mathcal{A}_1(L,Q)$, contain the same number N_p of variational parameters $\vec{\theta}$ and only differ by the incorporation of entanglement. Consequently, we are able to evaluate exclusively the role of this quantum resource in the performance of the QNN.

4.3 QNNs with NV centers

In this section, we discuss the experimental implementation of the unitary evolution described by (4.7) using NV centers, aiming to construct the quantum neural network (QNN). To build each layer, we apply the rotation operators $\hat{R}_x$ and $\hat{R}_y$. The rotation gates $\hat{R}_x$ and $\hat{R}_y$ can be realized by applying resonant microwave fields along the x- and y-axes, which interact with the NV center electron spin. To perform a rotation $\hat{R}_x(\theta)$ about the x-axis by an angle θ, we introduce a microwave field of appropriate frequency and phase, tuned to drive transitions between the $|0\rangle$ and $|1\rangle$ states, effectively defining a qubit within this two-level subspace.

To drive the spin from $|0\rangle \rightarrow |1\rangle$ the perturbing Hamiltonian must have off-diagonal matrix elements, thus $\hat{H}_{int}$ must have terms proportional to $\hat{\sigma}_x$ or $\hat{\sigma}_y$, which means that the $B(t)$ generated by the antenna is contained in the x-y plane. We can write the Hamiltonian for the $|0\rangle$ and $|1\rangle$ states:

$$
\begin{aligned}
\hat{H} &= \hat{H}_0 + \hat{H}_{int}, \\
\hat{H}_0 &= \frac{\omega_o}{2}\hat{\sigma}_z, \\
\hat{H}_{int} &= -\frac{\gamma_e B_x(t)}{2}\hat{\sigma}_x - \frac{\gamma_e B_y(t)}{2}\hat{\sigma}_y,
\end{aligned}
\tag{4.10}
$$

where we have considered $\hbar = 1$. Here $\hat{H}_0$ represents the static Hamiltonian that determines the energy splitting between the $|0\rangle$ and $|1\rangle$ states, with $\omega_0 = D + \gamma_e B_z$ as the associated resonance frequency. In this expression, γ_e is the gyromagnetic ratio of the NV center electron spin, and $\vec{B}\perp$ represents the perpendicular component of the magnetic field applied in the x-y plane. For the specific case of a rotating transverse field of constant amplitude:

$$
\begin{aligned}
B_x(t) &= B\cos(\omega t + \phi) \\
B_y(t) &= B\sin(\omega t + \phi) \implies \\
\hat{H}_{int}(t) &= -\frac{\gamma_e B}{2}(\cos(\omega t + \phi)\hat{\sigma}_x + \sin(\omega t + \phi)\hat{\sigma}_y) = \\
&= \frac{\Omega}{2}(e^{-i(\omega t+\phi)}\sigma_+ + e^{i(\omega t+\phi)}\sigma_-).
\end{aligned}
\tag{4.11}
$$

Where B is the amplitude of the driving magnetic field, ω its frequency, ϕ its phase and $\Omega = \gamma_e B$ is the Rabi frequency. In a geometrical picture, if we switch to a rotating frame co-rotating with the applied field, the Hamiltonian becomes effectively static in this frame, simplifying the integration of the Schrödinger equation. To achieve this, we move to a rotating frame about the z-axis by an angle ωt, where ω is the frequency of the rotating field. The unitary transformation to this rotating frame is given by:

$$
\hat{U}_{RF} = \exp\left\{-i\frac{\omega t}{2}\hat{\sigma}_z\right\}
\tag{4.12}
$$

Applying this transformation to the Hamiltonian yields the effective Hamiltonian in the rotating frame. The Hamiltonian in the rotating frame, $\hat{H}_{RF}$, is obtained by transforming the original Hamiltonian $\hat{H}$ as:

$$\hat{H}_{RF} = \hat{U}_{\mathrm{RF}} \hat{H} \hat{U}^{\dagger}_{\mathrm{RF}} - i \hat{U}_{\mathrm{RF}} \frac{d}{dt} \hat{U}^{\dagger}_{\mathrm{RF}} \tag{4.13}$$

Using this transformation, we obtain:

$$\hat{H}_{RF} = -\frac{\Delta}{2}\hat{\sigma}_z + \frac{\Omega}{2}(e^{-i\phi}\hat{\sigma}_+ + e^{i\phi}\hat{\sigma}_-) = -\frac{\Delta}{2}\hat{\sigma}_z + \frac{\Omega}{2}(\cos(\phi)\hat{\sigma}_x + \sin(\phi)\hat{\sigma}_y) \tag{4.14}$$

Where we have defined $\Delta = \omega - \omega_0$, which represents the detuning, or the difference between the frequency of the rotating field and the magnetic resonance frequency. This detuning parameter indicates how far the system is from resonance.

We can generalize this result by rewriting

$$\hat{H}_{RF} = \frac{1}{2}\vec{\Omega} \cdot \vec{\hat{\sigma}} \implies \vec{\Omega} = -\Delta \vec{e}_z + \Omega(\cos(\phi)\vec{e}_x + \sin(\phi)\vec{e}_y), \tag{4.15}$$

where $\vec{\hat{\sigma}} = \hat{\sigma}_x \vec{e}_x + \hat{\sigma}_y \vec{e}_y + \hat{\sigma}_z \vec{e}_z$. This allows to define a generalized Rabi frequency

$$\Omega_o = \left|\vec{\Omega}\right| = \sqrt{\Omega^2 + \Delta^2}. \tag{4.16}$$

The evolution of the system is given by the unitary operator:

$$\hat{U}_{Rabi}(t) = \exp\left(-\frac{i}{2}(\vec{\Omega} \cdot \vec{\hat{\sigma}})t\right). \tag{4.17}$$

This unitary evolution corresponds directly to the definition of single-qubit rotations

$$\hat{R}_{\gamma}(2\tau) = \exp(i\tau\hat{\sigma}_{\gamma}), \tag{4.18}$$

where $\hat{\sigma}_{\gamma}$ represents the Pauli matrix corresponding to the rotation axis $\gamma \in \{x, y, z\}$, and τ is the rotation angle.

To generate a desired rotation, we can control various parameters: the de-tuning Δ of the MW field the Rabi frequency Ω (which depends on the microwave power), the duration of the microwave field application t and the phase ϕ of the microwave field. By tuning these parameters appropriately, we can precisely manipulate the spin state and achieve the desired rotation. In the framework of a QNN, these Hamiltonian parameters Δ, Ω, t, ϕ serve as analogues of the trainable parameters of the network, such as weights, biases, and inputs $\vec{\omega}, \beta, \alpha, x$ which can be optimized by gradient descent to minimize a cost function.

After initializing the NV center with a laser pulse into the state $|0\rangle$, the final state after a subsequent microwave evolution, governed by the unitary operator $\hat{U}_{\mathrm{Rabi}}(t)$, is given by:

$$U_{Rabi}(t)\,|0\rangle = [\cos\left(\frac{\Omega_o t}{2}\right) + i\frac{\Delta}{\Omega_o}\sin\left(\frac{\Omega_o t}{2}\right)]\,|0\rangle - ie^{-i\phi}\frac{\Omega}{\Omega_o}\sin\left(\frac{\Omega_o t}{2}\right)|1\rangle \tag{4.19}$$

This describes the time evolution of the initial state $|0\rangle$ under the influence of the microwave field.

To generate entangling gates $\hat{E}^l$, we simply concatenate two-qubit entangling gates between NV centers. Entanglement between NV centers has previously been achieved experimentally. In [109], entanglement between NV center spins was demonstrated at a distance of approximately 25 nm. At these distances, magnetic dipole coupling is strong enough to achieve high-fidelity entanglement while still enabling individual spin addressing using super-resolution optical microscopy. In addition, efficient schemes for the preparation of entangled states between two separated nitrogen-vacancy (NV) centers in a spin-mechanical system have been developed via a dissipative quantum dynamical process [277]. Other approaches rely on engineered MW pulses using optimal control and dynamical decoupling sequences to achieve high-fidelity entanglement between NV centers [110].

Although the necessary ingredients for implementing quantum neural networks (QNNs) with NV centers are available, several experimental limitations must be considered when scaling the QNN to a larger number of qubits. To entangle multiple NV centers, they need to be placed close together, but this proximity introduces challenges in optically addressing them for readout and initialization. Additionally, not all pairs of NV centers can be entangled, as their positions are fixed within the diamond lattice, which limits entanglement to neighboring pairs. The requirement for NV centers to be close together can also negatively impact their coherence times because of strong dipole interactions between the centers, leading to decoherence and noise, which can degrade gate fidelity. Addressing these challenges requires continued research in advanced control sequences, algorithms, and improved fabrication and experimental techniques to mitigate these effects and enable the scaling of QNNs with NV centers.

In this chapter, we will not consider these practical effects in our investigation of QNNs, since our focus is on the theoretical framework and the necessary components for their implementation. While experimental limitations are crucial for real-world applications, the primary objective here is to explore the design, functionality, and potential of QNNs, assuming ideal conditions for gate operations and qubit interconnectivity.

4.4 Approximation power

4.4.1 Fourier decomposition of the QNN unitary

In order to characterize the expressivity of the QNN we adopt an agnostic approach and consider qubits as mathematical objects, avoiding any reference to a particular quantum platform. Using the Fourier decomposition of the unitary transformation produced by the QNN and compute the number of harmonics that do not vanish after encoding the output state through the observable $\hat{\mathcal{M}}$. We introduce a novel strategy for bounding the expressivity of the QNN [275, 259] that enables us to compute the Fourier amplitudes and identify zero coefficients.

For each qubit, the single layer unitary transformation given by Eq. (4.3) is decomposed into the fundamental frequencies $\pm\vec{\omega}_{l,q}$ of the qubit,

$$\begin{aligned}
\hat{\mathcal{L}}_{l,q}(\vec{x},\vec{\theta}_l) &= R_x(2(\vec{\omega}_{l,q}\cdot\vec{x}+\beta_{l,q}))R_y(2\alpha_{l,q}) = \\
&= \begin{pmatrix} \cos(\vec{\omega}_{l,q}\cdot\vec{x}+\beta_{l,q}) & -i\sin(\vec{\omega}_{l,q}\cdot\vec{x}+\beta_{l,q}) \\ -i\sin(\vec{\omega}_{l,q}\cdot\vec{x}+\beta_{l,q}) & \cos(\vec{\omega}_{l,q}\cdot\vec{x}+\beta_{l,q}) \end{pmatrix} \begin{pmatrix} \cos(\alpha_{l,q}) & -\sin(\alpha_{l,q}) \\ \sin(\alpha_{l,q}) & \cos(\alpha_{l,q}) \end{pmatrix} = \\
&= \hat{T}^+_{l,q}e^{i\vec{\omega}_{l,q}\cdot\vec{x}} + \hat{T}^-_{l,q}e^{-i\vec{\omega}_{l,q}\cdot\vec{x}},
\end{aligned} \tag{4.20}$$

where

$$\hat{T}^+_{l,q} = \frac{1}{2}\begin{pmatrix} t^-_{l,q} & -t^+_{l,q} \\ -t^-_{l,q} & t^+_{l,q} \end{pmatrix} e^{i\beta_{l,q}}, \quad \hat{T}^-_{l,q} = \frac{1}{2}\begin{pmatrix} t^+_{l,q} & t^-_{l,q} \\ t^+_{l,q} & t^-_{l,q} \end{pmatrix} e^{-i\beta_{l,q}}, \tag{4.21}$$

with $t^{\pm}_{l,q} = \cos(\alpha_{l,q}) \pm \sin(\alpha_{l,q})$. We use this expression to decompose a network into products of this sum. Then, we write these products as a factorization of single layers gates:

$$\hat{U}(\vec{x},\vec{\theta}) = \prod_{l=1}^{L}\bigotimes_{q=1}^{Q}(\hat{T}^+_{l,q}e^{i\vec{\omega}_{l,q}\cdot\vec{x}} + \hat{T}^-_{l,q}e^{-i\vec{\omega}_{l,q}\cdot\vec{x}}) = \prod_{l=1}^{L}\hat{u}_l, \tag{4.22}$$

with $\hat{u}_l = \bigotimes_{q=1}^{Q}(\hat{T}^+_{l,q}e^{i\vec{\omega}_{l,q}\cdot\vec{x}} + \hat{T}^-_{l,q}e^{-i\vec{\omega}_{l,q}\cdot\vec{x}})$. The harmonics generated by this transformation are combinations of $\omega_{l,q}$ with positive or negative sign. To compute the Kronecker product, we define $P = P(Q)$ as the set of all possible sign permutations of Q terms. For example, for $Q = 3$ we have

$$P(3) = \{\{+,+,+\},\{+,+,-\},\{+,-,-\},\cdots,\{-,-,-\}\}. \tag{4.23}$$

We denote P^k the k-th element in P, and P^k_n, the n-th element in P^k with $P^k_n = +$ or $-$ for $k = 1,...,2^N$ and $n = 1,...,N$.

Using this notation, and defining $\hat{T}_{l,q}[\pm] = \hat{T}^{\pm}_{l,q}$, we express the action of a single layer as

$$\hat{u}_l(\vec{x},\vec{\theta}) = \sum_{k=1}^{2^Q}\left(\bigotimes_{q=1}^{Q}\hat{T}_{l,q}\left[P^k_q\right]\right)\exp\left\{\left(i\sum_{q=1}^{Q}P^k_q\vec{\omega}_{l,q}\vec{x}\right)\right\} = \sum_{k=1}^{2^Q}\hat{B}^k_l e^{i\vec{m}^k_l\cdot\vec{x}}, \tag{4.24}$$

with $\hat{B}^k_l = \hat{B}^k_l(\alpha,\beta) = \bigotimes_{q=1}^{Q}\hat{T}_{l,q}\left[P^k_q\right]$ and $\vec{m}^k_l = \vec{m}^k_l(\vec{\omega}) = (\sum_{q=1}^{Q}P^k_q\vec{\omega}_{l,q})$. For illustration purposes, in the case $Q = 3$, ignoring the l subindex in $\hat{T}^{\pm}_{l,q}$ and $\vec{\omega}_{l,q}$ for clarity,

$$\begin{aligned}
\hat{u}_l(\vec{x},\vec{\theta}) &= (\hat{T}^+_3e^{i\vec{\omega}_3} + \hat{T}^-_3e^{-i\vec{\omega}_3}) \otimes (\hat{T}^+_2e^{i\vec{\omega}_2} + \hat{T}^-_2e^{-i\vec{\omega}_2}) \otimes (\hat{T}^+_1e^{i\vec{\omega}_1} + \hat{T}^-_1e^{-i\vec{\omega}_1}) = \\
&= \hat{T}^+_3 \otimes \hat{T}^+_2 \otimes \hat{T}^+_1 e^{i(\vec{\omega}_3+\vec{\omega}_2+\vec{\omega}_1)\cdot\vec{x}} + \hat{T}^+_3 \otimes \hat{T}^+_2 \otimes \hat{T}^-_1 e^{i(\vec{\omega}_3+\vec{\omega}_2-\vec{\omega}_1)\cdot\vec{x}} +
\end{aligned}$$

$$+ \quad \hat{T}_3^+ \otimes \hat{T}_2^- \otimes \hat{T}_1^- e^{i(\vec{\omega}_3 - \vec{\omega}_2 - \vec{\omega}_1)\cdot\vec{x}} + \cdots + \hat{T}_3^- \hat{\otimes} \hat{T}_2^- \otimes \hat{T}_1^- e^{i(-\vec{\omega}_3 - \vec{\omega}_2 - \vec{\omega}_1)\cdot\vec{x}} \quad (4.25)$$

Introducing entanglement on these architectures leads to a similar decomposition as Eq. (4.24), replacing the expansion coefficients $\hat{B}_l^k \to \hat{E}^l \hat{B}_l^k$, while the frequency spectrum remains the same.

Introducing the expression for $\hat{u}_l$ obtained in Eq. (4.24) into Eq. (4.22), the action of the whole transformation produced by the QNN is written as a sum of harmonic terms,

$$\begin{aligned} \hat{U}(\vec{x}, \vec{\theta}) &= \prod_{l=1}^{L} \hat{u}_l = \prod_{l=1}^{L} \sum_{k=1}^{2^Q} \hat{B}_l^k e^{i\vec{m}_l^k \cdot x} = \\ &= \sum_{j=1}^{(2^Q)^L} \left(\prod_{l=1}^{L} \hat{B}_l^{W_l^j} \right) \exp\left\{ \left(i \sum_{l=1}^{L} \vec{m}_l^{W_l^j} \cdot \vec{x} \right) \right\} = \sum_{j=1}^{2^{LQ}} \hat{C}_j e^{i\vec{M}_j \cdot \vec{x}}, \end{aligned} \quad (4.26)$$

where we have defined the expansion coefficients $\hat{C}_j = \hat{C}_j(\alpha, \beta) = \prod_{l=1}^{L} \hat{B}_l^{W_l^j}$, the Fourier frquencies $\vec{M}_j = \vec{M}_j(\vec{\omega}) = \sum_l \vec{m}_l^{W_l^j}$ and the indices W_l^j are defined in a similar fashion as P; we take $W(L, Q)$ as the set of ordered combinations of L elements which take values in $\{1, 2, ..., 2^Q\}$. For $L = 3$ and $Q = 2$,

$$W(3, 2) = \{\{1, 1, 1\}, \{1, 1, 2\}, \{1, 2, 1\}, ..., \{4, 4, 3\}, \{4, 4, 4\}\}. \quad (4.27)$$

We denote with W^j the $j - th$ element in W, and W_l^j the l-th element in W^j. For the previous example $W^2 = \{1, 1, 2\}$ and $W_1^2 = 1$. Alternatively, defining the element $X_{l,q}^j = P_q^{W_l^j}$, which takes the values $\pm$, we can write $\hat{C}_j = \prod_{l=1}^{L} \bigotimes_{q=1}^{Q} \hat{T}_{l,q}[X_{l,q}^j]$ and $\vec{M}_j(\vec{\omega}) = \sum_{l=1}^{L} \sum_{q=1}^{Q} X_{l,q}^j \vec{\omega}_{l,q}$. From the expansion in Eq. (4.26), we deduce that the total number of harmonics in the expansion of the unitary $\hat{U}_{L,Q}(\vec{x}, \vec{\theta})$ is $\mathcal{N}_p = 2^{LQ}$.

In Eq.(4.26) the product of the unitaries in each layer has been rewritten as a single summation that accounts for the total number of terms $\mathcal{N}_h$ in the partial Fourier decomposition of the network. The spectrum of the QNN has a size of $\mathcal{N}_h = 2^{LQ}$, and depends solely on the data encoding strategy, regardless of the presence of entanglement, which only affects the values of the matrix coefficients $\hat{C}_j$ of the Fourier series [275].

4.4.2 Fourier decomposition of the output of the QNN

The mapping of the QNN into the output function is obtained performing a measurement in the evolved system according to Eq. (4.4),

$$\begin{aligned} F(\vec{x}, \vec{\theta}) &= \langle 0 | \hat{U}^\dagger \hat{\mathcal{M}} \hat{U} | 0 \rangle = \\ &= \sum_{i=1}^{2^{LQ}} \sum_{j=1}^{2^{LQ}} \langle 0 | \hat{C}_i^\dagger \hat{\mathcal{M}} \hat{C}_j | 0 \rangle e^{i(\vec{M}_j - \vec{M}_i)\cdot\vec{x}} = \sum_{i=1}^{2^{LQ}} \sum_{j=1}^{2^{LQ}} \langle 0 | \hat{C}_i^\dagger \hat{\mathcal{M}} \hat{C}_j | 0 \rangle e^{i\vec{\Omega}_{j,i} \cdot \vec{x}}. \end{aligned} \quad (4.28)$$

We want to write the double sum in a single sum in order to count the total number of harmonics in the expansion. Some frequencies may appear more than once, meaning that $\vec{M}_j - \vec{M}_i = \vec{M}_k - \vec{M}_n$ for some combination of $i, j \neq k, n$. We can group together the 2^{2LQ} terms arising from the double sum of Eq. (4.28) and analyze all the possible values that $\vec{M}_j(\vec{\omega}) - \vec{M}_i(\vec{\omega})$ can yield,

$$\vec{\Omega}_{j,i} = \vec{M}_j - \vec{M}_i = \sum_{l=1}^{L}\sum_{q=1}^{Q}(X_{l,q}^j - X_{l,q}^i)\vec{\omega}_{l,q}. \tag{4.29}$$

Since $X_{l,q}^j = \{1, -1\}$, the difference $X_{l,q}^j - X_{l,q}^i$ can take the values $\{2, 0, -2\}$. For each frequency in Eq. (4.29), there exist three possible coefficients, and since there are LQ frequencies $\vec{\omega}_{l,q}$, we have 3^{LQ} different harmonic frequencies $\vec{\Omega}_{j,i}$. As previously, let us consider $R(D)$, with $D = LQ$, the group of the permutations $\{2, 0, -2\}$ of R elements, such as $R = \{\{2, 2, ..., 2\}, \{2, 2, ..., 0\}, \{2, 2, ..., -2\}, ..., \{-2, -2, ..., -2\}\}$. In this sense, R^k is the k-th element in R and R_d^k the d-th element in R^k, with $k = 1, ..., 3^D$ and $d = 1, ..., D$. Therefore, we can equivalently consider

$$\vec{\Omega}_{j,i} = \sum_{q=1}^{Q}\sum_{l=1}^{L}(X_{l,q}^j - X_{l,q}^i)\vec{\omega}_{l,q} \qquad \longleftrightarrow \qquad \vec{\Omega}_k = \sum_{d=1}^{D} R_d^k \vec{\omega}_d^*. \tag{4.30}$$

Defining $\vec{\omega}_d^*$ through a bijection with $\vec{\omega}_{l,q}$, such that $\vec{\omega}_1^* = \vec{\omega}_{1,1}$, $\vec{\omega}_2^* = \vec{\omega}_{1,2}$ ... $\vec{\omega}_D^* = \vec{\omega}_{L,Q}$. This allows us to rewrite Eq. (4.28), as a single sum with 3^{LQ} terms,

$$F(\vec{x}, \vec{\theta}) = \sum_{k=1}^{3^{LQ}} \langle 0| \hat{A}(R^k) |0\rangle \cdot \exp\left(i \sum_d R_d^k \vec{\omega}_d^* \cdot \vec{x}\right) = \sum_{k=1}^{3^{LQ}} c_k e^{i\vec{\Omega}_k \cdot \vec{x}}, \tag{4.31}$$

with $\hat{A}(R^k) = \hat{A}^k$ an operator that comes from the combination of $\hat{C}_i^\dagger \hat{\mathcal{M}} \hat{C}_j$ and is associated to one of the 3^{LQ} frequencies. For example, the coefficient $\hat{A}(\{2, 0, -2, 0\})$ is associated with the frequency $2\vec{\omega}_1^* - 2\vec{\omega}_3^*$ (or, equivalently, $2\vec{\omega}_{1,1} - 2\vec{\omega}_{2,1}$). Some of the coefficients $c_k = c_k(\alpha, \beta) = \langle 0| \hat{A}^k |0\rangle$ might be zero, and thus the sum only contains $N_h \leq 3^{LQ}$. Our goal in the next section is to determine the number of non-vanishing coefficients depending on the operator that is being used to map the QNN to the output function.

The number of terms in the expansion of $F(\vec{x}, \vec{\theta})$ given in Eq.(4.31) is $N_h \leq 3^{LQ}$. Equation (4.31) describes the family of functions that a given QNN can learn through two interrelated characteristics: the spectrum of Fourier frequencies $\vec{\Omega}_j \in \mathbb{R}^n$ accessible by the quantum model, and the tunability, that refers to the number of expansion coefficients $c_j \in \mathbb{R}$ that a class of QNN can control independently, and defines the set of attainable functions. It is important to notice that these two characteristics are fully determined by the $N_p = LQ(n + 2)$ topological hyper-parameters $\vec{\theta}_{l,q}$, and each set plays separate roles; $\vec{\omega}_{l,q}$ controls the frequency spectrum, while $\alpha_{l,q}$ and $\beta_{l,q}$, the amplitude of each Fourier term c_j. Crucially, the number of non-zero expansion coefficients N_h depends on the observable $\hat{\mathcal{M}}$ used to map the function $F(\vec{x}, \vec{\theta}) \to f(\vec{x})$.

Note that, in general, $N_h \gg N_p$. As a result, only a subset of both c_j and Ω_j may be totally adjustable, while the rest are constrained. The variational formulation of a specific machine learning problem is equivalent to finding the best fit for the Fourier decomposition. While the optimal combination depends on the specific problem to be solved –i.e., $f(\vec{x})$–, the expressivity of the network is determined by the topological parameters N_p and N_h. As we will show, a final global readout of the network leads to a larger set N_h compared to local readouts in a non-entangling QNN. This enriches the accessible functions that the QNN can access, leading to an enhancement of the network accuracy when approximating $f(\vec{x})$.

In the upcoming sections, we determine the number of non zero expansion coefficients N_h for different encoding strategies $\hat{\mathcal{M}}$ and network topologies.

4.4.3 One qubit network

For the particular case of a single qubit architecture $\mathcal{A}_0(L,1)$, we recursively count the number of vanishing $c_j(\alpha,\beta)$. According to Eq. (4.20), L layers acting on a single qubit produce the transformation

$$\hat{v} = \prod_{l=1}^{L} (\hat{T}_l^+ e^{i\vec{\omega}_l\cdot\vec{x}} + \hat{T}_l^- e^{-i\vec{\omega}_l\cdot\vec{x}}). \tag{4.32}$$

We need to compute the matrices $\hat{A}(R^k)$ from Eq. (4.31) for a QNN with just one qubit and L layers. The strategy consists in adding a new layer to a circuit with L layers, $\hat{U}_L \to \hat{U}_{L+1} = \hat{U}_L \hat{u}_l$. For a single qubit network, we simply have $\hat{u}_l = (\hat{T}_l^+ e^{i\vec{\omega}_l\cdot\vec{x}} + \hat{T}_l^- e^{-i\vec{\omega}_l\cdot\vec{x}})$. We analyze the action of adding this extra layer,

$$\begin{aligned}
\hat{U}_L^\dagger \hat{\mathcal{M}} \hat{U}_L &= \sum_{k=1}^{3^L} \hat{A}_L^k e^{i\vec{\Omega}_k\cdot\vec{x}} \to \\
\hat{u}_l^\dagger \hat{U}_L^\dagger \hat{\mathcal{M}} \hat{U}_L \hat{u}_l &= \sum_{k=1}^{3^L} \left[(\hat{T}_l^+)^\dagger e^{-i\vec{\omega}_l\cdot\vec{x}} + (\hat{T}_l^-)^\dagger e^{i\vec{\omega}_l\cdot\vec{x}}\right] \hat{A}_L^k \left[\hat{T}_l^+ e^{i\vec{\omega}_l\cdot\vec{x}} + \hat{T}_l^- e^{-i\vec{\omega}_l\cdot\vec{x}}\right] e^{i\vec{\Omega}_k\cdot\vec{x}} \\
&= \sum_{k=1}^{3^L} \Bigg\{ \left[(\hat{T}_l^+)^\dagger \hat{A}_L^k \hat{T}_l^+ + (\hat{T}_l^-)^\dagger \hat{A}_L^k \hat{T}_l^-\right] e^{i\vec{\Omega}_k\cdot\vec{x}} \\
&\quad + (\hat{T}_l^-)^\dagger \hat{A}_L^k \hat{T}_l^+ e^{i(\vec{\Omega}_k + 2\vec{\omega}_l)\cdot\vec{x}} \\
&\quad + (\hat{T}_l^+)^\dagger \hat{A}_L^k \hat{T}_l^- e^{i(\vec{\Omega}_k - 2\vec{\omega}_l)\cdot\vec{x}} \Bigg\} \\
&= \sum_{k=1}^{3^L} \sum_{a\in\{0,2,-2\}} \mathcal{H}_l^a[\hat{A}_L^k] e^{i(\vec{\Omega}_k + a\vec{\omega}_l)\cdot\vec{x}}.
\end{aligned} \tag{4.33}$$

Where we have introduced the superoperators

$$\begin{aligned}
\mathcal{H}_l^{0}[\hat{O}] &= (\hat{T}_l^{+})^\dagger \hat{O}\hat{T}_l^{+} + (\hat{T}_l^{-})^\dagger \hat{O}\hat{T}_l^{-}, \\
\mathcal{H}_l^{+2}[\hat{O}] &= (\hat{T}_l^{-})^\dagger \hat{O}\hat{T}_l^{+}, \\
\mathcal{H}_l^{-2}[\hat{O}] &= (\hat{T}_l^{+})^\dagger \hat{O}\hat{T}_l^{-}.
\end{aligned} \tag{4.34}$$

From the derivation in Eq. (4.33), we observe that adding a layer to a single qubit network adds three new frequencies to the Fourier spectrum: $\{\Omega_k\} \to \{\Omega_k, \Omega_k + 2\omega_l, \Omega_k - 2\omega_l\}$. The coefficients of the new network are directly obtained by applying the operators $\mathcal{H}_l^a$ to the coefficients A_L^k, resulting in a new set of coefficients $\{A_L^k\} \to \{A_{L+1}^k\} = \{\mathcal{H}_l^0[A_L^k], \mathcal{H}_l^{+2}[A_L^k], \mathcal{H}_l^{-2}[A_L^k]\}$. By defining the operation of adding an element $a \in \{0, 2, -2\}$ to a list R^k such as $\{R^k, a\} = \{R_1^k, R_2^k, ..., R_L^L, a\}$, we can identify the relationship between the matrices $\hat{A}_L$ and A_{L+1},

$$\hat{A}_{L+1}(\{R^k, a\}) = \mathcal{H}_{L+1}^a[\hat{A}_L(R^k)] \tag{4.35}$$

From this, we can recursively obtain any term as follows:

$$\hat{A}^k = \hat{A}(R^k) = \mathcal{H}_1^{R_1^k}[\mathcal{H}_2^{R_2^k}[...\mathcal{H}_{L-1}^{R_{L-1}^k}[[\mathcal{H}_L^{R_L^k}[\hat{\mathcal{M}}]]]...]]. \tag{4.36}$$

The result of Eq. (4.36) is very powerful, as it allows to study the dependence of the coefficients on the measured operator $\hat{\mathcal{M}}$ across different layer architectures and identify those that are zero. Specifically, for the layer definition given in Eq. (4.3), we ilustrate how $\mathcal{H}_{l,q}^a$ acts on each operator in spin basis,

$$\begin{aligned}
\mathcal{H}_l^{0}[\hat{\sigma}_x] &= \sin(2\alpha_l)\hat{\sigma}_z + \cos(2\alpha_l)\hat{\sigma}_x, \\
\mathcal{H}_l^{0}[\hat{\sigma}_y] &= 0, \\
\mathcal{H}_l^{0}[\hat{\sigma}_z] &= 0, \\
\mathcal{H}_l^{0}[\mathbb{I}] &= \mathbb{I},
\end{aligned} \tag{4.37}$$

$$\begin{aligned}
\mathcal{H}_l^{2}[\hat{\sigma}_x] &= 0, \\
\mathcal{H}_l^{2}[\hat{\sigma}_y] &= i\frac{e^{2i\beta_l}}{2}[\cos(2\alpha_l)\hat{\sigma}_z - \sin(2\alpha_l)\hat{\sigma}_x - i\hat{\sigma}_y], \\
\mathcal{H}_l^{2}[\hat{\sigma}_z] &= \frac{e^{2i\beta_l}}{2}[\cos(2\alpha_l)\hat{\sigma}_z - \sin(2\alpha_l)\hat{\sigma}_x - i\hat{\sigma}_y], \\
\mathcal{H}_l^{2}[\mathbb{I}] &= 0,
\end{aligned} \tag{4.38}$$

$$\begin{aligned}
\mathcal{H}_l^{-2}[\hat{\sigma}_x] &= 0, \\
\mathcal{H}_l^{-2}[\hat{\sigma}_y] &= -i\frac{e^{2i\beta_l}}{2}[\cos(2\alpha_l)\hat{\sigma}_z + \sin(2\alpha_l)\hat{\sigma}_x + i\hat{\sigma}_y],
\end{aligned}$$

$$\begin{aligned} \mathcal{H}_l^{-2}[\hat{\sigma}_z] &= \frac{e^{2i\beta_l}}{2}[\cos(2\alpha_l)\hat{\sigma}_z + \sin(2\alpha_l)\hat{\sigma}_x + i\hat{\sigma}_y], \\ \mathcal{H}_l^{-2}[\mathbb{I}] &= 0. \end{aligned} \tag{4.39}$$

If we use the observable $\hat{\mathcal{M}} = \hat{\sigma}_z$, then all the terms associated with sequences where $R_L^k = 0$, i.e., $R^k = \{R_1^k, ..., R_{L-1}^k, 0\}$, return a coefficient equal to zero due to $\mathcal{H}_l^0[\hat{\sigma}_z] = 0$. The recursive relation then gives:

$$\begin{aligned} \hat{A}(\{R_1^k, ..., R_{L-1}^k, 0\}) &= \mathcal{H}_1^{R_1^k}[\mathcal{H}_2^{R_2^k}[...\mathcal{H}_{L-1}^{R_{L-1}^k}[\mathcal{H}_L^0[\hat{\sigma}_z]]...]] \\ &= \mathcal{H}_1^{R_1^k}[\mathcal{H}_2^{R_2^k}[...\mathcal{H}_{L-1}^{R_{L-1}^k}[0]...]] = 0 \end{aligned} \tag{4.40}$$

In this case, out of the 3^L sequences we initially had, one-third satisfy $R_L^k = 0$. Therefore, the total number of non-zero harmonics is $N_h = 2\chi/3$, where χ represents the maximum number of harmonics, defined as $\chi = \max(N_h(L = 1)) = 3^L$.

Alternatively, if we choose the observable $\hat{\mathcal{M}} = \hat{\sigma}_x$, only sequences with terms $R_L^k = 0$ yield non-zero terms, resulting in $\chi/3$ harmonics, since $\mathcal{H}_l^2[\hat{\sigma}_x] = \mathcal{H}_l^{-2}[\hat{\sigma}_x] = 0$. The harmonics obtained with $\hat{\mathcal{M}} = \hat{\sigma}_x$ are precisely those that cannot be obtained with $\hat{\mathcal{M}} = \hat{\sigma}_z$. Thus, using a general operator $\hat{O} = u_o\mathbb{I} + u_x\hat{\sigma}_x + u_y\hat{\sigma}_y + u_z\hat{\sigma}_z$, we can potentially obtain $N_h = \chi$ harmonics.

The choice of layer definition also significantly impacts the number of harmonics. For example, consider defining an alternative layer as follows:

$$\hat{\mathcal{L}}_l^*(\vec{x}, \vec{\theta}_l) = R_x(2\alpha_l)R_y(2(\vec{\omega}_l \cdot \vec{x} + \beta_l)), \tag{4.41}$$

the new superoperators $\mathcal{H}^*$ act as follows:

$$\begin{aligned} \mathcal{H}_l^{*0}[\hat{\sigma}_y] &\propto \hat{\sigma}_y, \\ \mathcal{H}_l^{*0}[\mathcal{H}_l^{*\pm 2}[\hat{O}]] &\propto \hat{\sigma}_y. \end{aligned} \tag{4.42}$$

Therefore, any sequence ending with an array of zeros after a ± 2 term, such as $R^k = \{..., 2, 0\}$ or $R^k = \{..., -2, 0, 0, 0\}$, will make $\hat{A}(R^k) \propto \hat{\sigma}_y$. This implies that any sequence ending with a zero necessarily produces a $\hat{\sigma}_y$ term, except the sequence containing only zeros. Since $\langle 0|\hat{\sigma}_y|0\rangle = 0$, the only non-zero coefficients are those for which R_L^k takes the value $\{2, -2\}$. Thus, the total number of harmonics in this case is $N^h = 2\chi/3 + 1$, after including the sequence with all zeros. In a QNN build with the layer definition $\hat{\mathcal{L}}_l^*(\vec{x}, \vec{\theta}_l)$, the total number of harmonics becomes independent of the measured spin operator, which represents a significant deviation from the previously explored case.

For the particular layer architecture given by Eq. (4.3), the number of expansion terms N_h depends on the considered observable $\hat{\mathcal{M}}$, being the maximum number of achievable terms $\max(N_h) = \chi = 3^L$. As shown, the observables $\hat{\mathcal{M}} = \hat{\sigma}_z$ and $\hat{\mathcal{M}} = \hat{\sigma}_y$ lead to $N_h \leq 2 \cdot \chi/3$, while measuring the observable $\hat{\mathcal{M}} = \hat{\sigma}_x$ gives $N_h \leq \chi/3$. In general, such a layer topology is capable of reaching the maximal expressivity bound $N_h = \chi$ by measuring the operator $\hat{\mathcal{M}} = \hat{O} = u_o\mathbb{I} + u_x\hat{\sigma}_x + u_y\hat{\sigma}_y + u_z\hat{\sigma}_z$ along various

$Q=1$		$\hat{\mathcal{M}}$			
		$\hat{\sigma}_x$	$\hat{\sigma}_y$	$\hat{\sigma}_z$	$\hat{O}$
N_h	$\hat{\mathcal{L}}$	$\chi/3$	$2\chi/3$	$2\chi/3$	χ
	$\hat{\mathcal{L}}^*$	$2\chi/3+1$	$2\chi/3+1$	$2\chi/3+1$	$2\chi/3+1$

Table 4.1: Maximum number N_h of non-vanishing expansion coefficients when expanding the output of the network using one qubit ($Q = 1$) into a partial Fourier series. Different observables $\hat{\mathcal{M}}$ and the encoding architectures given by Eqs.(4.3) and (4.41) are considered. Here $\chi = 3^L$ is the spectrum bound.

directions defined by the coefficients $u_o, u_x, u_y, u_z \in \mathbb{R}$. Notice that using another layer topology when constructing a data re-uploaded QNN might lead to a different number of non-vanishing expansion coefficients. For example, the architecture given by $\hat{\mathcal{L}}_l^*(\vec{x}, \vec{\theta}_l)$ results in $N_h \leq 2 \cdot \chi/3 + 1$, regardless of the observable used for the readout. Table 4.1 presents the different achievable expresivities in terms of the observable $\hat{\mathcal{M}}$ and encoding layer.

4.4.4 Multiqubit architectures

The previous results can easily be generalized for multiqubit $\mathcal{A}_0(L, Q)$ architectures without entanglement by taking the outer product of the unitary acting on each qubit, i.e.,

$$\hat{U} = \bigotimes_{q=1}^{Q} \hat{v}_q, \tag{4.43}$$

with $\hat{v}_q = \prod_{l=1}^{L} (\hat{T}^+_{l,q} e^{i\vec{\omega}_{l,q}\cdot\vec{x}} + \hat{T}^-_{l,q} e^{-i\vec{\omega}_{l,q}\cdot\vec{x}})$. The absence of the entangling gates between layers allows an exchange of products over layers and qubits in Eq. (4.26) to recover Eq. (4.43).

Now, two different cases are considered depending on the election of the observable $\hat{\mathcal{M}}$. At first, we consider that the mapping $\hat{\mathcal{M}}$ of the whole system is composed of local measurements $\hat{\mathcal{M}}_q$ of the individual qubits $\hat{\mathcal{M}} = \sum_{q=1}^{Q} \hat{\mathcal{M}}_q$. As a result, the generated output is decomposed into

$$F(\vec{x}, \vec{\theta}) = \langle 0| (\bigotimes_{q=1}^{Q} \hat{v}_q)^\dagger (\hat{\mathcal{M}}_1 + ... + \hat{\mathcal{M}}_Q)(\bigotimes_{q=1}^{Q} \hat{v}_q) |0\rangle = \sum_{q=1}^{Q} \langle 0| \hat{v}_q^\dagger \hat{\mathcal{M}}_q \hat{v}_q |0\rangle \, . \tag{4.44}$$

Each term $\langle 0| v_q^\dagger \hat{\mathcal{M}}_q \hat{v}_q |0\rangle$ in the expansion produces $N_h(L, 1)$ coefficients, leading to a total of $N_h(L, Q) = Q \cdot N_h(L, 1)$ non-vanishing expansion coefficients of the partial Fourier series for the $\mathcal{A}_0(L, Q)$ architecture.

Alternatively, we can perform a global measurement of the network by defining the

$Q = 2, \hat{\mathcal{L}}$		$\hat{\mathcal{M}}$		
		$\hat{\sigma}_z^1 + \hat{\sigma}_z^2$	$\hat{\sigma}_z^1 \otimes \hat{\sigma}_z^2$	$\hat{O}_1 \otimes \hat{O}_2$
N_h	without $\hat{E}_2$	$4\chi/3$	$4\chi^2/9$	χ^2
	$\hat{E}_2$ all layers	$5\chi^2/9$	$4\chi^2/9$	χ^2
	$\hat{E}_2$ last layer	$4\chi^2/9$	$4\chi^2/9$	χ^2

Table 4.2: Maximum number N_h of non-vanishing expansion coefficients when expanding the network's output $F(\vec{x}, \vec{\theta})$ into a partial Fourier series using $Q = 2$ qubits. Different observables $\hat{\mathcal{M}}$ are considered when using the encoding architecture. In particular, the number N_h is compared with and without entanglement. Here N_h is compared with the maximum number of harmonics of a single qubit network $\chi = 3^L$.

observable $\hat{\mathcal{M}} = \otimes_{q=1}^{Q} \hat{\mathcal{M}}_q$. In this case,

$$F(\vec{x}, \vec{\theta}) = \langle 0| (\bigotimes_{q=1}^{Q} \hat{v}_q)^\dagger (\hat{\mathcal{M}}_1 \otimes \hat{\mathcal{M}}_2 \otimes ... \otimes \hat{\mathcal{M}}_Q)(\bigotimes_{q=1}^{Q} v_q) |0\rangle = \prod_{q=1}^{Q} \langle 0| v_q^\dagger \hat{\mathcal{M}}_q \hat{v}_q |0\rangle \,, \quad (4.45)$$

leading to $N_h(L, Q) = N_h(L, 1)^Q$ non-vanishing expansion coefficients. The same architecture can generate more harmonics by just modifying the measured observable.

4.4.5 Last layer entanglement

As commented on at the beginning of Sect.4.4 and further elaborated by Schuld et al. [275], entanglement does not extend the frequency spectrum of the unitary transformation given by Eq. (4.26), but only affects the values of the matrix coefficients $\hat{C}_j$. A systematic approach to analyze the full tunability of C_j is still needed. However, entanglement does affect the size of the spectrum of $F(\vec{x}, \vec{\theta})$ that involves the mapping of $f(\vec{x})$ through an observable $\hat{\mathcal{M}}$. To gain a physical understanding of the effects of introducing entanglement exclusively in the final layer, we examine a specific network architecture with $Q = 2$ and the observable $\hat{\mathcal{M}} = \hat{\sigma}_z^{tot} = \hat{\sigma}_z^1 + \hat{\sigma}_z^2$. When the last output layer incorporates an entangling gate in the form of Eq. (4.9), the resulting neural network is equivalent to a non-entangling $\mathcal{A}_0(L, 2)$ topology being mapped by the effective observable

$$\hat{\mathcal{M}}' = \hat{E}_2^\dagger \hat{\mathcal{M}} \hat{E}_2 = \hat{E}_2^\dagger \hat{\sigma}_z^{tot} \hat{E}_2 = \hat{\sigma}_x^1 \otimes \hat{\sigma}_x^2 - \hat{\sigma}_y^1 \otimes \hat{\sigma}_y^2. \quad (4.46)$$

In this case, $\hat{\mathcal{M}}'$ is a global observable and increases the number of non-zero expansion coefficients compared to the local $\hat{\mathcal{M}} = \hat{\sigma}_z^{tot}$ readouts. More generally, the exact number of generated expansion coefficients depends on the newly transformed observable $\hat{\mathcal{M}}'$ through $\hat{E}_2$.

4.4.6 Two qubit architecture

We can compute the superoperators $\mathcal{H}_l$ for networks with more qubits. When adding a new layer to an existing network with Q qubits, the number of harmonics increases by a factor of 3^Q. Consequently, the number of required superoperators also scales as 3^Q - one for each new frequency. This scaling makes the problem more complex as the number of qubits increases. However, the structure of these superoperators is predictable, allowing us to explore the role of entanglement. By following the same procedure used to derive Eq. 4.33, we obtain:

$$\hat{u}_l^\dagger \hat{U}_L^\dagger \hat{\mathcal{M}} \hat{U}_L \hat{u}_l = \sum_{k=1}^{3^L} \sum_{a_1 \in \{0,2,-2\}} \sum_{a_2 \in \{0,2,-2\}} \dots \sum_{a_Q \in \{0,2,-2\}} \mathcal{H}_l^{a_1,a_2,\dots,a_Q}[\hat{A}_L^k] e^{i(\vec{\Omega}_k + \sum_{q=1}^{Q} a_q \vec{\omega}_{l,q})\cdot\vec{x}}. \tag{4.47}$$

Let us consider all the superoperators $\mathcal{H}_l$ for a entangled two qubit network:

$$\begin{aligned}
\mathcal{H}_l^{0,0}[\hat{O}] &= \sum_{i=\pm}\sum_{j=\pm} (\hat{T}_{l,2}^i \otimes \hat{T}_{l,1}^j)^\dagger (\hat{E}_2^l)^\dagger \hat{O} \hat{E}_2^l (\hat{T}_{l,2}^i \otimes \hat{T}_{l,1}^j),\\
\mathcal{H}_l^{0,2}[\hat{O}] &= \sum_{i=\pm} (\hat{T}_{l,2}^i \otimes \hat{T}_{l,1}^-)^\dagger (\hat{E}_2^l)^\dagger \hat{O} \hat{E}_2^l (\hat{T}_{l,2}^i \otimes \hat{T}_{l,1}^+),\\
\mathcal{H}_l^{0,-2}[\hat{O}] &= \sum_{i=\pm} (\hat{T}_{l,2}^i \otimes \hat{T}_{l,1}^+)^\dagger (\hat{E}_2^l)^\dagger \hat{O} \hat{E}_2^l (\hat{T}_{l,2}^i \otimes \hat{T}_{l,1}^-),\\
\mathcal{H}_l^{2,0}[\hat{O}] &= \sum_{i=\pm} (\hat{T}_{l,2}^- \otimes \hat{T}_{l,1}^i)^\dagger (\hat{E}_2^l)^\dagger \hat{O} \hat{E}_2^l (\hat{T}_{l,2}^+ \otimes \hat{T}_{l,1}^i),\\
\mathcal{H}_l^{2,2}[\hat{O}] &= (\hat{T}_{l,2}^- \otimes \hat{T}_{l,1}^-)^\dagger (\hat{E}_2^l)^\dagger \hat{O} \hat{E}_2^l (\hat{T}_{l,2}^+ \otimes \hat{T}_{l,1}^+),\\
\mathcal{H}_l^{2,-2}[\hat{O}] &= (\hat{T}_{l,2}^- \otimes \hat{T}_{l,1}^+)^\dagger (\hat{E}_2^l)^\dagger \hat{O} \hat{E}_2^l (\hat{T}_{l,2}^+ \otimes \hat{T}_{l,1}^-),\\
\mathcal{H}_l^{-2,0}[\hat{O}] &= \sum_{i=\pm} (\hat{T}_{l,2}^+ \otimes \hat{T}_{l,1}^i)^\dagger (\hat{E}_2^l)^\dagger \hat{O} \hat{E}_2^l (\hat{T}_{l,2}^- \otimes \hat{T}_{l,1}^i),\\
\mathcal{H}_l^{-2,2}[\hat{O}] &= (\hat{T}_{l,2}^+ \otimes \hat{T}_{l,1}^-)^\dagger (\hat{E}_2^l)^\dagger \hat{O} \hat{E}_2^l (\hat{T}_{l,2}^- \otimes \hat{T}_{l,1}^+),\\
\mathcal{H}_l^{-2,-2}[\hat{O}] &= (\hat{T}_{l,2}^+ \otimes \hat{T}_{l,1}^+)^\dagger (\hat{E}_2^l)^\dagger \hat{O} \hat{E}_2^l (\hat{T}_{l,2}^- \otimes \hat{T}_{l,1}^-).
\end{aligned} \tag{4.48}$$

When there is no entanglement the definitions are the same, but removing the entangling gate $\hat{E}_2^l$. Again, we can build the matrices $\hat{A}(R^k)$ recursively:

$$\hat{A}(R^k) = \mathcal{H}_1^{R_1^k,R_2^k}[\mathcal{H}_{2,2}^{R_3^k,R_4^k}[\dots\mathcal{H}_{L-1}^{R_{D-3}^k,R_{D-2}^k}[\mathcal{H}_L^{R_{D-1}^k,R_D^k}[\hat{\mathcal{M}}]]\dots]]. \tag{4.49}$$

We analyze first a network with layer architecture given in Eq. (4.3), when $\hat{E}_2^l$ is introduce in all layers, and when we measure the obserbable $\hat{\mathcal{M}} = \hat{\sigma}_z^{tot} = \hat{\sigma}_z^1 + \sigma_z^2$. In this scenario we have,

$$\mathcal{H}_l^{0,2}[\hat{\sigma}_z^{tot}] = \mathcal{H}_l^{0,-2}[\hat{\sigma}_z^{tot}] = \mathcal{H}_l^{2,0}[\hat{\sigma}_z^{tot}] = \mathcal{H}_l^{-2,0}[\hat{\sigma}_z^{tot}] = 0. \tag{4.50}$$

Therefore, any sequence ending with one and only one zero in their two last terms, such as $R^k = \{..., a_{D-3}, 0, 2\}$ or $R^k = \{..., a_{D-3}, -2, 0\}$, yields a harmonic with zero amplitude, and as this happens for four out of nine cases, the total number of harmonics is $N_h \leq 4\chi^2/9$. Alternatively, if we measure the operator $\hat{\mathcal{M}} = \hat{\sigma}_z^1 \otimes \hat{\sigma}_z^2$ instead, a similar analysis shows that $N_h \leq 5\chi^2/9$. In both cases, the maximum number of harmonics can achieved by measuring a general operator $\hat{O}_1 \otimes \hat{O}_2$.

In Table 4.2, we present the spectrum sizes of $F(\vec{x}, \vec{\theta})$ generated by various mapping strategies and topologies for two-qubit QNNs. When considering architectures with entanglement across all layers, the factorization approach outilned in Eq. (4.44) is not applicable. Despite this increased complexity, we observe similar scaling behaviors in the QNNs. This indicates that the presence of entanglement across layers does not fundamentally alter the overall scaling trends seen when entanglement is introduced only in the last layer.

We can generalize the expressions from Eq. (4.48) to multiple qubits by analyzing the three possible values of a_q in $\mathcal{H}_l^{...,a_q,...}$ ::

$$\begin{aligned}
\mathcal{H}_l^{...,0,...}[\hat{O}] &= (... \otimes (\hat{T}_{l,q}^{+})^\dagger \otimes ...)(\hat{E}^l)^\dagger \hat{O} \hat{E}^l(... \otimes \hat{T}_{l,q}^{+} \otimes ...) + \\
&+ (... \otimes (\hat{T}_{l,q}^{-})^\dagger \otimes ...)(\hat{E}^l)^\dagger \hat{O} \hat{E}^l(... \otimes \hat{T}_{l,q}^{-} \otimes ...) = \\
&= \sum_{i=\pm} (... \otimes (\hat{T}_{l,q}^{i})^\dagger \otimes ...)(\hat{E}^l)^\dagger \hat{O} \hat{E}^l(... \otimes \hat{T}_{l,q}^{i} \otimes ...) \\
\mathcal{H}_l^{...,2,...}[\hat{O}] &= (... \otimes (\hat{T}_{l,q}^{-})^\dagger \otimes ...)(\hat{E}^l)^\dagger \hat{O} \hat{E}^l(... \otimes \hat{T}_{l,q}^{+} \otimes ...), \\
\mathcal{H}_l^{...,-2,...}[\hat{O}] &= (... \otimes (\hat{T}_{l,q}^{+})^\dagger \otimes ...)(\hat{E}^l)^\dagger \hat{O} \hat{E}^l(... \otimes \hat{T}_{l,q}^{-} \otimes ...).
\end{aligned} \tag{4.51}$$

With these definitions, we can derive similar equations to Eq. (4.49) and analytically investigate the structure of the coefficients c_j for any architecture.

4.5 Numerical results

For simple topologies, we were able to analytically characterize the expressivity of a network by counting the number of non-zero expansion coefficients in the partial Fourier decomposition. However, for complex deep QNNs, this procedure becomes more intrincate. An alternative approach involves directly Fourier transforming the generated output $F(\vec{x}, \vec{\theta}) \to \mathcal{F}(\vec{\Omega}, \vec{\theta})$, with the number of coefficients c_j determined by the count of peaks in the Fourier transform. This numerical procedure allows us to extrapolate the harmonics count to deep entangling $\mathcal{A}_1(L, Q)$ models straightforwardly. In Fig. 4.2, we plot the Fourier transform of the outputs generated by (a) $\mathcal{A}_0(2, 2)$ and (b) $\mathcal{A}_1(2, 2)$ using the same encoding observable $\hat{\mathcal{M}} = \sum_{q=1}^{Q} \hat{\sigma}_z^q$ and the random but identically initialized set of parameters $\vec{\theta}$. The number of peaks in both the architecture without

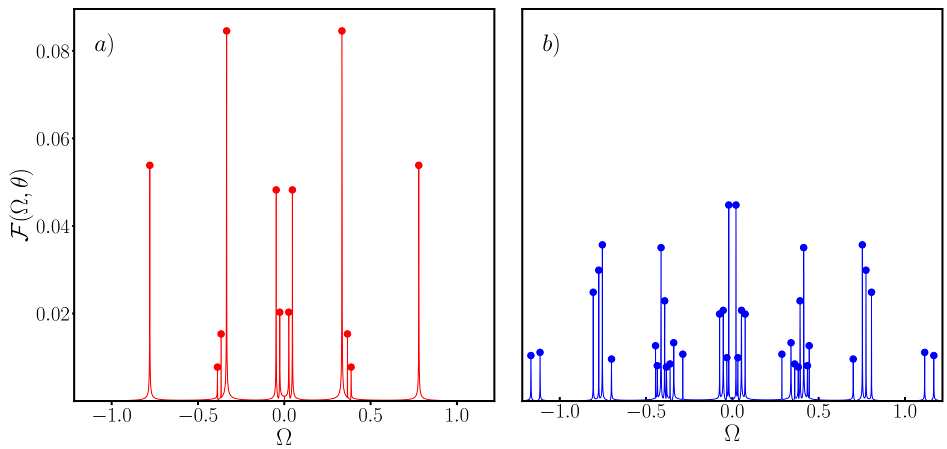

Fig. 4.2: Fourier transform of the output generated by a randomly initialized QNN showing different expansion coefficients c_j, by using (a) $\mathcal{A}_0^T(2,2)$ and (b) $\mathcal{A}_1^T(2,2)$. Sharing the same $\vec{x}$ and $\vec{\theta}$ values, both QNNs have the same number of variable parameters, however, the $\mathcal{A}_1^T(2,2)$ model generates more harmonics. The measured operator is $\hat{\mathcal{M}} = \hat{\sigma}_z^{tot} = \hat{\sigma}_z^1 + \hat{\sigma}_z^2$.

and with entanglement (12 and 36, respectively) matches the analytical expressions in Table 4.2. Although both $\mathcal{A}_0$ and $\mathcal{A}_1$ have the same number of tunable parameters, the inclusion of entanglement in the QNN triples the spectrum.

To quantify and visualize the ability of the network to generate non-zero expansion coefficients in the partial Fourier decomposition, we define the ratio $\Gamma = N_h/N_p$. This index quantifies the number of harmonics per adjustable parameter in the QNN. Considering the encoding observable described above $\hat{\mathcal{M}} = \sum_{q=1}^{Q} \hat{\sigma}_z^q$, for $\mathcal{A}_0(L,Q)$ models, $N_h = Q \cdot 2\chi/3$. Consequently, the ratio Γ grows as $3^L/L$, regardless of the number of qubits, as depicted in Fig. 4.3. In this figure, we compare this result with the Γ parameter of $\mathcal{A}_1(L,Q)$ models, which incorporate entangling gates in all layers. While both $\mathcal{A}_0$ and $\mathcal{A}_1$ have the same number of adjustable parameters N_p, remarkably, the mere presence of entanglement further amplifies the exponential relationship between Γ and L as the number of qubits increases.

4.5.1 Teacher-student benchmark

In this section, we systematically evaluate the neural network approximation capabilities for real-continuous functions when considering various architectures, i.e., network depth, number of qubits, and presence or absence of entanglement in all layers. To benchmark the QNNs and minimize any potential dataset bias, we employ the teacher-student scheme [257, 278]. The teacher model (T) generates datasets by mapping random inputs to outputs, and these datasets are subsequently learned by the student models (S). To assess the performance of the student models, we employ prediction maps to qualitatively compare and visualize the similarity between T and S, see 4.5.1. For a rigorous quantitative comparison, we benchmark the average performance [279] of both

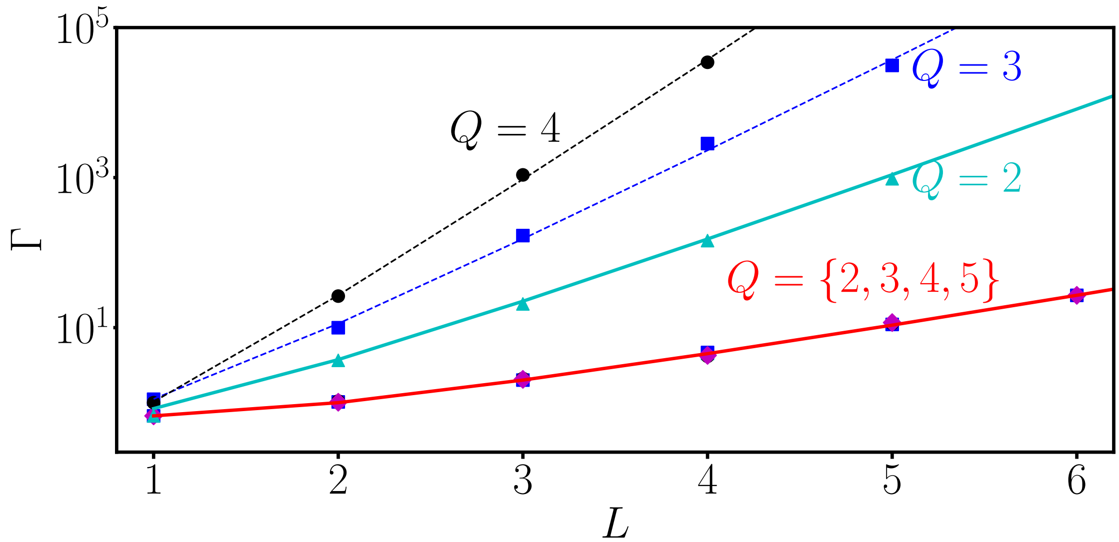

Fig. 4.3: Ratio Γ as a function of the number of layers L for different number of qubits Q, computed numerically through the procedure depicted in Fig. 4.2 (symbols). All the $\mathcal{A}_0$ models collapse to the same ratio independently of the number of qubits (red-solid line). entangling models $\mathcal{A}_1$ show a different exponential slope for $Q = 2$ (cyan triangles), $Q = 3$ (blue squares), and $Q = 4$ (black circles). The analytical results $\Gamma = 2(3^{L-1})/[(2+n)L]$ (red-solid line) and $\Gamma = 5(3^{L-1})^2/[(2+n)2L]$ (cyan-solid line) fit these trends. The dashed lines facilitate the visualization of the linear dependency. In all cases the measured operator is $\hat{\mathcal{M}} = \sum_{q=1}^{Q} \hat{\sigma}_z^q$.

models through the loss function in Eq. (4.5). subsectionA particular example

In this section, we discuss in more detail the results presented in Fig. 4.7, where different $\mathcal{A}_1^S(4, L)$ students are trained for five different $\mathcal{A}_1^T(4, 8)$ models. In Fig. 4.4a, we present the prediction map $F(\vec{x}, \vec{\theta})$ of one of these $\mathcal{A}_1^T(4, 8)$ teachers. The teacher prediction map is used as the target function $f(\vec{x})$ for the outputs $F(\vec{x}, \vec{\theta})$ of the students. For the case $L = 8$, we present in Figs. 4.4b and 4.4c the predictions of two S-models, $\mathcal{A}_0^S(4, 8)$ and $\mathcal{A}_1^S(4, 8)$, respectively, both initialized with the same set of parameters $\vec{\theta}$.

Alternatively to the values of the cost function presented in Fig. 4.7, these prediction maps allow to study the predictions locally, and understand which patterns and structures the models are able to learn. The student without entanglement is able to reproduce the overall pattern of the teacher. However, it fails when replicating smaller details, which we associate to higher frequencies. On the contrary, $\mathcal{A}_1^S$ makes a better work at approximating the teacher. Note that, in this case, both the teacher $\mathcal{A}_1^T(4, 8)$ and student $\mathcal{A}_1^S(4, 8)$ models are the same. However, the optimizer gets stuck in a local minimum during the minimization process, leading to small discrepancies $f(\vec{x}) - F(\vec{x}, \vec{\theta})$, see Fig. 4.4d.

The role of the teacher is to map the input data $\vec{x}$ through a QNN into a random output function $F(\vec{x}, \vec{\theta})$ by the observable $\hat{\mathcal{M}} = \sum_q^Q \hat{\sigma}_z^q$, which then becomes the target

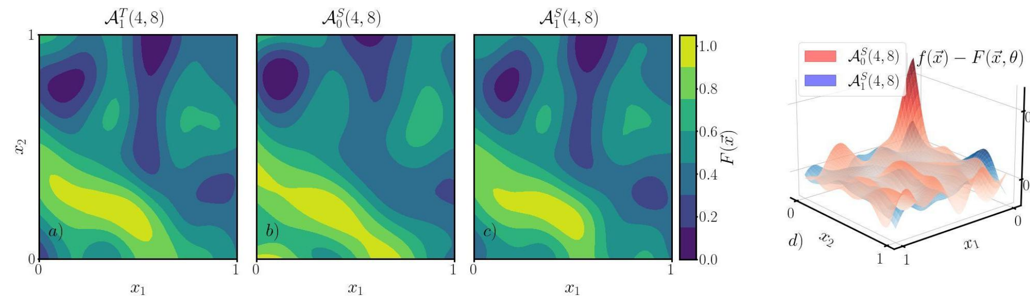

Fig. 4.4: *(a)* Bi-dimensional output generated by a teacher $\mathcal{A}_1^T(4,8)$. The contourplot corresponds to the target function to be approximated by the different student models. *(b)* Corresponging approximation generated by a student $\mathcal{A}_0^S(4,8)$ without entanglement and *(c)* by $\mathcal{A}_1^S(4,8)$ with entanglement. *(d)* Difference $f(\vec{x}) - F(\vec{x},\vec{\theta})$ for both student models.

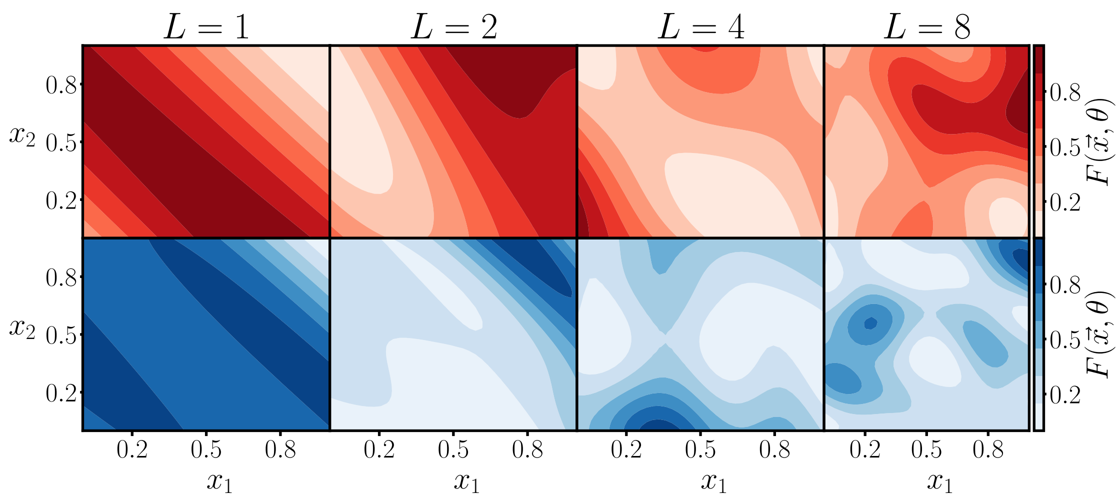

Fig. 4.5: Prediction maps generated by different T models of a QNN containing $Q = 4$ qubits in different number of layers. Upper (lower) panels correspond to QNNs of $\mathcal{A}_0^T(\mathcal{A}_1^T)$ architectures. Any pair $\{\mathcal{A}_0^T, \mathcal{A}_1^T\}$ with same L is equally initialized in the network parameters $\vec{\theta}$ and input $\vec{x}$, but differs in the presence (absence) of entanglement.

$f(\vec{x})$ of S models. All the adjustable parameters $\vec{\theta} \in [-\frac{\pi}{2}, \frac{\pi}{2}]$ and K input values $\vec{x} \in [0,1]^n$ are randomly initialized to avoid any possible bias on the datasets. The complexity of the target function $f(\vec{x})$ can be controlled by the depth of the teacher architectures.

In Fig. 4.5, we show the output functions generated by several T-models containing 4 qubits, without entanglement (upper panel) and with it (lower panel), when the input data is two-dimensional, $n = 2$. Deeper architectures (left to right) provide in general a 'richer' topology in $F(\vec{x},\vec{\theta})$.

First, we analyze the performance of the student as a function of the depth of the network, L. To this end, we focus on unidimensional ($n = 1$) regression problems. We

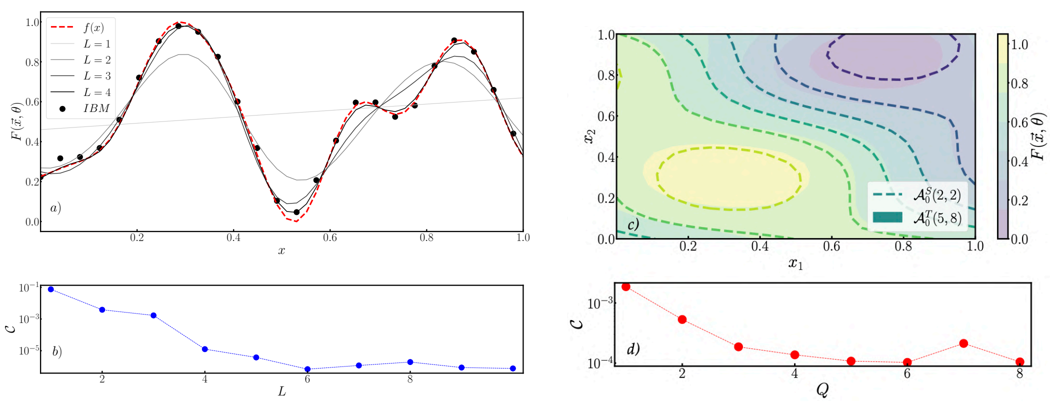

Fig. 4.6: *(a)* S-model outputs composed by a single qubit with different number of layers L (solid-lines) are listed to learn the targets $f(x^k)$ function randomly generated by the T-model $\mathcal{A}_0^T(10,10)$ (red-dashed). A single qubit QNN $\mathcal{A}_0^S(4,1)$ run in ibmq_belem shows its learnability (black circles). *(b)* Corresponding loss error $\mathcal{C}$ (4.5) in terms of the data re-uploads L. *(c)* Output of the teacher $\mathcal{A}_0^T(5,8)$ (continuous contour plot) for a two dimensional problem $n=2$ and the fitting result for a smaller $\mathcal{A}_0^S(2,2)$ student (dashed contour plot). *(d)* Corresponding loss error $\mathcal{C}$ for different student models $\mathcal{A}_0^S(2,Q)$ fitting the bi-dimensional data *(c)* generated by $\mathcal{A}_0^T(5,8)$ (red-dashed line). Parameters $K=400$ and $R=10$.

create a $\mathcal{A}_0^T(10,10)$ T-model, which randomly generates the output corresponding to the target function $f(x^k)$ that is depicted by the red-dashed line of Fig. 4.6a. Then, different $\mathcal{A}_0^S(L,1)$ S-models are trained to approximate this function. As inferred from Fig. 4.6b, the S-model's performance improves as the number of layers is increased, until it reaches a point of saturation, at which the minimum value of the loss function $\mathcal{C}$ becomes independent of L. For a fixed network topology, the particular value of $\min(\mathcal{C})$ and layer at which it saturates depend on the specific target function and input-data size. Note that a $\mathcal{A}_0^S(4,1)$ QNN programmed in ibmq_belem (black circles of Fig. 4.6a) already reaches $\mathcal{C}\sim 10^{-5}$, evidencing the capabilities of a single qubit as a universal approximator [274].

Secondly, we study the performance of QNNs in terms of the number of qubits, Q, by fixing a $\mathcal{A}_0^T(5,8)$ T-model architecture for a two-dimensional input data ($n=2$) and considering different $\mathcal{A}_0^S(2,Q)$ students. In Fig. 4.6c, we observe that a student with two qubits and two layers can produce an output function that closely resembles that of the teacher. In Fig. 4.6d, we represent the cost function as a function of the number qubits of the student. A similar trend is obtained, the approximation power of the S-models increases with the number of qubits until the loss function saturates.

Analogously to classical neural networks, where the approximation power increases with the number of hidden layers and neurons [280], the accuracy of the QNN increases with the amount of data re-uploadings (or layers) and number of qubits. However, in contrast to its classical counterpart, the QNN regression capabilities can be significantly enhanced with the incorporation of quantum resources, such as global readouts or entangling gates.

Therefore, our objective is to examine how entanglement influences the network approximation capabilities. For two-dimensional input data ($n = 2$), we generate different T-models, $\mathcal{A}_0^T(L_{Max}, Q)$ or $\mathcal{A}_1^T(L_{Max}, Q)$. Subsequently, we evaluated the performance of the S-models, $\mathcal{A}_0^S(L, Q)$ and $\mathcal{A}_1^S(L, Q)$, for both of these teacher models. The depth of the students ranges from 1 to L_{Max}, where L_{Max} represents the number of layers in the T-models. To expand the benchmark, each T model is randomly initialized M times, creating multiple target functions for students. As a result, for fixed teacher and student architectures, the QNN is evaluated $M \times R$ times, where R is the number of different initializations for the S-models.

In Fig. 4.7, we plot the average student performance $\bar{\mathcal{C}} = \sum_i^M \mathcal{C}_i/M$ on different realizations as a function of the number of layers for both the $\mathcal{A}_0^S$ and $\mathcal{A}_1^S$ models. We focus on the $\mathcal{A}_1^T$ target function, as it generates a more complex data structure due to the effect of an entangling readout. The case $\mathcal{A}_0^T$ is analyzed in 4.5.2. However, both scenarios lead to similar conclusions. When comparing the various plots in Fig. 4.7, it becomes apparent that, as the number of layers in the QNN increases, the differentiation in the performance of both $\mathcal{A}_0^S$ and $\mathcal{A}_1^S$ becomes increasingly noticeable. This observation is readily apparent in Fig. 4.3; for two pairs of QNN with the same number of qubits, $\mathcal{A}_0^S$ and $\mathcal{A}_1^S$, the difference in their values Γ increases with L, primarily due to the higher number of harmonics generated in the entangling network. A similar behavior is also observed when the number of qubits is increased in the $\mathcal{A}_1^S$ topology, as was already anticipated in Fig. 4.3. For a fixed number of layers in the entangling architecture, the steepness of Γ increases with Q, leading to a larger set of Fourier harmonics. However, this is not the case for $\mathcal{A}_0^S$ networks, since they all lead to the same Γ value, regardless of the number of qubits. As a consequence, the efficiency of different $\mathcal{A}_0^S$ models saturate to a common $\bar{\mathcal{C}}$ value. This behavior is more evident in the figures presented in 4.5.2. As a result, a deep QNN involving a global mapping of $f(\vec{x})$ leads to improvements of 1-2 orders of magnitude in the approximation accuracy compared to local readouts in a non-entangling network; see Fig. 4.7. Finally, note that, in general, deep entangling QNNs also present higher robustness over different realizations in the predicted output, as inferred from the smaller vertical lines of Figs. 4.7 and 4.8 showing the standard deviation $\Delta\mathcal{C} = \sqrt{\sum_i^M (\mathcal{C}_i - \bar{\mathcal{C}})^2/M}$.

4.5.2 Target function: the role of entanglement

Previously, we have analyzed the ability of both the $\mathcal{A}_0^S$ and $\mathcal{A}_1^S$ models to approximate a target function generated by an entangling QNN. Here, for completeness, we analyze the case of data generated by non-entangling models, $\mathcal{A}_0^T(L_{Max}, Q)$, and analyze the differences with the previous case. According to 4.5.1, the role of entanglement in the T models is to provide a more complex target function to approximate and thus increase the demands of the students. For the $\mathcal{A}_0^T(L_{Max}, Q)$ models, see *(a)-(c)* in Fig. 4.8, we observe a small difference in the global performance of both $\mathcal{A}_0^S$ and $\mathcal{A}_1^S$. In such cases, the overall accuracy of the entangling S-model beats the non-entangling QNN, except when simple networks (low number of layers L) are considered. This may be attributed

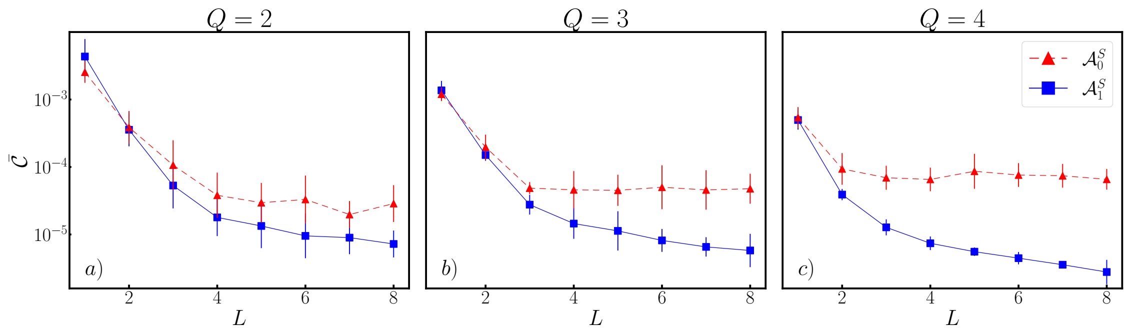

Fig. 4.7: Mean loss error $\bar{\mathcal{C}}$ as a function of the number of layers L for different student models $\mathcal{A}_0^S(L,Q)$ (red dashed-lines) and $\mathcal{A}_1^S(L,Q)$ (blue solid-lines). The target function is prepared by teacher models $\mathcal{A}_1^T(L_{Max},Q)$ containing entanglement and *(a)* $Q=2$, *(b)* $Q=3$, and *(c)* $Q=4$ qubits. Parameters: $n=2, K=400, R=5$, and $M=5$.

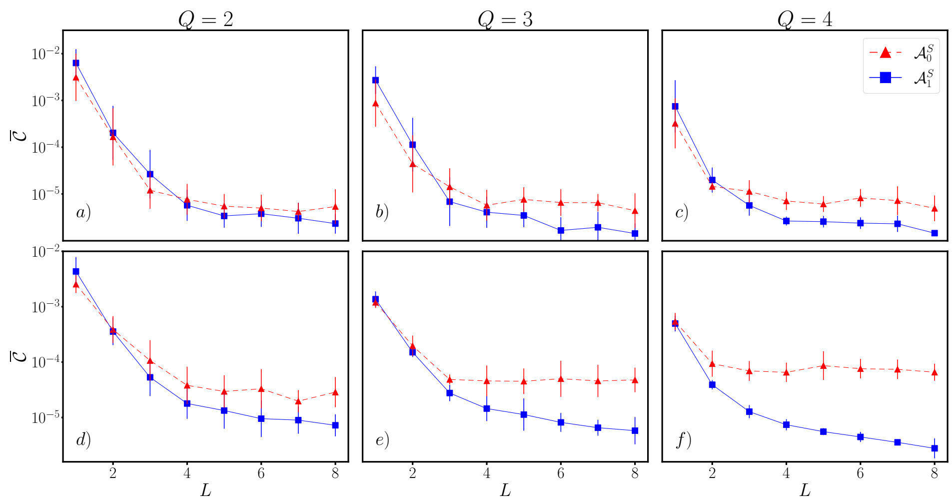

Fig. 4.8: Mean loss error $\bar{\mathcal{C}}$ as a function of the number of layers L for different student models $\mathcal{A}_0^S(L,Q)$ (red dashed-lines) and $\mathcal{A}_1^S(L,Q)$ (blue solid-lines). The target function is prepared by T-models $\mathcal{A}_0^T(L_{Max},Q)$ without and ($\mathcal{A}_1^T(L_{Max},Q)$ with) entanglement, top (bottom) panels. From left to right, the teacher QNN contains $Q=2$, $Q=3$, and $Q=4$ qubits. Same parameters as in Fig. 4.7.

to an overestimation of $f(\vec{x})$ due to the non-tunability of a larger set of coefficients c_j in the partial Fourier expansion (4.31). Note that increasing the complexity of the QNN (increasing Q) displaces the crossing point of $\bar{\mathcal{C}}$ plots to the left, indicating that small entangling networks $\mathcal{A}_1^S$ exceed the accuracy of $\mathcal{A}_0^S$ earlier. We also observed a faster saturation of the accuracy $\bar{\mathcal{C}}$ in $\mathcal{A}_0^S$ compared to $\mathcal{A}_1^S$. Although both QNNs have the same restricted number $N_p = LQ(2+n)$ of adjustable parameters and thus accessibility to the expansion Fourier basis elements $e^{i\vec{\Omega}_j\cdot\vec{x}}$, the larger spectra Ω_j of $\mathcal{A}_1^S$ compared to $\mathcal{A}_0^S$ reduces the misestimation of $f(\vec{x})$ by non-tunable expansion coefficients c_j. As we can see in the bottom panels *(d)-(f)*

The expressive power of the QNN primarily depends on its topological parameters.

However, when considering regression tasks, other factors such the QNN readout $\hat{\mathcal{M}}$ come into play. Generally, a larger Γ parameter tends to result in a smaller average error $\bar{\mathcal{C}}$, providing a higher accuracy when interpolating $f(\vec{x})$, except in two distinct scenarios. Firstly, for small QNNs (as depicted in Fig. 4.7a), or when dealing with simple $f(\vec{x})$ structures (as shown in Fig. 4.8), there can be an overestimation of $f(\vec{x})$. The additional harmonics introduced by $\mathcal{A}_1^S(L,Q)$ can lead to a less accurate estimation compared to the non-entangling model $\mathcal{A}_0^S(L,Q)$, resulting in a decrease of the network accuracy. Secondly, even though the expressive power grows exponentially with the number of layers, we observe a saturation in the accuracy of deep QNNs. Both phenomena can be attributed to the fact that the N_h Fourier coefficients have limited tunability due to the finite number $N_p = LQ(n+2)$ of adjustable parameters.

4.6 Outlook and conclusions

We have analyzed the expressivity of a universal data re-uploading QNN and systematically benchmarked its performance in regression tasks, showing the relevance of the observable that maps the network generated output and the target function. By using a partial Fourier series representation to quantify the expressivity of the QNN, we are able to limit the maximum expression power of the network. We show that the presence of entanglement, produced by a global readout of the QNN or by the incorporation of a final entangling layer, leads to the maximal expressivity of the network. As a result, the approximation capabilities improve with respect to those based on local readouts of the output qubits.

This work paves the way to several prospective research lines. For example, *(i)* searching for alternative mapping and encoding strategies to expand the partial Fourier decomposition of the generated output, and thus enlarge the approximation efficiency of the network, such as using different building blocks for the QNN like multi-level qudits [281] or unbounded quantum systems; *(ii)* looking for applications where the designed QNN acts as a new element in a larger quantum protocol. In this context, there is the potential to design novel neural network-based quantum gates [266], which expand the quantum computing toolkit and streamline the complexity of existing algorithms. These gates can be engineered to influence the response of specific observables to input signals [248], opening the door to new sensing schemes, as well as providing efficient representation and classification of large quantum many-body systems [282, 283].

Chapter 5

Conclusions

This thesis presents a comprehensive exploration of the properties, manipulation, and applications of nitrogen-vacancy (NV) centers in diamond, quantum neural networks, and their potential for advancing quantum technologies. Across the three chapters, we have systematically investigated and developed experimental, theoretical, and computational frameworks that contribute to the growing field of quantum science and technology. This thesis concludes by identifying several promising research topics and avenues for future exploration based on the findings and advances presented. These new directions address not only current challenges, but also leverage the developed techniques to push the boundaries of quantum science and technology further.

We successfully designed and implemented a confocal system capable of detecting and controlling single NV centers. This achievement is particularly significant, as it represents one of the first demonstrations of such a system in Spain, laying the groundwork for future quantum technology research in the region. The confocal setup, equipped with capabilities for coherent spin control and precise detection of NV center magnetic resonance, serves as a versatile tool for various quantum applications, including quantum sensing, biosensing, and quantum information processing.

The practical challenges and proposed enhancements, such as improved laser power measurement, more stable optical configurations, and the potential for further miniaturization, highlight the ongoing need for refinement in experimental setups. These improvements aim to improve the reliability, precision, and accessibility of the system, ultimately broadening its applicability and impact within the quantum research community.

The study on the PES of the NV center provides deep insights into the photon emission processes, linking the qubit state with the detected photon stream, and exploring state-readout optimization. By experimentally validating the PES model, we confirmed its utility in characterizing the dynamics of the center of NV in various scenarios, including magnetic sensing experiments. The characterization contribution extends beyond the NV centers, as the PES method can be adapted to other color centers and quantum systems. The ability of the model to incorporate other complex phenomena like ionization, wave-length dependence, and two-photon absorption offers a powerful tool for refining current NV center measurements, proposing new read-out techniques, and ultimately enhancing the sensitivity and precision of quantum sensing devices.

Finally, we analyzed the expressivity of universal data re-uploading Quantum Neural Networks (QNNs) and their performance in regression tasks. By quantifying the expressivity using a partial Fourier series representation, we identified the limitations and strengths of their approximation capabilities. The results demonstrate that entanglement, whether introduced through global readouts or entangling layers, significantly enhances the expressivity of the network and improves its approximation accuracy.

This work opens up new research avenues, including the exploration of alternative encoding strategies to expand the expressivity of the QNN and their integration into larger quantum protocols. The potential to design novel neural network-based quantum gates and their applications in quantum sensing and classification of quantum many-body systems underscores the versatility and promise of QNNs in advancing quantum computing and machine learning.

Overall, this thesis makes significant contributions to the field of quantum technologies by advancing the understanding and manipulation of NV centers, developing sophisticated models for their behavior, and exploring the potential of quantum neural networks. The experimental and theoretical frameworks presented herein not only provide valuable tools for current research but also lay the foundation for future innovations in quantum sensing, computing, and information processing. As the field continues to evolve, the findings and methodologies developed in this thesis are poised to play a crucial role in the next generation of quantum technologies.

References

[1] Jun John Sakurai and Jim Napolitano. *Modern quantum mechanics*. Cambridge University Press, 2020.

[2] Vladimír Mlynárik. Introduction to nuclear magnetic resonance. *Analytical Biochemistry*, 529:4–9, 2017.

[3] Takahiro Numai and Takahiro Numai. *Fundamentals of semiconductor lasers*. Springer, 2015.

[4] Andrew D Ludlow, Martin M Boyd, Jun Ye, Ekkehard Peik, and Piet O Schmidt. Optical atomic clocks. *Reviews of Modern Physics*, 87(2):637–701, 2015.

[5] Manish Chhowalla, Debdeep Jena, and Hua Zhang. Two-dimensional semiconductors for transistors. *Nature Reviews Materials*, 1(11):1–15, 2016.

[6] Rym Bouchendira, Pierre Cladé, Saïda Guellati-Khélifa, François Nez, and François Biraben. New determination of the fine structure constant and test of the quantum electrodynamics. *Physical Review Letters*, 106(8):080801, 2011.

[7] Tilo Steinmetz, Tobias Wilken, Constanza Araujo-Hauck, Ronald Holzwarth, Theodor W Hansch, Luca Pasquini, Antonio Manescau, Sandro D'odorico, Michael T Murphy, Thomas Kentischer, et al. Laser frequency combs for astronomical observations. *Science*, 321(5894):1335–1337, 2008.

[8] Gerd Binnig and Heinrich Rohrer. Scanning tunneling microscopy. *Surface science*, 126(1-3):236–244, 1983.

[9] Reinhold Kleiner, Dieter Koelle, Frank Ludwig, and John Clarke. Superconducting quantum interference devices: State of the art and applications. *Proceedings of the IEEE*, 92(10):1534–1548, 2004.

[10] Michael Sabet Salib. *Two-dimensional electrons confined in magnetic quantum wells*. Ph.d. dissertation, State University of New York at Buffalo, Buffalo, NY, 1998. ProQuest Dissertations & Theses Global, Publication No. 9833637.

[11] Steven Chu, JE Bjorkholm, A Ashkin, and Alex Cable. Experimental observation of optically trapped atoms. *Physical review letters*, 57(3):314, 1986.

[12] David J Wineland, Robert E Drullinger, and Fred L Walls. Radiation-pressure cooling of bound resonant absorbers. *Physical Review Letters*, 40(25):1639, 1978.

[13] Jarryd J Pla, Kuan Y Tan, Juan P Dehollain, Wee H Lim, John JL Morton, David N Jamieson, Andrew S Dzurak, and Andrea Morello. A single-atom electron spin qubit in silicon. *Nature*, 489(7417):541–545, 2012.

[14] Jonathan P Dowling and Gerard J Milburn. Quantum technology: the second quantum revolution. *Philosophical Transactions of the Royal Society of London. Series A: Mathematical, Physical and Engineering Sciences*, 361(1809):1655–1674, 2003.

[15] Jason Cong. Lightning talk: Scaling up quantum compilation–challenges and opportunities. In *2023 60th ACM/IEEE Design Automation Conference (DAC)*, pages 1–2. IEEE, 2023.

[16] Masoud Mohseni, Artur Scherer, K Grace Johnson, Oded Wertheim, Matthew Otten, Navid Anjum Aadit, Kirk M Bresniker, Kerem Y Camsari, Barbara Chapman, Soumitra Chatterjee, et al. How to build a quantum supercomputer: Scaling challenges and opportunities. *arXiv preprint arXiv:2411.10406 [quant-ph]*, nov 2024.

[17] Mark A Eriksson, Mark Friesen, Susan N Coppersmith, Robert Joynt, Levente J Klein, Keith Slinker, Charles Tahan, PM Mooney, Jack O Chu, and SJ Koester. Spin-based quantum dot quantum computing in silicon. *Quantum Information Processing*, 3:133–146, 2004.

[18] Morten Kjaergaard, Mollie E Schwartz, Jochen Braumüller, Philip Krantz, Joel I-J Wang, Simon Gustavsson, and William D Oliver. Superconducting qubits: Current state of play. *Annual Review of Condensed Matter Physics*, 11(1):369–395, 2020.

[19] Lilian Childress, Ronald Walsworth, and Mikhail Lukin. Atom-like crystal defects: From quantum computers to biological sensors. *Physics Today*, 67(10):38–43, 2014.

[20] Jun Ye and Peter Zoller. Essay: Quantum sensing with atomic, molecular, and optical platforms for fundamental physics. *Physical Review Letters*, 132(19):190001, 2024.

[21] David P DiVincenzo and Daniel Loss. Quantum computers and quantum coherence. *Journal of Magnetism and Magnetic Materials*, 200(1-3):202–218, 1999.

[22] Aviv Karnieli, Shai Tsesses, Renwen Yu, Nicholas Rivera, Zhexin Zhao, Ady Arie, Shanhui Fan, and Ido Kaminer. Quantum sensing of strongly coupled light-matter systems using free electrons. *Science advances*, 9(1):eadd2349, 2023.

[23] Frédéric Dupuis. The decoupling approach to quantum information theory. *arXiv preprint arXiv:1004.1641 [quant-ph]*, apr 2010.

[24] Derek F Jackson Kimball, Dmitry Budker, Timothy E Chupp, Andrew A Geraci, Shimon Kolkowitz, Jaideep T Singh, and Alexander O Sushkov. Probing fundamental physics with spin-based quantum sensors. *Physical Review A*, 108(1):010101,

2023.

[25] Jin Wang, Lin Zhou, Run-bing Li, Min Liu, and Ming-sheng Zhan. Cold atom interferometers and their applications in precision measurements. *Frontiers of Physics in China*, 4:179–189, 2009.

[26] Dietmar Drung, C Abmann, J Beyer, A Kirste, M Peters, F Ruede, and Th Schurig. Highly sensitive and easy-to-use squid sensors. *IEEE Transactions on Applied Superconductivity*, 17(2):699–704, 2007.

[27] Guoqing Wang. *Quantum Sensing and Simulation with Solid-State Defects*. PhD thesis, Massachusetts Institute of Technology, 2023.

[28] Romana Schirhagl, Kevin Chang, Michael Loretz, and Christian L Degen. Nitrogen-vacancy centers in diamond: nanoscale sensors for physics and biology. *Annual review of physical chemistry*, 65(1):83–105, 2014.

[29] Sungkun Hong, Michael S Grinolds, Linh M Pham, David Le Sage, Lan Luan, Ronald L Walsworth, and Amir Yacoby. Nanoscale magnetometry with NV centers in diamond. *MRS bulletin*, 38(2):155–161, 2013.

[30] Julia Michl, Jakob Steiner, Andrej Denisenko, Andre Bulau, Andre Zimmermann, Kazuo Nakamura, Hitoshi Sumiya, Shinobu Onoda, Philipp Neumann, Junichi Isoya, et al. Robust and accurate electric field sensing with solid state spin ensembles. *Nano letters*, 19(8):4904–4910, 2019.

[31] Junfeng Wang, Fupan Feng, Jian Zhang, Jihong Chen, Zhongcheng Zheng, Liping Guo, Wenlong Zhang, Xuerui Song, Guoping Guo, Lele Fan, et al. High-sensitivity temperature sensing using an implanted single nitrogen-vacancy center array in diamond. *Physical Review B*, 91(15):155404, 2015.

[32] David A Broadway, BC Johnson, MSJ Barson, Scott E Lillie, Nikolai Dontschuk, DJ McCloskey, Alexander Tsai, Tokuyuki Teraji, DA Simpson, Alastair Stacey, et al. Microscopic imaging of the stress tensor in diamond using in situ quantum sensors. *Nano Letters*, 19(7):4543–4550, 2019.

[33] Marcus W Doherty, Neil B Manson, Paul Delaney, Fedor Jelezko, Jörg Wrachtrup, and Lloyd CL Hollenberg. The nitrogen-vacancy colour centre in diamond. *Physics Reports*, 528(1):1–45, 2013.

[34] Takuya F Segawa and Ryuji Igarashi. Nanoscale quantum sensing with nitrogen-vacancy centers in nanodiamonds. a magnetic resonance perspective. *Progress in Nuclear Magnetic Resonance Spectroscopy*, 134:20–38, 2023.

[35] Shahriar Esmaeili, Paul Schmalenberg, Songtao Wu, Yuqing Zhou, Sean Rodrigues, Naveed Hussain, Taishi Kimura, Yukihiro Tadokoro, Shougo Higashi, Debasish Banerjee, et al. Evolution of quantum spin sensing: From bench-scale ODMR to compact integrations. *APL Materials*, 12(4):040901, April 2024.

[36] A Batalov, V Jacques, F Kaiser, P Siyushev, P Neumann, LJ Rogers, RL McMurtrie, NB Manson, F Jelezko, and J Wrachtrup. Low temperature studies of

the excited-state structure of negatively charged nitrogen-vacancy color centers in diamond. *Physical review letters*, 102(19):195506, 2009.

[37] AA Wood, A Lozovoi, RM Goldblatt, CA Meriles, and AM Martin. Wavelength dependence of nitrogen vacancy center charge cycling. *Physical Review B*, 109(13):134106, 2024.

[38] Yiwen Chu and Mikhail D. Lukin. Quantum optics with nitrogen-vacancy centers in diamond. In Claude Fabre, Vahid Sandoghdar, Nicolas Treps, and Leticia F. Cugliandolo, editors, *Quantum Optics and Nanophotonics*, volume 101 of *Lecture Notes of the Les Houches Summer School*, pages 229–270. Oxford University Press, Oxford, UK, 2017.

[39] D. Wirtitsch, G. Wachter, S. Reisenbauer, M. Gulka, V. Ivády, F. Jelezko, A. Gali, M. Nesladek, and M. Trupke. Exploiting ionization dynamics in the nitrogen vacancy center for rapid, high-contrast spin, and charge state initialization. *Physical Review Research*, 5(1):013014, January 2023.

[40] Paul Delaney, James C Greer, and J Andreas Larsson. Spin-polarization mechanisms of the nitrogen-vacancy center in diamond. *Nano letters*, 10(2):610–614, 2010.

[41] X.-D. Chen, C.-H. Dong, F.-W. Sun, C.-L. Zou, J.-M. Cui, Z.-F. Han, and G.-C. Guo. Temperature dependent energy level shifts of nitrogen-vacancy centers in diamond. *Applied Physics Letters*, 99(16):161903, October 2011.

[42] AP Nizovtsev, S Ya Kilin, C Tietz, F Jelezko, and J Wrachtrup. Modeling fluorescence of single nitrogen–vacancy defect centers in diamond. *Physica B: Condensed Matter*, 308:608–611, 2001.

[43] Jörg Wrachtrup, S Ya Kilin, and AP Nizovtsev. Quantum computation using the 13 c nuclear spins near the single NV defect center in diamond. *Optics and Spectroscopy*, 91:429–437, 2001.

[44] MD Lukin and PR Hemmer. Quantum entanglement via optical control of atom-atom interactions. *Physical review letters*, 84(13):2818, 2000.

[45] Wanli Yang, Zhenyu Xu, Mang Feng, and Jiangfeng Du. Entanglement of separate nitrogen-vacancy centers coupled to a whispering-gallery mode cavity. *New Journal of Physics*, 12(11):113039, 2010.

[46] Florian Dolde, Marcus W Doherty, Julia Michl, Ingmar Jakobi, Boris Naydenov, Sebastien Pezzagna, Jan Meijer, Philipp Neumann, Fedor Jelezko, Neil B Manson, et al. Nanoscale detection of a single fundamental charge in ambient conditions using the NV-center in diamond. *Physical review letters*, 112(9):097603, 2014.

[47] J-P Tetienne, T Hingant, J-V Kim, L Herrera Diez, J-P Adam, K Garcia, J-F Roch, S Rohart, A Thiaville, D Ravelosona, et al. Nanoscale imaging and control of domain-wall hopping with a nitrogen-vacancy center microscope. *Science*, 344(6190):1366–1369, 2014.

[48] Gopalakrishnan Balasubramanian, Andrii Lazariev, Sri Ranjini Arumugam, and De-wen Duan. Nitrogen-vacancy color center in diamond—emerging nanoscale applications in bioimaging and biosensing. *Current opinion in chemical biology*, 20:69–77, 2014.

[49] Bo Bao, Yu Hua, Ridong Wang, and Dachao Li. Quantum-based magnetic field sensors for biosensing. *Advanced Quantum Technologies*, 6(5):2200146, May 2023.

[50] Nati Aharon, Amit Rotem, Liam P. McGuinness, Fedor Jelezko, Alex Retzker, and Zohar Ringel. NV center based nano-NMR enhanced by deep learning. *Scientific Reports*, 9(1):17802, November 2019.

[51] Sora Kawai, Hayate Yamano, Takahiro Sonoda, Kanami Kato, Jorge J Buendia, Taisuke Kageura, Ryosuke Fukuda, Takuma Okada, Takashi Tanii, Taisei Higuchi, et al. Nitrogen-terminated diamond surface for nanoscale NMR by shallow nitrogen-vacancy centers. *The Journal of Physical Chemistry C*, 123(6):3594–3604, 2019.

[52] Mariusz Radtke, Ettore Bernardi, Abdallah Slablab, Richard Nelz, and Elke Neu. Nanoscale sensing based on nitrogen vacancy centers in single crystal diamond and nanodiamonds: Achievements and challenges. *Nano Futures*, 3(4):042004, 2019.

[53] Ekaterina Moreva. The biosensing with NV centers in diamond: Related challenges. *International Journal of Quantum Information*, 18(01):1941023, 2020.

[54] Vikas K Sewani, Hyma H Vallabhapurapu, Yang Yang, Hannes R Firgau, Chris Adambukulam, Brett C Johnson, Jarryd J Pla, and Arne Laucht. Coherent control of NV-centers in diamond in a quantum teaching lab. *American Journal of Physics*, 88(12):1156–1169, 2020.

[55] Eric M Kessler, Igor Lovchinsky, Alexander O Sushkov, and Mikhail D Lukin. Quantum error correction for metrology. *Physical review letters*, 112(15):150802, 2014.

[56] Linh My Pham, Nir Bar-Gill, Chinmay Belthangady, David Le Sage, Paola Cappellaro, Mikhail D Lukin, Amir Yacoby, and Ronald L Walsworth. Enhanced solid-state multispin metrology using dynamical decoupling. *Physical Review B—Condensed Matter and Materials Physics*, 86(4):045214, 2012.

[57] Jacob Biamonte, Peter Wittek, Nicola Pancotti, Patrick Rebentrost, Nathan Wiebe, and Seth Lloyd. Quantum machine learning. *Nature*, 549:195–202, 2017.

[58] Maria Schuld, Ilya Sinayskiy, and Francesco Petruccione. An introduction to quantum machine learning. *Contemporary Physics*, 56(2):172–185, 2015.

[59] X-L Ouyang, X-Z Huang, Y-K Wu, W-G Zhang, X Wang, H-L Zhang, L He, X-Y Chang, and L-M Duan. Experimental demonstration of quantum-enhanced machine learning in a nitrogen-vacancy-center system. *Physical Review A*, 101(1):012307, 2020.

[60] Maria Schuld, Ilya Sinayskiy, and Francesco Petruccione. Quantum computing for pattern classification. In *PRICAI 2014: Trends in Artificial Intelligence: 13th*

Pacific Rim International Conference on Artificial Intelligence, Gold Coast, QLD, Australia, December 1-5, 2014. Proceedings 13, pages 208–220. Springer, 2014.

[61] Laszlo Gyongyosi and Sandor Imre. Optimizing high-efficiency quantum memory with quantum machine learning for near-term quantum devices. *Scientific reports*, 10(1):135, 2020.

[62] Zainab Abohashima, Mohamed Elhosen, Essam H. Houssein, and Waleed M. Mohamed. Classification with quantum machine learning: A survey. *arXiv preprint arXiv:2006.12270 [quant-ph]*, jun 2020.

[63] Greta Andrini, Francesco Amanti, Fabrizio Armani, Vittorio Bellani, Vincenzo Bonaiuto, Simone Cammarata, Matteo Campostrini, Thu Ha Dao, Fabio De Matteis, Valeria Demontis, et al. Solid-state color centers for single-photon generation. In *Photonics*, volume 11, page 188. MDPI, 2024.

[64] O. Orwa, J. C. Santori, K. M. C. Fu, B. Gibson, D. Simpson, I. Aharonovich, A. Stacey, A. Cimmino, P. Balog, M. Markham, and J. Twitchen, D.˙Engineering of nitrogen-vacancy color centers in high purity diamond by ion implantation and annealing. *Journal of Applied Physics*, 109(8):083530, April 2011.

[65] Suzanne B. Van Dam, Michael Walsh, Maarten J. Degen, Eric Bersin, Sara L. Mouradian, Airat Galiullin, Maximilian Ruf, Mark IJspeert, Tim H. Taminiau, Ronald Hanson, and Dirk R. Englund. Optical coherence of diamond nitrogen-vacancy centers formed by ion implantation and annealing. *Physical Review B*, 99(16):161203, April 2019.

[66] Mikhail A Lobaev, Alexei M Gorbachev, Sergey A Bogdanov, Anatoly L Vikharev, Dmitry B Radishev, Vladimir A Isaev, and Mikhail N Drozdov. NV-center formation in single crystal diamond at different CVD growth conditions. *physica status solidi (a)*, 215(22):1800205, 2018.

[67] David A Hopper, Henry J Shulevitz, and Lee C Bassett. Spin readout techniques of the nitrogen-vacancy center in diamond. *Micromachines*, 9(9):437, 2018.

[68] Idan Meirzada, Sigal A Wolf, Alex Naiman, Uriel Levy, and Nir Bar-Gill. Enhanced spin state readout of nitrogen-vacancy centers in diamond using infrared fluorescence. *Physical Review B*, 100(12):125436, 2019.

[69] Sigal A. Wolf, Idan Meirzada, Gvirtzman Haim, and Nir BarGill. Nitrogen-vacancy singlet-manifold ionization energy. *Physical Review Applied*, 19(3):034076, March 2023.

[70] Marcus W Doherty, Victor M Acosta, Andrey Jarmola, Michael SJ Barson, Neil B Manson, Dmitry Budker, and Lloyd CL Hollenberg. Temperature shifts of the resonances of the NV-center in diamond. *Physical Review B*, 90(4):041201, 2014.

[71] I. Panadero, H. Espinós, L. Tsunaki, K. Volkova, A. Tobalina, J. Casanova, P. Acedo, B. Naydenov, R. Puebla, and E. Torrontegui. Photon-emission statistics for single nitrogen-vacancy centers. *Phys. Rev. Appl.*, 22:014035, Jul 2024.

[72] Kseniia Volkova, Julia Heupel, Sergei Trofimov, Fridtjof Betz, Rémi Colom, Rowan MacQueen, Sapida Akhundzada, Meike Reginka, Arno Ehresmann, Johann Reithmaier, Sven Burger, Cyril Popov, and Boris Naydenov. Optical and spin properties of NV center ensembles in diamond nano-pillars. *Nanomaterials*, 12:1516, 04 2022.

[73] Romana Schirhagl, Kevin Chang, Michael Loretz, and Christian L Degen. Nitrogen-vacancy centers in diamond: nanoscale sensors for physics and biology. *Annu. Rev. Phys. Chem*, 65(1):83–105, 2014.

[74] K. Jensen, V. M. Acosta, A. Jarmola, and D. Budker. Light narrowing of magnetic resonances in ensembles of nitrogen-vacancy centers in diamond. *Physical Review B*, 87(1):014115, jan 2013.

[75] Jia-Wei Ji, Yu-Feng Wu, Stephen C Wein, Faezeh Kimiaee Asadi, Roohollah Ghobadi, and Christoph Simon. Proposal for room-temperature quantum repeaters with nitrogen-vacancy centers and optomechanics. *Quantum*, 6:669, 2022.

[76] WL Yang, ZQ Yin, Y Hu, M Feng, and JF Du. High-fidelity quantum memory using nitrogen-vacancy center ensemble for hybrid quantum computation. *Physical Review A—Atomic, Molecular, and Optical Physics*, 84(1):010301, 2011.

[77] Chenyong Ju, Chao Lei, Xiangkun Xu, Dimitrie Culcer, Zhenyu Zhang, and Jiangfeng Du. NV-center-based digital quantum simulation of a quantum phase transition in topological insulators. *Physical Review B*, 89(4):045432, 2014.

[78] Florian Dolde, Helmut Fedder, Marcus W Doherty, Tobias Nöbauer, Florian Rempp, Gopalakrishnan Balasubramanian, Thomas Wolf, Friedemann Reinhard, Lloyd CL Hollenberg, Fedor Jelezko, et al. Electric-field sensing using single diamond spins. *Nature Physics*, 7(6):459–463, 2011.

[79] Viktor Ivády, Tamás Simon, Jeronimo R Maze, IA Abrikosov, and Adam Gali. Pressure and temperature dependence of the zero-field splitting in the ground state of NV centers in diamond: A first-principles study. *Physical Review B*, 90(23):235205, 2014.

[80] Andrey Jarmola, Sean Lourette, Victor M Acosta, A Glen Birdwell, Peter Blümler, Dmitry Budker, Tony Ivanov, and Vladimir S Malinovsky. Demonstration of diamond nuclear spin gyroscope. *Science advances*, 7(43):eabl3840, 2021.

[81] C Munuera-Javaloy, A Tobalina, and J Casanova. High-resolution NMR spectroscopy at large fields with nitrogen vacancy centers. *Physical Review Letters*, 130(13):133603, 2023.

[82] Man Zhao, Qijing Lin, Qingzhi Meng, Wenjun Shan, Liangquan Zhu, Yao Chen, Libo Zhao, and Zhuangde Jiang. Efficient fluorescence coupling microlens integrated fiber magnetometer probe based on nitrogen vacancy centers. *Optics Letters*, 48(15):4045–4048, 2023.

[83] Roland Albrecht, Alexander Bommer, Christian Deutsch, Jakob Reichel, and

Christoph Becher. Coupling of a single nitrogen-vacancy center in diamond to a fiber-based microcavity. *Physical review letters*, 110(24):243602, 2013.

[84] So Chigusa, Masashi Hazumi, Ernst David Herbschleb, Norikazu Mizuochi, and Kazunori Nakayama. Light dark matter search with nitrogen-vacancy centers in diamonds. *Journal of High Energy Physics*, 2025(3):083, March 2025.

[85] So Chigusa, Masashi Hazumi, Ernst David Herbschleb, Yuichiro Matsuzaki, Norikazu Mizuochi, and Kazunori Nakayama. Nuclear spin metrology with nitrogen vacancy center in diamond for axion dark matter detection. *Phys. Rev. D*, 111(7):075028, April 2025. Received 14 August 2024; Accepted 9 April 2025; Published 29 April 2025.

[86] Changhao Li, Rouhollah Soleyman, Mohammad Kohandel, and Paola Cappellaro. SARS-CoV-2 quantum sensor based on nitrogen-vacancy centers in diamond. *Nano letters*, 22(1):43–49, 2021.

[87] Yuchen Feng, Qi Zhao, Yuxi Shi, Guanyue Gao, and Jinfang Zhi. Recent applications of fluorescent nanodiamonds containing nitrogen-vacancy centers in biosensing. *Functional Diamond*, 2(1):192–203, 2022.

[88] Lilian Childress and Ronald Hanson. Diamond NV centers for quantum computing and quantum networks. *MRS bulletin*, 38(2):134–138, 2013.

[89] T Chakraborty, F Lehmann, J Zhang, S Borgsdorf, N Wöhrl, R Remfort, V Buck, U Köhler, and D Suter. CVD growth of ultrapure diamond, generation of NV centers by ion implantation, and their spectroscopic characterization for quantum technological applications. *Physical Review Materials*, 3(6):065205, 2019.

[90] Hanno Kaupp, Thomas Hümmer, Matthias Mader, Benedikt Schlederer, Julia Benedikter, Philip Haeusser, Huan-Cheng Chang, Helmut Fedder, Theodor W Hänsch, and David Hunger. Purcell-enhanced single-photon emission from nitrogen-vacancy centers coupled to a tunable microcavity. *Physical Review Applied*, 6(5):054010, 2016.

[91] Sheng-Kai Xia, Wen-Tao Lu, Xu-Tong Zhao, Ya-Wen Xue, Zeng-Bo Xu, Shi-Yu Ge, Yang Wang, Lin-Yan Yu, Yu-Chen Bian, Si-Han An, Bo Yang, Jian-Jun Xiang, and Guan-Xiang Du. Design of a compact integrated diamond NV center quantum probe. *Chinese Physics B*, 33(5):054202, may 2024.

[92] Jens Pogorzelski, Ludwig Horsthemke, Jonas Homrighausen, Dennis Stiegekötter, Markus Gregor, and Peter Glösekötter. Compact and fully integrated LED quantum sensor based on NV centers in diamond. *Sensors*, 24(3):743, 2024.

[93] Jan Stegemann, Marina Peters, Ludwig Horsthemke, Nicole Langels, Peter Glösekötter, Stefan Heusler, and Markus Gregor. Modular low-cost 3d printed setup for experiments with NV centers in diamond. *European Journal of Physics*, 44(3):035402, 2023.

[94] Daiki Misonou, Kento Sasaki, Shuntaro Ishizu, Yasuaki Monnai, Kohei M. Itoh,

and Eisuke Abe. Construction and operation of a tabletop system for nanoscale magnetometry with single nitrogen-vacancy centers in diamond. *AIP Advances*, 10(2):025206, feb 2020.

[95] Man Zhao, Qijing Lin, Qingzhi Meng, Wenjun Shan, Liangquan Zhu, Yao Chen, Tao Liu, Libo Zhao, and Zhuangde Jiang. All fiber vector magnetometer based on nitrogen-vacancy center. *Nanomaterials*, 13(5):949, 2023.

[96] Donggyu Kim, Mohamed I Ibrahim, Christopher Foy, Matthew E Trusheim, Ruonan Han, and Dirk R Englund. A CMOS-integrated quantum sensor based on nitrogen–vacancy centres. *Nature Electronics*, 2(7):284–289, 2019.

[97] Baixi Du, Kun Huang, Yunlong Nie, Zichuan Zhang, Ranran Xu, Jiangong Cui, and Jie Li. High-snr magnetic field sensing using portable confocal magnetometer probe based on nitrogen vacancy centers in diamond. *IEEE Sensors Journal*, 21(21):24665–24671, 2021.

[98] Gang-Qin Liu and Xin-Yu Pan. Quantum information processing with nitrogen–vacancy centers in diamond. *Chinese Physics B*, 27(2):020304, 2018.

[99] DM Toyli, DJ Christle, A Alkauskas, BB Buckley, CG Van de Walle, and DD Awschalom. Measurement and control of single nitrogen-vacancy center spins above 600 K. *Physical Review X*, 2(3):031001, 2012.

[100] S. C. Scholten, A. J. Healey, I. O. Robertson, G. J. Abrahams, D. A. Broadway, and J.-P. Tetienne. Widefield quantum microscopy with nitrogen-vacancy centers in diamond: Strengths, limitations, and prospects. *Journal of Applied Physics*, 130(15):150902, oct 2021.

[101] Jacob M Taylor, Paola Cappellaro, Lilian Childress, Liang Jiang, Dmitry Budker, PR Hemmer, Amir Yacoby, Ronald Walsworth, and MD Lukin. High-sensitivity diamond magnetometer with nanoscale resolution. *Nature Physics*, 4(10):810–816, 2008.

[102] Matthias Kost, Jianming Cai, and Martin B Plenio. Resolving single molecule structures with nitrogen-vacancy centers in diamond. *Scientific reports*, 5(1):11007, 2015.

[103] Zhaxylyk A Kudyshev, Demid Sychev, Zachariah Martin, Omer Yesilyurt, Simeon I Bogdanov, Xiaohui Xu, Pei-Gang Chen, Alexander V Kildishev, Alexandra Boltasseva, and Vladimir M Shalaev. Machine learning assisted quantum super-resolution microscopy. *Nature communications*, 14(1):4828, 2023.

[104] Thomas Oeckinghaus, Rainer Stöhr, Roman Kolesov, Julia Tisler, Friedemann Reinhard, and Jörg Wrachtrup. A compact, diode laser based excitation system for microscopy of NV centers. *Review of Scientific Instruments*, 85(7):073101, jul 2014.

[105] JH Shim, I Niemeyer, J Zhang, and D Suter. Room-temperature high-speed nuclear-spin quantum memory in diamond. *Physical Review A—Atomic, Molecular, and*

Optical Physics, 87(1):012301, 2013.

[106] Sebastian Zaiser, Torsten Rendler, Ingmar Jakobi, Thomas Wolf, Sang-Yun Lee, Samuel Wagner, Ville Bergholm, Thomas Schulte-Herbrüggen, Philipp Neumann, and Jörg Wrachtrup. Enhancing quantum sensing sensitivity by a quantum memory. *Nature communications*, 7(1):12279, 2016.

[107] D Marcos, Martijn Wubs, JM Taylor, R Aguado, Mikhail D Lukin, and Anders Søndberg Sørensen. Coupling nitrogen-vacancy centers in diamond to superconducting flux qubits. *Physical review letters*, 105(21):210501, 2010.

[108] Xing Rong, Jianpei Geng, Fazhan Shi, Ying Liu, Kebiao Xu, Wenchao Ma, Fei Kong, Zhen Jiang, Yang Wu, and Jiangfeng Du. Experimental fault-tolerant universal quantum gates with solid-state spins under ambient conditions. *Nature communications*, 6(1):8748, 2015.

[109] Florian Dolde, Ingmar Jakobi, Boris Naydenov, Nan Zhao, Sebastien Pezzagna, Christina Trautmann, Jan Meijer, Philipp Neumann, Fedor Jelezko, and Jörg Wrachtrup. Room-temperature entanglement between single defect spins in diamond. *Nature Physics*, 9(3):139–143, 2013.

[110] Florian Dolde, Ville Bergholm, Ya Wang, Ingmar Jakobi, Boris Naydenov, Sébastien Pezzagna, Jan Meijer, Fedor Jelezko, Philipp Neumann, Thomas Schulte-Herbrüggen, et al. High-fidelity spin entanglement using optimal control. *Nature communications*, 5(1):3371, 2014.

[111] Akihiro Kuwahata, Takahiro Kitaizumi, Kota Saichi, Takumi Sato, Ryuji Igarashi, Takeshi Ohshima, Yuta Masuyama, Takayuki Iwasaki, Mutsuko Hatano, Fedor Jelezko, et al. Magnetometer with nitrogen-vacancy center in a bulk diamond for detecting magnetic nanoparticles in biomedical applications. *Scientific reports*, 10(1):2483, 2020.

[112] Raffaele Santagati, Antonio A Gentile, Sebastian Knauer, Simon Schmitt, Stefano Paesani, Christopher Granade, Nathan Wiebe, Christian Osterkamp, Liam P McGuinness, Jianwei Wang, et al. Magnetic-field learning using a single electronic spin in diamond with one-photon readout at room temperature. *Physical Review X*, 9(2):021019, 2019.

[113] Christian L Degen, Friedemann Reinhard, and Paola Cappellaro. Quantum sensing. *Reviews of modern physics*, 89(3):035002, 2017.

[114] Sreetama Das, Jingfu Zhang, Stefano Martina, Dieter Suter, and Filippo Caruso. Quantum pattern recognition on real quantum processing units. *Quantum Machine Intelligence*, 5(1):16, 2023.

[115] Carl W Helstrom. Quantum detection and estimation theory. *Journal of Statistical Physics*, 1:231–252, 1969.

[116] Alexander S Holevo. *Statistical structure of quantum theory*. Springer Science & Business Media, 2001.

[117] Dénes Petz and Catalin Ghinea. Introduction to quantum Fisher information. In *Quantum probability and related topics*, pages 261–281. World Scientific, 2011.

[118] Jing Liu, Haidong Yuan, Xiao-Ming Lu, and Xiaoguang Wang. Quantum Fisher information matrix and multiparameter estimation. *Journal of Physics A: Mathematical and Theoretical*, 53(2):023001, 2020.

[119] Hossein T Dinani, Dominic W Berry, Raul Gonzalez, Jeronimo R Maze, and Cristian Bonato. Bayesian estimation for quantum sensing in the absence of single-shot detection. *Physical Review B*, 99(12):125413, 2019.

[120] Kwan Kit Lee, Christos N Gagatsos, Saikat Guha, and Amit Ashok. Quantum-inspired multi-parameter adaptive bayesian estimation for sensing and imaging. *IEEE Journal of Selected Topics in Signal Processing*, 17(2):491–501, 2022.

[121] Lukas J Fiderer, Jonas Schuff, and Daniel Braun. Neural-network heuristics for adaptive bayesian quantum estimation. *Prx Quantum*, 2(2):020303, 2021.

[122] Liang-Ying Chih. *Machine-Learning-Based Design of Quantum Systems for Extreme Sensing*. PhD thesis, University of Colorado at Boulder, 2022.

[123] Xin Meng, Youwei Zhang, Xichang Zhang, Shenchao Jin, Tingran Wang, Liang Jiang, Liantuan Xiao, Suotang Jia, and Yanhong Xiao. Machine learning assisted vector atomic magnetometry. *Nature Communications*, 14(1):6105, 2023.

[124] Hans Hohenfeld, Dirk Heimann, Felix Wiebe, and Frank Kirchner. Quantum deep reinforcement learning for robot navigation tasks. *IEEE Access*, 12:87217–87236, jan 2024.

[125] Suhui Jeong, Sanghyun Kim, and Jiwon Seo. Quantum support vector machine-based classification of GPS signal reception conditions. In *Workshops Program, Posters Program, Panels Program and Tutorials Program*, volume 2 of *Proceedings – IEEE Quantum Week 2024, QCE 2024*, pages 530–531, Montreal, Canada, September 2024. Institute of Electrical and Electronics Engineers, Inc.

[126] Dylan G Stone and Carlo Bradac. Machine and quantum learning for diamond-based quantum applications. *Materials for Quantum Technology*, 3(1):012001, 2023.

[127] Zhaxylyk A Kudyshev, Simeon I Bogdanov, Theodor Isacsson, Alexander V Kildishev, Alexandra Boltasseva, and Vladimir M Shalaev. Rapid classification of quantum sources enabled by machine learning. *Advanced Quantum Technologies*, 3(10):2000067, 2020.

[128] Peng Qian, Xue Lin, Feifei Zhou, Runchuan Ye, Yunlan Ji, Bing Chen, Guangjun Xie, and Nanyang Xu. Machine-learning-assisted electron-spin readout of nitrogen-vacancy center in diamond. *Applied Physics Letters*, 118(8):084001, feb 2021.

[129] Jianwei Wang, Stefano Paesani, Raffaele Santagati, Sebastian Knauer, Antonio A Gentile, Nathan Wiebe, Maurangelo Petruzzella, Jeremy L O'brien, John G Rarity, Anthony Laing, et al. Experimental quantum hamiltonian learning. *Nature Physics*,

13(6):551–555, 2017.

[130] Sanjay Gupta and R.K.P. Zia. Quantum neural networks. *Journal of Computer and System Sciences*, 63(3):355–383, 2001.

[131] Amira Abbas, David Sutter, Christa Zoufal, Aurélien Lucchi, Alessio Figalli, and Stefan Woerner. The power of quantum neural networks. *Nature Computational Science*, 1(6):403–409, 2021.

[132] Giacomo Nannicini. Fast quantum subroutines for the simplex method. *Operations Research*, 72(2):763–780, 2024.

[133] Liming Zhao, Zhikuan Zhao, Patrick Rebentrost, and Joseph Fitzsimons. Compiling basic linear algebra subroutines for quantum computers. *Quantum Machine Intelligence*, 3(2):21, 2021.

[134] Tameem Albash and Daniel A Lidar. Adiabatic quantum computation. *Reviews of Modern Physics*, 90(1):015002, 2018.

[135] Sofiene Jerbi, Casper Gyurik, Simon C Marshall, Riccardo Molteni, and Vedran Dunjko. Shadows of quantum machine learning. *Nature Communications*, 15(1):5676, 2024.

[136] Joseph Bowles, Shahnawaz Ahmed, and Maria Schuld. Better than classical? the subtle art of benchmarking quantum machine learning models. *arXiv preprint arXiv:2403.07059 [quant-ph]*, mar 2024.

[137] Anna Dawid, Julian Arnold, Borja Requena, Alexander Gresch, Marcin Płodzień, Kaelan Donatella, Kim A. Nicoli, Paolo Stornati, Rouven Koch, Miriam Büttner, Robert Okuła, Gorka Muñoz-Gil, Rodrigo A. Vargas-Hernández, Alba Cervera-Lierta, Juan Carrasquilla, Vedran Dunjko, Marylou Gabrié, Patrick Huembeli, Evert van Nieuwenburg, Filippo Vicentini, Lei Wang, Sebastian J. Wetzel, Giuseppe Carleo, Eliška Greplová, Roman Krems, Florian Marquardt, Michał Tomza, Maciej Lewenstein, and Alexandre Dauphin. *Machine Learning in Quantum Sciences*. Cambridge University Press, Cambridge, UK, jun 2025.

[138] Maria Schuld and Nathan Killoran. Is quantum advantage the right goal for quantum machine learning? *PRX Quantum*, 3:030101, jul 2022.

[139] Kaitlin Gili, Marta Mauri, and Alejandro Perdomo-Ortiz. Generalization metrics for practical quantum advantage in generative models. *Physical Review Applied*, 21(4):044032, 2024.

[140] Adrián Pérez-Salinas, Alba Cervera-Lierta, Elies Gil-Fuster, and José I. Latorre. Data re-uploading for a universal quantum classifier. *Quantum*, 4:226, February 2020.

[141] Loïc Rondin, Jean-Philippe Tetienne, Thomas Hingant, Jean-François Roch, Patrick Maletinsky, and Vincent Jacques. Magnetometry with nitrogen-vacancy defects in diamond. *Reports on progress in physics*, 77(5):056503, 2014.

[142] Fedor Jelezko and Jörg Wrachtrup. Single defect centres in diamond: A review. *physica status solidi (a)*, 203(13):3207–3225, 2006.

[143] Wesley Wei-Wen Hsiao, Yuen Yung Hui, Pei-Chang Tsai, and Huan-Cheng Chang. Fluorescent nanodiamond: a versatile tool for long-term cell tracking, super-resolution imaging, and nanoscale temperature sensing. *Accounts of chemical research*, 49(3):400–407, 2016.

[144] Kin On Ho, King Cho Wong, Man Yin Leung, Yiu Yung Pang, Wai Kuen Leung, King Yau Yip, Wei Zhang, Jianyu Xie, Swee K Goh, and Sen Yang. Recent developments of quantum sensing under pressurized environment using the nitrogen vacancy (NV) center in diamond. *Journal of Applied Physics*, 129(24):241101, 2021.

[145] HJ Mamin, M Kim, MH Sherwood, CT Rettner, K Ohno, DD Awschalom, and D Rugar. Nanoscale nuclear magnetic resonance with a nitrogen-vacancy spin sensor. *Science*, 339(6119):557–560, 2013.

[146] Alp Sipahigil, Michael Lurie Goldman, Emre Togan, Yiwen Chu, Matthew Markham, Daniel J Twitchen, Alexander S Zibrov, Alexander Kubanek, and Mikhail D Lukin. Quantum interference of single photons from remote nitrogen-vacancy centers in diamond. *Physical review letters*, 108(14):143601, 2012.

[147] Matthias Leifgen, Tim Schröder, Friedemann Gädeke, Robert Riemann, Valentin Métillon, Elke Neu, Christian Hepp, Carsten Arend, Christoph Becher, Kristian Lauritsen, et al. Evaluation of nitrogen-and silicon-vacancy defect centres as single photon sources in quantum key distribution. *New journal of physics*, 16(2):023021, 2014.

[148] Chun-Hsu Su, Andrew D Greentree, and Lloyd CL Hollenberg. Towards a picosecond transform-limited nitrogen-vacancy based single photon source. *Optics Express*, 16(9):6240–6250, 2008.

[149] Beatrice Rodiek, Marco Lopez, Helmuth Hofer, Geiland Porrovecchio, Marek Smid, Xiao-Liu Chu, Stephan Gotzinger, Vahid Sandoghdar, Sarah Lindner, Christoph Becher, et al. Experimental realization of an absolute single-photon source based on a single nitrogen vacancy center in a nanodiamond. *Optica*, 4(1):71–76, 2017.

[150] Lucio Robledo, Hannes Bernien, Toeno Van Der Sar, and Ronald Hanson. Spin dynamics in the optical cycle of single nitrogen-vacancy centres in diamond. *New Journal of Physics*, 13(2):025013, 2011.

[151] F. Poggiali, P. Cappellaro, and N. Fabbri. Measurement of the excited-state transverse hyperfine coupling in NV centers via dynamic nuclear polarization. *Phys. Rev. B*, 95:195308, May 2017.

[152] Marcis Auzinsh, Andris Berzins, Dmitry Budker, Laima Busaite, Ruvin Ferber, Florian Gahbauer, Reinis Lazda, Arne Wickenbrock, and Huijie Zheng. Hyperfine level structure in nitrogen-vacancy centers near the ground-state level anticrossing. *Physical Review B*, 100(7):075204, 2019.

[153] Viktor Ivády, Huijie Zheng, Arne Wickenbrock, Lykourgos Bougas, Georgios Chatzidrosos, Kazuo Nakamura, Hitoshi Sumiya, Takeshi Ohshima, Junichi Isoya, Dmitry Budker, et al. Photoluminescence at the ground-state level anticrossing of the nitrogen-vacancy center in diamond: A comprehensive study. *Physical Review B*, 103(3):035307, 2021.

[154] W Schmunk, Marco Gramegna, Giorgio Brida, Ivo Pietro Degiovanni, Marco Genovese, H Hofer, S Kück, L Lolli, MGA Paris, S Peters, et al. Photon number statistics of NV centre emission. *Metrologia*, 49(2):S156, 2012.

[155] Vasily V Temnov and Ulrike Woggon. Photon statistics in the cooperative spontaneous emission. *Optics express*, 17(7):5774–5782, 2009.

[156] Richard J. Cook. Photon number statistics in resonance fluorescence. *Phys. Rev. A*, 23:1243–1250, Mar 1981.

[157] Yujun Zheng and Frank L. H. Brown. Single-molecule photon counting statistics via generalized optical bloch equations. *Phys. Rev. Lett.*, 90:238305, Jun 2003.

[158] Benjamin D'Anjou and William A Coish. Enhancing qubit readout through dissipative sub-poissonian dynamics. *Physical Review A*, 96(5):052321, 2017.

[159] Canran Xu and Maxim G. Vavilov. Full counting statistics of photons emitted by a double quantum dot. *Phys. Rev. B*, 88:195307, Nov 2013.

[160] Samuel L Rudge and Daniel S Kosov. Counting quantum jumps: A summary and comparison of fixed-time and fluctuating-time statistics in electron transport. *The Journal of Chemical Physics*, 151(3):034107, 2019.

[161] Benjamin D'Anjou, Loutfi Kuret, Lilian Childress, and William A Coish. Maximal adaptive-decision speedups in quantum-state readout. *Physical Review X*, 6(1):011017, 2016.

[162] N. B. Manson, J. P. Harrison, and M. J. Sellars. Nitrogen-vacancy center in diamond: Model of the electronic structure and associated dynamics. *Phys. Rev. B*, 74:104303, Sep 2006.

[163] Howard J. Carmichael. *An Open Systems Approach to Quantum Optics: Lectures Presented at the Université Libre de Bruxelles, October 28 to November 4, 1991*, volume 18 of *Lecture Notes in Physics Monographs*. Springer-Verlag, Berlin; Heidelberg, 1 edition, may 1993.

[164] Frans Eduard van Dorsselaer and G Nienhuis. Quantum trajectories. *Journal of Optics B: Quantum and Semiclassical Optics*, 2(4):R25, 2000.

[165] Peter Zoller and Crispin W. Gardiner. Quantum noise in quantum optics: The stochastic schrödinger equation. In Serge Reynaud, Elisabeth Giacobino, and Jean Zinn-Justin, editors, *Quantum Fluctuations*, Les Houches Summer School Session LXIII. Elsevier Science Publishers B.V., Amsterdam, 1997. Lecture Notes for Les Houches Summer School LXIII on Quantum Fluctuations; 57 pp.

[166] Lucio Robledo, Hannes Bernien, Toeno van der Sar, and Ronald Hanson. Spin dynamics in the optical cycle of single nitrogen-vacancy centres in diamond. *New Journal of Physics*, 13(2):025013, feb 2011.

[167] Crispin Gardiner and Peter Zoller. *Quantum noise: a handbook of Markovian and non-Markovian quantum stochastic methods with applications to quantum optics*. Springer Science & Business Media, 2004.

[168] HF Arnoldus and G Nienhuis. Photon statistics of fluorescence radiation. *Optica Acta: International Journal of Optics*, 33(6):691–702, 1986.

[169] Krzysztof Ptaszyński. Waiting time distribution revealing the internal spin dynamics in a double quantum dot. *Physical Review B*, 96(3):035409, 2017.

[170] HJ Carmichael, Surendra Singh, Reeta Vyas, and PR Rice. Photoelectron waiting times and atomic state reduction in resonance fluorescence. *Physical Review A*, 39(3):1200, 1989.

[171] Sigal A Wolf, Itamar Rosenberg, Ronen Rapaport, and Nir Bar-Gill. Purcell-enhanced optical spin readout of nitrogen-vacancy centers in diamond. *Physical Review B*, 92(23):235410, 2015.

[172] Janine Riedrich-Möller, Sébastien Pezzagna, Jan Meijer, Christoph Pauly, Frank Mücklich, Matthew Markham, Andrew M. Edmonds, and Christoph Becher. Nanoimplantation and Purcell enhancement of single nitrogen-vacancy centers in photonic crystal cavities in diamond. *Applied Physics Letters*, 106(22):221103, jun 2015.

[173] Jan M Binder, Alexander Stark, Nikolas Tomek, Jochen Scheuer, Florian Frank, Kay D Jahnke, Christoph Müller, Simon Schmitt, Mathias H Metsch, Thomas Unden, et al. Qudi: A modular python suite for experiment control and data processing. *SoftwareX*, 6:85–90, 2017.

[174] B. D'Anjou. Generalized figure of merit for qubit readout. *Physical Review A*, 103(4):042404, apr 2021.

[175] Jixing Zhang, Tianzheng Liu, Sigang Xia, Guodong Bian, Pengcheng Fan, Mingxin Li, Sixian Wang, Xiangyun Li, Chen Zhang, Shaoda Zhang, and Heng Yuan. Efficient real-time spin readout of nitrogen-vacancy centers based on bayesian estimation. *IEEE Transactions on Industrial Electronics*, 71(10):13341–13350, oct 2024.

[176] Philipp Neumann, Johannes Beck, Matthias Steiner, Florian Rempp, Helmut Fedder, Philip R Hemmer, Jörg Wrachtrup, and Fedor Jelezko. Single-shot readout of a single nuclear spin. *science*, 329(5991):542–544, 2010.

[177] M Steiner, P Neumann, J Beck, F Jelezko, and J Wrachtrup. Universal enhancement of the optical readout fidelity of single electron spins at nitrogen-vacancy centers in diamond. *Physical Review B*, 81(3):035205, 2010.

[178] Harald Cramér. Sur un nouveau théorème-limite de la théorie des probabilités.

Actualités Scientifiques et Industrielles, 736:5–23, 1938.

[179] Andrew C Berry. The accuracy of the gaussian approximation to the sum of independent variates. *Transactions of the american mathematical society*, 49(1):122–136, 1941.

[180] Carl-Gustav Esseen. On the Liapunov limit error in the theory of probability. *Ark. Mat. Astr. Fys.*, 28:1–19, 1942.

[181] Herman Chernoff. A measure of asymptotic efficiency for tests of a hypothesis based on the sum of observations. *The Annals of Mathematical Statistics*, pages 493–507, 1952.

[182] Koenraad MR Audenaert, John Calsamiglia, Ramón Munoz-Tapia, Emilio Bagan, Ll Masanes, Antonio Acin, and Frank Verstraete. Discriminating states: The quantum Chernoff bound. *Physical review letters*, 98(16):160501, 2007.

[183] Rebecca E. K. Fishman, Raj N. Patel, David A. Hopper, Tzu-Yung Huang, and Lee C. Bassett. Photon-emission-correlation spectroscopy as an analytical tool for solid-state quantum defects. *PRX Quantum*, 4(1):010202, mar 2023.

[184] GS Buller and RJ Collins. Single-photon generation and detection. *Measurement Science and Technology*, 21(1):012002, 2009.

[185] Marcus W Doherty, Neil B Manson, Paul Delaney, Fedor Jelezko, Jörg Wrachtrup, and Lloyd CL Hollenberg. The nitrogen-vacancy colour centre in diamond. *Physics Reports*, 528(1):1–45, 2013.

[186] Darien J. Morrow and Xuedan Ma. Noisy detectors with unmatched detection efficiency thwart identification of single photon emitters via photon coincidence correlation. *arXiv preprint arXiv:2204.07654 [quant-ph]*, apr 2022.

[187] Sebastian KH Andersen, Shailesh Kumar, and Sergey I Bozhevolnyi. Ultrabright linearly polarized photon generation from a nitrogen vacancy center in a nanocube dimer antenna. *Nano letters*, 17(6):3889–3895, 2017.

[188] Martin Berthel, Oriane Mollet, Géraldine Dantelle, Thierry Gacoin, Serge Huant, and Aurélien Drezet. Photophysics of single nitrogen-vacancy centers in diamond nanocrystals. *Physical Review B*, 91(3):035308, 2015.

[189] Roland Albrecht, Alexander Bommer, Christoph Pauly, Frank Mücklich, Andreas W Schell, Philip Engel, Tim Schröder, Oliver Benson, Jakob Reichel, and Christoph Becher. Narrow-band single photon emission at room temperature based on a single nitrogen-vacancy center coupled to an all-fiber-cavity. *Applied Physics Letters*, 105(7):073113, 2014.

[190] Dirk Englund, Brendan Shields, Kelley Rivoire, Fariba Hatami, Jelena Vuckovic, Hongkun Park, and Mikhail D Lukin. Deterministic coupling of a single nitrogen vacancy center to a photonic crystal cavity. *Nano letters*, 10(10):3922–3926, 2010.

[191] Hamidreza Siampour, Shailesh Kumar, and Sergey I Bozhevolnyi. Chip-integrated

plasmonic cavity-enhanced single nitrogen-vacancy center emission. *Nanoscale*, 9(45):17902–17908, 2017.

[192] Andrei Faraon, Charles Santori, Zhihong Huang, Victor M Acosta, and Raymond G Beausoleil. Coupling of nitrogen-vacancy centers to photonic crystal cavities in monocrystalline diamond. *Physical review letters*, 109(3):033604, 2012.

[193] M. B. Plenio and P. L. Knight. The quantum-jump approach to dissipative dynamics in quantum optics. *Reviews of Modern Physics*, 70(1):101–144, jan 1998.

[194] Vadim V Vorobyov, Alexander Yu Kazakov, Vladimir V Soshenko, Alexander A Korneev, Mikhail Y Shalaginov, Stepan V Bolshedvorskii, Vadim N Sorokin, Alexander V Divochiy, Yury B Vakhtomin, Konstantin V Smirnov, et al. Superconducting detector for visible and near-infrared quantum emitters. *Optical Materials Express*, 7(2):513–526, 2017.

[195] A. Beveratos, R. Brouri, J.-P. Poizat, and P. Grangier. Bunching and antibunching from single NV color centers in diamond. In P. Tombesi and O. Hirota, editors, *Quantum Communication, Computing, and Measurement 3*, pages 261–267. Springer, Boston, MA, 2002.

[196] Guido Burkard, Daniel Loss, and Eugene V Sukhorukov. Noise of entangled electrons: Bunching and antibunching. *Physical Review B*, 61(24):R16303, 2000.

[197] Gerard Lachs. Effects of photon bunching on shot noise in photoelectric detection. *Journal of Applied Physics*, 39(9):4193–4199, 1968.

[198] Alexios Beveratos, Sergei Kühn, Rosa Brouri, Thierry Gacoin, J-P Poizat, and Philippe Grangier. Room temperature stable single-photon source. *The European Physical Journal D-Atomic, Molecular, Optical and Plasma Physics*, 18(2):191–196, 2002.

[199] I. Aharonovich, S. Castelletto, D. A. Simpson, A. D. Greentree, and S. Prawer. Photophysics of chromium-related diamond single-photon emitters. *Physical Review A*, 81(4):043813, apr 2010.

[200] Tim Schröder, Friedemann Gädeke, Moritz Julian Banholzer, and Oliver Benson. Ultrabright and efficient single-photon generation based on nitrogen-vacancy centres in nanodiamonds on a solid immersion lens. *New Journal of Physics*, 13(5):055017, 2011.

[201] Shen Li, Cui-Hong Li, Bo-Wen Zhao, Yang Dong, Cong-Cong Li, Xiang-Dong Chen, Ya-Song Ge, and Fang-Wen Sun. A bright single-photon source from nitrogen-vacancy centers in diamond nanowires. *Chinese Physics Letters*, 34(9):096101, 2017.

[202] Dmitry V Obydennov, Daniil A Shilkin, Evgeny V Lyubin, Maxim R Shcherbakov, Evgeny F Ekimov, Oleg S Kudryavtsev, Igor I Vlasov, and Andrey A Fedyanin. Saturation of fluorescence from NV centers in mie-resonant diamond particles. *J. Phys.: Conf. Ser.*, 1092(1):012102, 2018.

[203] Ilya P Radko, Mads Boll, Niels M Israelsen, Nicole Raatz, Jan Meijer, Fedor Jelezko, Ulrik L Andersen, and Alexander Huck. Determining the internal quantum efficiency of shallow-implanted nitrogen-vacancy defects in bulk diamond. *Optics Express*, 24(24):27715–27725, 2016.

[204] A. Gupta, L. Hacquebard, and L. Childress. Efficient signal processing for time-resolved fluorescence detection of nitrogen-vacancy spins in diamond. *Journal of the Optical Society of America B*, 33(3):B28, jan 2016.

[205] P. Maletinsky, S. Hong, M. S. Grinolds, B. Hausmann, M. D. Lukin, R.-L. Walsworth, M. Loncar, and A. Yacoby. A robust scanning diamond sensor for nanoscale imaging with single nitrogen-vacancy centres. *Nature Nanotechnology*, 7(5):320–324, apr 2012.

[206] V. Jacques, P. Neumann, J. Beck, M. Markham, D. Twitchen, J. Meijer, F. Kaiser, G. Balasubramanian, F. Jelezko, and J. Wrachtrup. Dynamic polarization of single nuclear spins by optical pumping of nitrogen-vacancy color centers in diamond at room temperature. *Physical Review Letters*, 102(5):057403, feb 2009.

[207] Kaupo Palo, Ülo Mets, Vello Loorits, and Peet Kask. Calculation of photon-count number distributions via master equations. *Biophysical journal*, 90(6):2179–2191, 2006.

[208] G Bédard. Dead-time corrections to the statistical distribution of photoelectrons. *Proceedings of the Physical Society*, 90(1):131, 1967.

[209] Klaus Mølmer, Yvan Castin, and Jean Dalibard. Monte Carlo wave-function method in quantum optics. *JOSA B*, 10(3):524–538, 1993.

[210] Megan J Stanley, Clemens Matthiesen, Jack Hansom, C Le Gall, Carsten HH Schulte, Edmund Clarke, and Mete Atatüre. Dynamics of a mesoscopic nuclear spin ensemble interacting with an optically driven electron spin. *Physical Review B*, 90(19):195305, 2014.

[211] CL Degen, M Poggio, HJ Mamin, and D Rugar. Role of spin noise in the detection of nanoscale ensembles of nuclear spins. *Physical review letters*, 99(25):250601, 2007.

[212] Tobias Staudacher, Fazhan Shi, S Pezzagna, Jan Meijer, Jiangfeng Du, Carlos A Meriles, Friedemann Reinhard, and Joerg Wrachtrup. Nuclear magnetic resonance spectroscopy on a (5-nanometer) 3 sample volume. *Science*, 339(6119):561–563, 2013.

[213] Carlos A Meriles, Liang Jiang, Garry Goldstein, Jonathan S Hodges, Jeronimo Maze, Mikhail D Lukin, and Paola Cappellaro. Imaging mesoscopic nuclear spin noise with a diamond magnetometer. *The Journal of chemical physics*, 133(12), 2010.

[214] Brendan J Shields, Quirin P Unterreithmeier, Nathalie P de Leon, H Park, and Mikhail D Lukin. Efficient readout of a single spin state in diamond via spin-to-

charge conversion. *Physical review letters*, 114(13):136402, 2015.

[215] Michal Gulka, Emilie Bourgeois, Jaroslav Hruby, Petr Siyushev, Georg Wachter, Friedrich Aumayr, Philip R Hemmer, Adam Gali, Fedor Jelezko, Michael Trupke, et al. Pulsed photoelectric coherent manipulation and detection of N-V center spins in diamond. *Physical Review Applied*, 7(4):044032, 2017.

[216] Petr Siyushev, Milos Nesladek, Emilie Bourgeois, Michal Gulka, Jaroslav Hruby, Takashi Yamamoto, Michael Trupke, Tokuyuki Teraji, Junichi Isoya, and Fedor Jelezko. Photoelectrical imaging and coherent spin-state readout of single nitrogen-vacancy centers in diamond. *Science*, 363(6428):728–731, 2019.

[217] Felix M Stürner, Andreas Brenneis, Julian Kassel, Uwe Wostradowski, Robert Rölver, Tino Fuchs, Kazuo Nakamura, Hitoshi Sumiya, Shinobu Onoda, Junichi Isoya, et al. Compact integrated magnetometer based on nitrogen-vacancy centres in diamond. *Diamond and Related Materials*, 93:59–65, 2019.

[218] P Siyushev, H Pinto, M Vörös, A Gali, Fedor Jelezko, and J Wrachtrup. Optically controlled switching of the charge state of a single nitrogen-vacancy center in diamond at cryogenic temperatures. *Physical review letters*, 110(16):167402, 2013.

[219] Lukas Razinkovas, Marek Maciaszek, Friedemann Reinhard, Marcus W Doherty, and Audrius Alkauskas. Photoionization of negatively charged NV centers in diamond: Theory and ab initio calculations. *Physical Review B*, 104(23):235301, 2021.

[220] Solveig Felton, AM Edmonds, Mark E Newton, PM Martineau, D Fisher, and DJ Twitchen. Electron paramagnetic resonance studies of the neutral nitrogen vacancy in diamond. *Physical Review B*, 77(8):081201, 2008.

[221] Nabeel Aslam, Gerhald Waldherr, Philipp Neumann, Fedor Jelezko, and Joerg Wrachtrup. Photo-induced ionization dynamics of the nitrogen vacancy defect in diamond investigated by single-shot charge state detection. *New Journal of Physics*, 15(1):013064, 2013.

[222] Kyu Young Han, Dominik Wildanger, Eva Rittweger, J Meijer, S Pezzagna, SW Hell, and Christian Eggeling. Dark state photophysics of nitrogen–vacancy centres in diamond. *New Journal of Physics*, 14(12):123002, 2012.

[223] Xiang-Dong Chen, Lei-Ming Zhou, Chang-Ling Zou, Cong-Cong Li, Yang Dong, Fang-Wen Sun, and Guang-Can Guo. Spin depolarization effect induced by charge state conversion of nitrogen vacancy center in diamond. *Physical Review B*, 92(10):104301, 2015.

[224] Robert Chapman and Taras Plakhotnik. Anomalous saturation effects due to optical spin depolarization in nitrogen-vacancy centers in diamond nanocrystals. *Physical Review B*, 86(4):045204, 2012.

[225] Idan Meirzada, Y Hovav, SA Wolf, and N Bar-Gill. Negative charge enhancement of near-surface nitrogen vacancy centers by multicolor excitation. *Physical Review*

B, 98(24):245411, 2018.

[226] Tse-Luen Wee, Yan-Kai Tzeng, Chau-Chung Han, Huan-Cheng Chang, Wunshain Fann, Jui-Hung Hsu, Kuan-Ming Chen, and Yueh-Chung Yu. Two-photon excited fluorescence of nitrogen-vacancy centers in proton-irradiated type Ib diamond. *The Journal of Physical Chemistry A*, 111(38):9379–9386, 2007.

[227] Jiazhao Tian, Ressa S Said, Fedor Jelezko, Jianming Cai, and Liantuan Xiao. Bayesian-based hybrid method for rapid optimization of NV center sensors. *Sensors*, 23(6):3244, 2023.

[228] A Gruber, A Drabenstedt, C Tietz, L Fleury, J Wrachtrup, and C von Borczyskowski. Scanning confocal optical microscopy and magnetic resonance on single defect centers. *Science*, 276(5321):2012–2014, 1997.

[229] David Le Sage, Koji Arai, David R Glenn, Stephen J DeVience, Linh M Pham, Lilah Rahn-Lee, Mikhail D Lukin, Amir Yacoby, Arash Komeili, and Ronald L Walsworth. Optical magnetic imaging of living cells. *Nature*, 496(7446):486–489, 2013.

[230] Guoqing Wang, Yi-Xiang Liu, Yuan Zhu, and Paola Cappellaro. Nanoscale vector ac magnetometry with a single nitrogen-vacancy center in diamond. *Nano Letters*, 21(12):5143–5150, 2021.

[231] qutools GmbH. Quantum Sensing by Diamond Magnetometer (quNV), n.d. Product information for the quNV quantum diamond magnetometer.

[232] CIQTEK Co., Ltd. Diamond Quantum Computer for Education, n.d. Overview of CIQTEK's diamond quantum computing solutions for educational use.

[233] Robert H Webb. Confocal optical microscopy. *Reports on progress in physics*, 59(3):427, 1996.

[234] Ariful Haque and Sharaf Sumaiya. An overview on the formation and processing of nitrogen-vacancy photonic centers in diamond by ion implantation. *Journal of Manufacturing and Materials Processing*, 1(1):6, 2017.

[235] Jixing Zhang, Lixia Xu, Guodong Bian, Pengcheng Fan, Mingxin Li, Wuming Liu, and Heng Yuan. Diamond nitrogen–vacancy center magnetometry: Advances and challenges. *arXiv preprint arXiv:2010.10231*, oct 2020. 17 pages, 12 figures, review article.

[236] Huijin Park, Junghyun Lee, Sangwook Han, Sangwon Oh, and Hosung Seo. Decoherence of nitrogen-vacancy spin ensembles in a nitrogen electron-nuclear spin bath in diamond. *npj Quantum Information*, 8(1):95, 2022.

[237] Julia Tisler, Gopalakrishnan Balasubramanian, Boris Naydenov, Roman Kolesov, Bernhard Grotz, Rolf Reuter, Jean-Paul Boudou, Patrick A Curmi, Mohamed Sennour, Alain Thorel, et al. Fluorescence and spin properties of defects in single digit nanodiamonds. *ACS nano*, 3(7):1959–1965, 2009.

[238] Herman Y Carr and Edward M Purcell. Effects of diffusion on free precession in nuclear magnetic resonance experiments. *Physical review*, 94(3):630, 1954.

[239] Saul Meiboom and David Gill. Modified spin-echo method for measuring nuclear relaxation times. *Review of scientific instruments*, 29(8):688–691, 1958.

[240] Jonas Bylander, Simon Gustavsson, Fei Yan, Fumiki Yoshihara, Khalil Harrabi, George Fitch, David G Cory, Yasunobu Nakamura, Jaw-Shen Tsai, and William D Oliver. Noise spectroscopy through dynamical decoupling with a superconducting flux qubit. *Nature Physics*, 7(7):565–570, 2011.

[241] Nir Bar-Gill, Linh My Pham, Chinmay Belthangady, David Le Sage, Paola Cappellaro, JR Maze, Mikhail D Lukin, Amir Yacoby, and Ronald Walsworth. Suppression of spin-bath dynamics for improved coherence of multi-spin-qubit systems. *Nature communications*, 3(1):858, 2012.

[242] Danny Villanueva, Alicia G. Gubieda, Lucía Gandarias, Ana Abad Díaz de Cerio, Iñaki Orue, José Ángel García, David de Cos, Javier Alonso, and M Luisa Fdez-Gubieda. Heating efficiency of different magnetotactic bacterial species: Influence of magnetosome morphology and chain arrangement. *ACS Applied Materials & Interfaces*, 16(49):67216–67224, 2024.

[243] Alfonso Rubio-Manzanares and Belén Piorno. Spain quantum industry. Technical report, AMETIC, Madrid, Spain, September 2022.

[244] Subhash C. Kak. Quantum neural computing. In Peter W. Hawkes, editor, *Quantum Neural Computing*, volume 94 of *Advances in Imaging and Electron Physics*, pages 259–313. Elsevier, 1995.

[245] Maria Schuld and Nathan Killoran. Quantum machine learning in feature Hilbert spaces. *Phys. Rev. Lett.*, 122:040504, Feb 2019.

[246] Juan Carrasquilla and Roger G. Melko. Machine learning phases of matter. *Nature Physics*, 13:431–434, 2017.

[247] Dong-Ling Deng, Xiaopeng Li, and S. Das Sarma. Quantum entanglement in neural network states. *Phys. Rev. X*, 7:021021, May 2017.

[248] G. Torlai, G. Mazzola, J. Carrasquilla, and et al. Neural-network quantum state tomography. *Nature Physics*, 14:447–450, 2018.

[249] Thomas Fösel, Petru Tighineanu, Talitha Weiss, and Florian Marquardt. Reinforcement learning with neural networks for quantum feedback. *Phys. Rev. X*, 8:031084, Sep 2018.

[250] Giuseppe Davide Paparo, Vedran Dunjko, Adi Makmal, Miguel Angel Martin-Delgado, and Hans J. Briegel. Quantum speedup for active learning agents. *Phys. Rev. X*, 4:031002, Jul 2014.

[251] Marcello Benedetti, John Realpe-Gómez, Rupak Biswas, and Alejandro Perdomo-Ortiz. Quantum-assisted learning of hardware-embedded probabilistic graphical

models. *Phys. Rev. X*, 7:041052, Nov 2017.

[252] G Sentís, M Guta, and G Adesso. Quantum learning of coherent states. *EPJ Quantum Technology*, 2:17, 2015.

[253] V Havlícek, A D Corcóles, K Temme, A W Harrow, and et al. Quantum-assisted learning of hardware-embedded probabilistic graphical models. *Nature*, 567:209, 2019.

[254] Yang Qian, Xinbiao Wang, Yuxuan Du, Xingyao Wu, and Dacheng Tao. The dilemma of quantum neural networks. *IEEE Transactions on Neural Networks and Learning Systems*, 35(4):5603–5615, apr 2024.

[255] Lena Funcke, Tobias Hartung, Karl Jansen, Stefan Kühn, and Paolo Stornati. Dimensional Expressivity Analysis of Parametric Quantum Circuits. *Quantum*, 5:422, March 2021.

[256] Kerstin Beer, Daniel List, Gabriel Müller, Tobias J. Osborne, and Christian Struckmann. Training quantum neural networks on NISQ devices. *arXiv preprint arXiv:2104.06081 [quant-ph]*, apr 2021. 15 pages, 6 figures.

[257] A. Gratsea and P. Humbeli. Exploring quantum perceptron and quantum neural network structures with a teacher-student scheme. *Quantum Mach. Intell.*, 4:15, 2022.

[258] Samuel A. Wilkinson and Michael J. Hartmann. Evaluating the performance of sigmoid quantum perceptrons in quantum neural networks. *arXiv preprint arXiv:2208.06198 [quant-ph]*, aug 2022.

[259] Berta Casas and Alba Cervera-Lierta. Multidimensional Fourier series with quantum circuits. *Phys. Rev. A*, 107(6):062612, jun 2023.

[260] Yudong Cao, Gian Giacomo Guerreschi, and Alán Aspuru-Guzik. Quantum neuron: An elementary building block for machine learning on quantum computers. *arXiv preprint arXiv:1711.11240 [quant-ph]*, nov 2017.

[261] Edward Farhi and Hartmut Neven. Classification with quantum neural networks on near term processors. *arXiv preprint arXiv:1802.06002 [quant-ph]*, feb 2018.

[262] E. Torrontegui and J. J. García-Ripoll. Unitary quantum perceptron as efficient universal approximator. *EPL (Europhysics Letters)*, 125(3):30004, mar 2019.

[263] Stefano Mangini, Francesco Tacchino, Dario Gerace, Chiara Macchiavello, and Daniele Bajoni. Quantum computing model of an artificial neuron with continuously valued input data. *Machine Learning: Science and Technology*, 1(4):045008, oct 2020.

[264] Yue Ban, Xi Chen, Erik Torrontegui, Enrique Solano, and Jorge Casanova. Speeding up quantum perceptron via shortcuts to adiabaticity. *Sci. Rep.*, 11:5783, 2021.

[265] Yue Ban, E. Torrontegui, and J. Casanova. Quantum neural networks with

multi-qubit potentials. *Sci. Rep.*, 13:9096, 2023.

[266] P. Huber, J. Haber, P. Barthel, J. J. García-Ripoll, E. Torrontegui, and C. Wunderlich. Realization of a quantum perceptron gate with trapped ions. *arXiv preprint arXiv:2111.08977 [quant-ph]*, nov 2021.

[267] Tarun Dutta, Adrián Pérez-Salinas, Jasper Phua Sing Cheng, José Ignacio Latorre, and Manas Mukherjee. Single-qubit universal classifier implemented on an ion-trap quantum device. *Physical Review A*, 106(1):012411, jul 2022.

[268] V Havlícek, A D Corcóles, K Temme, A W Harrow, and et al. Supervised learning with quantum-enhanced feature spaces. *Nature*, 567:209–212, 2019.

[269] Marek Pechal, Federico Roy, Samuel A. Wilkinson, Gian Salis, Max Werninghaus, Michael J. Hartmann, and Stefan Filipp. Direct implementation of a perceptron in superconducting circuit quantum hardware. *Physical Review Research*, 4:033190, sep 2022.

[270] M. S. Moreira, G. G. Guerreschi, W. Vlothuizen, J. van Straten, H. van Someren, J. Marques, H. Ali, N. Muthusubramanian, C. Zachariadis, M. Beekman, N. Haider, C. Almudever A. Bruno, A. Matsuura, and L. Dicarlo. Realization of a quantum neural network by repeat-until-success circuits in a superconducting quantum processor. *APS March Meeting Abstract*, page T37. 009, 2022.

[271] G. Cybenko. Approximation by superpositions of a sigmoidal function. *Mathematics of Control, Signals, and Systems*, 2(4):303–314, dec 1989.

[272] Michael A. Nielsen and Isaac L. Chuang. *Quantum Computation and Quantum Information: 10th Anniversary Edition.* Cambridge University Press, 2010.

[273] Marcello Benedetti, Erika Lloyd, Stefan Sack, and Mattia Fiorentini. Parameterized quantum circuits as machine learning models. *Quantum Science and Technology*, 4(4):043001, nov 2019.

[274] Adrián Pérez-Salinas, David López-Núñez, Artur García-Sáez, P. Forn-Díaz, and José I. Latorre. One qubit as a universal approximant. *Phys. Rev. A*, 104:012405, Jul 2021.

[275] Maria Schuld, Ryan Sweke, and Johannes Jakob Meyer. Effect of data encoding on the expressive power of variational quantum-machine-learning models. *Physical Review A*, 103:032430, Mar 2021.

[276] Yacob Ben-Aryeh. Quantum and classical correlations in bell three and four qubits, related to Hilbert-Schmidt decomposition. *arXiv preprint arXiv:1411.2720 [quant-ph]*, nov 2014.

[277] Xiao-Xiao Li, Peng-Bo Li, Sheng-Li Ma, and Fu-Li Li. Preparing entangled states between two NV centers via the damping of nanomechanical resonators. *Scientific reports*, 7(1):14116, 2017.

[278] Matthieu Zimmer, Paolo Viappiani, and Paul Weng. Teacher-student framework:

a reinforcement learning approach. In *AAMAS Workshop Autonomous Robots and Multirobot Systems*, 2014.

[279] Kurt Hornik. Approximation capabilities of multilayer feedforward networks. *Neural Networks*, 4:251–257, oct 1990.

[280] A.R. Barron. Universal approximation bounds for superpositions of a sigmoidal function. *IEEE Transactions on Information Theory*, 39(3):930–945, 1993.

[281] Sebastián Roca-Jerat, Juan Román-Roche, and David Zueco. Qudit machine learning. *Machine Learning: Science and Technology*, 5(1):015057, mar 2024.

[282] X. Gao and L. M. Duan. Efficient representation of quantum many-body states with deep neural networks. *Nat Commun*, 8(662), 2017.

[283] Cillian Harney, Stefano Pirandola, Alessandro Ferraro, and Mauro Paternostro. Entanglement classification via neural network quantum states. *New Journal of Physics*, 22(4):045001, apr 2020.